Colloidal Epitaxy

A Real-space Analysis

Colloïdale Epitaxy

Een Analyse in de Reële Ruimte

(met een samenvatting in het Nederlands)

Proefschrift ter verkrijging van de graad van doctor aan de Universiteit Utrecht op gezag van de Rector Magnificus, Prof. dr. W.H. Gispen, ingevolge het besluit van het College voor Promoties in het openbaar te verdedigen op maandag 30 september 2002 des namiddags te 16.15 uur

door

Jacob Pieter Hoogenboom

geboren op 01 december 1972, te Nijmegen

Universiteit Utrecht

Promotor: Prof. dr. Alfons van Blaaderen

verbonden aan de Faculteit Natuur- en Sterrenkunde van de Universiteit Utrecht en aan het FOM-Instituut voor Atoom- en Molecuulfysica te Amsterdam

N𝒲O

AMOLF FOM

'The larger the searchlight, the larger the circumference of the unknown'

Dick Taylor
(from The Tesseract by Alex Garland)

Table of contents

1

Introduction

In this introductory chapter, the three terms that together make up the title of this thesis, 'colloidal', 'epitaxy', and 'real-space', will be explained. For colloidal particles this includes the role of colloids as a model system in condensed matter physics and the use of colloids in various recently developed applications. Epitaxial crystal growth will be shortly explained, followed by a survey of research on colloidal epitaxy. Furthermore, a short overview on the use of patterned substrates in directing colloidal self-assembly for applications will be given, focusing mostly on controlled drying techniques. Finally, the principles of confocal microscopy and its use with colloids with a core-shell morphology will be given.

1.1 Colloids

1.1.1 What are colloidal particles?

The word colloid comes from the Greek word κολλα, which means glue. The use of the word colloid originates from Thomas Graham, who in a paper in 1861, used this term to classify materials that do not diffuse with water through a membrane[1], in other words, they cannot move through the pores of the membrane and thus seem to 'stick'. There is no strict definition of a colloidal particle in terms of well-defined requirements on its size, shape, or composition. Rather, the main characteristic that determines whether or not a particle is colloidal is based on its behavior: colloidal particles undergo Brownian motion.

A colloidal particle is a macroscopic entity, in general composed of a large number of atoms or molecules[1, 2]. The typical size of a colloidal particle ranges from a few nanometers to several micrometers, as indicated in Figure 1-1. At the bottom end, the colloidal size-range is bounded by large single molecules like polymers and proteins, and by so-called quantumdots or nanodots: small entities of only few atoms or molecules that display typical quantum-mechanical behavior. At the larger end of the size-range colloids are bounded by granular matter. Colloidal particles can be of either phase: solid, liquid or gas (see Table 1-1). In each phase the type of particle may vary further: solid particles may be solid in the strict sense, i.e. composed of covalently bonded atoms like e.g. SiO_2, or macromolecular, consisting of a network of entangled or cross-linked polymeric molecules like latex-particles in paint. Furthermore, not only the phase and type of colloid can vary in this size range, the phase of the medium in which these particles are suspended can be a solid material, a liquid or a gas. The various combinations of dispersing medium and type of colloid all bear different names and the most frequently occurring ones are given in Table 1-1 together with some examples[2]. Many of these classifications will sound more familiar to a broad audience than does the word colloid itself. In fact, despite the unfamiliarity of the term colloid, in every-day live we are surrounded by colloids. Milk, blood, and paint are just a few examples of colloidal suspensions.

As a consequence of the typical colloidal size-range and the fact that colloids are dispersed in an atomic or molecular medium, colloids undergo Brownian motion. A colloid is constantly being bombarded by solvent molecules, however at any instant the number of collisions is in general not completely equal at all sides, which leads to a net momentum transfer to the particle. This momentum is however highly overdamped by the solvent medium, so that displacements are only of a short range. Furthermore, the fluctuations in collisions with 'fluid'-molecules are completely uncorrelated so that the net trajectory of the particle over a larger time is completely erratic: the colloid displays a so-called 'random walk'. For granular matter, momentum of particles is such that these instantaneous fluctuations do not lead to net displacements. For low-density particles, Brownian motion can be observed for sizes up to several micrometers. For

Table 1-1 Classification of colloidal systems, after[2]

Particle type	Suspending medium	Name	Examples
solid	liquid	suspension / sol	paint, ink
liquid	liquid	emulsion	fat in water, salad dressing
gas	liquid	foam	whipped cream
solid/liquid	gas	aerosol	smoke / clouds,

instance, a recently synthesized model system of latex particles of 4 μm in diameter, still displays Brownian motion as observed under a confocal microscope[3].

As may be evident from the previous, the study of the behavior of colloidal matter is important to many areas in science and industry. Of course the food industry is a typical example hereof, but also in completely different areas like the production of paints and coatings, detergents, and body-care products (sun-cream), as well as in a process like oil-drilling, where the rheology of a clay-suspension plays a crucial role, a detailed knowledge of colloid science is essential. In the second part of the 20th century, two new fields of research in colloidal science were added, namely the use of colloids as a model system for studying the behavior of condensed matter, and the application and study of colloids in novel materials that owe their functionality directly or indirectly to the typical size of their colloidal building blocks. It are these last two developments
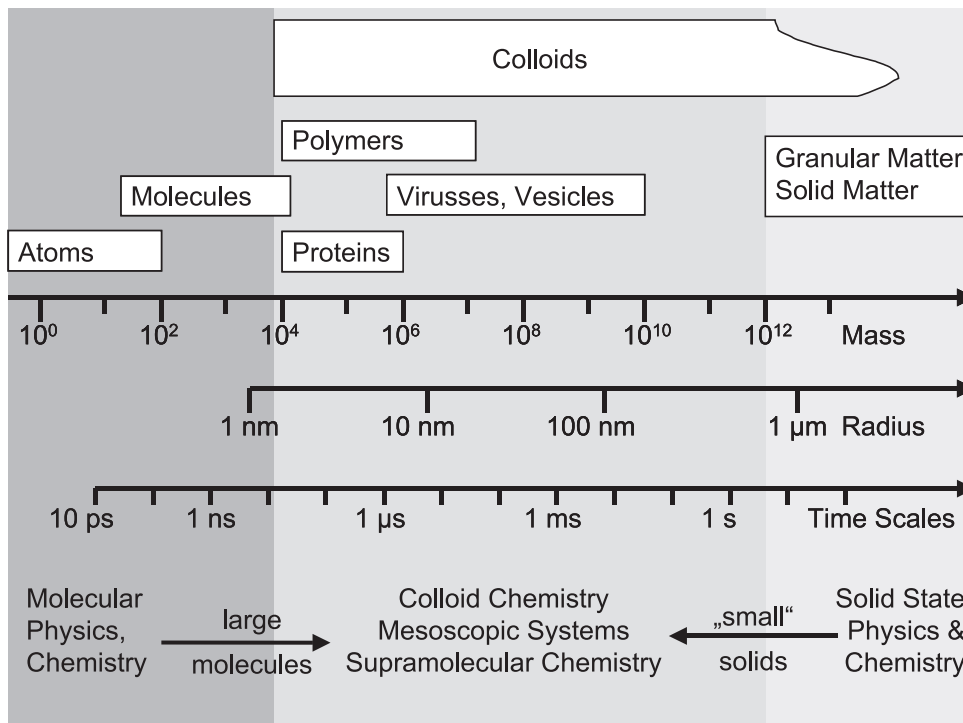
Figure 1-1 Overview of the typical size-and time-scales for colloidal particles, reproduced with permission from[161].

in which the research described in this thesis finds its motivation and application and as such, these are the subject of the next sections.

1.1.2 Colloids as a model system in condensed matter physics

Due to their Brownian motion colloids posses thermal energy that allows them to travel phase space just like atoms and molecules do. It was shown in the 1970's that the behavior of colloids in a solvent is in fact thermodynamically equivalent to that of atoms and molecules[4]. For an ensemble of colloids, statistical mechanical concepts analogous to those used in the theory of simple liquids can be applied, leading e.g. to similar equations of state when the pressure is replaced by an osmotic pressure. Furthermore, colloids in suspension show transitions between liquid-, solid-, and glass-like phases[5], similar to atoms and molecules. From an experimental point-of-view there are however several big advantages associated with the use of colloids with respect to atomic or molecular systems, which, together with this thermodynamic equivalence, make colloids an extremely useful and powerful model system.

The first experimental advantage is the larger size-range (see Figure 1-1). This allows for easy experimental techniques to probe colloidal structure, like light scattering and microscopy methods. Especially this last technique (see also section 1.3) is very powerful, as it gives a direct visualization of the local structure including structural aspects like defects and dislocations that are only visible in an averaged way in a technique like light scattering. For molecular systems direct observation on a single-particle length-scale is possible with for instance atomic force microscopy (AFM) or scanning tunneling microscopy (STM), but this is experimentally much more difficult than the simple, easy-to-handle techniques that can be used with colloidal systems. Furthermore, techniques like AFM and STM only probe surface structure, while with various light microscopy techniques on colloidal system it is possible to acquire quantitative 3D data[6-8].

Connected to the larger size range is the typical time-scale on which colloidal processes take place (see Figure 1-1). For instance the time-scale on which a 500 nm-radius particle in a dilute suspension of, for instance, water diffuses a distance equal to its own radius is half a second. These time-scales make a real-time analysis of colloidal processes possible using again simple experimental methods. This is clearly reflected in the fact that the first observations on colloidal dynamics, using a simple light microscope, were already made in the early 19th century by Richard Brown. Furthermore, if necessary to for instance follow the dynamics of a large, statistically relevant number of particles, these time-scales can be scaled up even further by dissolving particles in a solvent with a higher viscosity.

The third major advantage of the use of colloids as a model system is the possibility to chemically and physically modify particle and solvent properties. The manipulation of time-scales by modifying the solvent viscosity has already been mentioned above. However, by changing the solvent or using a mixture of various solvents, the refractive index of suspended

colloids can be matched to that of the solvent, which on the one hand minimizes Van der Waals attractions[9, 10] and on the other hand increases the depth of view in e.g. fluorescence microscopy. Recently, also solvent mixtures have been used that allow for simultaneous refractive-index and density matching[11, 12]. By varying the degree of density matching the influence of an external, one-dimensional force field on colloidal phase behavior can be examined. Apart from minimizing attractions by refractive-index matching, the interactions between colloids can be tuned over a much broader range by exploiting colloidal surface chemistry and solvent characteristics in combination with a detailed knowledge of colloidal interactions[9, 10]. In principle, the interaction potential between colloidal particles is very different from that of atoms or molecules. In most cases, the interaction between colloids can be well described by the Derjaguin-Landau-Verweij-and-Overbeek (DLVO) potential. This potential results from the combination of van-der-Waals attractions and the electrostatic interactions between the double layers created by colloidal surface charges and solvent (counter)ions. In a stable dispersion of colloids that bear a surface charge, the double layer repulsion gives rise to a large (~100 kT) repulsive barrier against aggregation in the deep van-der-Waals minimum at close contact. The range of this stabilizing repulsive interaction can be easily tuned by changing the amount of surface charge through the number of dissociable groups on the surface or through the pH of the solvent, or by varying the concentration of surface-charge screening counterions in the solution. In this last way the interaction potential can be changed from long-range repulsive through the occurrence of a small attractive secondary minimum to strongly attractive into the primary van-der-Waals minimum[10]. Apart from stabilization through double layer repulsion, colloids can be sterically stabilized by grafting polymeric chains on the surface, after which they can be dispersed in apolar solvents. This results in a short-ranged repulsive interaction, which leads to a hard-sphere like interaction[13, 14]. The addition to the colloidal suspension of a polymer that does not absorb on the particle surface leads to a short-range attractive interaction, called depletion attraction[15, 16]. Finally, the interactions between colloids can be made dipolar by application of external electric[17] or magnetic fields[18, 19]. Recently, a model system was devised in which the interactions can be varied from long-ranged repulsive -without the need for extensive ion-exchanging, which has to be done in solvents like water in order to get very low counter-ion concentrations- to hard-sphere like, to which furthermore a dipolar interaction of varying strength can be added by application of an AC electric field[20].

1.1.3 Research on the colloidal model system

The use of model colloidal particles dates back to the early work of Perrin in the beginning of the 20th century. Perrin prepared a system of monodisperse spherical colloids with which he studied the barometric height profile after sedimentation as well as translational and rotational Brownian motion. From all these three experiments he was able to determine the value of

Avogadro's number and thus he implicitly proofed the existence of atoms and molecules. For this work Perrin was awarded the Nobel Prize in 1926[1].

The development of model colloids to study atomic and molecular phase behavior started with the experimental validation of the hard-sphere liquid-solid or order-disorder transition. Due to its conceptual simplicity –no interactions between particles except for volume-exclusion– hard-spheres have been an appropriate theoretical model system for studying phase transitions. However, despite this conceptual simplicity, the hard-sphere system has been the subject of intense debate, especially regarding the question whether the hard-sphere system would indeed show a liquid-solid phase transition as predicted by Kirkwood[21]. As there are no energetic contributions to the free-energy of a hard-sphere system, the occurrence of a phase transition in this system would be driven by entropy alone. This idea was initially met with a lot of skepticism (see for instance the story (in Dutch) in reference[22]).

The first evidence that a freezing transition could indeed occur in the hard-sphere system came from computer simulations by Wood and Jacobson and Alder and Wainwright[23, 24]. In 1963, Luck, Klier, and Wesslau demonstrated that polymeric colloids formed ordered crystal structure when dried from suspensions[25]. Shortly thereafter, Sanders and co-workers showed that opal gemstones consist of regular packings of colloidal silica particles[26]. The experimental validation of the occurrence of a phase transition driven by entropy came with the work of Hachisu, Kobayashi and Kose[27, 28]. They demonstrated the transition from a disordered liquid-like colloidal phase to an ordered solid-like phase with increasing volume fraction of colloids in a system of charge-stabilized latex particles. The phase behavior of colloids that interact effectively as hard-spheres was later confirmed by Pusey and van Megen[29], who also demonstrated the occurrence of a glass transition when the system is quenched into a high-volume fraction state[30]. The phase behavior of hard-sphere particles is now well established: at volume fractions below the freezing point, $\varphi < \varphi_f = 0.494$, there is a disordered, liquid phase. Above the melting point, $\varphi > \varphi_m = 0.545$, hard-spheres order in a periodic, crystal phase. For volume fractions in between these two points, there is coexistence between a lower-density (φ_f) liquid phase and a higher-density (φ_m) crystal phase. At increasing volume fraction from the melting point, the hard-sphere crystal can be compressed up to diverging compressibility at the volume fraction for close-packing, $\varphi_{cp} = 0.74$. However, as demonstrated by Pusey and van Megen[30], the system can, for volume fractions larger than about 0.58, also be trapped in a disordered glass state.

Since then many studies have utilized colloids as a model system to test theories in condensed matter physics. Especially the possibility to perform microscopy measurements on two-dimensional (2D) systems[31-35] has been used in order to examine the Kosterlitz-Thouless-Halperin-Nelson-Young (KTHNY) scenario for 2D melting[36-39]. Although in 2D systems, long-ranged order associated with a true crystal phase cannot exist[40], a transition from a disordered liquid state to a crystalline phase with quasi long-range order occurs[40]. In the

---

KTHNY-scenario, the transition from the liquid state that is characterized by only short-ranged translational and bond-orientational order, to the solid state where both types of order are of quasi long-range, occurs via an intermediate phase called hexatic. In the hexatic phase translational order is still of short-range, but the bond-orientational order is already quasi long-range. For hard-sphere systems, the occurrence of the hexatic phase is still subject of debate[41, 42], but for 2D systems with attractive interactions the phase diagram does have a region where the hexatic phase is stable[32, 43]. Very recently, optical tweezers were used to create and study defects in 2D systems[44, 45].

Also the behavior of colloids in systems where the dimensionality ranges from 2D to 3D and the confinement has a pronounced effect on colloidal crystal structure, has been thoroughly investigated both theoretically and with computer simulations[46-51] as well as with colloidal model systems[52, 53].

Apart from the hard-sphere model systems, the previously mentioned ability to tune the interactions in colloidal systems has led to investigations on repulsive and attractive systems[16]. Colloids with long-range repulsive interactions show a liquid-solid transition at low volume fraction, but at higher volume fraction a martensitic solid-solid transition as well[54-56]. The addition of a non-absorbing polymer to a colloidal solution induces an effective short-range attractive interaction due to the mutual colloid-polymer excluded volume that is called depletion attraction[15]. The details of this interaction as well as the crystallization mechanisms of systems with an attractive potential are still being investigated theoretically as well as experimentally[16, 57-59]. Particles with induced magnetic or electric dipoles can serve as model systems to study 2D dipolar systems[34, 35] or 3D electro-rheological[17] and magneto-rheological[19, 60] fluids. Finally, experimental research on colloidal model systems has also been an inspiration for theoretical investigations. The 'like-charge attraction' between repulsive colloids confined between two glass plates is one clear example hereof, but also the invention of colloidal epitaxy[61, 62], the subject of this thesis, has inspired theoretical investigations and computer simulations[63, 64].

1.1.4 Colloids in the 'room at the bottom'

Many areas of science and technology have, in the last decades of the 20th century, seen a trend towards ever-increasing miniaturization of devices and functional components of devices. This first of all started in micro-electronics and related sciences, but also other areas of physics (e.g. optics), chemistry (micro-reactors, combinatorial chemistry), and biology (biotechnology) have seen similar trends towards or emerging research in the micro- and nanometer regime. Apart from the direction of 'macroscopic' science towards the micrometer regime, the description of and knowledge over quantum mechanics and atomic and molecular systems has evolved in such a way that it became possible to describe larger entities of atoms, in search of the crossover between quantum-mechanical and classical descriptions. These trends in the direction of science

were anticipated by Feynman, who stated that there was "plenty of room at the bottom"[65]. Although this statement to a large extent referred to the field of 'mesoscopic science', the miniaturization trends mentioned previously may be regarded as a top-down approach towards the "bottom". The nanometer-regime that forms this "bottom" is also the lower end of the colloidal size-range and the rise of science in the nano- to micrometer regime has led to an increasing interest in colloidal matter[66]. In a way, the "room at the bottom" that Feynman spoke about, is filled with colloids and colloidal materials.

Colloids find their way in medicine where they can be used for instance for the controlled release of drugs in the body by tuning the swelling properties of polymeric particles or by utilizing especially designed hollow capsules[67, 68]. These hollow capsules may also be used as chemical micro-reactors. Charge-stabilized colloidal particles embedded in a polymeric matrix were demonstrated to work as miniature chemical sensors[69, 70]. 'Bar-coded' colloids consisting of shells of different fluorescent dyes are useful in analytical and especially combinatorial chemistry[71]. Colloids are applied in catalysis, exploiting their large surface to volume ratio, or by using them as a precursor material to make a hollow network with the same characteristics[72, 73]. Two-dimensional arrays of colloids can be used as a mask for lithography in a technique called natural or nanosphere lithography[74-76]. Spherical colloids can serve as micro-lenses and 2D colloidal arrays as micro-lens arrays[77] that can for instance serve in projection lithography[78]. Other examples of functional colloids are magnetic colloids[79] and colloids with surface functional groups that can be used in electronic applications[80]. Finally, colloids are useful as probes, for instance attached to biomolecules for the use of optical tweezers in biology[81], or as a calibration standard for techniques like atomic force microscopy, scanning tunneling microscopy and near-field scanning optical microscopy[82, 83].

A special class of materials in which colloids find their application are the so-called photonic materials[84]. A photonic material is a material that has a 3D periodic dielectric structure[85, 86]. Some photonic applications result from the simple fact that the size range of colloids encloses the wavelength regime of visible light. This means for instance that a periodic array of colloids that have a refractive index different from that of their surrounding medium, can Bragg-reflect light, a fact that can be used in creation of an optical switch[70, 87].

Special attention in the field of photonic materials has been given to the development of materials with a complete photonic bandgap. In such a material light is not just Bragg-reflected when incident on a single specific crystal orientation, but the propagation of a small wavelength regime of light is completely prohibited in all crystallographic directions. As such, photonic bandgap materials hold the promise of acquiring unprecedented control over the propagation of light and of possibly playing a role in future optical integrated circuits, much alike electronic semiconductors do now[85, 86]. Since the first papers predicting the existence of photonic bandgaps much research has been devoted in search for such a material. Many of these attempts rely on the use of colloids, either as a precursor material for creating high-refractive index inverse-opal materials[88-91], or directly as the functional building block in a three-dimensional (3D) array like e.g. metallic[92] or core-shell colloids[93, 94].

1.2 Epitaxy

1.2.1 Epitaxial crystal growth

Epitaxial crystal growth is the growth of a crystal phase on the interface with another solid material. Just like the word colloid, the word epitaxy has its origins in the Greek language, being a contraction of the words τάξις meaning 'ordering' or 'order', and επι which means 'on'. Strictly speaking, also crystal growth of a one-component material after homogeneous nucleation involves epitaxial growth, namely that on its own crystal planes, but this is of course a rather trivial case. This is sometimes referred to as auto-epitaxy and is described by laws governing crystal growth. In all other cases, the structure, growth mechanism and physical characteristics of the crystallizing material close to the interface can differ considerably from those of the bulk, homogeneously crystallized material.

Epitaxial crystal growth may be influenced by the underlying substrate through a different geometry and periodicity of the substrate lattice as well as through different interaction strengths between the atoms and molecules in both lattices. Following Markov[95], epitaxial growth can be classified as either homo-epitaxy, when the differences in interaction potentials are negligible and the main epitaxial-growth influencing parameter of the substrate is its lattice geometry, or as hetero-epitaxy when the geometry of the substrate is of less importance and epitaxial growth is dominated by the interplay between the interaction strengths between various atoms and molecules.

In both the cases of homo- and hetero-epitaxial growth, the presence of the substrate potential leads to strain in the epitaxially growing crystal. If we neglect any chemical changes at the interface between the two materials, which in the case of atomic and molecular epitaxy can e.g. involve the formation of layers of adsorbed ions, or the formation of alloy or compound layers, this strain can be accommodated in the first few surface layers in two different ways. First of all, the strain can be homogeneously distributed throughout the epitaxial crystal layers, which leads to so-called pseudo-morphic growth: the epitaxial crystal adjusts its structure to that of the substrate. Secondly, the strain can be periodically built in into the epitaxial crystal, for instance through the formation of misfit dislocations. Pseudo-morphic growth can, when the combination of surface and volume free energies for a few layers of a metastable phase is lower than that for the stable phase, even give rise to the occurrence of a metastable crystal phase. In the case of metals, the energy differences between hcp, bcc, and fcc crystal structures are rather small, which is for instance evidenced in a dependence of equilibrium crystal structure on the amount of filling *d*-orbitals[96, 97]. Various metals can be epitaxially grown in a crystal structure that is metastable in bulk crystal growth, such as bcc Co on Cr[98, 99], bcc Cu on Fe[100], hcp Cu on W, and bcc Pd on W[101].

Clearly, when the epitaxially growing crystal becomes thicker, the effect of the substrate will, on moving away from the interface gradually disappear from the epitaxial crystal phase. The extent onto which epitaxial strain proceeds, depends on a lot of factors, like the amount of strain in the surface layers, the relative free energies of the different surfaces and phases, and the ambient conditions like temperature at which growth took place. The epitaxial phase can only consists of only a few pseudomorphic layers, but it may also involve several different phases, with strain relaxation extending over more than 30 molecular layers[102]

1.2.2 Colloidal epitaxy

Where in atomic and molecular systems crystallization often occurs on the solid substrate of another material, in colloidal systems heterogeneous crystal nucleation frequently takes place at the sample wall. However, contrary to the situation for atomic and molecular systems, this wall is flat on the length-scales of the colloids, providing the system with a uniform substrate potential. Heterogeneous nucleation at the wall is initiated by layering of the colloidal liquid at the flat wall as was demonstrated by van Winkle and Murray[103]. Lithographic techniques and the recently developed technique of directly sticking colloids to a substrate[104-107], give the possibility to pattern substrates with a potential that is periodic on length-scales comparable to that of colloidal particles. Colloidal crystallization on such a patterned substrate is, in analogy with atomic and molecular epitaxy, called colloidal epitaxy[61].

In the first papers on colloidal epitaxy, the technique was shown to be able to direct colloidal crystallization of hard-sphere like particles to pure fcc without the occurrence of stacking faults. This was done by using a polymeric substrate that had been patterned with electron-beam lithography with a periodic pattern of cylindrical holes. This patterned substrate then serves as a template for crystallization. For both a substrate pattern symmetry of fcc(100)[61] and of fcc(110)[62], the crystal orients with the corresponding plane along the substrate, following the template. At a plain wall, both the fcc(100)- and the fcc(110)-plane have, for hard-spheres, a higher interfacial free energy than the fcc(111)-plane[108]. This difference is overcome by the (entropic) potential generated by the template. For templates that have a lattice spacing mismatch with respect to the distances in the colloidal crystal, crystallization in the first few layers was found to be frustrated, leading to defect formation, followed at increasing distance from the template wall by relaxation to either the template lattice or to fcc(111)-oriented planes.

Lin et al. have demonstrated that colloidal epitaxy can also be used in systems with attractive (depletion) interactions[109]. They created templates by imprinting of a grating in a polymeric substrate layer. This results in either a pattern of lines, or, after repeated imprinting, in a square (fcc(100)) pattern of pillars. The line pattern was found to induce a variety of 2D phases that, however, due to the occurrence of defect-lines and dislocations, were not strictly long-range periodic. For the square pattern they observed 3D fcc crystal growth at the wall.

Recently, theoretical calculations and computer simulations have been carried out by Heni and Löwen, by which they examined the effects of surface patterns on the prefreezing or wetting

behavior of a colloidal liquid[63, 64]. They found that a hexagonal surface pattern, as well as an hcp($1\bar{1}00$) induced wetting of the hard-sphere crystal at volume fractions considerably below the bulk freezing point. Furthermore, prefreezing at higher supersaturation than for these two planes occurred at fcc(100)- and fcc(110)-patterned substrates. This wetting and prefreezing occurs first at a surface pattern that is about 3.5% stretched along both lattice directions compared to distances expected for hard-sphere crystal volume fractions. This fact is in agreement with the fact that prefreezing and wetting occurs at lower volume fractions than bulk freezing. Finally, an interesting point to note is that, inspired by experiments on colloidal epitaxy, epitaxial crystal formation has also been observed in a system of non-Brownian (granular) spheres subjected to continuous shaking[110].

1.2.3 The use of templates in assembling 2D and 3D colloidal crystals

The self-assembly of colloidal particles under the influence of convection and capillary forces generated during the drying of a colloidal suspension is an important technique to assemble colloids for applications[111, 112]. As such both the mechanisms for colloidal ordering during drying as well as the application of these particle assemblies have been investigated thoroughly since the late 1980's[74, 113-116]. In the last few years, however, the increased interest in colloidal materials that was described in paragraph 1.1.4, has lead to a boost of activities concerning colloidal self-assembly during drying. This research includes improvements of the controlled drying techniques developed by Denkov and co-workers[113-115], as well as investigations on how to direct self-assembly by drying on patterned substrates following the early work of Deckman et al. at Exxon Research[116].

In 1999, Colvin and co-workers demonstrated the growth of several millimeter (lateral dimensions) large single-crystal hexagonal stackings of colloidal particles with controlled thickness by controlled drying[117]. In their set-up the substrate that is to be patterned with colloids is placed vertically in a container that is open at the top and that is filled with colloidal suspension. Colloids order on the substrate during the slow evaporation of the solvent. The number of hexagonal layers that are deposited can be controlled by changing the volume fraction or the solvent (usually ethanol). Comparable results can be obtained by the carefully controlled, slow withdrawal of the substrate from the suspension[118]. The growth of hexagonally stacked crystal layers in between two substrate plates has also been demonstrated[119]. In these techniques the size-range of particles that can be used is however limited to particles with a diameter of about 400 nm (for silica colloids in ethanol or water) due to particle sedimentation. Several groups have recently reported the growth of crystals of larger particles. Ye et al. and Goldenberg et al. reported the growth of crystals of large polymeric particles by performing vertical controlled drying at elevated temperatures (up to 95ºC for particles suspended in water)[120, 121]. The growth of crystals of silica particles was demonstrated by Vlasov et al.

who used a temperature gradient from bottom to top of the sample to generate a particle flux opposing sedimentation[91].

As mentioned previously, these controlled drying techniques always lead to the formation of colloidal crystals composed of hexagonally arranged layers oriented parallel to the substrate. Considerable research has been devoted to directing colloidal crystallization during solvent evaporation. These techniques can be roughly divided in those that use patterns or confinements like grooves or capillaries to form localized colloidal assemblies, and techniques that direct the structure and orientation of large crystals. These techniques are sometimes also called graphoepitaxy, like in the early work of Deckman et al.[116]. They demonstrated the formation of crystalline stripes of latex colloids in the grooves of a line grating. They furthermore observed the orientation of linear chains of colloids when the spacing of the grating was comparable to that of the particle diameter.

Similar crystalline stripes can be made using the soft-lithography technique of Micro-Molding In Capillaries (MIMIC). Here, the elastomeric mold that is commonly used in soft-lithography, is used to cover parts of the substrate. If the mold structure consists of an open, interconnected structure, the open channels or voids can be filled with a colloidal suspension by capillary action. By drying the suspension after the elastomer has been filed, the substrate has been patterned with a connected structure of colloidal crystals[122]. Yang and Ozin have made similar structures, but patterned the open structure directly in V-shaped grooves in the substrate[123]. Colloidal crystallization is then strongly influenced by the confinement of the grooves, which, for these grooves as well as for pyramidal-shaped micro-wells, leads to an fcc(100)-oriented top layer. Colloidal crystallization in confined micro-wells can also be used to create unusual colloidal aggregates[124] (see also chapter 2), although this is clearly limited to very small quantities. A more useful application is to use this as a model system for testing theoretical predictions on the influence of confinement in colloidal ordering[125]. Note for instance the extraordinary pentagonal ordering of the centers particles in the second layer in the template holes in Figure 2-6d.

One-dimensional gratings with a period comparable to the particle diameter have also been used in the vertical controlled drying technique[126]. By small variations of the ratio between grating period and particle diameter, two-dimensional arrays with oriented hexagonal, centered rectangular, square or striped symmetry can be made. Similar one- and two-layer colloidal structures on 1D gratings were made by a procedure using both drying and sonification by Yi et al.[127]. Such a combined procedure was also used by Xia and co-workers, who in their set-up[128] used patterned surfaces to make regular 2D colloidal arrays as well[77]. A better control over particle ordering is achieved when a 2D pattern of holes or pillars is used on which a colloidal suspension is dried[62]. Recently, Velikov et al. used a 2D hexagonal colloid-patterned layer to direct the assembly of smaller particles during vertical controlled drying[129]. By repeating this procedure layer-by-layer dried binary colloidal crystals can be made which can even have structure that do not form in bulk binary suspensions.

Apart from relief structures like grooves and capillaries, also non-geometrical patterns with different surface properties can be used to direct colloidal assembly. Hammond and co-workers developed a technique to selectively coat a substrate with stripes of polyelectrolyte layers, which they used in colloidal assembly[130-132]. The charged polyelectrolyte layers strongly attract colloids with opposite surface charges, which stick irreversibly to the patterned areas. In this way single-layer thick colloid patterned stripes or colloidal chains can be created. The random process of particle sticking however leads to disordered stripes, contrary to use of gratings, grooves, or capillaries. Ordered arrays of colloids on flat, patterned substrates can, however, be achieved by exploiting differences in the wettability of differently patterned regions[133, 134]. Aizenberg et al. demonstrated that when the electrostatic interaction is weaker than the capillary forces generated during drying of the suspension, the drying of the substrate can cause particle rearrangements on the patterned areas. In this way ordered assemblies of similarly sized and arranged clusters of particles can be created, but furthermore, also 2D crystalline arrays can be fabricated in which the repeating unit consists of a single particle[133]. Where in this work the chemical pattern was created by soft-lithography, the same group of researchers showed single-particle assembly on substrates chemically patterned by selective UV-exposure[135]. Furthermore, chemical or charge patterns for controlled particle deposition have been made using atomic force microscopy[136] and dip-pen lithography[137].

As is evident from the preceding paragraphs almost all techniques reported so far are used to create 2D colloidal arrays. The technique of colloidal epitaxy mentioned in the previous paragraph, can be used to direct 3D colloidal crystal growth[61, 62, 109]. The creation of dried, epitaxially grown crystals for applications has also been reported by Braun et al.[138] and by Yin et al.[139]. In the first approach, Braun et al. used regular colloidal epitaxial crystal growth to grow an fcc(100)-oriented crystal in suspension. By using hydrazine hydrate as a solvent with a small amount of poly(vinyl alcohol) added, the epitaxial crystal could be dried with minimal distortions. Yin et al. cleverly used the square oriented crystal lattices that form in the pyramidal micro-wells used by Yang and Ozin as a template for successive 3D (100)-oriented colloidal crystallization[139].

1.3 Real-space analysis

1.3.1 Analysis in Real-space and Fourier-space

As was mentioned in section 1.1.2, one of the main advantages of the use of colloids as a model in condensed matter physics is the easy experimental accessibility of the colloidal size- and time-scales. These experimental methods can be divided in those that probe the structural frequency or Fourier spectrum, like light scattering, (small-angle) x-ray scattering or neutron scattering, and methods that probe structure directly in the spatial, or real-space domain, like light

microscopy, electron microscopy or atomic force microscopy. When imaging in Fourier-space, one obtains overall averaged structure functions. This has the advantage that this information is well averaged and that information over relatively large volumes in the sample is obtained at once. However, imaging in Fourier-space suffers from the inversion-problem: the resulting structure function has to be fitted by a priori making assumptions about the real-space structure. Furthermore, information on locally occurring phenomena in the sample, like defects in a crystal, is only obtained in an averaged way, thus loosing a considerable amount of information. In real-space methods, this local spatial information is clearly resolved, but here the question of obtaining reasonable statistical accuracy may become a problem. As an example of the different strengths of real-space versus imaginary space, research on the crystal structure of hexagonally stacked colloids, like that performed in chapter 8 of this thesis, may serve: For a statistically accurate determination of the relative amount of stacking-faults, a light scattering study, which directly provides the structure factor that can be fitted to provide this number, is the most appropriate tool. However, this method fails if there are e.g. pure stacking-fault free face centered cubic crystals besides heavily faulted or even randomly stacked crystals. In order to obtain information about for instance the location and faulted-grain size, one has to revert to real-space methods.

1.3.2 Confocal Microscopy

The confocal microscope[140] was invented (and patented[141]) by Marvin Minsky in 1955[142]. As will be explained in more detail below, the main characteristic of a confocal microscope compared to a regular bright field microscope, is the rejection of out-of-focus light by sequential imaging of single focal points in the sample. Thus, a confocal microscope, if operated with a pinhole as described below, requires point-by-point scanning of a sample in order to built up a single image. The resolution with which this image is finally retrieved is however much better than in a conventional bright field microscope. An alternative to the use of a pinhole and point-by-point scanning is the use of a rotating Nipkov-disk[140]. When scattering in the sample can be minimized, for instance by using a fluorescently labeled refractive-index matched sample, repeated 2D scanning at different height in the sample, gives the possibility of performing a 3D volume reconstruction. Despite this potential of 3D high-resolution imaging, Minsky's invention remained almost unnoticed. One of the reasons for this was the fact that in order to get a reasonable signal in confocal microscopy, a bright light source was needed. Minsky himself used several approaches to accomplish this, as mentioned in his 'memoir on the invention', but the possibility to use a laser light source that became available later, meant the true solution to this problem. In the 1980's the confocal microscope was 'reinvented' by several research groups, among which the group of Brakenhoff in Amsterdam. Since then, confocal scanning laser microscopy, in short confocal microscopy, has, mostly in biology, become an important tool for performing 3D sample analysis[143, 144].
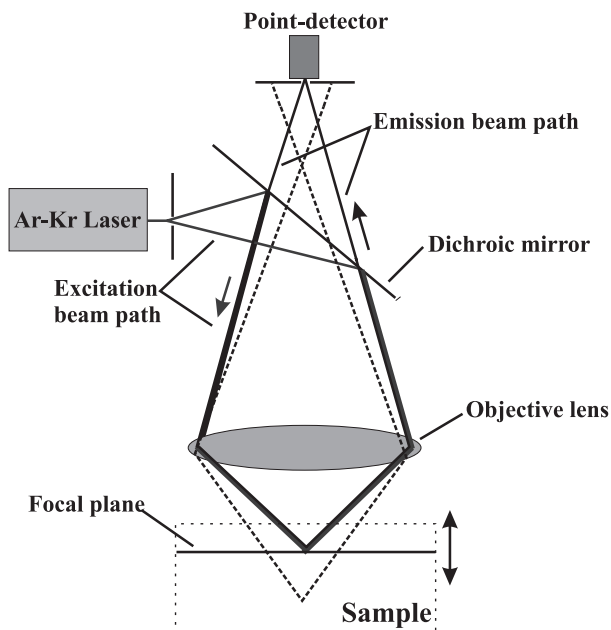
The operating principle of a confocal microscope is fairly simple, but very powerful. A schematic drawing of the main components for a confocal microscope, used with a fluorescence species, is depicted in Figure 1-2. The operating principle is exactly similar for use in reflection, with the only difference being the denomination of the respective light rays for illumination and detection. As the use of a fluorescence confocal microscope gives the possibility of performing a 3D analysis of large volumes in (colloidal) samples, the following explanation will assume the use of a fluorescence probe.

The main difference of a confocal microscope compared to a regular bright field microscope is the use of two pinholes. One of these pinholes is placed in the back focal plane of the objective in front of the light source. The other pinhole, the actual 'work-horse' of the microscope, is placed in the focal plane in front of the detector (Figure 1-2). Consequently, the detector can just be a point detector, usually a photo multiplier tube. Now, light excited in the sample in the focal point of the objective is precisely imaged in the opening of the detector pinhole (see the straight lines in Figure 1-2). Light that is excited from any point in the sample outside a small region around the focal point is, to a large extent, blocked by the detector pinhole (see the dashed lines in Figure 1-2). In this way, a single point anywhere in a 3D sample can be accurately imaged. By scanning this point laterally through the focal plane, a 2D image of a slice through the sample can be made. For a fluorescently labeled sample of which the refractive index is matched to that of the solvent, the depth of imaging is only limited by the working distance of the objective. With the use of a high numerical aperture lens this is typically a few hundred micrometers.

The second confocal pinhole, placed in front of the light source, serves to create a point source. This point source is focused to a diffraction-limited spot in the sample. The intensity distribution of excitation light inside the sample is given by the point-spread function (PSF) of the microscope lens system. This PSF is a strongly peaked function that, in the focal plane, is, ideally, given by the Airy function[145, 146]:

$$I(v) = \left(\frac{2J_1(v)}{v} \right)^2 , \qquad (1.1)$$

Figure 1-2 Schematic image of the operating principle of a confocal microscope. The straigth lines indicate the path followed by excitation and detected emission light (assuming fluorescence microscopy). The dashed lines indicate the beam path of light generated by an out-of-focus source, which is effectively rejected by the pinhole aperture of the point-detector.

where $J_1(v)$ is the first-order Bessel function, $v = 2 \cdot \pi (NA) r / \lambda$ with λ the wavelength of the light, $r = (x^2 + y^2)^{1/2}$ the distance from the center point, and NA the numerical aperture of the lens defined as: $NA = n \cdot \sin\theta$. In this last expression, n is the refractive index of the immersing medium of the lens and θ is half the total collecting angle of the lens. The distance towards the first minimum in the Airy function gives the Rayleigh resolution criterion: $r_1 = 0.61 \cdot \lambda / NA$. In this first maximum about 82% of the total intensity is contained. The excitation light is thus already strongly focused in the volume that is going to be imaged. The emitted light is proportional to the intensity with which fluorophores are being excited. As imaging occurs through the same objective, the distribution of excitation light in the plane of detection is proportional to the square of the PSF. The use of the pinhole in front of the light source thus greatly enhances resolution. Note that increasing the opening diameter of the pinhole enlarges the imaged volume in the sample and makes the confocal microscope work more like a regular microscope. This increases the signal-to-noise ratio, as it enhances the collected intensity. The optimal size of the detector pinhole is approximately given by the diameter of the Airy disk, see e.g. the reference by Sandison et al.[147] for more details on signal-to-noise ratios in confocal microscopy.

The equations given above describe the form of the PSF in the focal plane perpendicular to the optical axis. Along the optical axis, the form of the PSF is however quite different. The form of the PSF in a plane that contains the optical axis is given by a sinc-function:

$$I(u) = \left(\frac{\sin\left(\dfrac{u}{4}\right)}{\dfrac{u}{4}} \right)^2 , \tag{1.2}$$

where $u = k(NA)^2 z / n$ with z the distance along the optical axis. The distance to the first minimum in this function is $z_1 = 2 \cdot n \lambda / (NA)^2$. With a refractive index of about 1.5, it follows that $z_1 = 3.4 \cdot r_1$. It should be noted that apart from the higher order maximums in the focal plane and along the optical axis, the 3D Airy function also exhibits higher order maximums above and below the focal plane that are displaced away from the optical axis (intensity profiles of this function can for instance be found in references[145], and [146]. The first order maximums of these can especially give non-negligible peak intensities that are important to consider in the design of a colloidal model system for 3D confocal analysis.

1.3.3 3D Analysis and the use of core-shell colloids

As described above, confocal microscopy gives the possibility to perform a 3D volume analysis of a colloidal sample. However, also with for instance differential interference contrast microscopy, detailed volume investigations in nearly refractive-index matched systems can be carried out[8]. The working distance from the sample wall that can be achieved with fluorescence

I   **II**   **III**

(a)

I   **II**   **III**

(b)
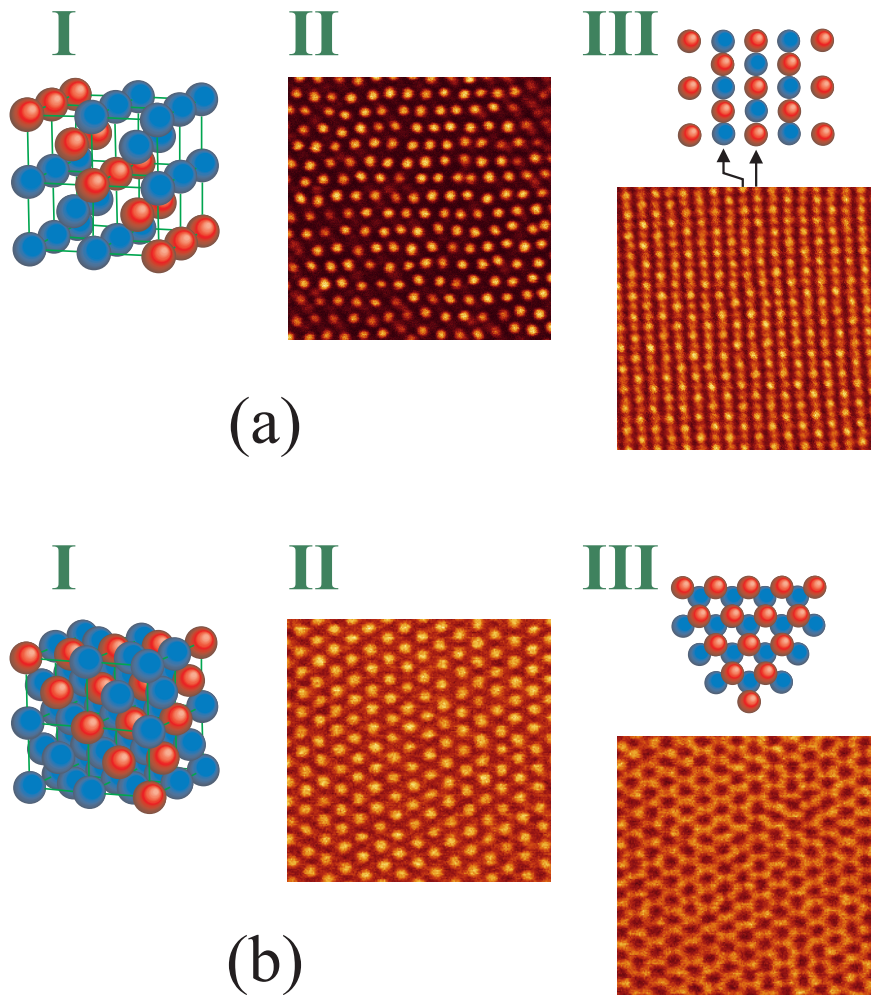
Figure 1-3 Examples of 2D confocal microscopy images (Leica TCS NT-2, 1.4 NA, 100x, excitation wavelength: 488 nm) for different crystal structures in a system with long-ranged repulsive interactions. Particles are 1.2 μm PMMA spheres uniformly labeled with the fluorescent dye NBD as described in [3]. (a) A low-volume fraction BCC crystal (I), together with a confocal image of the densest plane in the BCC-crystal, the (110)-plane (II). Separate particles that are completely fluorescent can still be detetected due to the repulsive interaction. In a confocal image taken in between two crystal planes (III) the intensity profiles of successive planes start to overlap, which for the BCC(110)-plane leads to a striped image. (b) A high-density FCC-crystal with the same sequence (I-III) of images. In III it can be clearly seen that in between two layers separate particles can not be detected anymore.

confocal microscopy and the resolution with which quantitative 3D data can be retrieved, are, however, far beyond those of other techniques including non-fluorescence confocal microscopy[148].

In order to achieve the determination of particle coordinates with high resolution the simple use of fluorescently labeled colloids is not enough. In the case of colloidal particles that have a long-ranged repulsive interaction, liquid-solid phase transitions can occur at rather low volume fractions[54]. The interparticle spacing is then large enough to prevent overlap of the intensity profiles of neighboring particles (see also Figure 1-3). These intensity profiles are the result of a convolution of the microscopic PSF (see e.g. equations (1.1) and (1.2)) with a single particle's
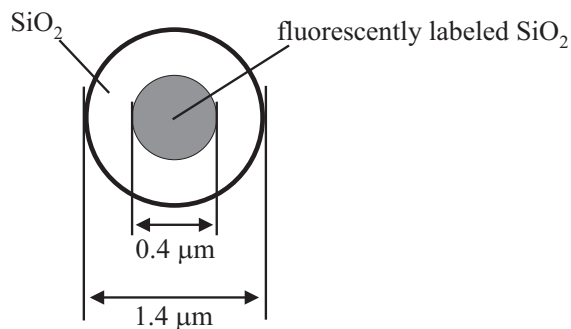
Figure 1-4 Core-shell morphology for colloids used for quantitative 3D confocal microscopy. The sizes indicated correspond to those of the particles used in several of the following chapters.

(spherical) form factor. As is evident from the previous paragraph, the problem of overlapping intensity profiles is worst in the direction parallel to the optical axis. This can for instance be seen in Figure 1-3b-III. At decreasing interparticle distance and thus at higher volume fractions, this will result in an impossibility to determine bulk coordinates. For a system of particles with short-ranged, or even hard-sphere like interactions, this will, for completely fluorescent particles, occur in the entire interesting region of the phase diagram.

A way around this problem is the use of colloids with a core-shell morphology (see Figure 1-4). At first, relatively small (radius of about 100 to 200 nm) colloids are synthesized that are labeled with a fluorescent dye. These particles are then used as seeds in a subsequent seeded-growth synthesis without the fluorescent dye present. These procedures have especially in the case of silica been well investigated. Various fluorescent dyes, like fluorescein[149], rhodamine[150], and eosin[151], and other optically active molecules, like erbium[152], can be covalently attached to the silica network using a modification of the usual Stöber-synthesis[149, 153]. The seeded-growth can be performed in a well-controlled continuous feed process as described by Giesche[154]. With this procedure the final sphere diameter can be controlled up to several nanometer. Furthermore, the seeded-growth procedure sharpens the size distribution of the particles[155]. The polydispersity, the deviation in particle diameter relative to the average, is about 4 to 5% for the seed particles from the Stöber particles, which after seeded growth results in a final polydispersity of about 1 to 2% for spheres with a diameter larger than 1 μm. Instead of using the Stöber synthesis for making the core particles, also a micro-emulsion synthesis can be performed[156]. In this way the core polydispersity can be reduced to below 1%, which will result in extremely low polydispersities for the final particles. For an accurate detection of a single sphere's intensity profile along the optical axis in the case of nearly hard-sphere particles, it was found that a 400 nm-diameter core particle labeled with fluorescein, needs an outer non-fluorescent silica shell with a final diameter of about 1 μm or larger. The precise ratio depends however on various parameters like the emission wavelength of the fluorescent dye (540 nm for the dye fluorescein isothiocyanate that we have used), the numerical aperture and PSF of the optical system, and the amount of refractive index matching.

In Figure 1-5 an example is shown of a 2D confocal image of an hcp crystal of hard-sphere like, core-shell silica particles. The image has been taken in approximately 18 μm above the first layer at the sample cell wall. Apart from the in-focus particles, particles in a next layer are also vaguely visible, as also indicated in the reconstruction in the top right corner. The interparticle spacing in the image is 1.46 μm compared to a total diameter of 1.4 μm, while only the 0.4 μm-diameter core is visible in the image. For each of these 2D images, feature coordinates can be
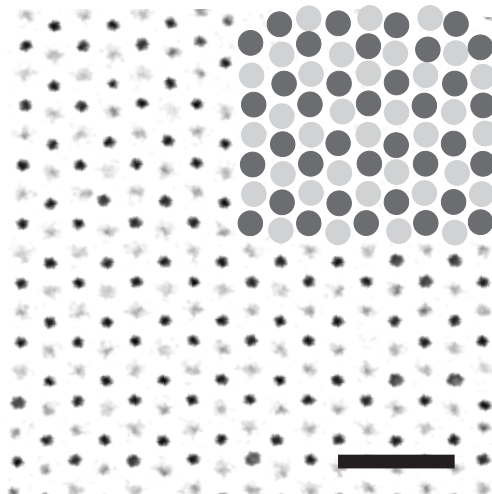
Figure 1-5 Confocal image (Leica TCS NT-2, 1.4 NA, 100x, excitation wavelength: 488 nm) taken 18 µm deep in a suspension containing an hcp-crystal of hard-sphere like core-shell colloids. The particles have an outer radius of 700 nm and a fluorescently (FITC) labeled silica shell with a radius of 200 nm. Particles in the next layer are vaguely visible in between the particles in focus. In the top right corner spheres have been drawn on the positions of the retrieved 3D coordinates projected in the image plane. The length of the scalebar is 5 µm.

retrieved following the procedures described by Crocker and Grier[157]. For the whole set of 2D feature coordinates, 3D coordinates can be retrieved as is described for instance in chapters 4 and 7 of this thesis. The top right corner of Figure 1-5 shows spheres (diameter not to scale) drawn over the 3D coordinates of the particles visible in the confocal image, projected onto the image plane.

The 3D imaging using confocal microscope of a fluorescently labeled core-shell system was first demonstrated in 1992[158]. Shortly after, Verhaegh et al. showed the possibility of imaging a binary system consisting of particles labeled with two different dyes, fluorescein and rhodamine[150]. The first demonstration of the possibility to retrieve full 3D coordinate set of a colloidal sample came with the analysis of the structure of a hard-sphere glass in 1995[159]. This paper was quickly followed by more research on hard-sphere glass formation[11, 160], the analysis of epitaxially grown hard-sphere fcc-crystals[61, 62], gelation[6, 7], and nucleation events in a hard-sphere system[12].

1.4 Thesis layout

The work described in this thesis is organized as follows. In chapters 2 and 3 techniques for making templates for use with colloidal epitaxy will be described. In the second chapter we will focus on lithographic techniques, i.e. electron-beam lithography and further wet and dry etching, and soft-lithography. In chapter three a technique that relies on the use of optical tweezers to directly stick colloids on a substrate will be described. These colloid-patterned substrates can be used in a wide variety of applications, among which the use as a template in colloidal epitaxy.

In chapters four and five the real-space study of colloidal epitaxy on two different model systems forms the central point. In chapter four a model system of hard-sphere like colloids is examined, with which we demonstrate the growth of the metastable hexagonal close packed crystal. Furthermore, a detailed analysis on the effects of template-crystal mismatch and structural relaxation will be presented. In chapter four colloidal epitaxy is demonstrated for a system of density-matched colloids interacting through long-ranged repulsive interactions. For this system epitaxial growth is examined on a template that consists of a one-dimensional pattern of lines, which is found to induce, among others, formation of an otherwise metastable face centered cubic structure and of a one-dimensional string liquid surface layer in a three-dimensional crystal.

In chapter six, the use of templates in controlled drying techniques that are commonly used for assembling colloidal crystals for applications, will be examined. Finally, in chapters seven and eight, the crystallization of micron-sized silica colloids on a flat substrate in the gravitational field is analyzed. In chapter seven the liquid-crystal transition that takes place during particle sedimentation is examined in detail. This knowledge is first of all useful for an a priori understanding of crystal growth in an external field, but may furthermore serve as a first step to later compare results on epitaxial crystallization. In chapter eight, we will focus on the structural aspects of colloidal crystals grown during sedimentation and more specifically on the occurrence of stacking faults.

2

Lithographic techniques for making templates for colloidal epitaxy

In this chapter the various techniques that we have used for patterning substrates for colloidal epitaxy will be presented. These techniques rely on either electron-beam lithography or soft-lithography. For electron-beam lithography the direct writing of colloidal-epitaxy templates in a poly(methylmethacrylate) layer will be discussed, as well as the transfer of this pattern to solid substrates like glass, quartz or silicon using subsequent wet etching or plasma-etching. These solid substrates can also be used as a master for soft-lithography. For soft-lithography the replication of patterns in polyurethane relief structures will be shown as well as the chemical patterning of glass substrates using a sol-gel mixture that contains a silane-coupling agent. Several examples of the use of silicon, polyurethane and silane-coupling agent coated templates will be given for colloids with diameters ranging from 140 nm to 1.4 μm.

2.1 Introduction

Various areas of research in science and technology have in the past decades seen a trend towards the investigation and use of materials with sizes in the micro- to nanometer regime. This has also led to an increased interest in colloids and materials made of colloids. With the size-range of colloids, which typically spans the range from several nanometers to micrometers, and with the possibility to chemically control particle composition and particle interactions, colloids find their way to applications such as photonics[70, 84, 162], electronics[80], sensors[69, 70], drug delivery[68], and combinatorial chemistry[71]. A large number of these applications rely on the ability of colloids to self-assemble, which allows for an easy and fast technique to make functional two-dimensional (2D)[114] and three-dimensional (3D) colloidal arrays[70, 84, 162]. The possibility to control and direct colloidal self-assembly is of great interest for most of these applications. One of the possible techniques that were recently introduced is the use of a patterned substrate, a method called colloidal epitaxy[61, 62]. Colloidal epitaxy can also be used in combination with the technique of controlled drying, where the slow evaporation of a colloidal suspension is used to arrange colloids in 2D and 3D crystals with controllable thickness[114, 117]. In this chapter the lithographic techniques that we have used to pattern substrates for colloidal epitaxy will be presented. Apart from these lithographic techniques we also used a new method that relies on the use of optical tweezers to directly position and stick colloids on a substrate, which will be discussed in the next chapter.

The development of techniques for printing and patterning has a long history throughout human development[163]. The oldest of the lithographic techniques that are currently in use in science and industry is photolithography, invented in the late 1950's. In photolithography a pattern contained on a mask is transferred to a resist material by UV-illumination of the resist through the mask. The resist material undergoes a chemical (conformational) change upon exposure. For a so-called positive resist, i.e. a resist material that becomes dissolvable after exposure, this is usually a depolymerization reaction, while for a negative resist, where the unexposed parts are being dissolved, a cross-linking process occurs. Depending on the type of resist used, the exposed or the unexposed parts of the substrate material are being dissolved after writing with a relief pattern as a result. This relief structure may serve as a mask for further processing, like e.g. wet etching or plasma etching. Apart from resist-illumination, exposure to UV-light can also be used to induce localized chemical changes in a self-assembled monolayer (SAM) by which a chemically patterned substrate can be made that can e.g. be used for colloidal deposition[135].

Photolithography is the main tool in the fabrication of micro-electronics and every new development in making printable feature sizes smaller, has led to increased storage capabilities and faster operation speeds of computers. The feature sizes that are achievable with photolithography are however limited by the wavelength of the UV-light that is used, which has led to the development of other techniques for printing and lithography that can be used for even

smaller features. These include extensions of photolithography to the deep ultraviolet and X-ray regime, as well as techniques like electron-beam lithography and, very recently, soft-lithography[163, 164].

The basic principle of electron-beam lithography is similar to that of photolithography, but with exposure of the resist material to a focused electron beam instead of UV-light. Contrary to photolithography, there is no mask being used and the pattern is directly written in the resist material. Electron-beam lithography allows for the creation of patterns with lateral dimensions ~ 20 nm in size with recently reported widths of single lines down to 5 nm[165]. The main limitations in electron-beam lithography are the generation and diffusion of secondary electrons in the resist material, the so-called proximity-effect, and the polymeric nature of the resist material that for instance causes swelling of unexposed parts. The resist relief structure can be directly used as a template for colloidal epitaxy, or it may again serve as a mask for further etching. However, just like with photolithography, exposure to the focused electron-beam can also be used to induce a chemical change in the top layer of a substrate only[166]. Such an approach has for instance been used to selectively remove exposed patches of a uniformly nanoparticle-coated substrate[167].

A very recent alternative to photolithography is the use of soft-lithography. The term soft-lithography comprises a series of techniques popularized and developed by the group of G. M. Whitesides at Harvard University that utilize elastomeric negative molds for pattern replication and printing. The initial work mostly involved the creation of polymeric molds of an existing pattern and the selective printing, called micro-contact printing (μCP), of functional thiol-molecules on gold surfaces. However, a boost of activities following the first papers, has since then shown the applicability of the technique to a wide range of patternable substrates and printable materials. The main advantages of soft-lithography is that these techniques are cheap and easy-to-handle, that they do not rely on clean-room facilities except for the creation of the master, and that they can be used with a large variety of chemicals and other materials. For excellent reviews see Xia and Whitesides[164], and Michel and co-workers[163].

Several groups have used soft-lithography either to directly pattern colloids on a substrate, or for the creation of templates for colloidal assembly. Already in the early stages of the development of soft-lithography, its usefulness in directing colloidal crystallization was shown. The elastomeric mold, when consisting of an open, interconnected structure, can be used to cover parts of the substrate, while the open channels or voids are being filled with a colloidal suspension by capillary action. In general, this method is called Micro-Molding in Capillaries (MIMIC). By drying the suspension after the elastomer has been filed, the substrate has been patterned with a connected structure of colloidal crystals[122].

More approaches towards directing colloidal crystallization have been taken using soft-lithography to pattern a SAM. Most of this work uses the elastomeric stamps to 'ink' a solution that contains molecules with reactive thiol-groups, which is subsequently transferred to a gold-coated substrate by μCP[164]. The large amount of research that has been performed on soft-lithography since the early papers, has however led to a very wide variety of patternable

substrates and transferable molecules[163, 168, 169]. Finally, a very promising development is the growth of poly(acrylic acid) (PAA) relief structures on various types of substrates using soft-lithography as shown by the group of Crook[170, 171]. In their approach a substrate, either gold, titania or silicon, is first partly passivated by using an elastomeric mold that has been inked with hexadecanethiol. The unpassivated regions are subsequently coated with a SAM of sulfanylundecanoic acid that contains an endgroup that after further treatment can be grafted with poly(acrylic acid). Using this method is a very convenient way to replicate the PMMA-templates that are otherwise made with electron-beam lithography.

2.2 Electron-beam lithography

2.2.1 Direct writing of templates in PMMA

For the use of templates in colloidal epitaxy experiments, mostly PMMA-patterned substrates were used. As these templates were used on an inverted confocal microscope, transparent substrates had to be used. In a first approach thin glass cover slides (Chance no. 1) were coated with an approximately 11.5 nm-thick layer of gold. This thin a gold layer does not completely wet the glass substrate but rather consists of separate islands. This however does not form a limitation for electron-beam lithography as long as the layer remains conductive. The gold-coated films de-wet further in time and thus have to be used for further processing shortly after deposition. A second type of conductive layer that was used was indiumtinoxide (ITO), which is commonly used as a transparent electrode. ITO was sputtered onto the same glass cover slides by Thin Film Devices (Anaheim, US), with the following specifications as stated by the supplier: 88% transmission at 588 nm, conductivity 50 Ω/sq, surface/defect-ratio 80/50. The thickness of the coating was not precisely known but on the order of several 100 nm with a non-uniformity of less than 0.05 (stated by the supplier).

Glass slides were cleaned by immersion in chromosulfuric acid (Fluka) for at least 20 minutes and subsequently rinsed with demineralized water and ethanol (Merck, absolute grade). After coating with the conductive material the substrate was spin-coated (Fairchild Convac Spincoater 1001) at 1000 rpm for 30 seconds with a solution of chlorobenzene that contained 4wt% of PMMA (MicroChem Corp., 950k). The spin-coated substrate was then baked on a hotplate (HG Präzitherm) for one hour at 175°C. The PMMA-layer was fluorescently labeled with pyromethene 580 (Exciton) by dissolution of 10^{-3} wt% of dye in the chlorobenzene-PMMA-solution. Dissolving larger amounts of dye was found to significantly hinder particle recognition close to the surface in confocal microscopy analysis. After electron-beam writing (see below) the PMMA-coated substrate was immersed in a 1:3 volume mixture of methylisobutylketone and 2-propanol (IPA) for 1 minute. The dissolution reaction was stopped by rapidly transferring the substrate to pure IPA.

Table 2-1 Process parameters for various patterns in electron-beam lithography

Pattern	Radius (nm)	Substrate[1]	dose (μC/cm^2)	defocus (nm)
lines	-	A	700	150
hcp(1100) / dhcp	500	A	125,000	800
hcp(1100) / dhcp	600 - 700	A	240,000	800
hcp(1100) / dhcp	700	A	240,000	800
hcp(1100) / dhcp	> 800	A	270,000	1050
fcc(100)	500	B	23,750,000	-
fcc(100)	450	B	20,000	700
fcc(100)	90	C	600,000	100
fcc(100) [2]	70	C	250	100
fcc(100)	450	C	70,000	600

[1] The different letters indicate the following substrates (from bottom to top layer):
    A: glass / Au or ITO / PMMA
    B: glass / Cr / PMMA (as-received maskplate)
    C: Si / S1813 / Ge / PMMA
[2] This pattern was written without switching off the electron beam between subsequent exposures

Patterns were written directly in the PMMA-layer using an electron-beam pattern generator (Philips EBPG-5 HR-100 FEG). Patterns consisted of periodic arrays of holes, except for samples used in experiments with long-ranged repulsive colloids, where a pattern of equally spaced horizontal lines was used (see Table 2-1). As this line-pattern is relatively straightforward to generate, the description of the writing-process parameters will be restricted to the patterns consisting of holes. An overview of several typical patterns and the crucial parameters is given in Table 2-1. For each pattern different radii for the holes in the pattern are listed, where both lattice distances can be expressed in terms of this radius, respectively as $(2R\sqrt{3}, 4R\sqrt{(2/3)})$ for hcp(1100)[172] and $(2R, 2R)$ for fcc(100)[61]. In both these patterns (see Figure 2-1 and Figure 2-3 respectively for examples) at least two neighboring holes are ideally touching. The EBPG was operated at a voltage of 100kV.

The holes were written by a single exposure at each of the lattice sites. For patterns consisting of holes with a radius less than approximately 100 nm and a spacing of less than 300 nm, considerably faster writing can be achieved by leaving the electron beam on during displacement, as will be shown below. As exposure to too high an electron-dose leads to inversion of the PMMA back to positive type, thus rendering the over-exposed parts undissolvable, the beam width resolution was set to 100 nm. Furthermore, the electron-beam was defocused to typically ¾ of the desired hole-diameter (see Table 2-1). Proximity effects give the actual hole-diameter the appropriate size. Furthermore, these proximity effects make the pattern, especially in the case of the ideal (i.e. corresponding to close packing of the resulting three-dimensional lattice) lattice, very sensitive to the dose of the electron beam, as indicated in Figure 2-1 for an hcp(1100)-pattern. Note that the slight asymmetry of the electron beam profile becomes clearly visible due to the proximity effect, as indicated by the arrows in Figure 2-1. For the fcc(100)-lattice a large
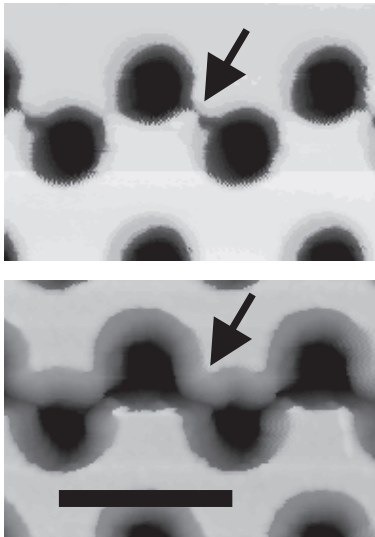
Figure 2-1 AFM images of an hcp(1100)-template in PMMA. The top figure has been written with an electron-beam dose of 135.000 μC/cm², the figure at the bottom with a dose of 140.000 μC/cm², the defocus has in both cases been set to 800 nm. The arrows indicate the positions where the asymmetry in the hole pattern becomes visible in an overlap between neighboring holes. The depth of the holes in the middle (dark area) is 450 nm. The length of the scalebar is 4 μm.

amount of overlap leads to the formation of a lattice of pillars, as shown in Figure 2-3b. For the same reason, stretching of the lattice distances away from close packing leads to a reduction in the actual hole diameter at the same electron dose, typically by a factor of about 0.8 in the diameter for a stretch of 1.3 or larger. The depth of the holes given in Figure 2-1 was 450 nm corresponding to complete dissolution of the PMMA, as measured by Atomic Force Microscopy (AFM, Park Scientific Instruments) in tapping mode. The depth profile at the edges of the holes also varies with dose and distance between the holes (as can be seen in Figure 2-1), but was always found to have a radius of curvature much larger than the radius of the hole opening.

This patterned PMMA-layer can be directly used in colloidal-epitaxy experiments, both as a model hard-sphere template like with silica particles in a refractive-index matching solution mixture of glycerol and water[61, 62, 172][1] and with PMMA-particles in refractive-index and density-matched mixtures like tetralin, cis-decalin and carbon tetrachloride[11], as well as as a long-ranged repulsive boundary like with PMMA-particles in a solvent mixture of cycloheptylbromide/ cis-decalin[173][2]. However, the PMMA templates are less suited for use in for example controlled drying experiments[114, 117], for use as a master in soft-lithography, or for photonic applications where the final goal is to achieve a single high refractive-index material device of e.g. Si[91]. In controlled drying techniques solvents most commonly used are ethanol and water[114, 117], which either dissolve or delaminate the PMMA-layer. In soft-lithography (see the paragraph on soft-lithography below) the PMMA-layer was often found to be stripped off from the substrate together with the poly(dimethylsiloxane) (PDMS) master. In the next paragraph two approaches to transfer the PMMA-pattern to glass or quartz, respectively silicon will be described.

---

[1] the low amount of water (volume ratio of water: glycerol = 1: 4.15 in this mixture was not found to affect the PMMA-layer, contrary to pure water which delaminates PMMA from the substrate.

[2] recently Yethiraj and van Blaaderen have shown that, in this particular solvent mixture, interactions between PMMA-particles can be tuned over a broad range covering hard-sphere like, long-ranged repulsive and strongly dipolar[20].

2.2.2 Pattern transfer to solid substrates

The patterned PMMA-layer that was described in the preceding paragraph can also serve as a mask for further processing, as indicated in Figure 2-2. For the applications listed above, two different approaches were taken. For use as a soft-lithography master, a template was created in a thick quartz plate, following the procedure listed in Figure 2-2. For use in controlled drying techniques with the final goal to obtain an all-silicon photonic device, the procedure in Figure 2-2 was slightly modified by making a four-layer substrate as explained below.

The quartz substrates used were as-delivered square maskplates (HOYA) for photolithography that had a 80 nm-thick Chromium layer, a 20 nm-thick anti-reflection coating layer (which for the processing described here is treated similarly as the Cr-layer) and a top PMMA-layer. The PMMA-layer was patterned with electron-beam lithography as described above with the parameters listed in Table 2-1. The pattern was transferred to the Cr-layer by using a Cr-etchant (Merck). Subsequently, the quartz-plate was exposed to a 50 sccm CHF_3 / 2.5 sccm O_2 Reactive Ion Etch (RIE, Leybold Z 401S, 50 W, -350 V, at 8 µbar for 50 minutes). The Cr-mask can be completely removed by again performing a wet etch, but for soft-lithography this final step is not necessary.

Silicon wafers were patterned by a similar repetition of RIE-steps using a three-layer mask consisting of Microposit SHP1813 photoresist (S1813, Shipley), Ge, and PMMA. The S1813 was dissolved in propyleneglycol monomethyletheracetate (PGMEA, 12.5 vol%). Silicon wafers (Virginia Semiconductors) were cut to the desired lateral sizes and spin-coated with S1813 at 3000 rpm for 1 minute. The S1813 was subsequently baked on a hotplate with a starting temperature of 100°C that was increased with 10°C every 5 minutes to a final temperature of 200°C. The baking time at 200°C was one hour. A ~25 nm-thick Ge layer was sputtered on the S1813-coated wafer before again spin-coating with PMMA. First, a 4wt% solution of PMMA containing the primer hexamethyldisilizane in chlorobenzene was spin-coated at 3000 rpm until the substrate had a

Figure 2-2 Schematic illustration of the patterning of solid substrates using electron-beam lithography and wet and/or reactive ion etching. For patterning relief structures in silicon a four-layer mask consisting of Si, S1813-resist, Ge, and PMMA was used following a similar sequence of steps as depicted here

35

(a) (b)
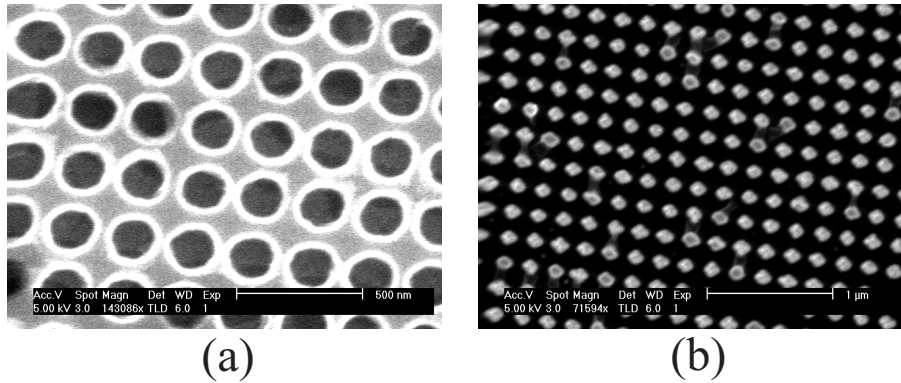
Figure 2-3 (a): SEM image of a square symmetric silicon template with a lattice spacing of 221 nm and a depth of about 70 nm. The PMMA-layer has been exposed with a dose of 635,000 $\mu C/cm^2$. (b): Like (a) but with a lattice spacing of 204 nm and equally spaced silicon pillars as a result of proximity effects.

dry appearance, followed by spin-coating a plain 4wt% PMMA-solution in chlorobenzene at 2500 rpm. After PMMA-coating the samples were again baked on a hotplate, this time at 175°C for one hour. The desired pattern was then written in the PMMA-layer using electron-beam lithography and development as described above. Before transferring the pattern to the Ge-layer, a 15-seconds descum was applied to the sample using an O_2-plasma (20sccm, 40 W, -170 V at 8 μbar). The subsequent RIE-steps were as follows: Ge: 9.0 sccm $SiCl_4$ / 9.0 sccm Cl_2 / 10.5 sccm He (65 W, 250 V at 10 μbar, 60 seconds), S1813: 20 sccm O_2 (40 W, -170 V, at 8 μbar, 10 minutes), and Si: 9.0 sccm $SiCl_4$ / 9.0 sccm Cl_2 / 10.0 sccm He (40 W, 200 V, at 10 μbar). The etch-rate in the Si-wafer was about 25 nm/min.

Alternatively, Si substrates can be patterned using only a spin-coated and patterned PMMA-layer as a mask, but the relatively high etching speed of PMMA in the Cl_2-plasma, together with the difficulty in preparing sufficiently homogeneous PMMA-films with a thickness of 600 nm or larger, limits the maximum achievable pattern depth in that case to about 150 nm. For the three-
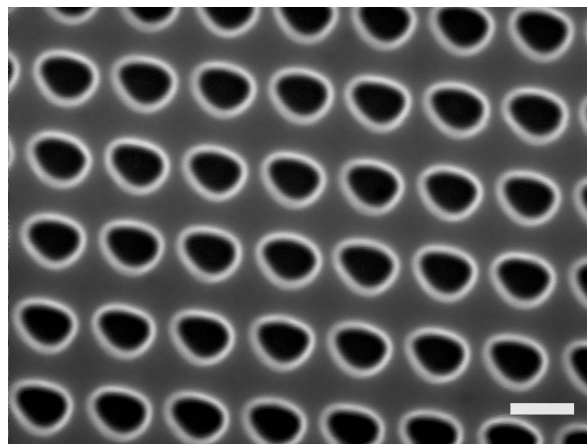
Figure 2-4 SEM image of a square-symmetric pattern of holes with a spacing of 140 nm in silicon. The PMMA-layer was written without switching the electron-beam off in between successive lattice positions. The scalebar indicates 100 nm.
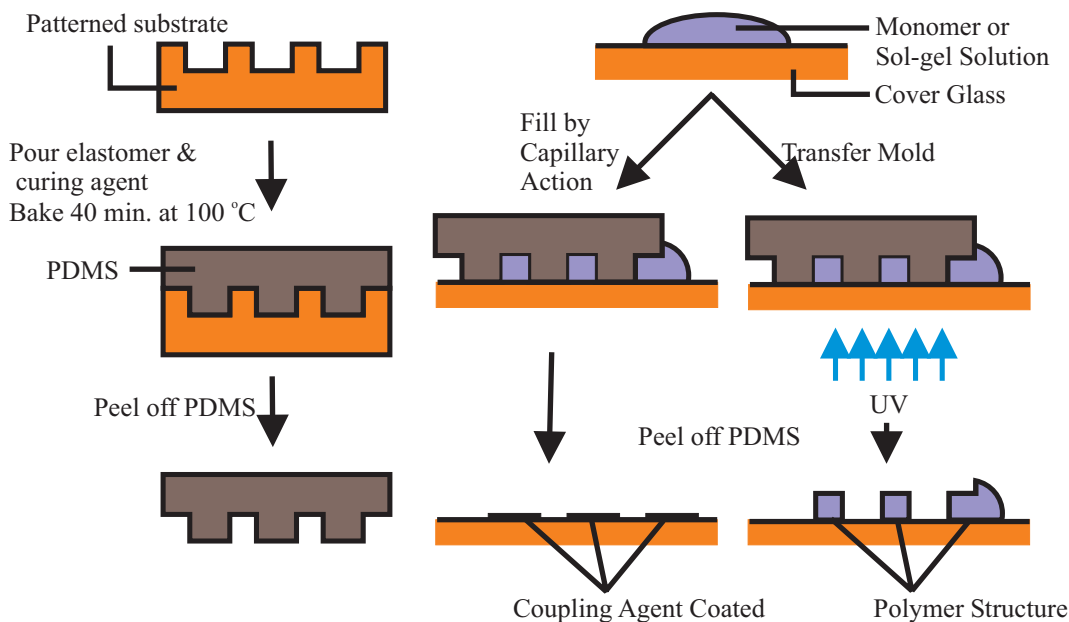
Figure 2-5 Schematic illustration of the soft-lithography techniques used in this study. The scheme to the left depicts the making of the elastomeric mold of a solid relief structure. The scheme to the right illustrates micromolding in capillaries (MIMIC) and micro-transfer molding (µTM).

layer mask a pattern depth of about 500 nm can be easily achieved. Several examples of Si-templates are given in Figure 2-3. As mentioned before, for patterns consisting of holes with a radius less than approximately 100 nm and a spacing of less than 300 nm like those in Figure 2-3, considerably faster electron beam writing can be achieved by direct writing with a continuous electron beam. The maximum achievable hole radius listed above is due to the limited electron-beam dose in this case. The continuous writing process leads to a reduction of writing time in the EBPG of about 12 times. In Figure 2-4 an example of a pattern in Si, in distances comparable to that in Figure 2-3a, but with the continuous electron-beam writing, is shown. As can be seen this process slightly enhances the pattern asymmetry, but the overall periodicity and the lattice spacing are not disturbed.

2.3 Soft-lithography

2.3.1 Mold preparation

Here, we will focus on the two soft-lithography techniques that we have used for making templates for colloidal epitaxy, which are micro-Transfer Molding (µTM) and MIMIC. The basic outline for soft-lithography is given in Figure 2-5. For the description of the creation of the patterned masters we refer to the section on electron-beam lithography.

The first step for all soft-lithography methods involves the creation of an elastomeric mold, depicted on the left-hand side of Figure 2-5. PDMS precursor and curing agent (Dow Corning

Sylgard 184) were mixed in a 1 to 10 weight ratio. This mixture was then brought under a low pressure with a small vacuum pump (Laboport) for 15 minutes in order to remove air bubbles from the solution mixture. The substrate bearing the master pattern was spin-coated with a thin layer of soap solution (about 5wt% of dishwasher detergent in water) or, in the case of large quartz plates, was dip-coated in a soap solution and dried in an oven at 100°C or under a stream of nitrogen. The elastomeric precursor mixture was then poured next to and allowed to flow over the patterned area in order to minimize the entrapment of air in the holes of the pattern. In principle, this procedure could be carried out in a vacuum chamber, but a good correspondence between original and replicated pattern depth was always observed. Small amounts of air that get trapped in the micro-wells can diffuse through the PDMS mold[164]. The substrate was then placed in an oven at 100°C for 1 hour. The modulus of the PDMS mold (on the order of 1 N/mm^2) can be doubled by increasing the curing time to 24 hours. Recently, Bietsch and Michel discussed various characteristics of the mold like elasticity and adhesion in relation to conformal contact and pattern stability[174]. Furthermore, several other materials for soft-lithography that allow for printing of smaller feature sizes than the PDMS elastomer, were recently suggested[175].

The elastomeric material can be directly used as a template for particle assembly, for instance in order to create a micro-lens array aligned in the PDMS elastomer[78], but with non-hexagonal symmetry. If necessary, the mold can be made hydrophilic by a 15-seconds exposure to an O$_2$-plasma within about 24 hours prior to use[176]. However, for most other applications, like controlled drying, the elastomeric material is not a very practical material to use. The original master pattern can however be easily transferred to another substrate using the PDMS mold. Two examples of pattern replication, µTM and MIMIC, are depicted on the right-hand side of Figure 2-5.

2.3.2 Relief patterns

In order to make a relief pattern, a poly-urethane (PU; Norland OA 71 and/or 73) UV-adhesive was used. The substrates used were as-received glass cover slides (Chance no. 1). A small drop of adhesive was placed on the glass slide and the PDMS mold was then slowly rolled into this drop. The mold was pressed onto the glass surface using a weight and exposed to a UV lamp for about 15 minutes. After removal of the PDMS mold, a solid PU copy of the original pattern has been created on glass. Alternatively to the procedure given above, the PDMS mold could be placed on the glass slide with a drop of adhesive placed next to it, which then fills the voids between the cover slide and the PDMS mold by capillary action. This procedure is called MIMIC. As most of the patterns for colloidal epitaxy consist of arrays of holes, the PDMS molds will all contain an interconnected void structure that allows the use of MIMIC. In Figure 2-6 two examples of PU templates made with soft-lithography are given. Note the particularly good reproduction of the

(a)   (b)

(c)   (d)
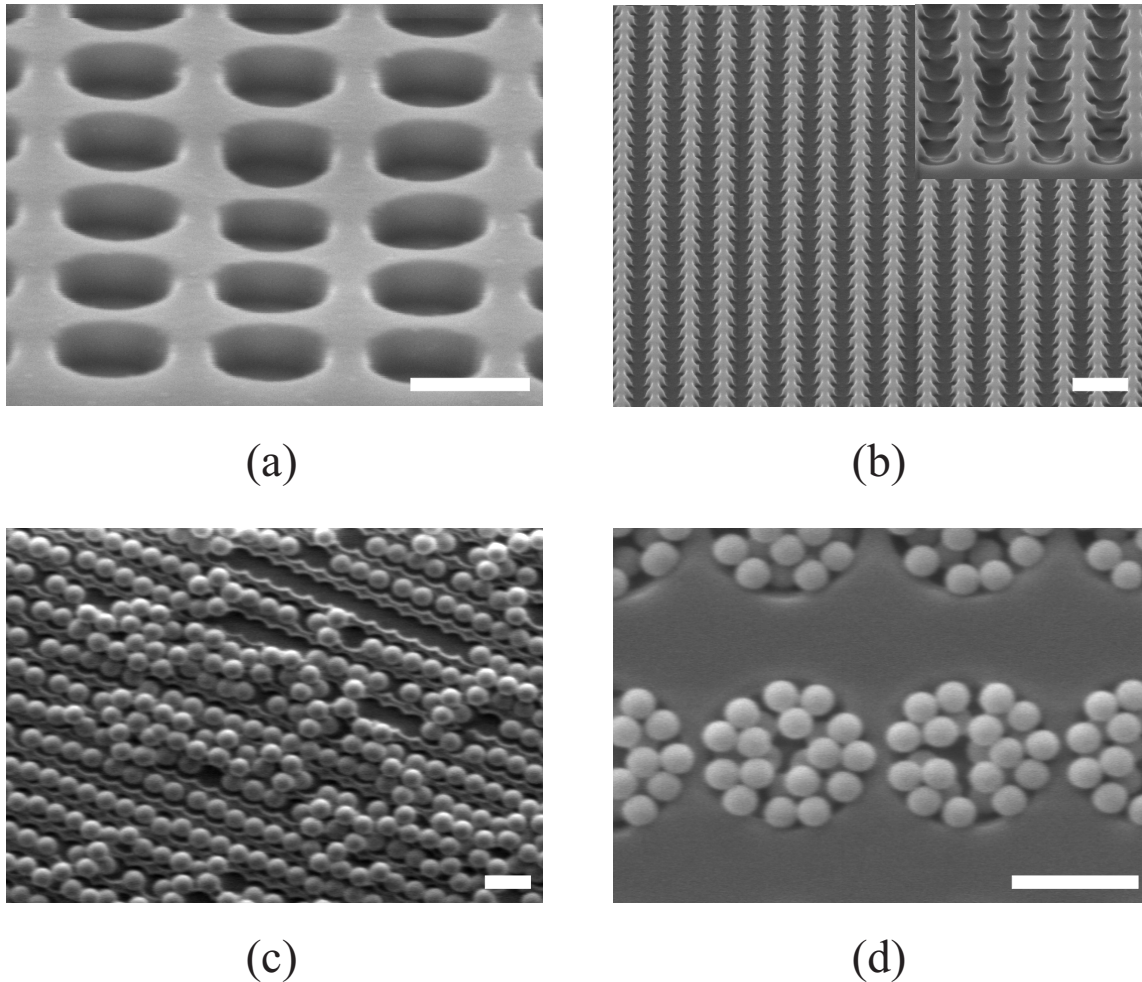
Figure 2-6 (a) and (b): SEM images of polyurethane (PU) templates made via soft-lithography. The templates consist of equally spaced rows of holes (fcc(110)-pattern). The inset in (b) shows an enlargement, where the fine reproduction of the overlap region between neighboring holes is visible. (c): 870 nm-diameter silica colloids arranged on a PU template with a 1 μm spacing like in (b). (d): 220 nm-diameter silica colloids that crystallized in the 1.2 μm-diameter holes of a PU-template in a controlled drying experiment. Scalebars are 2 μm in (a) and (c), and 1 μm in (b) and (d).

small features on the places where two cylindrical holes touch in the fcc(110)-pattern in Figure 2-6b.

2.3.3 Non-geometrical chemical patterns

Apart from a relief structure, a surface pattern consisting of areas with different chemical functionality can also be used to direct colloidal self-assembly, for instance by exploiting electro-static attraction and/or by modifying the wetting properties of the different areas[112, 130, 133, 134]. Here, an example will be given where a glass substrate is selectively coated with a silane-coupling agent (see Figure 2-7).
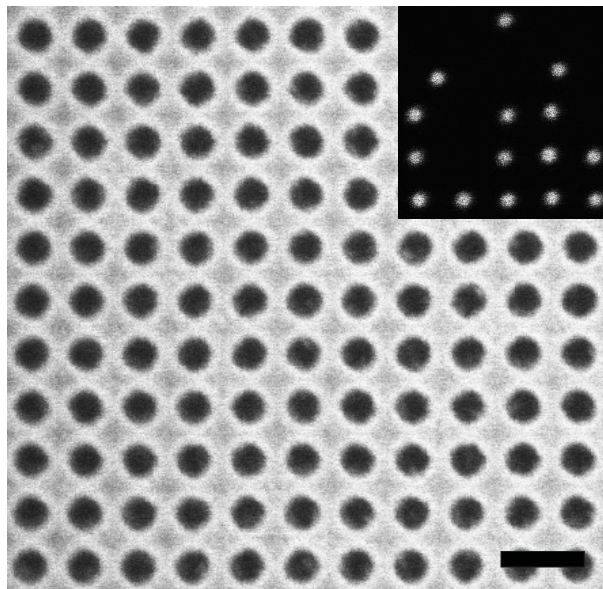
Figure 2-7 Fluorescence confocal microscopy image of a glass substrate that has been selectively patterned with the silane coupling agent-dye mixture APS-FITC (light areas) using MIMIC. The length of the scalebar is 3 µm. The inset shows a confocal image of 1.4 µm-diameter silica particles with a 400 nm-diameter core arranged on an APS-patterned template after drying from an ethanol-solution.

The fluorescent dye fluorescein isothiocyanate (FITC, Sigma) was coupled to the amino-group of the silane coupling agent 3-aminopropyltriethoxysilane (APS) by dissolving 0.34 grams of FITC in a mixture of 6.2 ml of ethanol (Merck, absolute grade) and 1.9 ml of APS (Fluka) and stirring the solution for 12 hours. A glass cover slide (Chance no. 1) was cleaned by immersion for at least 20 minutes in chromosulfuric acid (Fluka) and subsequent rinsing with demineralized water and ethanol. The glass slide was then placed on a support halfway a large vessel that contained ethanol until just below this support. An fcc(100) PDMS mold that was cut in such a way that the interconnected negative pattern structure was exposed to two opposite sides, was then placed on the glass cover slide.

The APS-FITC-mixture was mixed with ethanol and ammonia (Sigma, 25wt%) in a 5:31:1 (APS:ethanol:ammonia) ratio and a small drop (typically 15 µl) was placed on the glass slide next to one of the open sides of the PDMS mold. The PDMS mold filled with the reaction solution by capillary action. Meanwhile small amounts of reaction solution were added to the reservoir drop to prevent drying. When the mold was completely filled with the reaction solution, ethanol was dropped on both open sides of the PDMS mold, without completely soaking the mold in ethanol. After 20 minutes the PDMS mold was pulled from the glass slide, immediately followed by rinsing the glass slide with ethanol. The APS-FITC coated glass slide was imaged using fluorescence confocal microscopy (Leica TCS NT-2). As can be seen in Figure 2-7 the original 1 µm-lattice spacing pattern is perfectly replicated by the APS-FITC coating. For particle assembly glass slides coated with APS only (without FITC) were used, following the same procedure as given above, without the APS-FITC-coupling.

The inset in Figure 2-7 shows a confocal microscopy image of the ordering of 1.4 µm-diameter silica colloids that have a 400 nm-diameter fluorescently labeled silica core after drying of a low volume-fraction suspension in ethanol over an APS-patterned glass slide. The silica colloids arrange in the square symmetry of the template. As the sample was dried while the substrate was kept in a horizontal position, the different wetting properties of the patterned and unpatterned areas are causing particle ordering, maybe in combination with electrostatic attraction between silica colloids and APS-coated areas. Similar experiments were described and analyzed by Aizenberg et al.[133]. At the end of the drying process the different wetting characteristics result in a break-up of the wetting film where capillary forces of the meniscus of the drying film direct particles to the center of the areas with the best wetting of the liquid. Further experiments to determine whether the particles arrange at the uncoated glass areas or at the APS-coated areas, for instance by examining particle ordering at a fluorescently labeled pattern like the one shown in Figure 2-7, have not been carried out.

2.4 Summary

In this chapter the various lithographic techniques that were used to pattern substrates for use in colloidal epitaxy experiments are presented. The creation of patterns that consist of regular arrays of holes with diameters and spacing ranging from about 100 nm to 1.4 µm in a PMMA-layer using electron-beam lithography is demonstrated. These PMMA-templates can be used directly in colloidal epitaxy experiments or they can serve as a mask for pattern transfer into glass or silicon substrates. These solid substrates can be used as templates in combination with techniques that rely on the controlled drying of a colloidal suspension. We furthermore demonstrate how these solid substrates can serve as a master for soft-lithography. The elastomeric molds that are created from these master templates, are used to transfer the original pattern to a polyurethane relief structure. The use of these molds in chemically patterning a glass substrate using a sol-gel mixture that contains a silane-coupling agent is demonstrated as well. Examples are given of the use of silicon, polyurethane and silane-coupling agent coated templates in controlled drying techniques with silica colloids that range in diameter from 140 nm to 1.4 µm.

2.5 Acknowledgements

3

Patterning surfaces with colloidal particles using optical tweezers

A method for positioning colloidal particles on surfaces in any designed pattern is described. Optical tweezers are used to bring particles from a reservoir to the substrate where opposite surface charges are used to immobilize particles on the surface. Both chemical surface modification and polyelectrolyte coating of either substrate or colloids make the method generally applicable. We show that using this technique large, two-dimensional patterns can be created that can be dried without distortions by critical point drying. As an example we demonstrate the positioning of 79 nm-radius metallodielectric particles and we show how two-dimensional patterns can be used to direct three-dimensional epitaxial crystal growth. The method is inexpensive, relatively fast and can be fully automated.

3.1 Introduction

Colloidal particles are the building blocks for materials that find applications in many diverse fields of research. The typical particle sizes ranging from several nanometer to a few micrometers and the chemical tunability of particle morphology make colloids interesting for photonic[77, 162, 177], electronic[80, 178], magnetic and sensor[69, 179] applications. The two-dimensional arrangement of colloids on a substrate is of interest for most of these applications. Several recent examples include the use of colloidal monolayers as microlens arrays[77, 78] and arrays of closely spaced metal nanoparticles that can serve as sub-wavelength, plasmon-mode waveguides[76, 177, 180]. Two-dimensional colloid-patterned substrates also find use as calibration standards in techniques like Near-field Scanning Optical Microscopy, Atomic Force Microscopy (AFM), and Scanning Tunneling Microscopy. Furthermore, they can be used for further processing, like for example as a (deposition) mask for lithography[75, 76], or as a template in subsequent three-dimensional self-assembly[61].

Recently reported techniques for arranging colloids in two-dimensional patterns that rely on self-organization, like template-directed self-assembly[61, 77, 130, 133] and patterning of self-assembled monolayers[167], offer a high processing speed, but lack local control over pattern structure. Direct single-particle patterning[105-107, 181] does offer a much higher level of control over particle positions and composition of the structure, but the techniques reported so far are limited in particle number or particle morphology. In this chapter a method is described that allows the creation of two-dimensional structures of any desired, locally well-defined pattern using optical tweezers and that can be used on a large variety of particle morphologies and a wide range of particle sizes. The use of optical tweezers has the advantage that there is no need for contact with a probe, as is the case when a micro-robot[181] or an AFM is used. Furthermore, the combination of the fact that particles are bonded through electrostatic interaction to oppositely charged substrates with the wide variety of available techniques for chemical and physical surface modification allows a large variety of particle sizes and morphologies to be used. Apart from examples of the use of our technique for micron- and submicron-sized particles, we will also show the application of these patterns in three-dimensional colloidal epitaxy.

3.2 Experimental details

In our setup optical tweezers[81, 182] are created by focusing a continuous-wave infrared laser beam (Spectra Physics 10W, 1064nm) to a diffraction-limited spot using a high numerical aperture objective (100x, numerical aperture = 1.4, oil immersion) on an inverted optical microscope (Leica DM IRB). The position of the tweezers in the sample is controlled using acousto-optical deflectors (AOD) (IntraAction) or by moving a high-accuracy (0.5 nm) piezo-electrically controlled microscope stage (Physik Instr.). Apart from the possibility to position

particles in a single-particle trap like in the examples shown below, the high scanning speed of the AOD's (max. 100 kHz) also makes it possible to create a time-shared multiple trap, that can trap at least 100 particles simultaneously. The sample cell consists of a bottom glass cover slide and a top substrate with a surface charge opposite to that of the colloids, spaced approximately 10 μm apart. The whole sample can be imaged using bright field or Differential Interference Contrast (DIC) microscopy using a charge-coupled device camera or by confocal microscopy (Leica TCS NT-2).

Particles are being selected and trapped in a reservoir and then brought to the surface for positioning. This reservoir can be created in two different ways, depending on the sedimentation coefficient of the particles. If this coefficient is large enough to prevent particles in suspension from sticking to the top surface due to Brownian motion, sedimentation will naturally form a reservoir at the bottom glass plate of the sample. Otherwise, a reservoir has to be created that is displaced perpendicular to the optical axis with respect to the patterning area, e.g. by using a gradient in particle concentration. In the first case, where particles only have to be brought upwards after trapping, the optical tweezers can also be focused just at the upper plate. Now the potential field that creates the optical tweezers is used to drive a particle upwards to a position on the upper plate instead of moving a trapped particle. By leaving the beam focused at the top substrate and rapidly switching positions once a particle is immobilized, this allows for faster positioning, but in this way one cannot discriminate between particles in e.g., a mixture of particle types. Because in all these cases image processing of the trapped sphere can take place at any stage of the patterning procedure, the process can be automated. In the present chapter we used particles that can be trapped stable in three dimensions using a single beam optical trap, but we want to remark that the technique last mentioned only requires two-dimensional stable trapping, resembling 'laser-driven particle propagation'[183], and that the conditions for 3D stable trapping used in this research improve the accuracy for positioning particles that can only be trapped stable in 2D.

The silica and metallo-dielectric particles shown in the examples below were all made following procedures described in the literature[149, 154, 184]. Particles were suspended in ethanol or water and particle concentrations were chosen such that if all particles were sedimented, they would cover approximately 20% of the bottom glass plate. A typical concentration was $10^7\,\mathrm{ml}^{-1}$. Electrostatic interaction is used to immobilize particles on the top substrate. In case natural surface charges of either substrate or particles in suspension are too low or not of opposite sign, they can be changed by surface modification. Our glass cover slides were coated with a layer of 3-aminopropyltriethoxysilane (APS) (Fluka)[149, 185], which renders the glass surface positively charged. To this end the glass slide were placed in a mixture of 140 ml ethanol (Merck, absolute grade) and 4.5 ml ammonia (Sigma, 25wt%). 23.0 ml APS was added followed by thoroughly mixing of the suspension, after which the coating reaction was allowed to proceed for 1 hour under gently stirring using a magnetic stirrer. Glass slides were rinsed several times with ethanol and dried in air. We have also coated substrates and particles with a few nanometer thick layer of adsorbed polyelectrolytes (we used poly(allylamine hydrochloride)
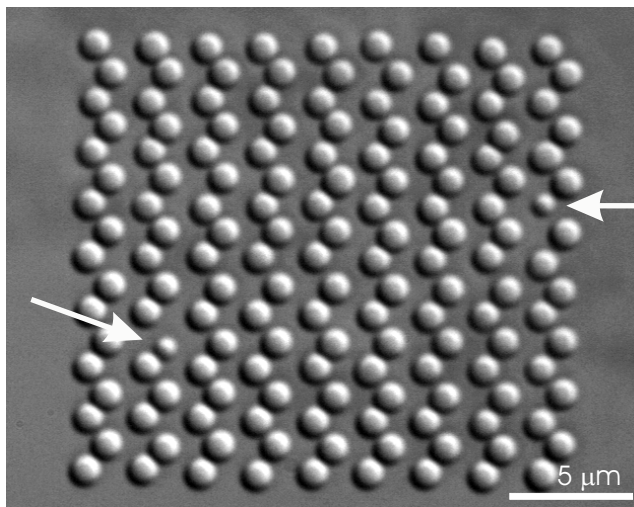
Figure 3-1: Image of a pattern of 153 1.4 μm diameter silica particles arranged on a hcp(1100) lattice, taken with DIC microscopy in suspension. The arrows indicate two smaller particles that have been incorporated as defects in the pattern.

and/or poly(styrene sodium sulfonate)) using a layer-by layer assembly technique[67, 186]. This technique has proven to work for a large variety of particles, including organic, inorganic, hybrid and uncharged colloids (for a recent review see[187]). Patterned substrates can be dried using critical point drying (CPD) with liquid CO_2. In the critical point dryer (Emscope CPD 750), the sample cell is placed under ethanol in the CPD chamber and then opened. After closing the chamber, the sample is flushed several times with liquid CO_2, until all the ethanol has been replaced with liquid CO_2. The CPD chamber is then heated so that the CO_2 is brought above the critical point. After depressurizing, the sample has been dried without the surface tension of a liquid-gas interface distorting the patterned structure (see ref.[188] for further details). The images shown below have all been taken in suspension.

3.3 Results and discussion

3.3.1 2D Patterning of colloids

Figure 3-1 shows a DIC-image of 153 silica particles of 700 nm-radius patterned on an APS coated glass cover slide. Particles have been placed with the symmetry of a (1100)-plane of a hexagonally close packed crystal. The accuracy of positioning (root-mean-square deviation of actual vs. designated position) was determined with image processing to be 73 nm. Note that in solution, particle excursions in the trap are limited to several nanometers only. When the position of the trap is moved towards the glass surface, particle excursions increase due to reflections affecting the potential gradient in the trap. This can be improved considerably by using a counter-
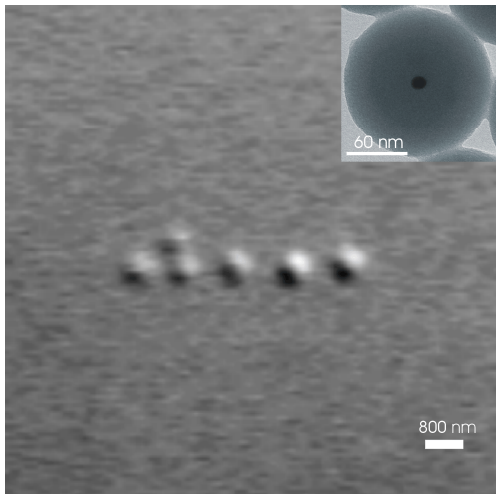
Figure 3-2 Metallo-dielectric particles consisting of a 7.5 nm-radius gold core coated with a silica shell with outer radius 79 nm, arranged in a line pattern. The interparticle spacing is 1 μm. A sixth particle has been placed above the second particle from the left. Image taken in DIC. The inset shows a TEM image of the particles used, with the gold core clearly visible.

propagating beam, thus creating a more symmetric and stiffer trap over the interface, or by reducing reflections at the surface.

As an illustration of how defects or a second type of particles can be incorporated into a structure, two smaller particles have been placed in the structure as indicated by the white arrows in Figure 3-1. Using our technique, incorporation of a different particle type into a structure is easier to achieve then when immobilizing larger assemblies of particles at once using e.g. time-shared optical tweezers in combination with photo-polymerization[107]. Furthermore, the use of electrostatic attraction between particles and substrate allows for a wider range of particles and substrates to be used than with single-particle photo-thermal fixation[77] or local photo-polymerization[105].

Apart from the micron-sized silica particles shown in Figure 3-1, we have also applied our method to 7.5 nm-radius gold particles coated with a silica shell with a outer radius of 79 nm (see the TEM image in the inset in Figure 3-2). Arrangement of functional particles in this size range in plasmon wire structures has been suggested as a route to high efficiency sub-wavelength waveguides[177, 180]. Because of their smaller size compared to the 700 nm silica particles, a sample cell containing a particle concentration gradient was used, where particles were trapped in the high-concentration part of the sample and then moved towards the other end containing the patterned region. In Figure 3-2 a line pattern of the metallo-dielectric core-shell particles is shown. The pattern consists of 5 particles spaced 1 μm apart, with a sixth particle arranged above the second one from the left. This demonstrates the range of particle sizes for which this technique can be used as well as its applicability for patterning particles with a functional morphology.

3.3.2 3D Epitaxial self-assembly

Finally, we want to show how this two-dimensional 'do-it-yourself' organization can be used to direct three-dimensional self-organization by colloidal epitaxy. First, we patterned a structure consisting of a rectangular array of four by five particles surrounded by a rectangle of particles with equal interparticle spacing. The patterned 500 nm-radius silica particles have a 100 nm
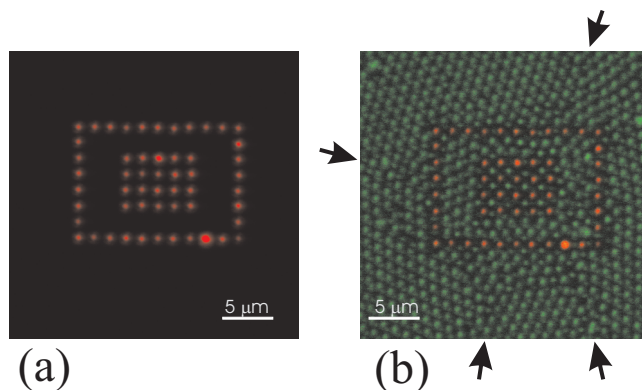
Figure 3-3 Fluorescence confocal microscopy images of (a): a pattern of 1 μm-diameter silica particles labeled with RITC (red), (b): after addition of FITC labeled (green) particles. The image in (b) has been taken with the focus in between the first and the second layer so that in the central square particles from both the first (red) and the second (green) layer can be seen. The arrows indicate defect-lines in the surrounding crystal originating from the patterned structure.

radius core labeled with rhodamine isothiocyanate (RITC). Figure 3-3a shows a confocal microscopy image of this structure. After patterning, the sample cell was washed with water to remove excess particles, inverted and a small amount of particles with the same outer radius of 500 nm but labeled with a fluorescein isothiocyanate (FITC) dye (200 nm core radius) was added.

Figure 3-3b shows both the initially patterned particles in red and the added FITC particles in green, 16 hours after addition. The added FITC particles have crystallized in hexagonal sheets parallel to the glass wall, as is observed for a flat silica wall on which particles are free to diffuse. This is probably due to the fact that the APS-coated surface lost most of its positive surface charge by exposure to CO_2 in water (H_2CO_3) during the washing step, making an additional coating step as described by Vossen et al.[185] unnecessary. These FITC particles are slightly out-of-focus, causing the hexagonal lattice to be blurred out, so that the particles in the second layer above the square pattern could also be imaged. These particles are clearly visible as green particles in between the red particles and follow the square symmetry of the pattern, showing that a small grain can locally direct epitaxial growth. Similarly, the pattern could be made containing built-in defects (like in Figure 3-1) in order to study the relaxation of defects in three-dimensional epitaxy.

In Figure 3-3b effects of the pattern on the in-plane crystallization can also be observed. First of all the distance between the array and the rectangular boundary has a clear impact on ordering of particles in between. By varying this distance and boundary structure the influence of confinement and boundary conditions on two-dimensional colloidal crystallization can be examined in a systematic way. Secondly, defect-lines in the surrounding hexagonal crystal, indicated by the arrows in Figure 3-3b, originate from the pattern. This again shows how with such patterns the role of defects in two- and three-dimensional crystal growth can be examined. A

thorough understanding of defect formation and the ability to manipulate defects is critical for the use of colloidal structures in photonic as well as many other applications. Furthermore, by positioning particles on top of a crystal and subsequent further growth, e.g., by controlled drying as described by Velikov et al.[129], defects can be created inside a three-dimensional crystal.

3.4 Conclusions

A method was demonstrated that enables the creation of large patterns of a wide variety of (functional) colloidal particles on surface-activated substrates with a resolution significantly below particle size using optical tweezers. Defects or impurities can be completely avoided or, if desired for a specific application, built into the structures at any desired position, which makes this procedure suitable for the creation of photonic, electronic and magnetic materials. The structures can be dried without distortions using critical point drying. We have shown the application of such patterns in colloidal epitaxy, showing the possibility to both locally manipulate self-assembly as well as to study the evolution of defects in two- and three-dimensional crystallization.

3.5 Acknowledgements

4

Epitaxial growth of a hard-sphere hcp crystal and the effects of template-crystal (mis)match

We demonstrate the epitaxial growth of metastable hard-sphere hcp and 'double-hcp' (dhcp) crystals using a surface pattern that directly dictates the stacking sequence. A detailed 3D analysis based on real-space measurements is performed on crystal structure as a function of template-crystal mismatch, which demonstrates the possibilities of colloidal epitaxy as a model system for studying the effects of a patterned substrate on crystal structure. Perfect template-induced hcp-crystal growth occurs at an isotropically deformed template. At deformed lattices we observe growth of a non-close-packed superstructure and of a perfectly layered and (100)-aligned fcc crystal. Small mismatches lead to increased out-of-plane displacements followed by a structural breakup in 'crystal' grains where particle positions in successive layers are strictly periodic and 'defect' grains where these positions are displaced with respect to each other. The volume fraction of crystals grown on mismatched templates was found to vary drastically. For the reconstructed fcc(100)-aligned crystal the volume fraction was 0.8 times lower than that of the hcp- and untemplated crystals. At an anisotropically stretched surface pattern, increasing the hexagonal c/a-ratio, these displacements as well as the mutual orientation of these grains are directed perpendicular to the stretched direction.

4.1 Introduction

The presence of a periodically modulated external potential, like e.g. a substrate, can drastically influence crystallization[95]. In the case of atoms and molecules, epitaxial crystallization has been the subject of intense research over the past decades, mostly driven by its importance for the fabrication of semiconductor devices. For atomic and molecular systems, a systematic evaluation of the interplay between substrate structure and crystallization behavior is however hampered by the difficulties involved in the analysis of structures on a single-particle level and in a systematic manipulation of properties on the appropriate length- and time-scales.

Colloids show phase transitions in thermodynamic equivalence to atomic and molecular systems, but contrary to atoms and molecules, their typical length- and time-scales are easily accessible for experimental techniques like light microscopy and light scattering[16]. The colloidal model system has already been frequently, and successfully, used for investigating both homogeneous crystallization[12, 55, 189, 190] and crystallization close to a wall[103, 191]. Recently, these studies have received a great impulse when it was shown that it is possible to perform a full three-dimensional (3D) real-space analysis by using confocal microscopy and fluorescently labeled colloids[158, 159]. The possibilities of this technique were further demonstrated by several papers addressing hard-sphere glass formation[11, 159, 160], crystal nucleation[12], and epitaxial hard-sphere crystallization[61, 62].

Several different techniques, like e.g. electron-beam lithography, soft-lithography[164] and optical tweezers[104], provide the possibility to pattern substrates on length scales comparable to those of colloids. The manipulation of colloidal crystallization by using patterned templates, i.e. colloidal epitaxy[61, 62], extends the use of the colloidal model system to include epitaxial crystallization as well. For the simplest colloidal model system, that of Brownian hard-spheres, we will demonstrate in this chapter how a well-chosen substrate pattern can direct crystallization to an otherwise meta-stable crystal structure.

Apart from this theoretical interest, crystallization of colloidal particles has also gained recent interest from a practical point of view. The fact that the wavelength-range of visible light falls in the middle of the colloidal regime not only enables aforementioned experimental techniques, it also makes colloids and colloidal crystals suitable building blocks for photonic applications including photonic bandgap materials. The most commonly used techniques for making colloidal crystals for photonic, as well as other applications, rely on self-assembly[91, 114, 117, 192, 193]. The ability to direct this self-assembly process on an easy and straightforward way, can greatly enhanced the possibilities for creating functional colloidal materials. Colloidal epitaxy is in this respect one of the most promising techniques, as it gives the possibility to direct crystal structure and orientation[61, 62, 172], it is applicable to colloids with a wide range of interaction potentials[109, 173], it can be used in combination with other assembly techniques[77, 129], and, as we will show in the present chapter, provides a way to grow crystals that are metastable in bulk crystallization.

The colloidal model system that we have studied in this research is the conceptually simplest model system that shows a freezing transition upon increasing density, namely the hard-sphere system. This freezing transition is located at a volume fraction of $\varphi = 0.494$. For volume fractions in between this volume fraction and the melting transition at $\varphi = 0.545$, there is coexistence between a low-density liquid phase and a crystal phase[23, 24]. At $\varphi = 0.545$ and higher there is a single close-packed crystal phase that compacts at increasing volume fraction. As the interaction potential between hard-spheres accounts for excluded volume interactions only, all hard-sphere structures have zero energy. However *entropic* interactions lead to differences in the total free-energy, but these are rather small for the various close-packed structures, on the order of 10^{-4} k_bT per particle at the melting transition[194-199], where k_b is Boltzmann's constant.

The equilibrium crystal structure for hard-sphere like particles is the close-packed face-centered cubic (fcc) crystal, the structure that is highest in free energy is the hexagonal close packed (hcp) crystal. All the other possible stacking sequences, both regular stackings like the double hexagonal close packed (dhcp) crystal, as well as non-periodic stacking sequences that are strictly speaking not crystalline, have intermediate free energies[198]. Due to the small free energy differences, stacking faults are likely to occur so that the stacking sequence of hard-sphere crystals can deviate appreciably from the ideal fcc stacking. Furthermore, for small crystallites, with less than ~ 30000 particles per plane, a completely random stacking sequence of close-packed planes, denoted with random hexagonal close packed (rhcp), was found to be the most stable structure[199], so crystals grown via a nucleation-and-growth-mechanism will initially have a rhcp structure. This is in correspondence with observations in space[200] and on earth[189, 201-203]. The subsequent relaxation of the rhcp structure to fcc is estimated to be slow, with time-scales on the order of months to years for 200 nm-diameter particles[199, 204].

One of the techniques that were shown to lift this apparent degeneracy and induce formation of a perfect fcc stacking is colloidal epitaxy. Furthermore, it was shown possible to orient the crystal with both the (100)-plane[61] as well as the (110)-plane[62], which has an even higher surface free-energy[108], aligned over the bottom, templated wall. In this chapter, we will show that it is not only possible to direct hard-sphere crystallization towards the crystal structure with the lowest free energy, but that the most metastable crystal structure, the hcp-stacking, can be grown as well. The template that will be used for hcp-crystal formation, the hcp(1100)-plane, can be easily modified to direct any of the other possible stacking sequence, which will be shown by growing a so-called double hexagonal close-packed (dhcp) crystal. These results are interesting in view of recent theoretical work on HS crystallization on structured walls that predicted complete wetting of the metastable hcp crystal at a suitably patterned substrate[63, 64]. Other theoretical predictions, like the fact that the optimal lattice constants of the template are larger than those of the bulk crystal, are reproduced in this research as well.

Isotropically and anisotropically stretched hcp(1100)-template lattices were used to study the effects of template-crystal mismatches on epitaxial crystallization. Among our observations is the growth of a superstructure that consists of six differently stacked non-close packed planes with a stretched hcp(1100)-symmetry. The occurrence of a non-close packed HS crystal has, to our

knowledge, never been predicted theoretically. The possibility to create metastable and non-close packed crystal structures opens up ways to unexplored photonic crystals.

Two other results clearly show the potential of colloidal epitaxy together with three-dimensional real-space analysis as a model system for epitaxial crystallization and as a tool to study defect formation and (epitaxial) stress relaxation in molecular crystals. At a template unit cell of which both lattice vectors have the same relative amount of shrinkage with respect to the unit cell that gives rise to hcp crystallization, we observe a reconstruction of the colloidal surface layer towards an fcc(100)-plane, similar to (100)-hcp(1100) reconstructions observed in atomic hetero-epitaxy of e.g. Co and Cu[98, 99, 101]. Secondly, a mismatch between template and crystal dimensions is in general found to lead to an increase in density in between lattice planes[98, 99]. A thorough understanding of and control over defect formation is furthermore crucial for photonic applications of colloidal materials[205]. In this respect, the ability to exactly control the stacking sequence of a colloidal crystal allows for a direct experimental test of theoretical work on the effect of stacking faults on the optical properties of inverse opals[206].

The remainder of this chapter is organized as follows. First we will discuss our experimental model system and the various order parameters that we calculate in order to examine colloidal crystal structure. Then we will present and discuss results on the growth of hcp and dhcp crystals, after which we will focus on the evolution of crystal structure as a function of template-crystal mismatch. The starting point for this will be the investigation of unit cells that are isotropically shrunken with respect to the hcp(1100)-template that gives rise to the best quality hcp crystal. This analysis includes the epitaxial hcp(1100)-fcc(100) transition. Then results for an isotropically stretched template will be presented, followed by an anisotropically stretched template, where the ratio between the two lattice distances is increased. Finally, the occurrence of a non-close packed superstructure will be discussed.

4.2 Experimental details

4.2.1 Core-shell colloids

Silica colloids with a core-shell morphology were used in order to make quantitative 3D confocal microscopy possible. The core of the particles contained the fluorescent dye fluorescein isothiocyanate (FITC) covalently attached to the silica through the silane-coupling agent 3-aminopropyltriethoxysilane. Synthesis of these particles is described in detail in ref[149]. The core diameter was measured with both static light scattering (SLS), $d = 400$ nm, and transmission electron microscopy (TEM), $d = 386$ nm. These core particles were grown larger with an unlabelled silica shell using a seeded growth procedure as described by Giesche[154]. For the final particle diameter we found $d = 1.384\ \mu m$ by TEM and $d = 1.404\ \mu m$ by SLS. The polydispersity, defined as the standard deviation of particle sizes relative to the mean, was

determined by TEM to be 0.015. In the seeded-growth procedure that was used to coat the fluorescently labeled core particles with a non-fluorescent shell, instabilities in the reaction mixture may affect particle growth in two unfavorable ways. Firstly, an uncontrolled, local increase in counter-ion concentration may lead to the formation of aggregated doublet particles, so-called dumbbells. Secondly, an uncontrolled increase in the local concentration of silicic acid may lead to the nucleation of smaller, non-fluorescent particles, instead of condensation on the surface of the seed particles. In the final dispersion that was used the concentrations of both 'impurities' were well below 1%.

Particles were suspended in a refractive-index matching solution of demineralized water and glycerol (Sigma) in a volume ratio of 1:6.5. The conditions for refractive-index matching were determined by measuring the transmission of different mixtures two days after dispersing a low volume fraction of particles. Due to the refractive-index matching the Van der Waals attractions between the particles are reduced, leading, for particles in this size-range, to a steeply repulsive interaction due to surface charges and residual counter-ion concentrations. This results in an almost hard-sphere like interaction. In order to calculate an effective hard-sphere radius, R_{HS}, we calculated the 3D radial distribution function, 3D-$g(r)$ as defined below, for a crystal grown in the same sample as that for the experiments described below, but at a plain, untemplated wall. The definition of the 3D-$g(r)$ is:

$$g(r) = \frac{1}{\rho^2} \left\langle 2 \sum_{i=1}^{N-1} \delta(\vec{r} - \vec{r}_i) \sum_{j=i+1}^{N} \delta(\vec{r}' - \vec{r}_j) \right\rangle, \qquad (4.1)$$

where the indices i and j denote any of the in total N particles and r denotes the distance between $\vec{r}$ and $\vec{r}'$. In the calculation of 3D-$g(r)$, both these last two vectors are composed of the full 3D coordinates of a single particle. From the position of the first maximum we found $2R_{HS} = 1.460$ μm. For a close-packed crystal this corresponds to a volume fraction of $\varphi = 0.65$.

4.2.2 The sample cell and the hcp(1100)-template

A sample cell was made by gluing (General Electric Silicon Rubber Adhesive RTV 102) a bottomless bottle with an internal diameter of 12.85 mm to a 22 mm-diameter glass slide (Chance no.1) that had been coated and partly patterned as described below. The sample cell was rinsed several times with the water-glycerol mixture before filling it with about 1.2 ml of colloidal suspension. Colloids were homogeneously dispersed with a volume fraction of $\varphi_0 = 0.0015$. For the experiments with anisotropically deformed template unit cells (see the discussion on the template patterns below) suspensions with an initial volume fraction of $\varphi_0 = 0.005$ were used. By sedimentation, colloids accumulated and crystallized at the bottom wall.
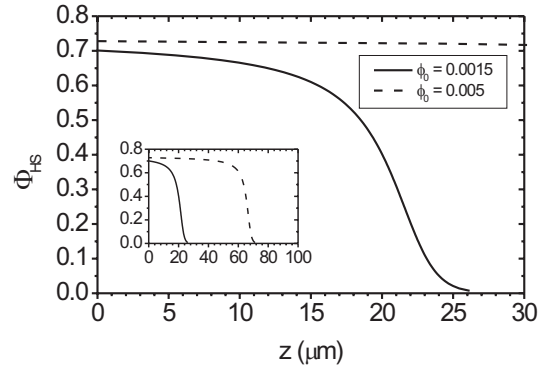
Figure 4-1 Calculated dependence of the volume fraction in the sediment as a function of height for hard-spheres at the two different initial volume fractions used in this study. The straight curve with $\varphi_0 = 0.0015$ corresponds to the experiments with the isotropically stretched and shrunken templates, the dashed curve with $\varphi_0 = 0.005$ corresponds to the experiments with the anisotropically stretched templates. In the inset the decay of the ($\varphi_0 = 0.0015$)-graph is visible as well.

With the initial volume fractions and total volume given above, the volume fraction at the bottom of the sample, φ_1, can be calculated, equating the gravitational pressure to the balancing osmotic pressure:

$$\varphi_1 = \frac{\varphi_0 \cdot Pe \cdot (H/R) \cdot \varphi_m}{3\varphi_m + \varphi_0 Pe \cdot (H/R)}, \qquad (4.2)$$

where H is the total height of the sample solution from the bottom wall to the meniscus, R is the particle radius, φ_m is the volume fraction at maximum compression, which is $\varphi_m = 0.74$ for crystallized hard-spheres. Pe is the Peclet number which is defined as $Pe = 4/3\pi R^4 (\Delta\rho)g/(kT)$ with $\Delta\rho$ the density difference between particles and solvent, g the gravitational constant, k Boltzmann's constant and T the temperature. For our initial volume fractions of $\varphi_0 = 0.0015$ and $\varphi_0 = 0.005$, we get values for φ_1 of $\varphi_1 = 0.70$ and $\varphi_1 = 0.73$ respectively. With these values, the volume fraction profile of the sediment is given according to[207]:

$$Pe \cdot \frac{h}{R} = \left[\frac{3\varphi_m}{\varphi_m - \varphi} + 3\ln\left(\frac{\varphi}{\varphi_m - \varphi} \right) \right]_{\varphi(h)}^{\varphi_1}, \qquad (4.3)$$

where h is the height from the bottom wall. The calculated volume fraction profiles for hard-spheres are given in Figure 4-1.

The bottom wall consisted of a glass slide (Chance no.1), coated successively with an 11.5 nm-thick gold layer and a 450 nm-thick poly(methylmethacrylate) (PMMA) layer. The PMMA (MicroChem Corp., 950k, 4wt% in chlorobenzene) layer was doped with the fluorescent dye pyromethene 580 (Exciton Inc.) by dissolving typically 10^{-3}wt% of dye in the PMMA-
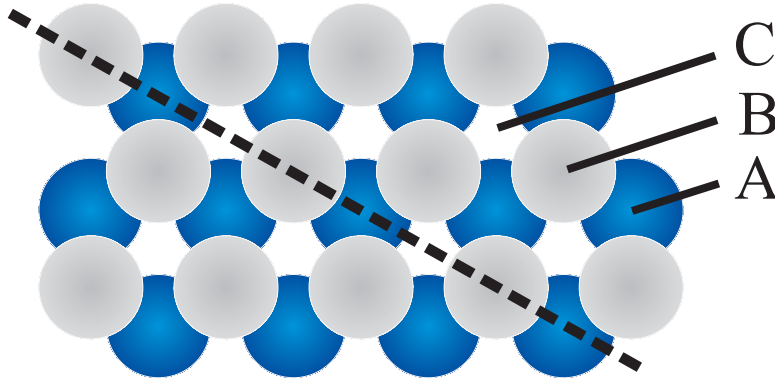
Figure 4-2 Schematic drawing of close packed hexagonal planes in an hcp-crystal, with the A-, B-, and C-positions indicated. The hcp(1100)-plane is perpendicular to the close packed planes, its orientation indicated by the dashed line.

solution prior to spin-coating. This PMMA layer was partly patterned using electron-beam lithography. Each single pattern consisted of 500 by 500 unit cells. The depth of the cylindrical holes in the pattern was 450 nm, equivalent to the PMMA-layer thickness.

On a plain, flat, hard wall hard-sphere particles crystallize in close packed hexagonal layers parallel to this surface. These hexagonal layers correspond to the (111)-plane of the fcc crystal. In Figure 4-2 a sketch of particle positions in this layer is given. For the next hexagonal layer there are two distinct stacking possibilities, denoted by *B* and *C*, while positions in the first layer are indicated by *A*. The template we have chosen for our experiments is a crystal plane that runs perpendicular to the hexagonal ground plane and contains the *A*, *B*, and *C* positions, as indicated by the dashed line in Figure 4-2. For fcc and hcp crystals this corresponds to the fcc(110)-plane and hcp(1100)-plane respectively, where for the fcc-lattice crystal planes are denoted with the indices of the three cubic lattice vectors, while for the hcp-lattice we use the three vectors associated with the hexagonal ground plane and the direction perpendicular to this as the fourth index. In order to only distinguish fcc- and hcp-stackings there are more possible choices for the template plane, for instance fcc(110) vs. hcp($\bar{1}100$)[63, 64], but the hcp(1100)-plane gives us the further advantage to directly dictate any of the intermediate stacking sequences as well by inserting 'stacking faults' on the template. A confocal image of the resulting hcp(1100)-template is given in Figure 4-3a. An example of another stacking sequence dictated by the template, namely the *ABCBA*-sequence, is given in Figure 4-6a. This sequence corresponds to a double hexagonal close packed (dhcp) crystal.

The dimensions of the hcp(1100) unit cell are given by the distances *a* and *c*, indicated in Figure 4-3a. For spheres of radius *R*, these distances are given by $a = 2R\sqrt{3}$ and $c = 4R\sqrt{(2/3)}$. The length of the *c*-vector is twice the distance between close packed planes. The coordinates of the B-position in the unit cell are given by ($a/3$, $c/2$). The actual values of *a* and *c* were varied by stretching or shrinking the unit cell along these two directions. The resulting dimensions were scaled to the effective hard-sphere dimensions $a_{HS} = 2R_{HS}\sqrt{3}$ and $c_{HS} = 4R_{HS}\sqrt{(2/3)}$, with R_{HS} calculated as described above. The values of a/a_{HS} ($= c/c_{HS}$) are given in Table 4-1. In the remainder of this chapter we will denote deformations with $a/a_{HS} = c/c_{HS} > 1$ as positive, isotropic
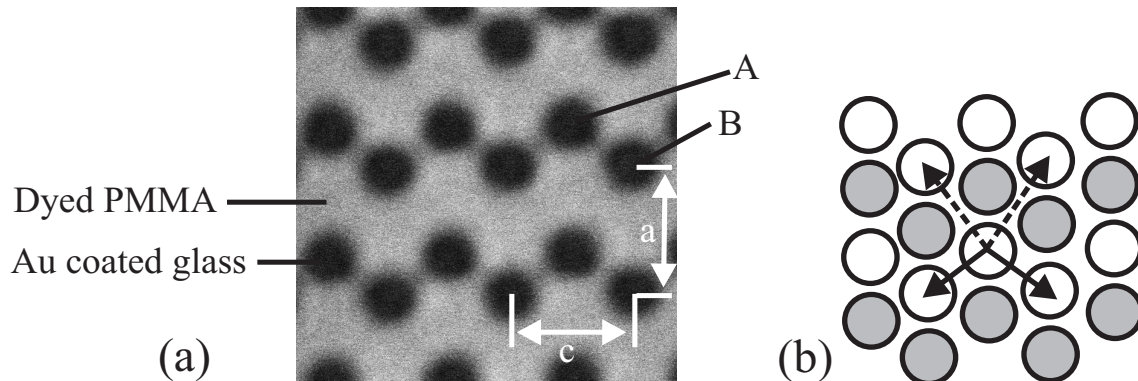
Figure 4-3. (a): Confocal microscopy image of an hcp(1100)-template, with the characteristic ABA-sequence of the close packed planes that grow perpendicular to the template indicated. The distances a and c span the 2D unit cell and their lengths are in this image 2.08 μm and 1.96 μm respectively. (b): Drawing of the projection of sphere positions in 2 successive hcp(1100)-layers. The solid arrows indicate the in-plane nearest neighbor distances r_1, r_2; the dashed arrows the next-nearest neighbor distances r_3, r_4.

deformations, deformations with $a/a_{HS} = c/c_{HS} < 1$ as negative, isotropic deformations, and finally deformations with $c/c_{HS} > a/a_{HS}$, as anisotropic deformations.

4.2.3 Structural analysis

After sedimentation, samples were analyzed with an inverted confocal microscope (Leica TCS-NT 2). The 488 nm line of an ArKr laser was used to excite the FITC fluorophores in the particle cores. The use of particles with a non-fluorescent shell as described above, allows for a 3D analysis. 2D images parallel to the optical axis were taken with a typical spacing along the optical axis (further denoted as the z-direction) of $\Delta z = 122$ nm. In each of these images feature coordinates and intensities were retrieved using procedures similar to those described by Crocker and Grier[157]. Features belonging to a single-sphere's intensity profile were then grouped together in columns sorted on their z-coordinate. This intensity profile is the z-component of a convolution of the Point Spread Function (PSF) of our microscope with the spherical profile of the core particles. A Gaussian function was constructed of which the full-width-at-half-maximum was fixed at a value that was such that this Gaussian function mimicked the z-axis component of the convolution of the PSF with the spherical core profile. Each of the intensity-profiles in the 3D data set was then fitted to this Gaussian and the position of the maximum was taken as a particle's z-coordinate. This z-coordinate has an accuracy of ±30 nm.

With the sets of 3D particle coordinates that were thus obtained, an analysis of crystal structure was carried out. Our analysis started by calculating the linear number density perpendicular to the bottom wall by integration of the 3D density profile over the lateral (xy-) coordinates:

$$\rho_z = \int\limits_{z-\frac{\Delta z}{2}}^{z+\frac{\Delta z}{2}} \iint \sum_{i=1}^{N} \delta(x - x_i)\delta(y - y_i)\delta(z - z_i)\,dxdydz\,, \qquad (4.4)$$

where the summation runs over all N particles and a constant binsize of $\Delta z = 0.040$ μm is taken. The integration over x and y runs over the full size of the scan field, which was 100 x 100 μm.

At a plain wall, hard spheres crystallize in hexagonal layers oriented parallel to the bottom wall. For a templated crystal we also expect crystal planes to be oriented parallel to the (templated) bottom wall, but with an in-plane symmetry dictated by the template. In both cases the positions of these layers will be visible by a peaked structure of ρ_z. Based on the minima in ρ_z particles were uniquely assigned to layers parallel to the bottom wall.

Volume fractions were calculated by direct particle counting in layers three to ten from the bottom. These volume fractions were scaled to the hard-sphere volume fraction. As can be seen in Figure 4-1, the volume fraction calculated over layers 3 to 10 is, for the sample with $\varphi_0 = 0.0015$, dependant on the layer spacing. In order to account for the decreasing volume fraction in the sample, the hard-sphere volume fraction was determined by averaging the volume fraction as given in Figure 4-1 over the same range in z as that spanned by layers 3 to 10.

For the particles in each layer we calculated three order parameters that together describe the effect of the (deformed) template on crystal structure. In the following we will indicate layers with the index i and the 2D particle coordinates in layer i with $r_i = (x,y)$. First, we calculated the in-plane 2D analog of the radial distribution function. The definition is equal to that given in equation (4.1), with the exception that now the integration only runs over the lateral coordinates of particles whose z-coordinate falls between the two minima in ρ_z that define the layer. We denote this function with 2D-$g(r)$ to indicate the difference with the 3D-$g(r)$ defined above. Secondly, a measure for the asymmetry of the distribution of nearest-neighbor and next-nearest neighbor distances was calculated. As can be seen in Figure 4-3b, the first four nearest neighbors in the hcp(1100)-unit cell occupy two sets of distinct distances, $\{\vec{r}_1,\vec{r}_2\}$ (indicated with the solid arrows) vs. $\{\vec{r}_3,\vec{r}_4\}$ (indicated with the dashed arrows), where the order (1,2,3,4) is determined by increasing distance from the center particle. For an hexagonal, fcc(111) plane, as well as for instance for an fcc(100) plane, these four distances all have similar values. In order to quantify this distribution we have used the function ξ that, for a particle in layer i at position r_j, is defined as:

$$\xi(r_j) = \frac{1}{\sqrt{2}-1}\left(\frac{|\vec{r}_{j3}|}{|\vec{r}_{j2}|} - 1\right), \qquad (4.5)$$

where r_{j2} and r_{j3} denote the position of the second and third neighbor of particle j with the order as given above. The scaling is used to map the value of ξ for an ideal hcp(1100)-lattice to 1. Note however that the possible values for this parameter are not limited to $<0,1>$. The value for ξ can continuously vary and may become larger than 1. It only gives a measure of the asymmetry of

nearest-neighbor distances in comparison to that in the hcp(1100)-lattice. However, a pure fcc(110)-lattice (that we however did not find to occur in our experiments, except for local stacking faults at high template deformations) will give identical values as the hcp(1100)-lattice.

The ξ-parameter was found to give identical results as using the mean-squared-distance (msd) between neighboring particles, summed over each particle's four nearest neighbors. However, the distributions of values for ξ for hcp(1100) and the symmetric unit cells listed above were found to be more clearly separated then for the msd-criterion. Furthermore, we only included the distances to the second and third nearest neighbor, as this was found to give better results than using all first four nearest-neighbor distances, probably due to the influence of defects. For instance, with the definition given above, a vacancy in an hcp(1100)-lattice will map the result for half of its neighbors to zero and for the other half to one. Thus it will not give any intermediate values.

In order to also quantify orientational order in each layer, the 2D local hexagonal bond-orientational order parameter[208] was calculated for a projection of particle positions $r_{i,i+1}$ from two successive layers:

$$\psi_6^{proj}\left(r_j\right) = \frac{1}{N_b}\sum_k \exp\left(i6\theta\left(r_{jk}\right)\right), \tag{4.6}$$

where the summation k runs over all, in total N_b, neighboring particles of a particle j in layers i and $i+1$, and the angle θ is the angle that the bond-vector between particles j and k makes with an arbitrary fixed reference axis. As can be seen in Figure 4-3b, a projection of hcp(1100)-layers gives an almost hexagonal symmetry and thus a distribution of values for ψ_6^{proj} close to 1. For other possible hard-sphere crystal planes like fcc(111) and fcc(100), a two-layer projection does not give rise to projected hexagonal symmetry. With the parameters ξ and ψ_6^{proj} a classification of (hcp) crystal structure is given. If the layer-averaged (or in the case of ψ_6^{proj} two-layer averaged) values $<\xi>_i$ and $<\psi_6^{proj}>_{i,i+1}$ both give a value larger than 0.5, crystal structure is denoted as hcp.

In order to discriminate the fcc(100)-symmetry the *single-layer* four-fold bond-orientational order parameter, defined as in equation (4.6), but with a factor 4 instead of 6 in the exponent and with a scaling of the value of ψ_4 with the nearest-neighbor distance, was calculated as well. If the parameters ξ and ψ_6^{proj} gave average values smaller than 0.5 while the average $<\psi_4>_i$ was larger than 0.5, the structure was labeled as fcc(100). Furthermore, an hexagonal lattice was identified with the *single-layer* averaged six-fold bond-orientational order parameter being larger than 0.5. Finally, a structure was denominated as disordered when the density profile did not show clear, periodic minima except for a few layers over the template (we always found layering to occur at the bottom wall) and the order parameters defined before did not correspond to any of the criteria given for these first four layers. This typically meant that $<\xi>_i$ was larger than 0.5, while $<\psi_6^{proj}>_{i,i+1}$ was smaller than 0.5.

Apart from the order parameters defined above that were used to identify the structure over the template, we have also examined the extent to which particle coordinates in successive layers

followed the positions dictated by the template. To this end the coordinates that correspond to the positions given by the template and the second layer of the ideal 3D crystal of which the template layer is the first were used. These coordinates were denoted with $\vec{r_T}$, Starting from these positions, particles differing in height in the sample were connected by linking positions $\vec{r_T}$ to the nearest particle coordinates in the first two layers, with a cutoff-radius of 0.5 μm, and repeating this procedure with these coordinates and that in the next two layers. Such a set of connected *xy*-positions of particles in the sample will be denoted as the Lateral Displacement Curve (LDC). For all LDC's that were retrieved in this way, the 2D root-mean-squared displacement relative to the template was calculated as:

$$\Delta_n = \left\langle \left| \vec{r_n} - \vec{r_T} \right|^2 \right\rangle, \tag{4.7}$$

where $n = 2 \cdot i + 1$ and i is the layer index starting from the template. In order not to be affected by point defects like vacancies, an intermediate lattice position is allowed to be unoccupied, with the LDC being 'restored' afterwards. For a perfect epitaxially grown crystal, the lattice positions $\vec{r_T}$ are periodically repeated in all crystal planes parallel to the template. Then the root-mean-squared displacements Δ_n are just the vibrations of a particle around its lattice site and the distribution of Δ_n for all n will have a maximum at a relatively small, non-zero value. For a sample where there is hardly any correlation between successive layers and thus between these layers and the template, LDS's will still be constructed, though now the distribution will flatten between zero and the cut-off radius and furthermore, due to the small difference between cut-off radius and particle radius, respectively 0.5 μm and 0.77 μm, and the fact that a particle is allowed to disappear in one intermediate layer, there will be a peak for small values of Δ corresponding to restored, uncorrelated particle positions. This last fact can also be observed when examining the extent to which LDC's persist through the sample. The plots of all 2D LDC's will provide information about possible correlations in the direction of particle displacements in successive layers.

4.3 Results

4.3.1 HCP and DHCP crystals

In Figure 4-4 confocal images of a crystal grown on a template with lattice constants of $a = 2.67$ μm and $c = 2.51$ μm are shown. Figure 4-4a shows the first crystal layer over the template and as can be seen the template symmetry (Figure 4-3a) is fully replicated by the silica particles. In Figure 4-4b, denoting the 18th layer in the crystal, corresponding to a depth of approximately 14 μm, it can be seen that the ABA-stacking is still preserved, showing the growth of a perfect, stacking-fault free hcp-crystal. The hcp crystal was found to be monocrystalline over

(a)   (b)
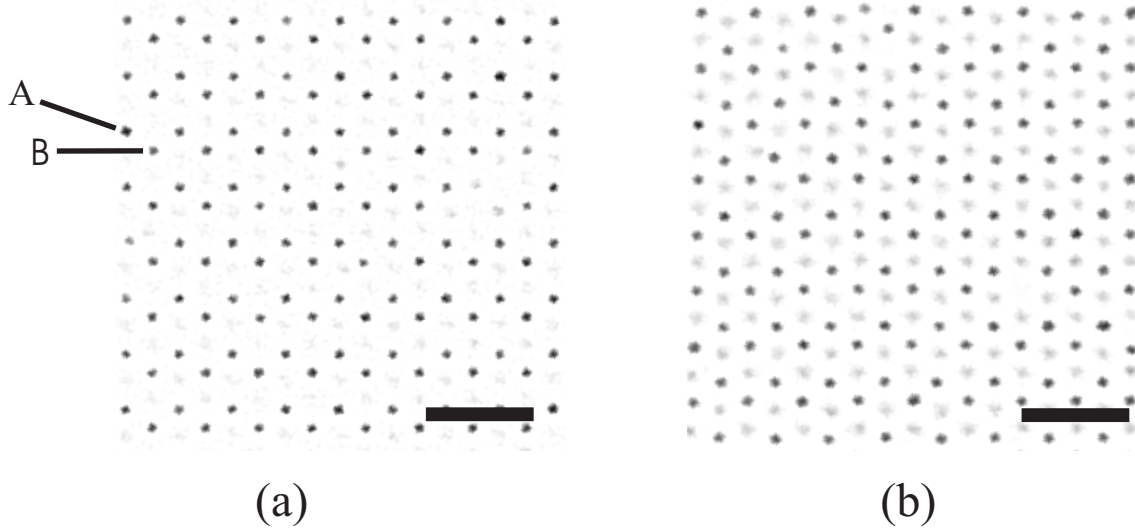
Figure 4-4 Confocal images of (a) the first layer of a templated hcp crystal and (b) the 18th layer in the crystal, with the 19th layer vaguely visible as well (see also Figure 1-5). Scalebars are 5 μm.

the full area of the template (1.33 x 1.26 mm^2). Furthermore, hcp crystal structure was found to extend as far as the thickness of our crystal, which was approximately 20 μm.

As mentioned in the previous section, we give a classification of (hcp) crystal structure as a function of template-crystal mismatch, based on the values for $<\xi>_i$ and $<\psi_6^{proj}>_{i,i+1}$. This however is just an *indicative* qualification, with, as we will see in detail below, the occurrence of defects and especially dislocations slowly increasing at increasing absolute deformations. For negative isotropic deformations with a/a_{HS} from 0.959 to 0.822, we observe a reconstruction to an fcc crystal structure with the (100)-plane aligned on the template. For a deformation of $a/a_{HS} =$ 0.986, order parameters for the bottom layers indicate an hcp-structure, while for the tenth layer

Table 4-1 Values for the various order parameters for isotropic template deformations.

a/a_{HS}	$<\psi_6^{proj}>_{3,4}$	$<\xi>_3$	$<\psi_4>_3$	$<\psi_6^{proj}>_{10,11}$	$<\xi>_{10}$	$<\psi_4>_{10}$	Structure[*]	φ/φ_{HS}[†]
0.753	0.35	0.09	0.41	0.36	0.18	0.44	DIS	0.84
0.822	0.24	0.08	0.62	0.29	0.16	0.52	FCC	0.74
0.890	0.21	0.11	0.93	0.25	0.22	0.72	FCC	0.77
0.959	0.34	0.23	0.86	0.46	0.19	0.80	FCC	0.90
0.986	0.58	0.66	0.84	0.34	0.43	0.85	H-F	0.85
1.055	0.73	0.84	0.72	0.72	0.83	0.73	HCP	0.92
1.068	0.73	0.82	0.71	0.73	0.83	0.72	HCP	0.82
1.151	0.66	0.98	0.57	0.75	0.80	0.66	HCP	0.88
1.247	0.33	0.81	0.44	0.32	0.86	0.45	DIS	0.81

[*]DIS stands for disordered, H-F for HCP in layer 3 to FCC in layer 10.

[†]The error margin in the volume fraction is ±5·10^{-3}.
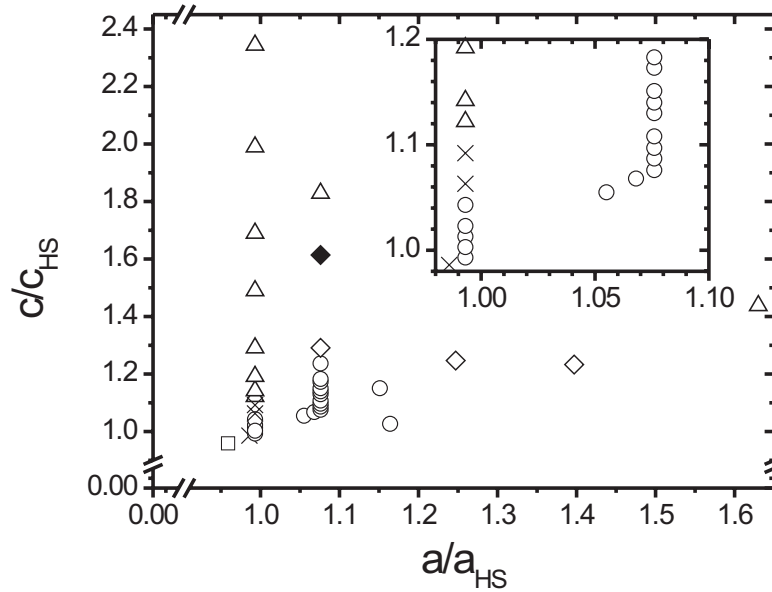
Figure 4-5 Schematic graph of crystal phases versus scaled lattice constants. The open symbols denote the occurrence of a stable phase from the template onwards: hcp ($\circ$), fcc ($\square$), or hexagonally stacked ($\triangle$); crosses (x) indicate that the structure was hcp(1100) in the third layer, while fcc(100) in the tenth layer. The filled diamond indicates a non-close packed structure. The open diamonds denote a disordered state in the first layers above the template.

from the bottom in-plane structure is of fcc(100)-type. For large deformations, $a/a_{HS} = 0.753$ and $a/a_{HS} = 1.247$, strong distortions of the hcp crystal lead to disorder in the first few layers above the template after which an hexagonally stacked crystal that is tilted with respect to the bottom wall develops. The values for all order parameters for the isotropic deformations are given in Table 4-1. Note that for the hcp (1100)-oriented crystals, $\langle \psi_4 \rangle_i$ has a value higher than 0.5 as well, though these values are smaller than those for the fcc-crystals. The resulting evolution of crystal structure as a function of stress caused by an isotropic deformation relative to the effective hard-sphere unit cell is given in Figure 4-5. Results for anisotropic stretches of the template, where the axis-ratio, $c/c_{HS} \cdot (a/a_{HS})^{-1}$ was varied, are indicated in Figure 4-5 as well.

As visible in Figure 4-5, the stability regime of the hcp crystal is remarkably shifted from the values one would expect based on the effective hard-sphere diameter that was calculated in the same sample on an untemplated part of the bottom wall. As we will see below, a perfectly layered hcp-crystal was found at $a/a_{HS} = c/c_{HS} = 1.055$.

As mentioned in the previous section, the stacking sequence in the hcp(1100)-plane is directly dictated by the template. As the hcp crystal structure is the close packed hard-sphere stacking sequence with the highest free energy[198] the above result indicates that it should be possible to incorporate stacking faults in any desired position in an fcc or hcp crystal by simply shifting one row of positions in the template over a distance of $\pm a/3$. In this way one could for instance experimentally test theories on the influence of stacking faults on the optical properties of
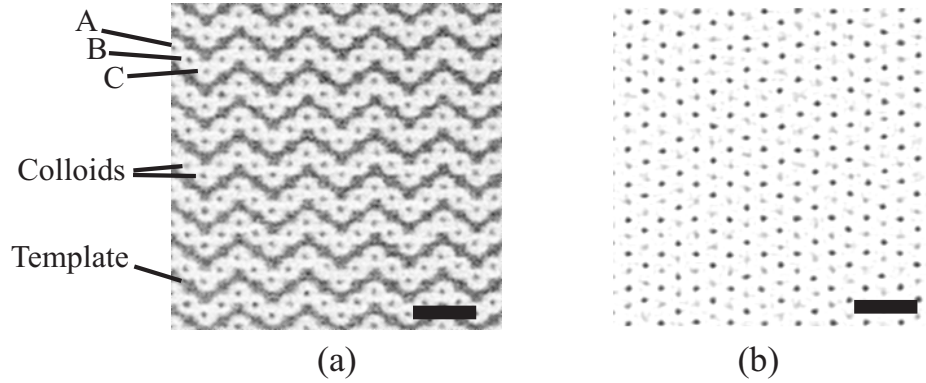
Figure 4-6 Confocal images of (a): template and particles in the first layer of a dhcp (ABCBA) crystal, and (b): the 10th layer at a depth of 8 μm. The lenght of the scalebar is in both images 5 μm.

photonic crystals[206]. We have checked this possibility by using an *ABCBA*-template, which corresponds to the stacking of a double hexagonal close packed (dhcp) crystal.

Figure 4-6a shows the dhcp-template with the *ABCBA*-sequence visible. In this image colloids in the first, perfectly templated, crystal layer are visible as well in between the template. In Figure 4-6b the 10th layer is shown. The total thickness of the crystalline part of the sediment of about 20 μm corresponds to a perfectly stacked dhcp crystal of 30 layers. For the dhcp-crystal we observed a similar shift of the stability regime to positive deformations of the unit cell as for the hcp crystal. Furthermore, perfectly layered dhcp crystal growth was found to occur, within the experimental resolution determined by the discrete values of a/a_{HS}, at the same a/a_{HS} as for the hcp-crystal that we will analyze below. At negative deformations of the unit cell, also the dhcp-template gives rise to a surface reconstruction towards fcc(100), although we did not, at the deformations studied, observe a perfectly layered, defect-free fcc-crystal as in the case of the hcp-crystal.

4.3.2 Negative isotropic deformations and the fcc-crystal

In Figure 4-5 and Table 4-1 it can be seen that an isotropic shrinkage of the hcp(1100) unit cell leads to fcc crystallization. We will first look at the evolution of crystal structure as a function of unit cell deformation for this hcp-fcc transition starting from the hcp-stability regime. In Figure 4-7 the first ten peaks (layers) in the linear number density ρ_z are given for various values of a/a_{HS} ranging from 1.055 to 0.753. Here, the position of the first peak in ρ_z has been taken as $z = 0$, as we did not retrieve the exact position of the bottom wall from our confocal data sets. As can be seen, we start in Figure 4-7 with a perfectly layered structure, where the density in between layers falls to zero. This is expected for a templated crystal where crystal planes run parallel to the patterned bottom wall. The crystal shown on the top left in Figure 4-7 corresponds to the confocal images shown in Figure 4-4, i.e. the hcp crystal. From the linear number density in Figure 4-7, follows an interlayer spacing of $\Delta z = 0.73\pm0.01$ μm, in correspondence with the
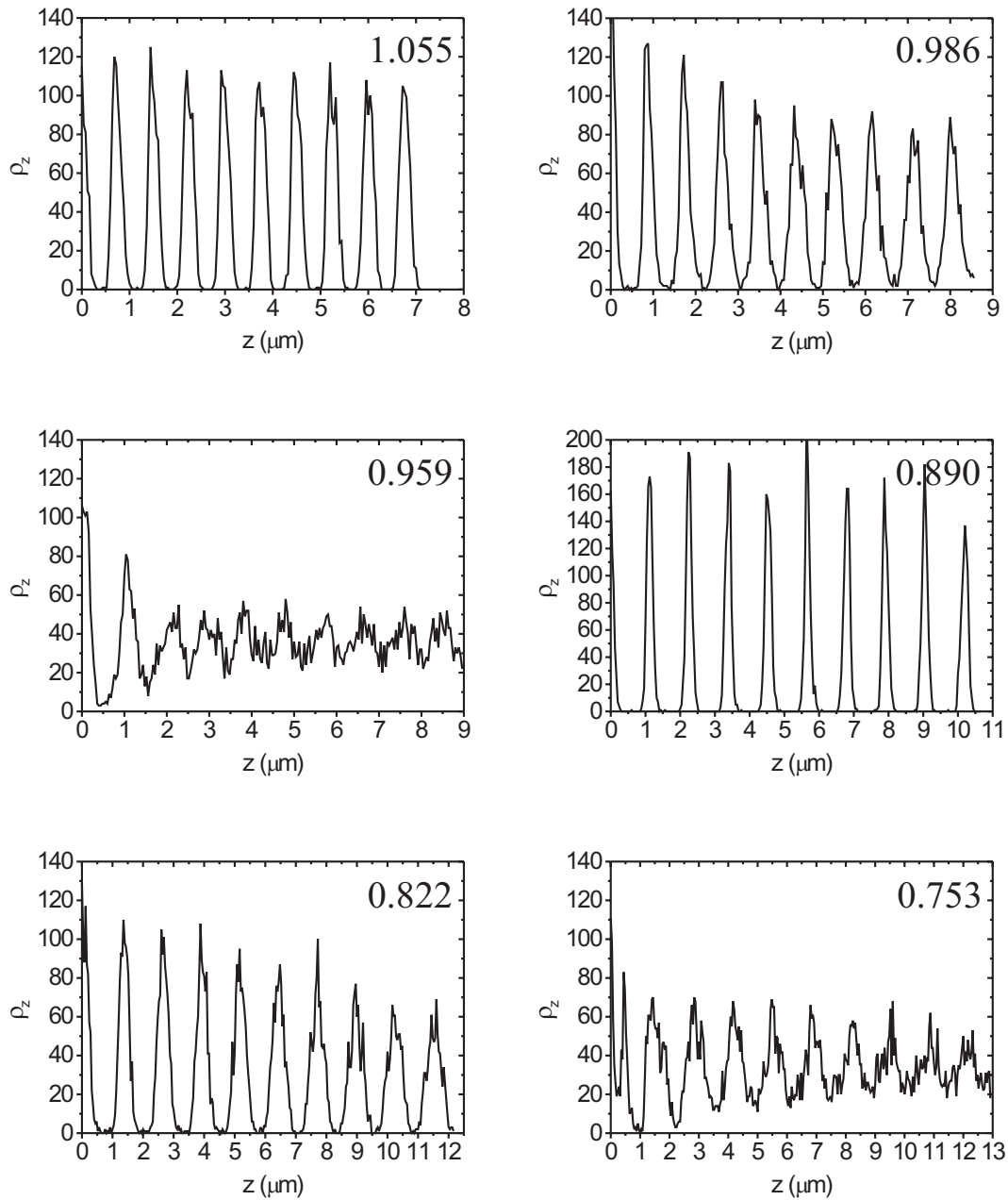
Figure 4-7 The linear number density of particles perpendicular to the hcp(1100)-template at different template-crystal mismatch. The values in the top right corners of every graph give the corresponding value for a/a_{HS}. The figures with $a/a_{HS} = 1.055$ and 0.890 correspond to 'perfect' hcp and fcc crystals respectively.

value of $\Delta z_{HS} = R_{HS} = 0.730$ μm expected for an hcp(1100)-plane based on the effective hard-sphere radius and an osmotic pressure that gives rise to almost close-packed conditions.

At smaller a/a_{HS}, the width of the peaks increases, which is accompanied by a decreasing peak height, an increasing interlayer density, and an increase in the total height of the first ten layers (note the changing scale on the *z*-axis in Figure 4-7). These are all indications of out-of-plane
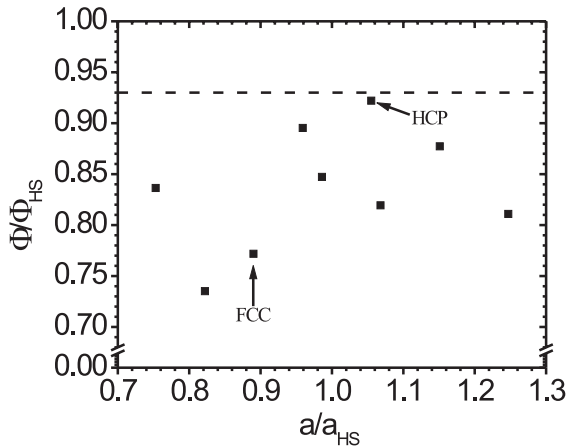
Figure 4-8 Calculated volume fractions of the epitaxially grown crystals as a function of template-crystal mismatch for the isotropically stretched hcp(1100)-template. The volume fractions have been scaled to the hard-sphere volume fraction given in Figure 4-1, averaged over the same height in the sediment as layers three to ten.

displacements of particles, and, at further decreasing a/a_{HS}, small grains of particles that move up or down with respect to the average layer position. In between $a/a_{HS} = 0.986$ and $a/a_{HS} = 0.959$ this leads to overlapping of successive peaks, and, at $a/a_{HS} = 0.959$, a uniform density with oscillations after the first two layers.

This trend is however interrupted at $a/a_{HS} = 0.890$, where crystal structure is again perfectly layered, with interlayer-density sharply falling to zero. This situation corresponds to an (100)-oriented fcc crystal structure. Note that for $a/a_{HS} = 0.890$ also the scale on the ρ_z-axis has changed with respect to the other graphs in Figure 4-7. This, together with the increased interlayer distance is in correspondence with the higher in-plane density of the fcc(100)-plane compared to the hcp(1100)-plane[1]. For the interlayer spacing at $a/a_{HS} = 0.890$, we find $\Delta z = 1.14\pm0.01$ μm, which is a factor of 1.11 higher than the value of $\Delta z_{HS} = 1.03$ μm that would be expected based on the effective hard-sphere radius. Even when we would take an interparticle distance that corresponds to the stretched hcp(1100)-lattice ($d = 1.54$ μm), the interlayer spacing of $\Delta z = 1.14\pm0.01$ μm for the (100)-oriented fcc-crystal is still a factor 1.05 higher than the value of $\frac{1}{2}d\sqrt{2}$ that would be expected.

At negative deformations of the template unit cell larger than $a/a_{HS} = 0.890$, the same behavior of out-of-plane displacements is found but then for the fcc-crystal as can be seen in the last two graphs in Figure 4-7. Note that for $a/a_{HS} = 0.753$ the first layer has a split peak indicating the formation of a new layer of upwards displaced particles.

In Figure 4-7 we saw a large variation in layer-width and layer-spacing over template-crystal mismatch, due to particle displacements and defects. In Figure 4-8 it can be seen that these displacements also drastically influence the volume fraction calculated over layers three to ten. For the crystal at $a/a_{HS} = 1.055$ a volume fraction of $\varphi/\varphi_{HS} = 0.92$ is found, which is in close correspondence with the value of $\varphi/\varphi_{HS} = 0.93$ that is found for the untemplated close-packed crystal. The out-of-plane displacements that occur when a/a_{HS} becomes smaller lead to a strong decrease of φ/φ_{HS}. Remarkably, a further increase in out-of-plane displacements (see Figure 4-7) leads again to an increase in volume fraction. The reason for this may be the possibility to accommodate a larger number of particles per layer at a larger layer width, through cooperative out-of-plane displacements, similar to the buckling mechanism observed in confined systems[48,

---

[1] The hcp(1100)-plane has an equal in-plane density as the fcc(110)-plane.
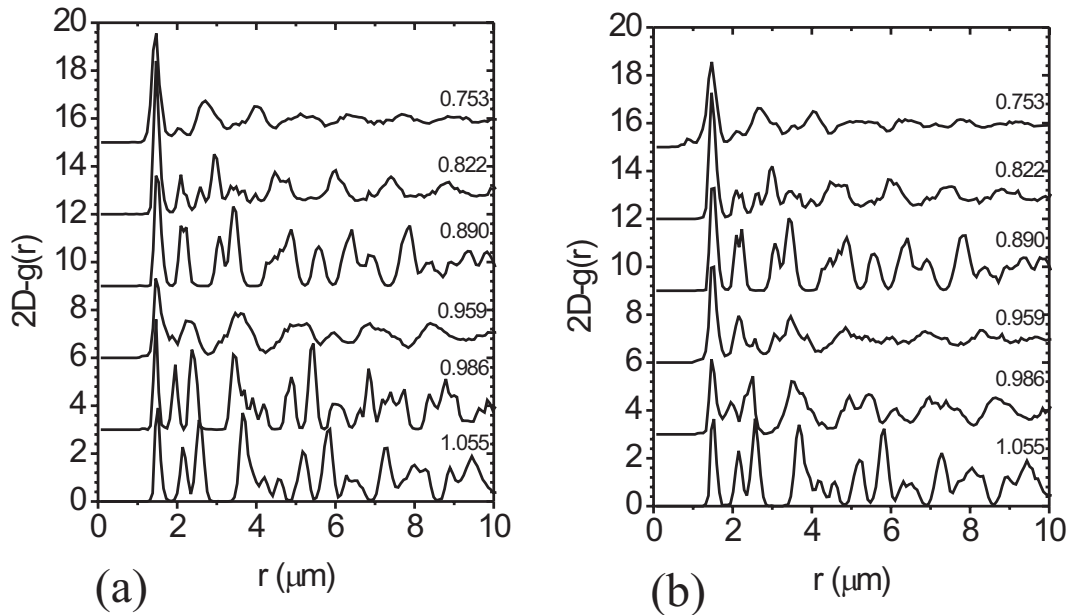
Figure 4-9 In-plane (2D) radial distribution functions for the epitaxial HCP-FCC transition (a) at the third layer from the template and (b) at the tenth layer from the template. Curves for different values of ε are shifted by 3 for clarity. Values for a/a_{HS} are indicated at the right side of every curve.

50]. Note however that we do not observe the splitting of a single peak into two separate peaks, apart from in the first layer at $a/a_{HS} = 0.753$. The fcc-crystal that grows at $a/a_{HS} = 0.890$ has a volume fraction that is about 0.8 times lower than that of the hcp- and the untemplated close-packed crystals.

In Figure 4-9 the 2D-$g(r)$ for layers three and ten is shown over the same range of a/a_{HS}. Between the curves for $a/a_{HS} = 1.055$ and $a/a_{HS} = 0.986$, a small shift of all peak positions *except for the first peak* towards smaller distances can be seen. There are however no further qualitative differences between the forms of both curves up to at least the first ten peaks. This shift of peak positions can have two reasons. It may result from neglecting the z-coordinate of particles in this layer. As we saw that the range of z-coordinates in a single layer widens (Figure 4-7), projection of these z-coordinates onto a single layer will lead to an underestimation of true interparticle separations. This however would show up in a shift of all peak positions, including the first peak. A second cause may be an in-plane shift in particle positions, for instance by a small change in the orientation of nearest neighbors. This will preserve the nearest-neighbor distance and thus the position of the first peak in 2D-$g(r)$, but will change the positions of next-nearest neighbors, i.e. of all higher-order peaks. This is also what we observe for the first two curves in Figure 4-9.

At $a/a_{HS} = 0.959$ peak positions have smeared out and overlapped and only small, broad oscillations survive. Where initially particle-displacements only caused a small shift in peak positions, here these displacements have disturbed the underlying crystal lattice so severely that even the short-range order is not visible anymore. At $a/a_{HS} = 0.890$ the long-ranged crystallinity of the fcc(100)-lattice becomes visible. Note that the center position of the shifted second and
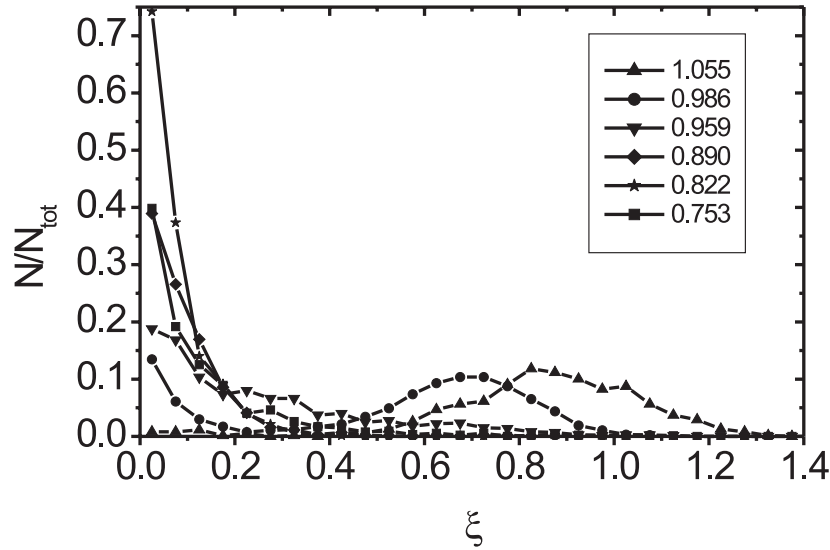
Figure 4-10 Distributions of the ξ-parameter for different values of a/a_{HS} along the HCP-FCC transition. The different symbols correspond to the different values of a/a_{HS} as given in the inset.

third peak of the distorted hcp(1100)-lattice exactly corresponds to the position of the second peak in the fcc(100)-lattice. This corresponds to the transition to a more symmetric unit cell, where the four nearest neighbors have similar distances. Further shrinkage of the template unit cell again distorts first long-ranged and later short-ranged crystalline order. Between $a/a_{HS} = 0.890$ and $a/a_{HS} = 0.822$ particle displacements out of the second peak lead to a new peak in between second and third peak, and particles are redistributed from the fourth peak to the joint third peak.

In Figure 4-9b, showing the 2D-$g(r)$ for the tenth layer from the bottom, it can be seen whether the in-plane order at the bottom of the sample corresponds to a 3D crystalline phase or whether it is a stressed surface state slowly relaxing towards the bulk of the dispersion. The 2D-$g(r)$ of the tenth layer for both the perfect hcp(1100)- and fcc(100)-lattices at $a/a_{HS} = 1.055$ and $a/a_{HS} = 0.890$ respectively are exactly similar to that for the third layer, in peak positions as well as in peak heights. However, the shifted hcp(1100) lattice that had sharp peaks and long-ranged order in the third layer at $a/a_{HS} = 0.986$, can be clearly seen to correspond to a stressed state. All peaks have broadened and overlapped and for instance the position of the third peak shifts back to the hcp(1100)-lattice. Note however also the sharp decrease in height of the first peak, indicating that the stressed lattice expands as a whole, including nearest-neighbor distances. For the distorted fcc(100)-lattice at $a/a_{HS} = 0.822$, there is much less change in structure between layer 3 and layer 10. Apparently, the fcc(100)-oriented lattice is better capable of maintaining a stressed crystalline structure. This is in accordance with visual observation with the confocal microscope where the fcc(100)-crystal structure with out-of-plane displaced grains was found to
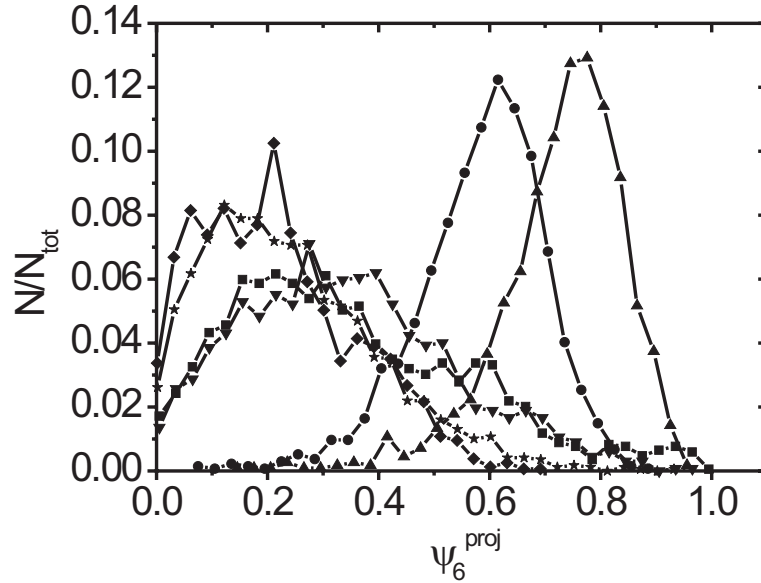
Figure 4-11 Distribution plot of the projected six-fold bond-orientational order parameter ψ_6^{proj} for the HCP-FCC transition. The different symbols correspond to a/a_{HS} = 1.055 (up-triangle), 0.986 (circle), 0.959 (down-traingle), 0.890 (diamond), 0.822 (star), and 0.753 (square).

extent deep into the bulk of the dispersion (see for instance Figure 5-2 and Figure 6-4 for confocal images of the same effect in other systems).

In Figure 4-10 the distribution of ξ over particles in the fourth layer is shown. As can be seen, the shift in higher-order peak positions that was observed in the 2D-$g(r)$ from a/a_{HS} = 1.055 to a/a_{HS} = 0.986 corresponds to a shift of the distribution of ξ from centered at about 0.9 to centered at 0.7. Furthermore, a small second distribution can be seen of particles that have a value of ξ close to zero. The shift of the main distribution to lower values corresponds to a decreasing asymmetry of the in-plane unit cell, which corresponds to the in-plane shifts of particle positions that we identified based on the behavior of the 2D-$g(r)$. The distribution close to zero indicates that these shifts have transformed a small amount of unit cells to a symmetric distribution of nearest-neighbors, i.e. an fcc(100)-symmetry. The relative number of spheres that have a value of zero is equal to the ratio of areas under both distributions. At a/a_{HS} = 0.959, the distribution around zero has risen and possesses a long tail that slowly decays to zero at about 0.8. For more negative a/a_{HS} a large peak at zero that sharply decays to zero remains, indicating the complete transformation to the fcc(100)-lattice.

For the distribution of ψ_6^{proj} (Figure 4-11) the same behavior, including the initial shift of the whole distribution going from hcp(1100) to fcc(100) can be clearly observed. The widest distributions again correspond to a/a_{HS} = 0.959 and a/a_{HS} = 0.753, the values that showed the least pronounced translational correlations in the 2D-$g(r)$.

69

(a)

(b)

(c)

(d)
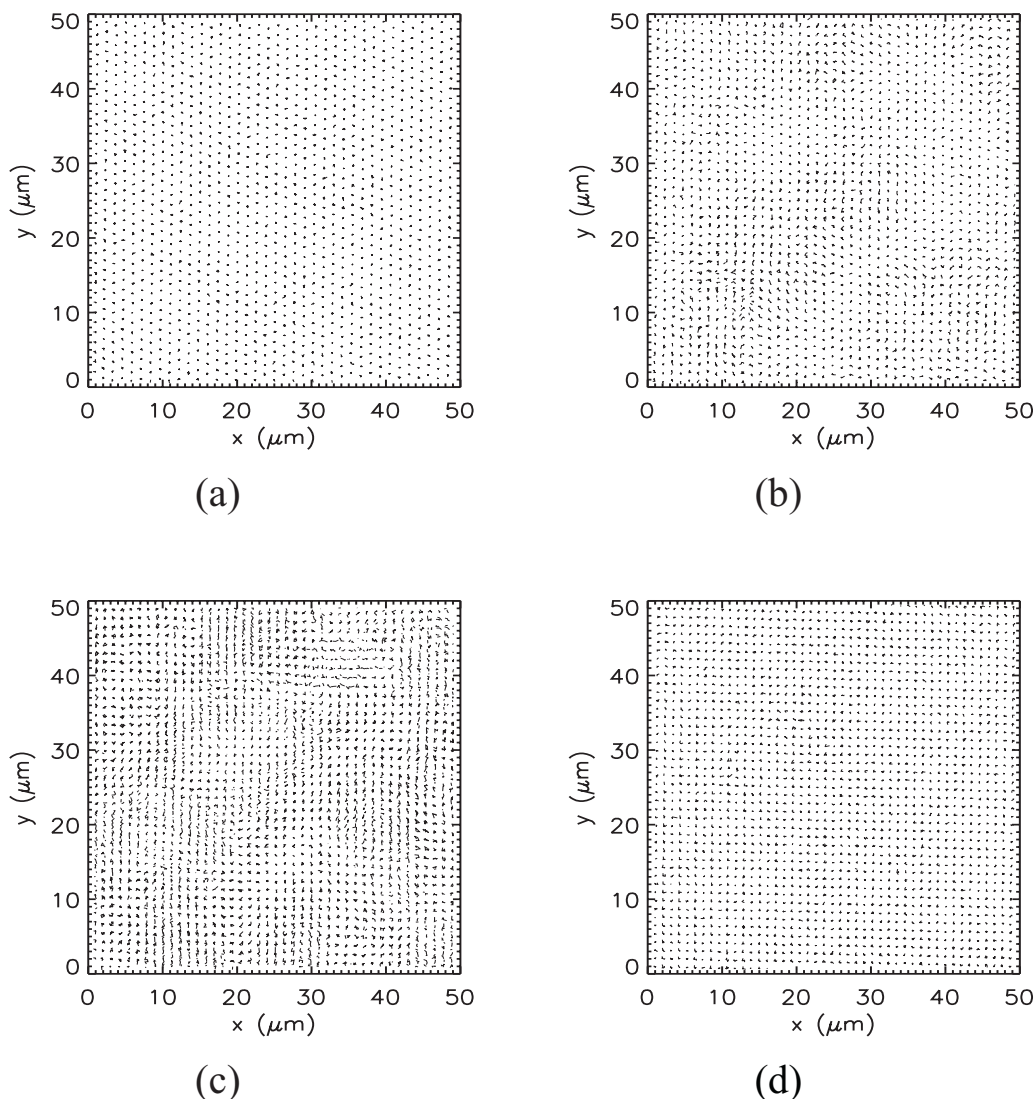
Figure 4-12 See caption with figures e-f on next page.

In Figure 4-12 particle coordinates in subsequent layers have been linked together into Lateral Displacements Curves (LDC's), with all connected lateral coordinates projected into a single xy-plane. In this way, it becomes visible to what extent order, as expressed by single-particle displacements with respect to the template persists in the z-direction. In Figure 4-12a and 4-12d, the perfectly repeating lattices of both hcp(1100), giving rise to a projected hexagonal symmetry, and fcc(100), showing a projected square symmetry, are clearly visible. Furthermore the shift in the orientation of nearest-neighbors between $a/a_{HS} = 1.055$ and $a/a_{HS} = 0.986$ is also visible when comparing Figure 4-12a and 4-12b: the clear hexagons from Figure 4-12a have been slightly distorted and a transition towards a more square symmetric lattice can already be seen. There are also small regions, like in the top left corner of Figure 4-12b where dislocations propagate in successive layers. This behavior of small regions where lateral particle coordinates are invariant

(e)   (f)
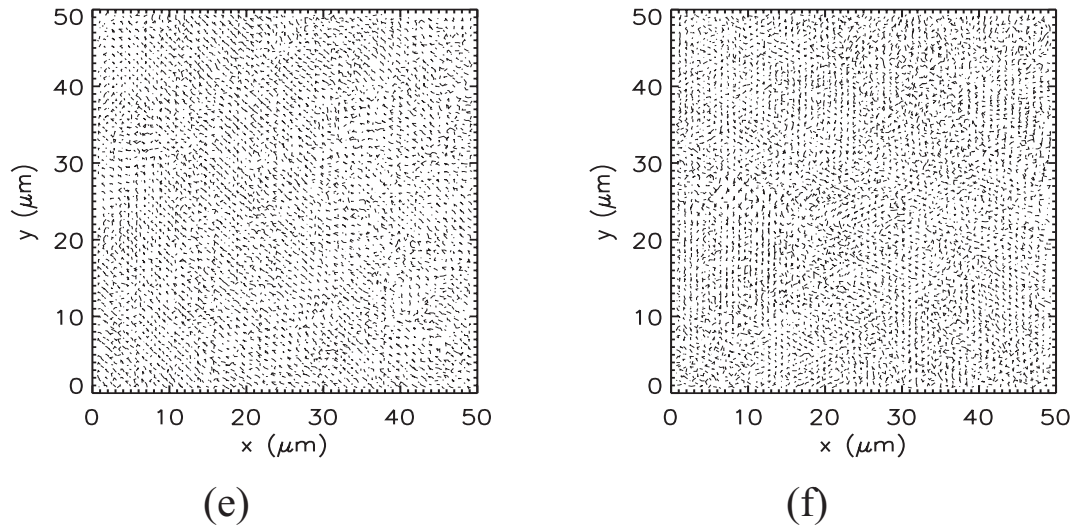
Figure 4-12 Lateral Displacements Curves (LDC's) of particles in the first twenty layers above the template. (a): a/a_{HS} = 1.055, (b): a/a_{HS} = 0.989, (c): a/a_{HS} = 0.959, (d): a/a_{HS} = 0.890, (e) a/a_{HS} = 0.822, (f) a/a_{HS} = 0.753. Figures (a) and (d) again correspond to 'perfect' hcp and fcc crystals respectively. In the other figures directional shifts in particle positions due to stress relaxation are visible.

over a translation in height and regions where these coordinates have a broader spread, can even more clearly be seen for larger template-crystal stresses in Figure 4-12c. Thus, the initial relaxation of stress caused by a template deformation is relaxed in localized defect grains that persist in height in the sample. The fact that a single dislocation persists in height is not so surprising as this basically says that a defect or dislocation in a layer disturbs ordering in successive layers. However, what is surprising is the fact that these dislocations are grouped in localized grains and that the lateral displacements in such a defect-grain seem to be *directional*, with the direction of successive displacements being uniform over several ten particle diameters wide (Figure 4-12c and 4-12f), or even almost uniform throughout the entire crystal (as in Figure 4-12e). Note that this direction in Figure 4-12e is along one of the fcc(100)-lattice vectors.

In Figure 4-13 the behavior of the root-mean-squared displacement with respect to the template, Δ_n, is shown. First, in Figure 4-13a the distribution of values for Δ in all layer-doublets n is shown. As can be seen, the distribution for the hcp-crystal at a/a_{HS} = 1.055 is sharply peaked with a maximum for Δ smaller than 0.1 μm. This is exactly in correspondence with what one would expect for a perfectly layered crystal and with the trajectory-plot in Figure 4-12a. For smaller ε the peak-positions shifts to larger Δ, showing the larger displacements of particles with respect to the template that could also be observed in Figure 4-12b and 10c. At a/a_{HS} = 0.959 we can see a split distribution consisting of a sharp peak at $\Delta = 0$ μm and a broad one with a shallow peak at $\Delta = 0.25$ μm that slowly decays to zero at $\Delta = 0.80$ μm. For a/a_{HS} = 0.890, the distribution sharpens again with the peak position shifting back to $\Delta = 0.20$ μm. Furthermore, the distribution at $\Delta = 0$ μm has disappeared again. This illustrates the transition to the fcc-lattice. Note as well that the area under the curve has become larger, showing that an increased number of particles belongs to a trajectory that can be linked to the template. This can also be seen in the inset in
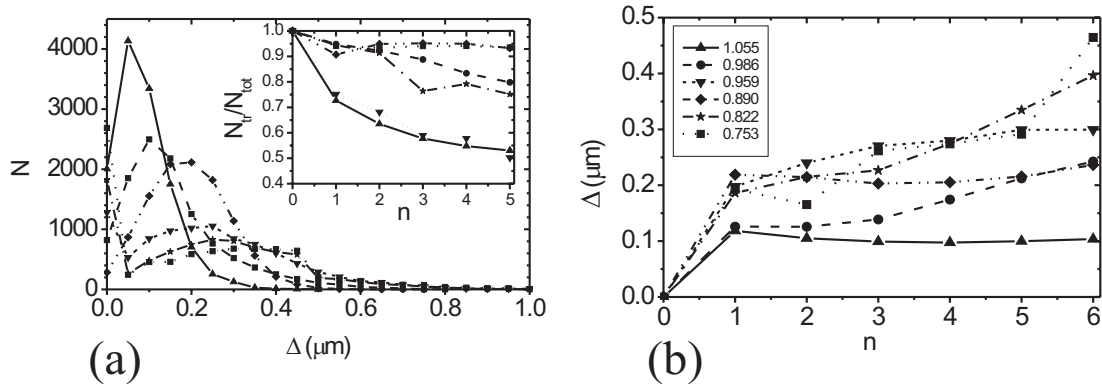
Figure 4-13 (a) Distribution of the root-mean-squared xy-displacements Δ of particles in successive layers. The inset shows the relative number of particles contained in LDC's as a function of two-layer index n. The different lines correspond to $a/a_{HS} = = 1.055$ (solid), 0.986 (dash), 0.959 (short dash), 0.890 (dash-dot-dot), 0.822 (dash-dot), and 0.753 (dot). (b) The averaged Δ as a function of n. The symbols correspond to different values of a/a_{HS} as given in the inset. Lines connecting data for each a/a_{HS} have been drawn to guide the eye, where the line type for each a/a_{HS} corresponds to that in (a).

Figure 4-13a where the relative number of particles that are linked in a trajectory is plotted as a function of depth in the sample.

In Figure 4-13b Δ_n is shown as a function of double-layer index. Here it can be clearly seen that the sharp distribution with averaged value of $<\Delta> = 0.1$ μm that we observed for $a/a_{HS} = 1.055$, corresponds entirely to lattice vibrations as its averaged value is constant throughout the crystal. Relative to the mean interparticle distance this value $<\Delta>/R_{HS} \approx 0.07$, which is well below the Lindemann criterion that stated that the relative mean-squared displacement has a value of 0.15 at melting[209]. A similar situation can be observed for $a/a_{HS} = 0.890$, corresponding to the (100)-oriented fcc-crystal. Thus we can conclude that the larger offset of $<\Delta> = 0.2$ μm is due to the mismatch of the fcc(100)-lattice with the template. For all other values of a/a_{HS}, $<\Delta>$ increases as a function of depth in the sample. Note that $n = 5$ corresponds to eighth layers deep. For $a/a_{HS} = 0.986$, we see that in the bottom of the sample $<\Delta>$ starts at 0.1 μm, but starts slowly increasing after the first six layers due to the relaxation of the stressed template positions. For the other values of ε, this also happens starting from the 'fcc'-value of $\Delta = 0.2$ μm, where for the two smallest values of ε the curves are rapidly diverging.

4.3.3 Positive isotropic deformations of the hcp(1100)-lattice

The same analysis that was performed above on the structural evolution over negative isotropic deformations of the hcp(1100)-template, can be carried out over positive, stretched, deformations. The behavior of the linear number density as function of a/a_{HS} (not shown) is similar to that shown for negative deformations: starting from a perfectly layered crystal, peaks gradually broaden due to out-of-plane displacements and again overlap, leading to a situation
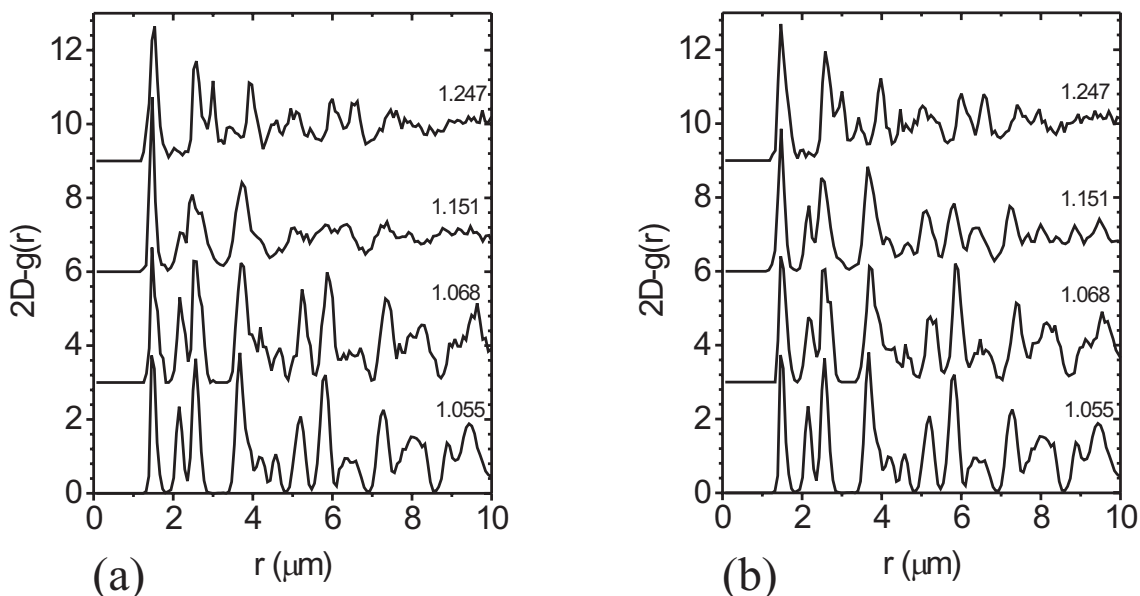
Figure 4-14 In-plane (2D) radial distribution functions for the isotropically stretched HCP template (a) at the fourth layer from the template and (b) at the tenth layer from the template. Curves for different values of a/a_{HS} are shifted by 3 for clarity. Values for a/a_{HS} are given on the right side of each curve.

with a constant offset density with small oscillations for $a/a_{HS} = 1.247$. For this highest value of a/a_{HS} the layers are not well-defined anymore after eight layers as the oscillations decay and only a constant density with a single-binsize wide noise peaks remains. Both for the isotropic expansion as well as for isotropic shrinkage of the template unit cell around the optimal value, there is a sharp decrease in φ/φ_{HS}, followed again by an increase when the number of out-of-plane displacements further increases. For $a/a_{HS} = 1.247$, the layer spacing of layers three to eight was extrapolated to find the position of a 'tenth' layer for comparison with the other results.

In Figure 4-14 the in-plane 2D-$g(r)$ for the third and for the tenth layer above the template is given, again starting with $a/a_{HS} = 1.055$, the value that corresponds to hcp-crystal growth. Already at $a/a_{HS} = 1.068$ the effect of the expanded template can be seen, resulting in displacements of a small amount of particles towards larger particle–particle separations than for $a/a_{HS} = 1.055$: the second curve from the bottom shows peak broadening to larger distances, especially in the small extra 'kinks' in the first and third maximum. Furthermore, the density in between second and third peak increases. At $a/a_{HS} = 1.151$ this effect is more pronounced: the second and third peak almost completely overlap and the long ranged correlations disappear. At the largest isotropic deformation of $a/a_{HS} = 1.247$, sharp peaks are again coming up, but their relative positions do not seem to correspond anymore to the hcp(1100)-lattice.

When looking at Figure 4-14b, it can be seen that the stressed structure in the bottom layers relaxes back to the hcp(1100)-lattice when moving further away from the template. Even at $a/a_{HS} = 1.151$, the translational correlations in the 2D-$g(r)$ of the tenth layer correspond to those
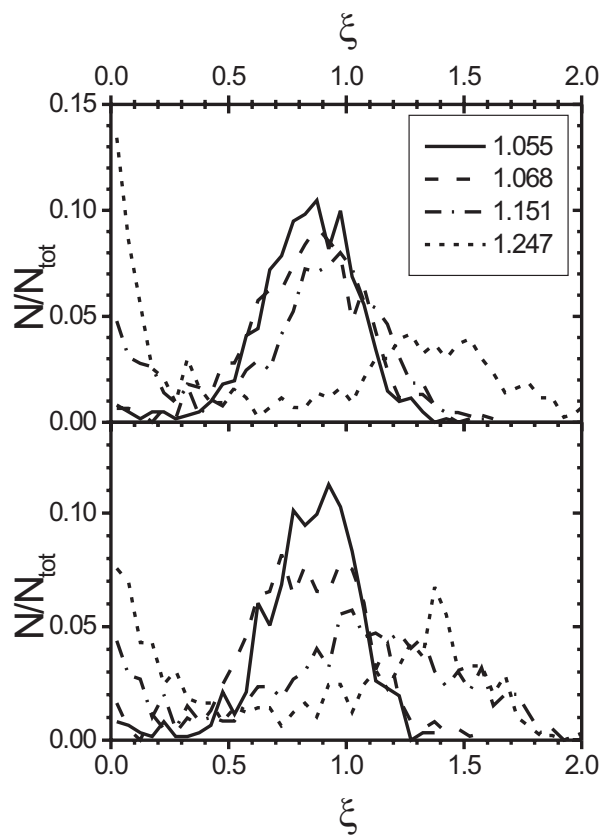
Figure 4-15 Distributions of the ξ-parameter for different values of a/a_{HS} for a stretched HCP-template. The lower curves give values for the fourth layer in the sample, the upper curves for the tenth layer in the sample. Different line types correspond to the different values for a/a_{HS} as given in the inset.

of the hcp(1100)-lattice over up to 10 μm, indicating the possibility for rearrangements from the stressed surface layers.

The behavior of the ξ-parameter (Figure 4-15) is consistent with the behavior described above. Initially, at $a/a_{HS} = 1.068$ the distribution broadens indicating small particle displacements from the hcp(1100)-lattice. Then, for larger a/a_{HS}, the distribution shifts to higher values of ξ. Thus, though the deformation of the unit cell is isotropic, the distribution of nearest-neighbor distances becomes more asymmetric. In fact, in Figure 4-14 it can be seen that the nearest-neighbor distance remains constant throughout the deformations, so the positions of next-nearest neighbors shift relatively more with the deformed lattice than do nearest-neighbors. As can be seen this shift of the distribution sets through, while meanwhile also a peak at zero develops corresponding to defected regions with a close-packed unit cell. The relaxation towards the hcp(1100)-lattice at especially the template with $a/a_{HS} = 1.151$ can also be clearly seen when comparing the distributions for third and tenth layer.
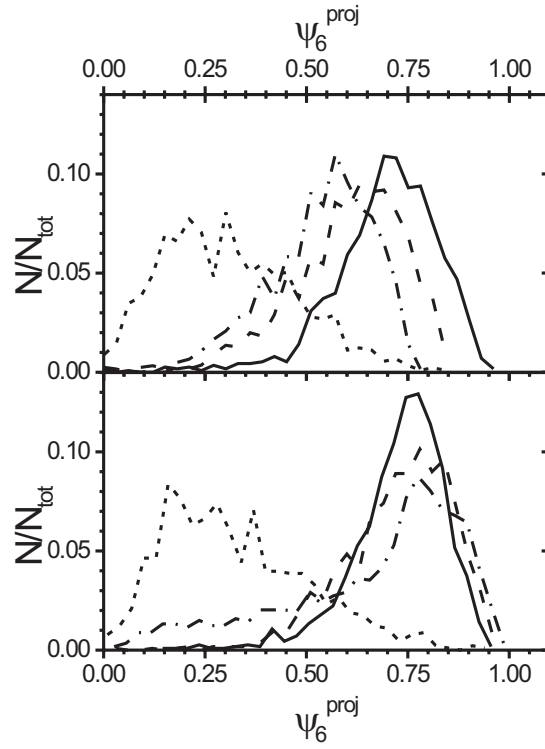
Figure 4-16 Distribution plot of ψ_6^{proj} for the stretched HCP-template for a projection of third and fourth layer (lower curves) and tenth and eleventh layer (upper curves). The different lines correspond to $a/a_{HS} = 1.055$ (solid), 1.068 (dash), 1.151 (dash-dot), and 1.247 (short dash).
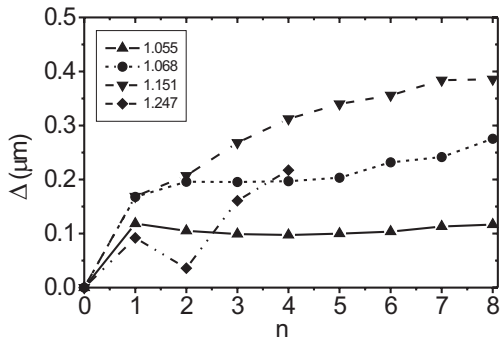
Figure 4-17 Root-mean-squared displacements of particles relative to the template as a function of double-layer index for different values of a/a_{HS} for the stretched hcp(1100)-template.
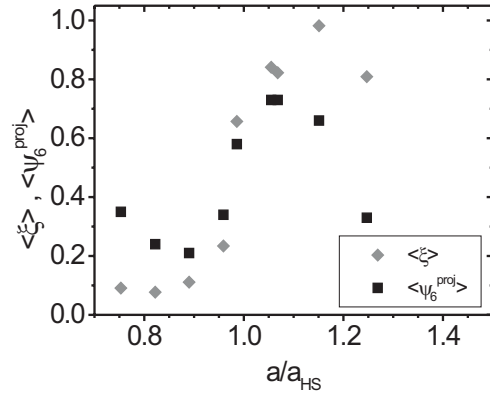
Figure 4-18 The development of both the layer-averaged values for the order parameters ξ and ψ_6^{proj} as a function of template-crystal mismatch for the isotropically stretched templates.
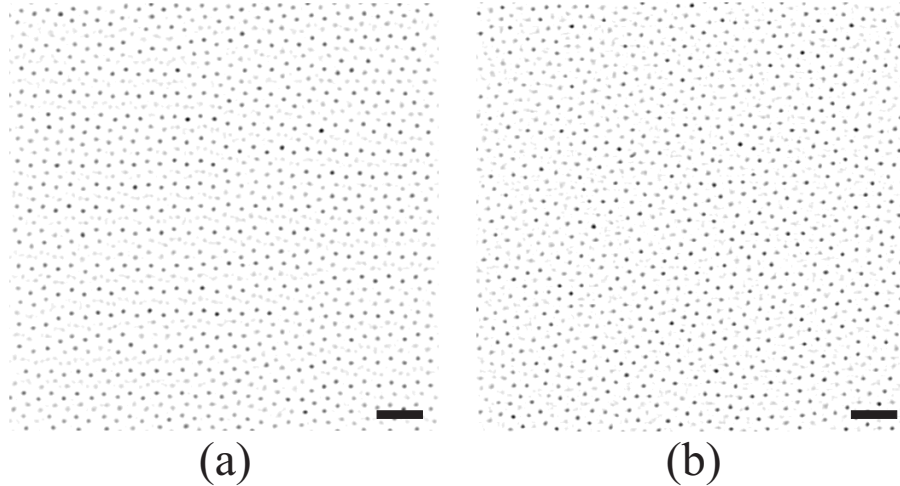
Figure 4-19 Confocal microscopy images of colloidal structures that were qualified as disordered in this study. (a): At a height of 3 μm above a template with a/a_{HS} = 1.247. Structuring in the template direction is still visible, but with a lot of defects and height differences (vague out-of-focus particles). (b): At a height of 1.3 μm above a template with a/a_{HS} = 1.630 and a/a_{HS} = 1.438. In both images the scalebar indicates 5 μm.

In Figure 4-16 it can be seen that the deformed nearest-neighbor distributions still maintain a strong hexagonal symmetry in a two-layer projection up to a/a_{HS} = 1.151. Although the decay towards zero becomes of longer range, the main distribution remains centered around 0.8, corresponding to the hcp(1100)-lattice. Also indicative of a relaxation process, is the flattening of the root-mean-squared displacements with respect to the template (Figure 4-17) for a/a_{HS} = 1.068 at n = 3, corresponding to the fourth layer, to a value of Δ = 0.2 μm. For a/a_{HS} = 1.151 the curve seems to be slowly converging as well, though a thicker crystal has to be examined to clarify whether this is actually the case. For a/a_{HS} = 1.247 the relative number of particles contained in LDC's is already below 0.6 at n = 2 (not shown) and, as mentioned before, after eight layers it is not possible anymore to distinguish individual layers. In fact the distribution of values for Δ showed a single peak at zero (not shown), like the first peak in the distributions for the lowest values of ε in Figure 4-13a, indicating that almost all of these LDC's consist of uncorrelated positions.

Finally, in Figure 4-18 the values for both $<\xi>_3$ and $<\psi_6^{proj}>_{3,4}$ are shown for all of the isotropically stretched templates, both positive and negative. Here, the influence of the deformations of the template on both order parameters can be clearly seen: the ξ-parameter follows the direction of the deformation, becoming larger for stretching the template and smaller for shrinking, while ψ_6^{proj} indicates the disturbance of in-plane symmetry when the template is deformed with respect to a/a_{HS} = 1.055. Figure 4-19 shows two examples of structures that were denoted as disordered according to the criteria given before. As can be seen for the isotropic deformation with a/a_{HS} = 1.247 the structure of the template is still locally visible, but with a considerable amount of defects, including 'stacking faults', which destroy local symmetry and translational order. At a template deformation with a/a_{HS} = 1.630 and c/c_{HS} =1.438 no effect of the template other than the absence of ordering is visible anymore.
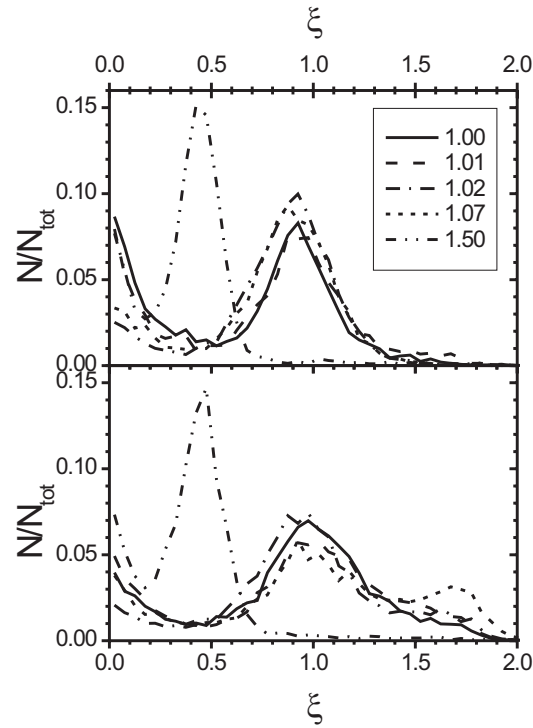
Figure 4-20 The distribution of the ξ-parameter for the anisotropically stretched template with $a/a_{HS} = 1.08$. The different line types correspond to the different values of the axis-ratio, $c/c_{HS}\cdot(a/a_{HS})^{-1}$, as given in the inset. The lower curves correspond to the fourth layer, the upper curves to the tenth layer.

4.3.4 Anisotropic (c/a-)deformations

Starting from two points for the isotropically stretched template, an anisotropic stretch of the template in the direction of the c-axis was performed. The structural evolution for these deformations is given in Figure 4-5. Both stretches were performed starting from a unit cell with $(a/a_{HS}, c/c_{HS})$-values slightly off from the regime that was identified as the best for growing an hcp-crystal, namely at $(a/a_{HS}, c/c_{HS}) = (0.99, 0.99)$ and at $(a/a_{HS}, c/c_{HS}) = (1.08, 1.08)$. Starting from the shrunken unit cell ($a/a_{HS} = 0.99$) the hcp-crystal remains stable up to $c/c_{HS} = 1.05\cdot a/a_{HS} = 1.04$, after which (111)-oriented crystals grow over the template. From the stretched template ($a/a_{HS} = 1.08$) the stability regime is larger, up to $c/c_{HS} = 1.15\cdot a/a_{HS} = 1.24$, leading at $c/c_{HS} = 1.5\cdot a/a_{HS}$ to a new supercrystal structure that we will treat in the next section. For templates with a larger stretch, a (111)-oriented crystal nucleates in this case as well. For both series, an anisotropic stretch of the template unit cell with $c/c_{HS} = 1.02$ leads to better hcp-crystal quality than for $c/c_{HS} = 1.0$ and $c/c_{HS} = 1.01$. As this behavior was found to be similar for both series, we will limit ourselves here to the series starting from $(a/a_{HS}, c/c_{HS}) = (1.08, 1.08)$.
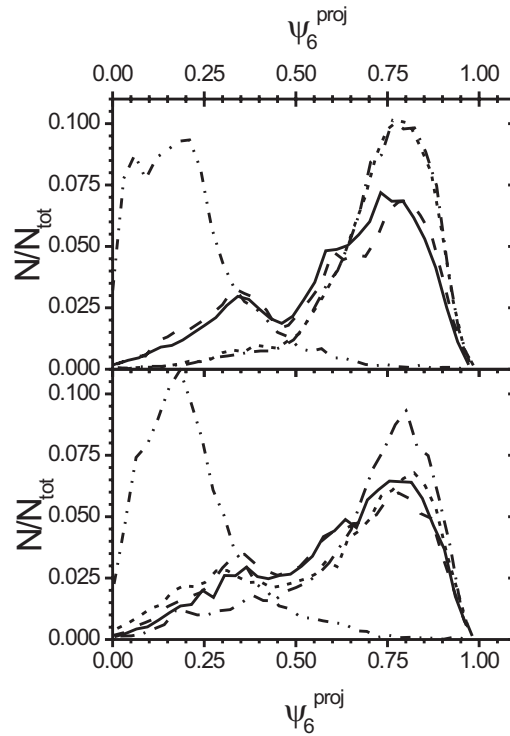
Figure 4-21 Distribution plots for ψ_6^{proj} for the anisotropically stretched template with $a/a_{HS} = 1.076$ for a projection of fourth and fifth layer (lower curves) and tenth and eleventh layer (upper curves). Different line types correspond to axis ratios of $c/c_{HS} \cdot (a/a_{HS})^{-1} = 1.00$ (solid line), 1.01 (dash), 1.02 (dash-dot), 1.07 (dash-dot-dot), and 1.50 (short dash) respectively.

In Figure 4-20 the ξ-parameter for 5 different values of $c/c_{HS} \cdot (a/a_{HS})^{-1}$ is given. The bottom curves correspond to the fourth layer from the bottom, the upper curves for the tenth layer. As can be seen, all curves for $c/c_{HS} = 1.0 \cdot a/a_{HS}$ to $1.07 \cdot a/a_{HS}$ have a main distribution with a maximum slightly below $\xi = 1.0$, corresponding to what was seen before for a template stretched compared to the ideal values, together with a smaller distribution of values close to 0.0, indicating the presence of defects. For the fourth layer, the maximum of the distribution decreases going from $c/c_{HS} = 1.0 \cdot a/a_{HS}$ to $1.01 \cdot a/a_{HS}$, but at $c/c_{HS} = 1.02 \cdot a/a_{HS}$ increases again and shifts from 0.95 to a slightly smaller value of 0.85. Furthermore, the distribution at $\xi = 0$, and thus the number of defects, decreases. This behavior is even more pronounced in the tenth layer. Where for $c/c_{HS} = 1.0 \cdot a/a_{HS}$ and $1.01 \cdot a/a_{HS}$ the maximum of the distribution at $\xi = 0$ has doubled relative to the fourth layer, this is not the case for $c/c_{HS} = 1.02 \cdot a/a_{HS}$ and even $1.07 \cdot a/a_{HS}$. The increase of peak height at $\xi = 1.0$ and the shift of this distribution towards slightly smaller values has also become more pronounced. For all four curves this distribution has sharpened, indicating that the distribution of nearest-neighbor distances for particles where this distribution is hcp(1100)-like has relaxed from the stressed stretched unit cell of the template towards ideal hcp(1100) higher in the sample. This change is more pronounced for $c/c_{HS} = 1.02 \cdot a/a_{HS}$ and
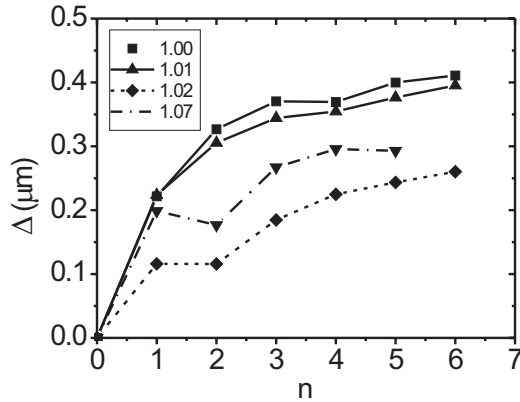
Figure 4-22 Root-mean-squared displacements with respect to the template as a function of double-layer index for the anisotropically stretched template with $a/a_{HS} = 1.076$. The values in the inset give the different values of the axis ratio $c/c_{HS} \cdot (a/a_{HS})^{-1}$.

$1.07 \cdot a/a_{HS}$ than for $c/c_{HS} = 1.0 \cdot a/a_{HS}$ and $1.01 \cdot a/a_{HS}$. For $c/c_{HS} = 1.07 \cdot a/a_{HS}$ the small distribution of large asymmetries at $\xi = 1.7$ in the fourth layer, has disappeared in layer ten.

The distribution of ψ_6^{proj} for layers three and four and layers ten and eleven are shown in the lower and upper part of Figure 4-21 respectively. Here, the increase in crystalline order for $c/c_{HS} = 1.02 \cdot a/a_{HS}$ compared to $1.0 \cdot a/a_{HS}$ and $1.01 \cdot a/a_{HS}$ is even more clearly visible. Already in layers three and four the curve for $c/c_{HS} = 1.02 \cdot a/a_{HS}$ has a 1.5 times higher maximum than for $c/c_{HS} = 1.0 \cdot a/a_{HS}$ and $1.01 \cdot a/a_{HS}$, while the small shoulder at $\psi_6^{proj} = 0.35$ has disappeared. In layers ten and eleven these differences are even better visible. Furthermore, the large increase in hcp-crystal order higher in the sample for $c/c_{HS} = 1.07 \cdot a/a_{HS}$ is also clearly evident: not only has the maximum value increased to almost 0.1, similar to the relaxation at $c/c_{HS} = 1.02 \cdot a/a_{HS}$, the shoulder at $\psi_6^{proj} = 0.35$ that has become more pronounced for $c/c_{HS} = 1.0 \cdot a/a_{HS}$ and $1.01 \cdot a/a_{HS}$, has completely disappeared for $c/c_{HS} = 1.07 \cdot a/a_{HS}$.

In Figure 4-22, the root-mean-squared displacements relative to the template are shown. Here it can also be seen that the displacements with respect to the template become less at slight variation of the c/a-axis ratio. If we look at the plots of these LDC's, in Figure 4-23 shown for $(a/a_{HS}, c/c_{HS}) = (0.99, 0.99)$ and axis ratios of 1.0 and 1.02 respectively, the breakup of structure over a mismatch-template in hcp-grains and defect-grains that we have seen before for the isotropic stretches in Figure 4-12, is also visible here. Furthermore, the correlations in displacements in these defect-grains again show up. However, when comparing Figure 4-23a and 4-23b it can be noted that there is a remarkable transition in both the relative positions of hcp- and defect grains as well as in the directional correlations in particle displacements in these defect-grains. On the template that is stretched in the c-axis direction, both the hcp- as well as the defect-grains are elongated parallel to this direction and alternate perpendicular to this c-axis direction. In the defect-grains the displacements of particles relative to particle positions in previous and successive layers are strongly directed perpendicular to the direction of the c-axis and thus to the direction of the stretch of the template. For the template with $(a/a_{HS}, c/c_{HS}) = (1.08, 1.08)$ a similar directionality of displacement-correlations was observed, but with the displacements being parallel to the c-axis direction.

(a)

(b)

Figure 4-23 Lateral Displacement Curves (LDC's) for an anisotropically stretched template with a/a_{HS} = 0.99 for (a) an axis ratio of $c/c_{HS} \cdot (a/a_{HS})^{-1}$ = 1.00, and (b) an axis ratio 1.02.

4.3.5 Non-close packed HS crystal

In Figure 4-20 it can be seen that at $c/c_{HS} = 1.50 \cdot a/a_{HS}$ the distribution of ξ contains a remarkably sharp and, compared to the hcp-distributions also narrow, distribution centered at 0.5. This strongly indicates the emergence of a structure with a replicating unit cell that has half the asymmetry in nearest-neighbor distances than has the hcp(1100) unit cell. The distribution of ψ_6^{proj} in Figure 4-21 shows a distinct peaked distribution as well, here with a maximum at $\psi_6^{proj} = 0.20$. The behavior of these two order parameters is different from that of the other crystalline structures that we encountered over the hcp(1100)-template before, like fcc(100) (see Figure 4-10 and Figure 4-11) and hexagonal.

In Figure 4-24a ρ_z for the structure on this template is shown. The structure consists of sharp layers, with a peak width comparable to that of the hcp- and fcc-crystal in Figure 4-7a and 4-7d. The distance between the peaks has a constant value of $\Delta z = 0.50 \pm 0.01$ μm. The constant 'offset' density of about 0.15 times the average peak height is caused by small defect grains that were found to coexist with this structure (also note the distribution of ξ at zero in Figure 4-20). The fact that there is a split first peak is probably caused by the fluorescence of the template, which makes the determination of particle positions close to the template harder. The small interlayer spacing of 0.50 μm suggests a low in-plane density. In fact, if we look at the 2D-$g(r)$ in Figure 4-24b, it can be seen that the first peak of the hcp(1100)-lattice is almost completely absent. Thus the mean interparticle distance has increased towards a value of about 2 μm, showing that indeed the in-plane density is lower than for the close-packed planes. The first two peaks in 2D-$g(r)$ actually fall on the same positions as the second and third peak in the hcp(1100)-2D-$g(r)$. For larger distances peak positions in both functions slowly run out of registry with each other

(a) (b)
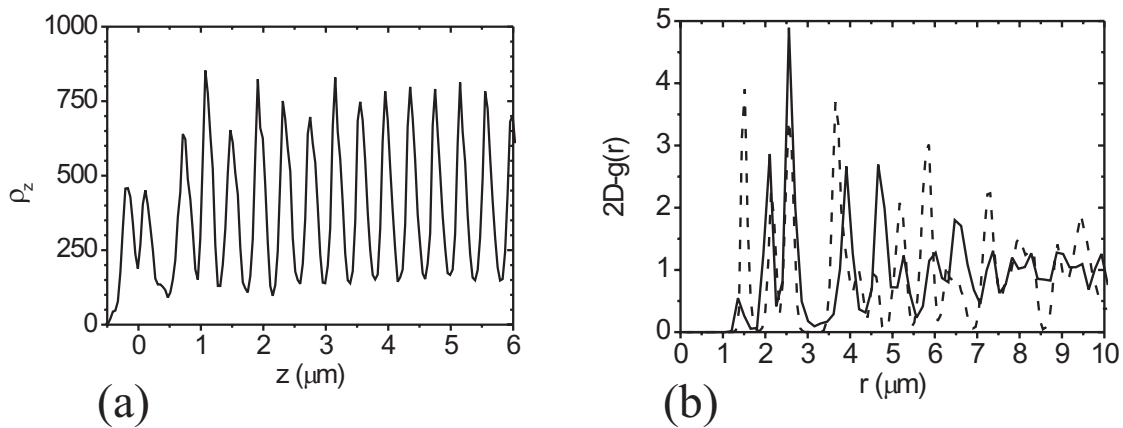
Figure 4-24 (a) Linear number density perpendicular to the template for a crystal at an anisotropically stretched template with $a/a_{rc} = 1.076$ and an axis ratio of $c/c_{rc} \cdot (a/a_{rc})^{-1} = 1.50$.
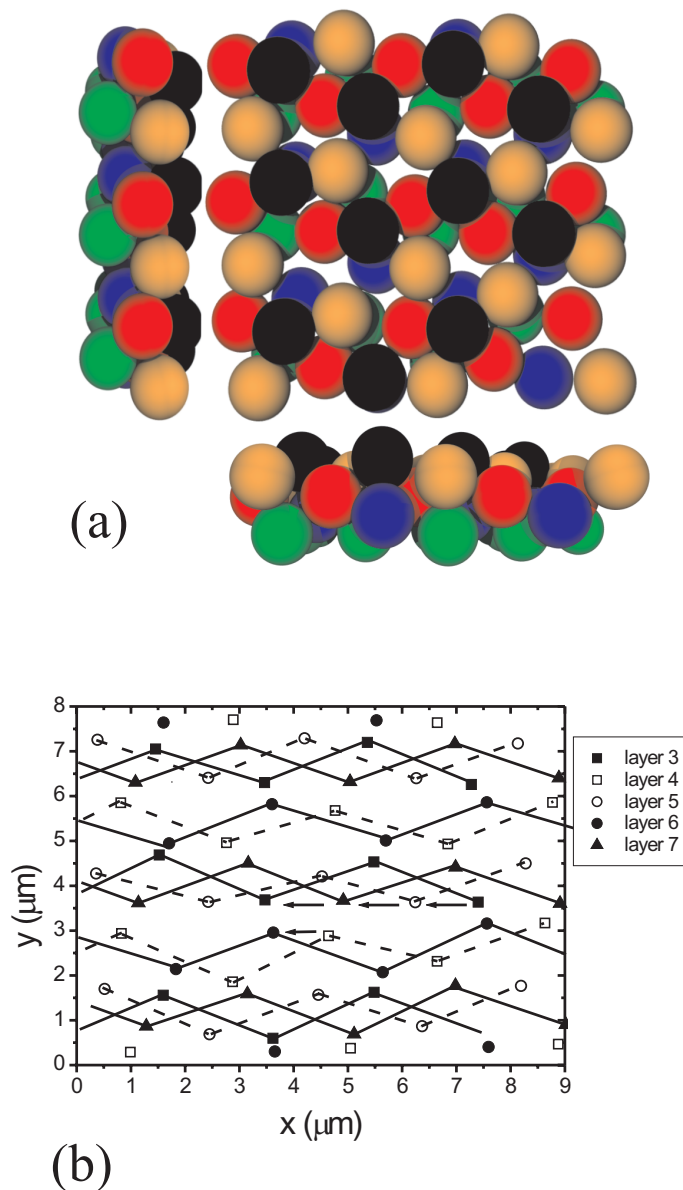
Figure 4-25 (a) Image showing particle coordinates in a small part of our real-space data-set in layers three to seven for the crystal at an anisotropically stretched template with $a/a_{HS} = 1.076$ and an axis ratio of $c/c_{HS} \cdot (a/a_{HS})^{-1} = 1.50$. The image in the middle shows a top view, the other two the respective side views. Spheres, with diameter drawn to scale, have been colored corresponding to their layer-index: black for the top layer, then for subsequent layers respectively gold, red, blue and green. (b) A projection of xy particle coordinates for the spheres in (a) onto a single layer. The symbols corresponding to the different layers are given in the legend next to the graph. Positions indicated with filled symbols have been connected with solid lines, open symbols with dashed lines, in order to indicate the template-induced alignment. The arrows indicate the shift in particle positions with the original template *ABA*-sequence between layers 3, 5, 7, and 9 (=3) and layers 4 and 6 respectively.

In Figure 4-25a an image of a small part of the crystal is shown with spheres drawn at the determined *xyz*-positions. Both the small interlayer spacing as well as the open in-plane structure are clearly visible in this image. Figure 4-25b shows the *xy*-coordinates for particles in Figure 4-25a projected onto a single plane. The positions in successive layers exactly follow the zigzag of the stretched hcp(1100)-lattice with the coordinates for particles in layers *i* and *i*+1 falling in different 'lanes' displaced in the *a*-axis direction. The extra space created by stretching the template in the *c*-direction is accommodated by shifting positions in layers *i* and *i*+2 within these lanes by 1 μm as indicated with the arrows drawn in Figure 4-25b. These shifts indicate that the structure should be periodic when translated over six layers and indeed we have found that the particle positions in the ninth layer fall on top of those in layer three.

For the hard-sphere scaled volume fraction of this crystal we found a value of $\varphi/\varphi_{HS} = 0.78$, compared to $\varphi/\varphi_{HS} = 0.92$ for the crystal grown on a templateless part of the bottom wall. This value is however higher than that for the best hcp-crystal in this series of anisotropic deformations, namely that at $c/c_{HS} = 1.02$ a/a_{HS}, which was $\varphi/\varphi_{HS} = 0.74$. This again highlights that the distorted crystals that grow at the deformed templates are, strictly speaking, not close packed as well. As noted before and visible in Figure 4-20 and Figure 4-21 the non-close packed superstructure alternates with defect grains. This can be due to the fact that our deformed hcp(1100)-template is not the best-suited template to grown this crystal structure. The most obvious choice for the 'ideal' template would seem a template that has an anisotropic stretch of the axis ratio of 1.50, like in this case, but starting from the ideal hcp(1100)-plane or, as there may again be prefreezing or wetting, starting from the hcp(1100)-template that generated the best quality hcp-crystal. It would certainly be interesting to further examine the growth conditions for this peculiar hard-sphere crystal structure.

4.4 Summary and discussion

In this chapter we have demonstrated the possibility to grow crystal structures that are metastable in bulk crystallization using colloidal epitaxy. For colloids interacting through a hard-sphere like potential, an hcp(1100)-pattern was found to induce hcp crystal formation. Modification of this surface pattern gives the possibility to directly dictate the crystal's stacking sequence, which was illustrated by growth of a 'double hcp' (dhcp) crystal.

For the hcp(1100)-template the evolution of crystal structure over template-crystal mismatch was studied using a 3D real-space analysis. The first step in our analysis consisted of examining the degree of layering parallel to the template. A template-crystal mismatch was found to lead to out-of plane displacements of particles, in accordance with observations in molecular epitaxy[98, 99]. Thus in further research on colloidal epitaxy, the width of peaks and/or the relative depth of minima in the linear number density perpendicular to the template may be used as parameters for probing the quality of the epitaxially grown crystal and for identifying the best conditions for epitaxial crystal growth. Relatively small values for the layer width and an interlayer density of

essentially zero correlate with sharp peaks and long-ranged in-plane order as evidenced in the 2D-$g(r)$ and with the indications given by the other order parameters that we have used. For the hcp-crystal these conditions were met at an isotropically stretched template with lattice parameters $a/a_{HS} = c/c_{HS} = 1.055$. Scaling the template isotropically from these values led to the out-of-plane displacements mentioned above. For a template where the unit-cell dimensions were shrunken to $a/a_{HS} = 0.89$, there was a structural transition to a (100)-oriented fcc-crystal. Further shrinkage as well as large isotropic stretches led to disorder in the first layers over the template. The volume fraction of the epitaxially grown crystal was found to vary with template-crystal mismatch, with the highest volume fraction crystal growing at the isotropically stretched template.

For a hard-sphere system in zero-gravity, Heni and Löwen recently showed that non-hexagonal surface patterns prefreeze and/or wet at a unit-cell of which both lattice spacings are stretched by a factor of 1.035[63, 64]. This may be readily explained by the fact that a solution crystallizing at lower volume fractions than bulk freezing has correspondingly larger lattice parameters than for a crystal at bulk volume fractions. Thus our result that an isotropically stretched template grew the best quality hcp-crystal may be an indication that the hcp(1100) shows prefreezing or even wetting. For this isotropically stretched template we however also found the highest volume fraction, which was furthermore almost similar to the volume fraction of the untemplated close-packed crystal, so not in correspondence with what one would expect for a stretched unit cell. The reason why this higher volume fraction was reached, was the fact that the distance between the hcp(1100)-planes in this crystal was smaller than what would be expected for the stretched hcp(1100)-lattice vectors. This is probably caused by compression of the crystal when more particles sediment and crystallize on top of it: at first a few layers prefreeze at the stretched template, but when during sedimentation the pressure increases, the crystal cannot isotropically compact as decreasing the in-plane lattice vectors would result in an increase in interlayer distance opposite to the gravitational field. Thus the stretched in-plane lattice vectors are preserved and the interlayer distance in the crystal is smaller to accommodate the higher volume fraction. For the (100)-oriented fcc crystal an approximately 0.8 times lower volume fraction than that of the hcp-crystal was found, that was also lower than that for any of the other defected hcp-crystals. The quality of the crystal as judged from the behavior of the various order parameters used, was however comparable to that of the best hcp-crystal. Furthermore, the in-plane nearest neighbor distance did not noticeably change between the hcp and the fcc crystal indicating that the fcc-crystal also showed prefreezing. Apparently, the (1100)-oriented hcp crystal can be compressed much more to accommodate the increasing osmotic pressure than the (100)-oriented fcc crystal. Indeed, for the fcc crystal we found a layer spacing that was a factor 1.11 higher than the expected value based on the effective hard-sphere radius, while for the (1100)-oriented hcp crystal these two values corresponded.

The dependence of volume fraction on template-crystal mismatch starting from the stretched template that yielded the highest volume fraction and best quality crystal, was as follows: A small deviation of lattice parameters from the ideal ones led to a sharp decrease in volume fraction after

which there was again a rise in volume fraction when the layer-width further increased. The reason for this may be the possibility to accommodate a larger number of particles per layer at a larger layer width, through cooperative out-of-plane displacements, similar to the buckling mechanism observed in confined systems[48, 50].

Based on layer-wise defined order parameters the structural evolution was examined in more detail. This analysis showed the structural relaxation in subsequent layers above a mismatch-template. However, it should be noted that the sample used in the experiment with isotropically shrunken and expanded unit cells, consisted of only thin crystals, with a sediment thickness of about 20 μm. As such the osmotic pressure at the tenth layer is considerably lower than at the template. This however hardly changed the calculated hard-sphere volume fraction calculated over the range in z spanned by the first ten layers. Furthermore, in the experiments with the anisotropically stretched templates a higher initial volume fraction was used, which resulted, over the range of layers examined, in a constant volume fraction of almost 0.74 corresponding to complete compaction. In these crystals relaxation and rearrangements as a function of height in the crystal were still observed. It is known from molecular epitaxy that structural transitions can take place at over 20 layers above a mismatch-substrate[102]. For a system of density-matched colloids, we have recently found that stressed surface crystals can extent for over thirty layers deep[173]. The extent of epitaxial crystal structure and its dependence on sediment thickness needs to be explored in more detail in further research, both for the mismatch structures as well as for the 'perfect' epitaxial crystals. This will also give additional insight into the strength of the entropic interaction of the templated wall with the hard-sphere system.

By analyzing particle positions in successive layers with respect to template and to each other, and thus constructing lateral (xy-) displacements curves (LDC's), the location of and correlations between dislocations and defects were studied. The root-mean-squared displacements in these LDC's provided a sensitive order parameter for crystal quality. For the hcp-crystal these were found to be constant at 0.14 times the particle radius, for the fcc crystal constant at 0.28 times the particle radius. For small mismatches these values increased and diverged higher in the crystal. Furthermore, these trajectory-plots gave insight in correlated displacements of particle due to surface stress. At increasing mismatch and thus increasing particle displacements with respect to perfect crystal positions there was a structural breakup in 'crystal'-grains and 'defect'-grains, with these displacements being localized in the latter. Furthermore, particle displacements in these defect-grains are strongly correlated in their direction. For a template that was anisotropically stretched in the c-axis direction both these particle displacements as well as the shape of these crystal and defect-grains were directed perpendicular to this c-axis direction. These results strongly suggest the application of correlation functions in analyzing local stress and local 'defect' grains.

The structural analysis presented in this work was mostly based on a layer-wise, 2D analysis. Although for an epitaxially grown crystal, defects and dislocations caused by a template-crystal mismatch affect the crystal structure in a 3D way, as also followed from the results presented above. A thorough investigation of stress relaxation in epitaxially grown crystals, especially in

the cases where the interlayer density has increased to substantial non-zero values and thus the definition of layers is not strictly applicable anymore, has to include 3D order parameters as well, especially for the larger template-crystal mismatches. By performing a 3D analysis information about dislocations concentrations, distances between bound dislocation pairs, and correlation lengths, can be retrieved.

The variation of the *c/a*-ratio by anisotropically stretching the template unit cell starting from either a slightly isotropically shrunken or stretched unit cell compared to the ideal values for epitaxial growth, was found to lead to better quality crystal as evidenced by the criteria mentioned above. For both the shrunken and the stretched unit cell, this occurred at a 1.02 stretch of the *c*-axis. For the shrunken unit cell, larger deformations finally led to the occurrence of (111)-oriented hexagonally stacked crystals. For the stretched unit cell a non-close packed superstructure occurred at a 1.50 stretch along the *c*-axis. This structure consisted of regularly stacked crystal planes that followed the stretched hcp(1100)-lattice, with the stacking being periodic over six crystal layers. This result even more clearly shows the possibility to create metastable crystal structures using colloidal epitaxy and opens perspectives for the growth of colloidal, hard-sphere quasi-crystals.

5

Epitaxial crystal growth of charged colloids

A pattern of repulsive, charged lines is demonstrated to direct three-dimensional (3D) crystallization in a system of long-ranged repulsive, density-matched colloids. At volume fractions where the bulk phase behavior leads to bcc crystallization, the 1D template was found to induce formation of a metastable fcc crystal. bcc crystals were oriented with the (100)- or the (110)-plane, with two-fold twinning, parallel to the template. The template further induced prefreezing of the (100)-plane. At a large mismatch between template and interparticle spacing, 1D strings formed in the surface layer of a 3D crystal.

5.1 Introduction

Research on model colloids has gained renewed interest both due to their use in materials like photonic crystals, and because of their use as a condensed-matter model system with the possibility of three-dimensional real-space analysis[7, 61, 159]. Colloidal epitaxy, the manipulation of colloidal crystallization by using patterned surfaces[61], is one example of a recently introduced technique that stimulated research in both applied[77, 110, 138] and fundamental physics[63, 64, 109]. So far, experiments reported were performed on systems with short-ranged interactions and in a gravitational field[61, 109, 138].

In this chapter we will show the extension of colloidal epitaxy to systems with a long-ranged repulsive (LRR) interaction potential. The phase-diagram of colloids with LRR interactions shows a martensitic solid-solid transition[54, 210]. At relatively low volume fractions a transition from the liquid state to a body-centered cubic (bcc) crystal occurs, followed at higher volume fractions by a bcc to face-centered cubic (fcc) transition. The tunability of lattice parameters in these colloidal crystals by factors like ionic strength and surface potential make LRR colloids suitable for a variety of applications, such as sensors and photonic switches[69, 87]. The results that will be presented in this chapter will be of relevance both for an understanding of how boundary conditions influence phase transitions in soft repulsive colloidal systems as well as for achieving more control over these systems in applications.

5.2 Experimental details

A one-dimensional (1D) pattern of lines that has a surface charge similar to that of the colloids was used as a template. The reason for choosing a 1D substrate pattern is two-fold. Firstly, a 1D template is easy to make. Secondly, if perfect epitaxial growth of a 3D crystal is possible with a 1D template, we would expect a system with LR potentials to be most successful. In this respect we want to note that 3D crystal growth, and even inducing long-range 2D order, was unsuccessful with a 1D line-pattern in the case of short-ranged attractive colloids[109]. Below it will be shown that e.g. for a templated, square-symmetric surface-plane there is no anisotropy corresponding to the 1D lines present in the 2D crystal plane anymore. The results presented here can be easily extended to more complex surface patterns by directly patterning a substrate with a surface-layer of colloids[104].

All experiments were carried out at volume fractions where bcc crystals were found to be the stable crystal phase on the time-scales of our experiments (typically several days) and we therefore call this the equilibrium phase. As fcc crystal formation may proceed via formation of a bcc critical nucleus[211, 212], we however cannot exclude the possibility that this bcc phase is meta-stable. The role of gravity in the epitaxial growth process was eliminated by nearly density-
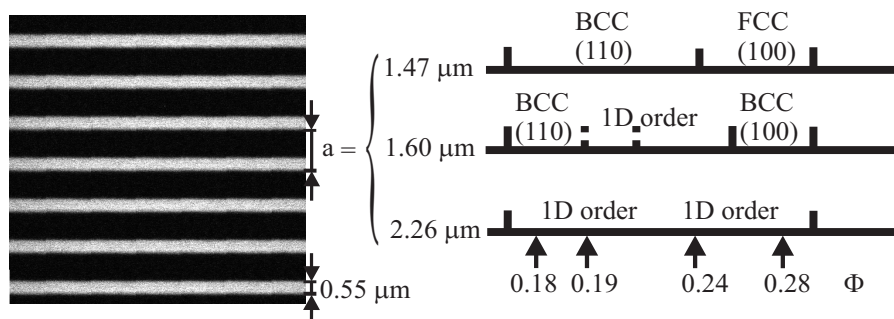
Figure 5-1 Confocal image of the striped template pattern (to the left) with the width and spacings of the lines indicated. Light areas correspond to PMMA, dark areas to 450 nm lower ITO-coated glass. For every line spacing the phase diagram of surface-layer symmetry is given. For (110)- and (100)-planes the 3D crystal structure is given as well. Phase boundaries have been indicated with an accuracy of ±0.02, dashed lines indicate a coexistence region between neighboring phases. Volume fractions at which a detailed 3D structure analysis was performed are indicated at the bottom.

matching colloids and solvent and directing the resulting small effective gravitational force (on the order of $-10^{-2}g$, with g the earth gravitational constant) *away* from the templated wall.

In the following, the phase behavior with respect to volume fraction and template spacing will be classified by the symmetry of colloids in the surface plane, for which we found three distinct effects. Our first observation is the formation of a square symmetric surface plane that, depending on template spacing, was found to belong to a metastable fcc crystal as well as a bcc crystal phase. Secondly, we observed alignment of the bcc(110) plane along the template lines with twinning occurring deeper in the crystal. Finally, the template was found to induce purely 1D order directed along the lines. In this last case a rearrangement to a 3D ordered crystalline phase was found to take place in the first few layers. At higher volume fractions, this reconstructed crystal was still directed by the template and maintained a distorted non-cubic structure extending over 30 layers deep. The surface-induced 'phase behavior' is indicated in Figure 5-1. The three different effects will be discussed in detail below.

Patterns of 1000 lines, 0.550 μm wide and 2 cm long with constant spacing, were made with electron-beam lithography in a 450 nm-thick fluorescently labeled poly(methylmethacrylate) (PMMA) layer[61]. A template and the various line spacings are shown in Figure 5-1. For all images shown later the orientation of the template is the same as in Figure 5-1. The colloids were fluorescently labeled, sterically stabilized PMMA spheres[3, 213]. In the refractive-index matching solvent mixture used, a 0.74/0.26-volume ratio mixture of cycloheptylbromide (CHB) and cis-decalin (CD) that density matches the spheres to effective $-10^{-2}g$, the sphere diameter is 1.05 μm. The surface potential was found to be 100 mV with $\kappa r \leq 2.5$, with κ the inverse Debye length and r the radius of the spheres[20].

A 100 μm-thick capillary sample cell, containing a gradient in particle volume fraction of (4±1) vol% over 2 mm after equilibration, was made with the template mounted on the bottom side corresponding to highest effective gravitational energy. Samples were analyzed using fluorescence confocal microscopy (Leica TCS-SP2, 100x N.A.). 3D particle coordinates were retrieved as described in reference[61]. For the volume fractions indicated in Figure 5-1, a

detailed analysis was performed starting with calculation of the linear number density as a function of distance to the template, ρ_z, by integration of 3D particle coordinates over the coordinates parallel to the template. For all volume fractions ρ_z showed layering due to the presence of the wall and to crystallization. Layers were defined through the clear minima in ρ_z. Particles in the same layer were used to calculate 2D-order parameters, such as the 2D coordinate auto-correlation function (2D-CACF) and its radial average, the 2D radial distribution function (2D-*g(r)*). The 2D-*g(r)* has been defined before (see equation (4.1) on page 55), the 2D-CACF is given as:

$$CACF(\vec{r}) = \int \rho(\vec{u})\rho(\vec{u}+\vec{r})d\vec{u} , \qquad\qquad (5.1)$$

where the vectors are 2D and the integration runs over the lateral dimensions of the scanfield.

The volume fraction at a specific point in our sample was measured by direct particle counting and checked by measuring the dimensions of the crystal lattice of untemplated bcc crystals. At the low volume fraction end ($\varphi \approx 0.10$) structure was liquid-like, while at the higher volume fraction end ($\varphi \approx 0.30$), at an untemplated wall, the sample contained bcc crystals only.

5.3 Results

5.3.1 Square symmetry (FCC/BCC(100)).

A square symmetric arrangement of spheres at the template, as shown in Figure 5-2, was found at volume fractions between 0.24-0.28 and template spacings between 1.47 μm and 1.60 μm. We attribute the local out-of-plane displacements, like in the lower left corner of Figure 5-2b to stress relaxation due to a small template-crystal mismatch[172]. In the linear number density ρ_z (Figure 5-2c), this effect can be seen as a decrease in peak height and increase in peak-width from layer one to four. The structure however remains clearly layered and the interlayer spacing was found to have a constant value of $\Delta z = 1.12 \pm 0.01$ μm.

For layers one and four the 2D-*g(r)* is given in Figure 5-2d. As can be seen all peak positions are in perfect correspondence with an ideal lattice for both layers. The positions of neighboring particles remain unaltered despite the broadening of layers in ρ_z. The in-plane nearest-neighbor distance is $d = (1.44 \pm 0.02)$ μm, which indeed has a small mismatch with the template spacing of 1.47 μm. The ratio $d/\Delta z = 1.29$ shows that the 3D structure is a metastable fcc crystal ($d/\Delta z \sim \sqrt{2}$). At similar volume fractions but a larger line spacing of 1.60 μm, we observed $d/\Delta z$ -values of 1.88, corresponding to a bcc crystal structure ($d/\Delta z \sim 2$), as indicated in Figure 5-1.

The average width of the 2D-CACF-peaks (see inset in Figure 5-2a) in the directions parallel and perpendicular to the template lines was found to be equal within the error margins. Thus combined LR line-sphere interactions for the (100)-plane induce 2D crystalline order that bears

(a)

(b)

(c)

(d)
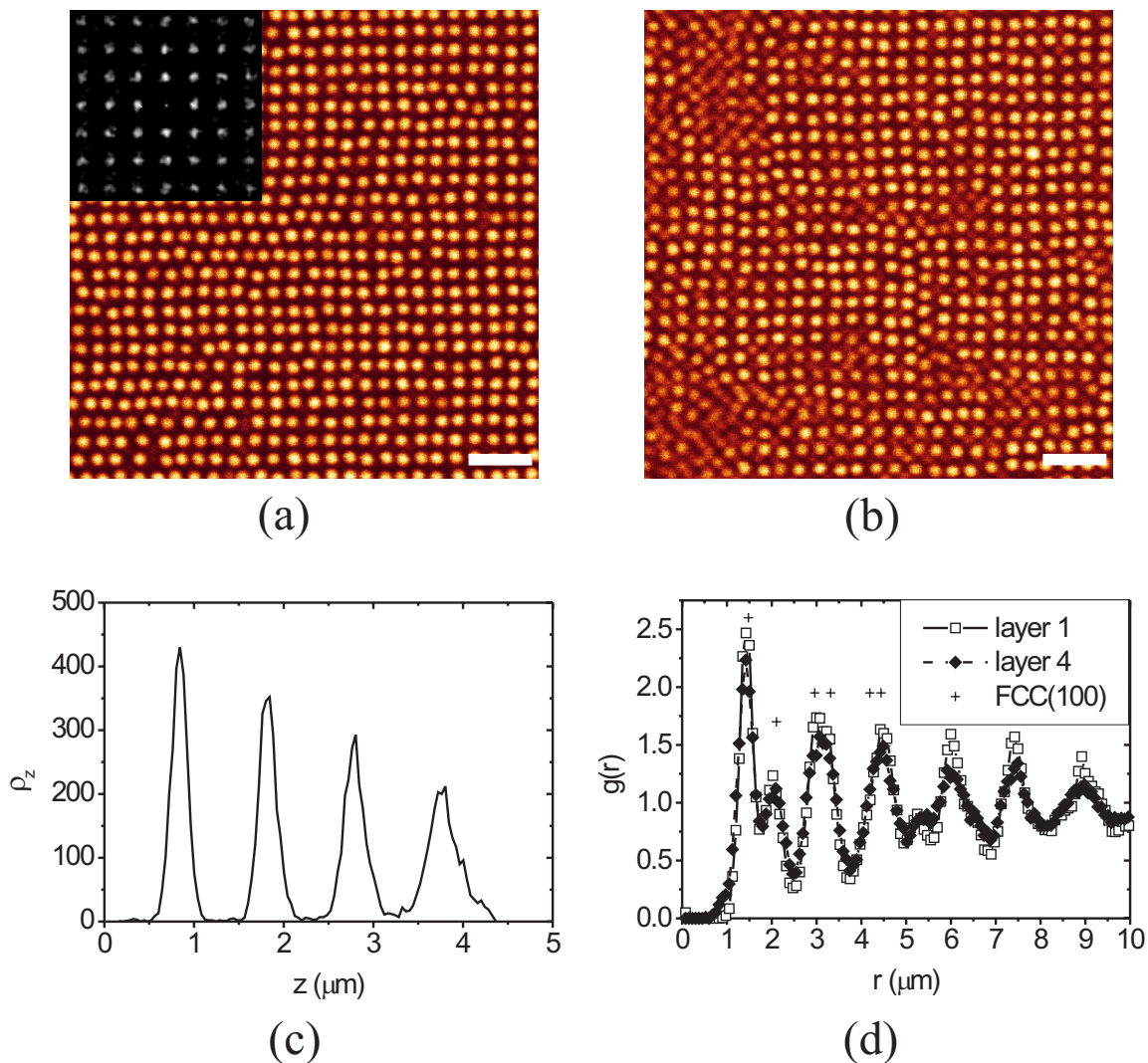
Figure 5-2 Confocal images of (a): the first layer, and (b): the fifth layer in a templated, (100)-oriented fcc crystal ($\varphi = 0.28$ and $a = 1.47$ μm). The inset in (a) shows the 2D coordinate autocorrelation graph of the surface layer, calculated using the full 3D particle coordinates. The scalebar length is 5 μm. (c): The 2D density in the direction perpendicular to the template. (d): Radial distribution functions for layer one (open squares) and layer four (filled diamonds). Open circles indicate the position of the first six different neighbor-distances in an ideal fcc or bcc (100)-plane.

no anisotropy of the 1D template anymore. This holds, even though there is a small mismatch between template and interparticle spacings, indicated by the stress relaxation mentioned before.

Finally, we want to note that this template was found to induce prefreezing of one to two square symmetric layers at volume fractions where both the bulk structure as well as the surface layers at a plain wall were liquid-like. This is in qualitative agreement with recent findings of Heni and Löwen who showed that for a hard-sphere system 2D surface patterns can induce strong prefreezing before bulk crystallization or prefreezing at a smooth wall occurs[63, 64]. However, it would be interesting to investigate whether in the case of hard-spheres a 1D template is sufficient to induce prefreezing as well.

5.3.2 BCC(110)

At a plain, untemplated wall bcc crystals orient with the densest plane, the (110)-plane, parallel to the wall. Figure 5-3a shows how the line-template orients the bcc(110)-plane. Two of the four nearest neighbors, at a distance d, are aligned along the direction of the template lines. The other two nearest neighbors can orient at an angle of +/- 54.74° with the template lines, but the line-template frustrates the position of the two next-nearest neighbors at $1.15d$ (see Figure 5-3a). The 3D-orientation of a bcc single-crystal is given by the striped pattern that is visible when successive bcc(110)-layers are being projected (Figure 5-3b). As can be seen two-fold twinning shows up immediately above the surface layer. The angle between the two orientations was measured to be $110(\pm 1)°$, in correspondence with the values given before.

The 2D-CACF shows that positional correlations within the template lines are stronger and of longer range than perpendicular to the lines. The average full-width-at-half-maximum of correlation peaks up to second order is 1.5 times larger in the direction parallel to the lines than perpendicular to the lines. Contrary to the (100)-plane the 1D pattern of lines in this case does not fit with the (110)-symmetry, which results in a potential of mean force between spheres in which the 1D template potential can still be recognized.

(a)   (b)
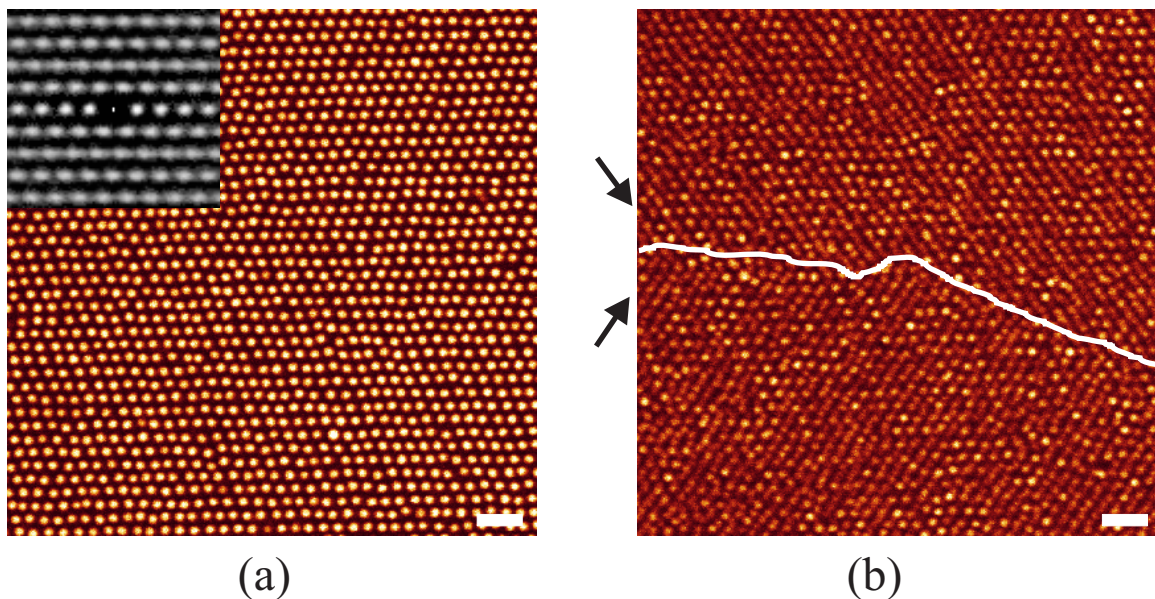
Figure 5-3 Confocal images focused (a): at a surface layer with bcc(110)-symmetry, and (b): in between the second and third layer above (a) ($a = 1.60\,\mu m$, $\phi = 0.18$). The inset in (a) shows the corresponding 2D coordinate autocorrelation graph. The arrows in (b) denote the two twinned orientations visible in the two-layer bcc(110)-projection. The white line indicates the grain boundary. The scalebars are 5 μm in length.

5.3.3 1D-Ordering.

At a line spacing of 2.26 μm particles in the surface layer have a 1D symmetry, with no positional correlation between particles in successive rows (Figure5-4a). The increase in the template spacing lowers the potential minimum in between the lines, eventually screening sphere-sphere interactions from neighboring rows. Apparently, also combined interactions of spheres in successive rows via spheres in the second layer are too small compared to the interactions between spheres and lines to induce 2D in-plane ordering, even in the higher volume-fraction end of the bcc regime shown here. At low volume fractions ($\varphi = 0.18$, 0.19) the structure reconstructs in a few layers to polycrystalline bcc. With increasing volume fraction however, the line pattern templates particle positions in the second layer as well. Here, the relative contribution of the lines to the potential, both directly and through the 1D string liquid in the first layer, compared to the contribution of neighboring spheres, is smaller, which gives rise to the emergence of 2D, and thus 3D order (Figures 5-4c to 5-4e). At a volume fraction of 0.24, the oriented crystal extents at least 60 μm (over 100 layers), which was our maximum depth of view. Note the perfect correspondence for the positions of rows of particles in Figures 5-4c to 5-4e, which is exactly the template spacing of 2.26 μm.

In the surface layer positional correlations between next-nearest neighbors in the direction of the template lines are more localized than correlations between nearest neighbors due to a buckling of particles within the lines. The addition of isotropic nearest-neighbor interactions to a single line-sphere-line interaction potential gives rise to a shift of the single, parabolic minimum to two minima, slightly displaced from the centerline. Here, the increase in sphere-line energy will be overcome by a decreased sphere-sphere potential. Comparing Figures 5-4c to 5-4e, it can be seen that this buckling is not present anymore as 3D ordering emerges.

The ratio between nearest-neighbor distances parallel and perpendicular to the template direction in Figure 5-4e (i.e. along the dashed lines) is 1.61. Planes with similar symmetry can be found in fcc and hexagonal close packed (HCP) crystals, but with ratios of $\sqrt{2}$ and $\sqrt{3}$ respectively. The distance between successive planes has a constant value of $d/2.07$. We expect this stressed body-centered tetragonal (BCT) crystal to relax to either bcc or fcc in the bulk, but it was found to extent at least 30 layers deep. Indicative of a relaxation process, the angle between the two in-plane lattice directions in Figure 5-4e is slightly off from 90°, namely 86($\pm$1)°. Further experiments have indicated that the ratio between the lengths of the in-plane lattice-vectors in at least the first twelve layers can be stretched to values approaching 1.7 by changing the line width. In this way it may be possible to grow an HCP-crystal of spheres with a LRR interaction. At the smaller line distance of 1.60 (see Figure 5-1), we did observe planes where this in-plane ratio was 1.37, almost equal to the ideal fcc(110)-ratio, but here the interlayer distance was not constant in the first four layers and the structure reconstructed to tilted bcc(110) hereafter. These results indicate that more complex colloidal surface and bulk phases can be induced in systems with LRR interactions when more elaborate surface patterns, for instance by directly patterning
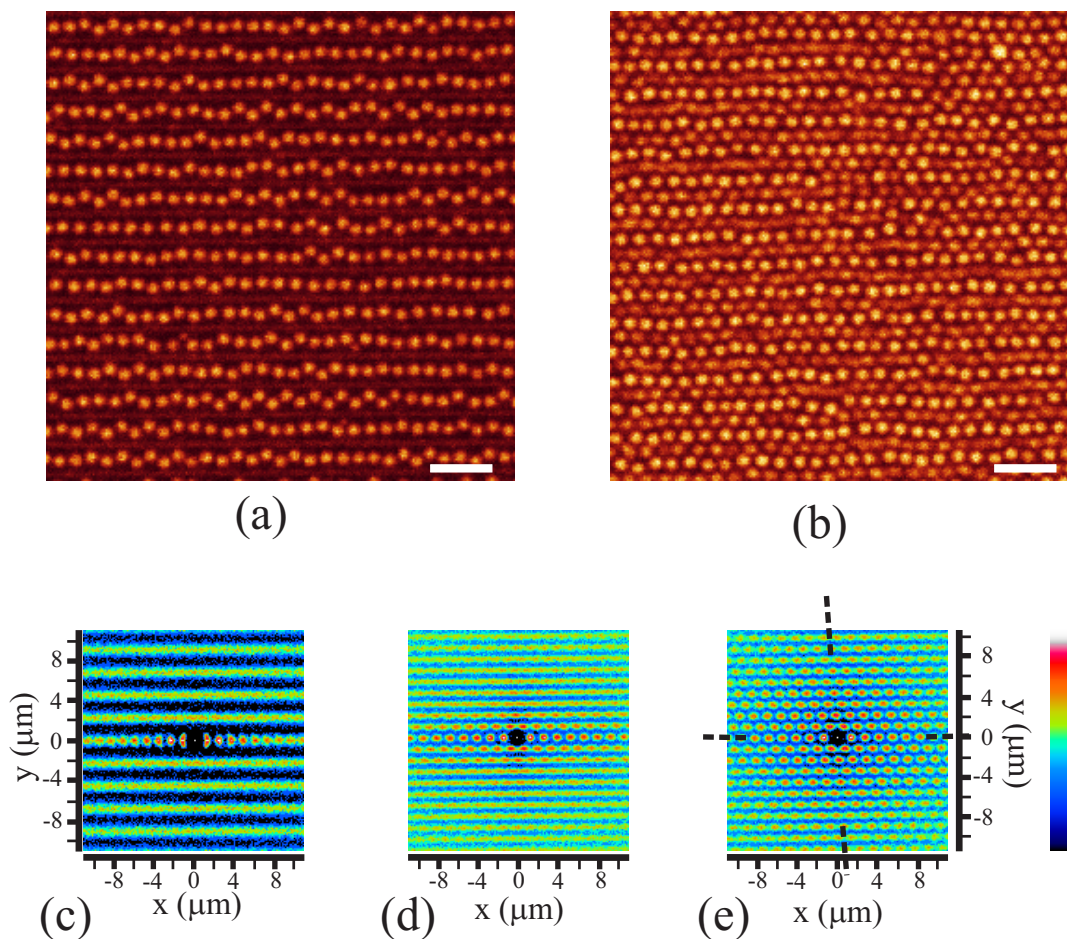
Figure 5-4 Confocal images and 2D coordinate autocorrelation graphs for a system exhibiting a 1D ordered surface plane ($a = 2.26 \mu m$, $\phi = 0.24$). (a) and (b) are confocal images of colloids (a): in the surface layer, and (b): at a depth of 15 μm. The scalebars denote 5 μm. Coordinate autocorrelation graphs are given for (c): the surface layer, (d): layer four and five with coordinates from both layers projected onto a single plane (which causes the frequency doubling compared to (a)), and (e): a depth of 15 μm using again a two-layer projection. The color table is given on the right (blue = 0, white = 1). The dashed lines in (e) indicate the two in-plane lattice-directions.

colloids on a surface[104], are created. By dissolving a polymerizable precursor, these structures can be solidified in a polymer matrix for device applications[69, 87].

5.4 Conclusions

We have shown the possibility of epitaxial growth of colloids with long-ranged repulsive interactions in a density-matched system, where epitaxial growth is solely driven by the substrate potential. This substrate potential was created by 1D charged lines, which were found to direct 3D crystal structure over a broad range of volume fractions. Among our observations is the growth of a metastable fcc crystal in the volume-fraction regime where bcc is the equilibrium

structure. At increasing line spacing, the structure in the surface layer changes to a 1D string liquid due to screening of sphere-sphere interactions by the line potential. At increasing volume fractions, the substrate potential of the template induces ordering in layers beyond the surface layer, until at a volume fraction of 0.24 a 3D crystalline structure is observed that maintains a metastable non-cubic structure for over 30 layers deep. At volume fractions where structure is liquid-like, the 1D template was found to induce prefreezing of 1 to 2 square symmetric layers.

5.5 Acknowledgements

6

Template-induced colloidal self-assembly during solvent evaporation

The use of templates in directing colloidal crystallization in controlled drying techniques has been examined. Template-induced colloidal crystallization is demonstrated in a tilted-horizontal setup of the templated substrate for crystals that are both a few layers as well as more than 100 layers thick. Furthermore, at templates that possess a mismatch with respect to the colloidal dimensions, a reconstruction in surface orientation of the crystal takes place. The strain relaxation phenomena observed on these mismatched templates are similar to those observed in epitaxial crystal growth in suspension during slow sedimentation. For vertical controlled drying, where in general there is more control over crystal thickness and uniformity, template-induced growth was examined for silica colloids ranging in diameter from about 100 nm to over 1 µm. Our results indicate that the ability to form a templated crystal is crucially dependant on the surface topography of the template. For a square symmetric fcc(100)-template, two-dimensional crystal growth was only observed on a pillar-shaped template.

6.1 Introduction

The ability of colloidal particles to self-assemble into two-dimensional (2D) and three-dimensional (3D) crystalline structures lies at the heart of many studies in nano- and micron-scale materials science. Techniques most commonly used are bulk crystallization followed by polymerization, colloidal crystallization by sedimentation followed by either drying or polymerization, and so-called controlled drying techniques that rely on the slow evaporation of solvent in a colloidal suspension. This last series of techniques was pioneered by Nakayama and Denkov and co-workers[113-115, 214], who in detail examined the role of capillary forces at the liquid-air meniscus[111]. A new impetus to the use of controlled drying in colloidal assembly was given by Jiang et al. in 1999[117]. They demonstrated the growth of large, single-domain 3D colloidal crystals with controlled thickness on a substrate that is placed vertically in a slowly evaporating suspension. Later it was demonstrated that similar results can be obtained when the substrate is slowly retrieved from the suspension[118], extending the work of Nagayama and co-workers.

Due to particle sedimentation, the vertical controlled drying technique used by Jiang et al. only works for particle-solvent combinations of which the particle sedimentation velocity does not exceed the solvent evaporation rate. In the case of colloidal dispersions of silica particles in ethanol and water, this means that the technique is limited to the use of particles with a diameter below about 400 nm. For polymeric particles it was shown that performing this procedure at an elevated temperature, thus increasing solvent evaporation, provides a way around this problem[120, 121]. For polystyrene colloids, deposition of particles with a diameter up to 2.5 µm from a suspension of water was shown possible at a temperature of 95ºC[120]. Recently, Vlasov et al. used a temperature gradient with the higher temperature at the bottom of the suspension vial in order to oppose sedimentation[91]. In this way, they managed to deposit large single crystals of 855 nm-diameter silica particles.

One of the limitations of the controlled drying techniques is the fact that crystal formation is limited to close packed planes that have a hexagonal orientation with respect to the substrate. The stacking of close packed planes has a two-fold degeneracy. Three successive hexagonally stacked planes can be either of face centered cubic (fcc; *ABC*-sequence) type or of hexagonal close packed (hcp; *ABA*-sequence) type. Although there are indications that crystals grown by controlled drying possess a high amount of fcc stacking, the occurrence of stacking faults can in principle not be ruled out. Crystal growth starting from another crystal plane without stacking degeneracy would circumvent this problem. Furthermore, for certain applications a specific orientation of the crystal with respect to the substrate may be desired, for instance in the creation of a photonic stop band. Finally, the possibility to grow other crystal structures than fcc, would mean a major extension of the technique of controlled drying.

Considerable research has been devoted to directing colloidal self-assembly[84, 112]. Most of these techniques involve patterning of the substrate, either with a relief pattern or chemically (i.e.

without a geometrical component). In the first case for instance electrostatic interactions bind particles to specific sites at the substrate[130-133, 137]. In case the strength of this binding interaction is smaller than the capillary forces generated by the liquid-air meniscus during drying, the different wettabilities of patterned and unpatterned regions can further direct particles to a well-defined lattice[133]. The application of this technique is so far however limited to 2D particle assemblies.

Relief patterns, or templates, have mostly been used to manipulate colloidal crystallization in suspension. When the pattern mimics a well-chosen crystal plane, colloidal crystallization occurs epitaxially on this patterned template[61]. This technique has been called colloidal epitaxy. With colloidal epitaxy it is possible to direct the orientation of large, single-domain colloidal crystals and furthermore the growth of crystal structures that are metastable without the use of the template has recently been demonstrated[172, 173]. The applicability of template-induced ordering together with controlled drying techniques would make the application of other crystal orientations and crystal structures possible.

The ordering of a 2D layer of colloids on a template with an fcc(110)-pattern was demonstrated by van Blaaderen[62, 162]. Furthermore, 2D colloidal assemblies can be made on templates that only consist of a pattern of one-dimensional lines[126]. Braun et al. have demonstrated how crystals grown by epitaxy can be dried with minimal distortions[138]. They used hydrazine hydrate as the solvent, with added poly(vinyl alcohol). The use of hydrazine hydrate minimizes surface tension forces during solvent evaporation and the poly(vinyl alcohol) stabilizes the particles. The use of templates directly in combination with the drying procedure to order colloids would allow for a much easier procedure. Recently, Xia and co-workers used a template consisting of a large periodic array of pyramidal-shaped holes to grow (100)-oriented fcc crystals[139]. In the confinement generated by the pyramidal holes, colloids crystallize with a square symmetric orientation exposed at the top[123]. The periodic array of holes thus creates a layer of square symmetrically arranged colloids that templates the growth of the crystal on top of the substrate. In the approach taken by Xia and co-workers, the colloidal crystal is grown in a specially designed sample cell in which particles are subjected to compacting hydrodynamic flow and ultrasonification during crystallization[192].

Epitaxial crystal growth during controlled drying at a vertically placed substrate has recently been shown by Velikov et al.[129]. They used a single hexagonally ordered layer as a template for crystallization of smaller spheres. Depending on the initial volume fraction of small spheres, a variety of different 2D assemblies of small spheres on the larger spheres was achieved. In this way binary colloidal crystals can be grown using repetitive layer-by-layer controlled drying steps.

In this chapter we will investigate the feasibility of the use of directing colloidal self-assembly during drying for particles that range in diameter from about 100 nm to over 1 μm. After a brief outline of the experimental procedures, template-induced ordering during drying at horizontally placed substrates will be discussed first. Then, results on the growth of 2D arrays of small particles during vertical controlled drying will be shown. Finally, the vertical controlled drying of

silica spheres with a diameter of 870 nm will be discussed and we will present some preliminary results on the vertical template-induced drying of these larger particles.

6.2 Experimental

6.2.1 Colloids and templates

Silica colloids with different diameters were used. Fluorescent silica particles with an outer diameter of 140 nm were made using a micro-emulsion synthesis[156]. Particles were labeled with the fluorescent dye fluorescein isothiocyanate (FITC) that was covalently attached to the silica network through the silane-coupling agent 3-aminoprpyltriethoxysilane (APS)[149]. As controlled drying of these particles was found to lead to disordered deposits, the particles were coated with an approximately 15 nm-thick layer of plain silica using a seeded-growth process. The particles were removed from the reaction mixture (that apart from ethanol contained ammonia and water) by four times repeated steps of centrifugation, removal of supernatant and redispersion in ethanol.

Particles with outer diameters of 870 nm and 1400 nm were prepared by seeded-growth following the procedure outlined by Giesche[154]. The seed particles were 404 nm in diameter and labeled with FITC using a similar procedure with APS as for the smaller particles. For the drying experiments these particles were dispersed in pure ethanol, or in double demineralized water for use with the polyurethane templates, like described for the smaller particles. All diameters were measured using static light scattering, except for the 15 nm-thick plain silica surface coating of the micro-emulsion particles, which was only measured by scanning electron microscopy (SEM). This value was in good correspondence with that calculated based on the amount of silica precursor added to the reaction mixture.

The procedures to pattern substrates in order to make templates for use in the drying experiments have been outlined in detail in chapter 2. For the 1.4 μm-diameter particles we used polyurethane templates made via soft-lithography. The templated area was surrounded by a higher polyurethane boundary to contain the drying colloidal suspension as is schematically shown in Figure 6-1. The inner edge of this boundary was coated with silicon glue (General Electric RTV 102) to prevent a concave drop shape. For the 170 nm as well as the 870 nm-diameter particles templates were created directly in a silicon substrate (see chapter 2 for details). The substrates were used both in a tilted-horizontal set-up as well as with the vertical drying method (see Figure 6-1). For the experiments concerning the vertical drying of 870 nm-diameter particles plain silicon substrates were cut from 6-inch silicon wafers (Virginia Semiconductors, P-doped, (100) orientation, single side polished) to final dimensions of about 8 x 60 mm. The tilt angle in the tilted-horizontal set-up was always in between 2º and 10º. In the vertical drying method, the substrates always had a small angle with the vertical director, ranging from about 20º
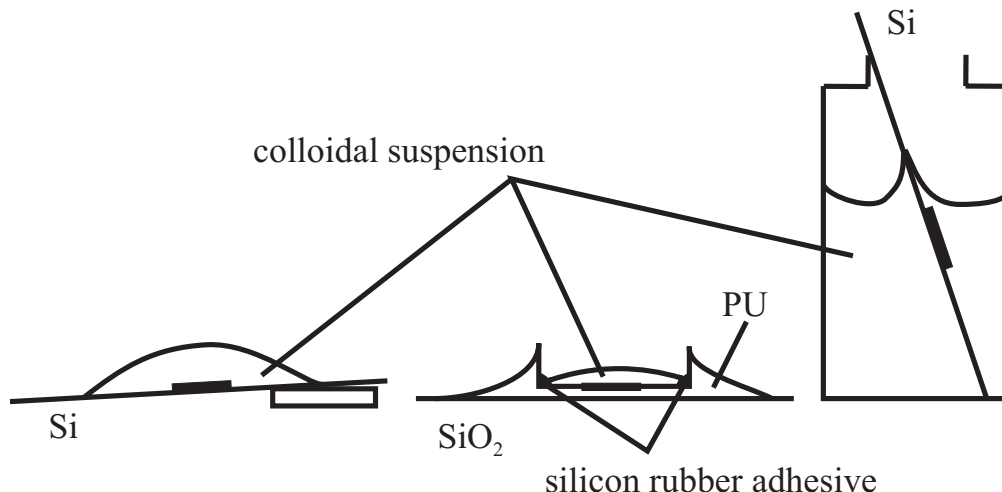
Figure 6-1 Schematic illustration of the various ways in which substrates were placed for controlled drying. The first two drawings illustrate the tilted-horizontal setup with silicon and polyurethane substrates respectively, the drawing on the right hand side illustrates the setup for vertical controlled drying. Apart from slightly tilted as in this illustration, the substrate was also placed almost completely vertical as in Figure 6-2. The thicker dark areas indicate the position of the templated area on the substrate.

(as depicted on the right hand side of Figure 6-1) to 2º at maximum (as in Figure 6-2). The substrates were placed with the polished side up, as in Figure 6-1.

Samples were analyzed with fluorescence confocal microscopy (Leica TCS-NT2) and with SEM (Philips FEI XL30 SFEG). For confocal microscopy analysis the samples were mildly sintered at 80ºC overnight and then immersed in a refractive-index matching mixture of glycerol and water.

6.2.2 Deposition conditions

All substrates were rinsed with ethanol before use. For the drying in a horizontal set-up, templated substrates were placed on a granite table in a thermostated room (T = 20.5 ± 0.5ºC). After placing a small drop of suspension on the substrate (typically about 20 μl) the substrate was covered with a measurement beaker to protect against airflow.

For the vertical drying of the 140 nm-particles on a templated silicon substrate, a 20 ml scintillation vial (Packard Biosciences) was cleaned by filling with chromosulfuric acid (Fluka). After about 15 minutes, the bottle was rinsed several times with demineralized water and ethanol and dried in an oven. The templated substrate was rinsed with ethanol and also dried in an oven. Small notches were made in the scintillation bottle at opposite sides at the top so that it could hold a substrate in almost complete vertical position as in Figure 6-2. After cooling of the vial and the substrate in a stream of nitrogen, the bottle was placed on a granite table as described above and filled with the colloidal suspension. The templated substrate was placed vertically in the suspension. The whole set-up was then covered with a larger beaker.
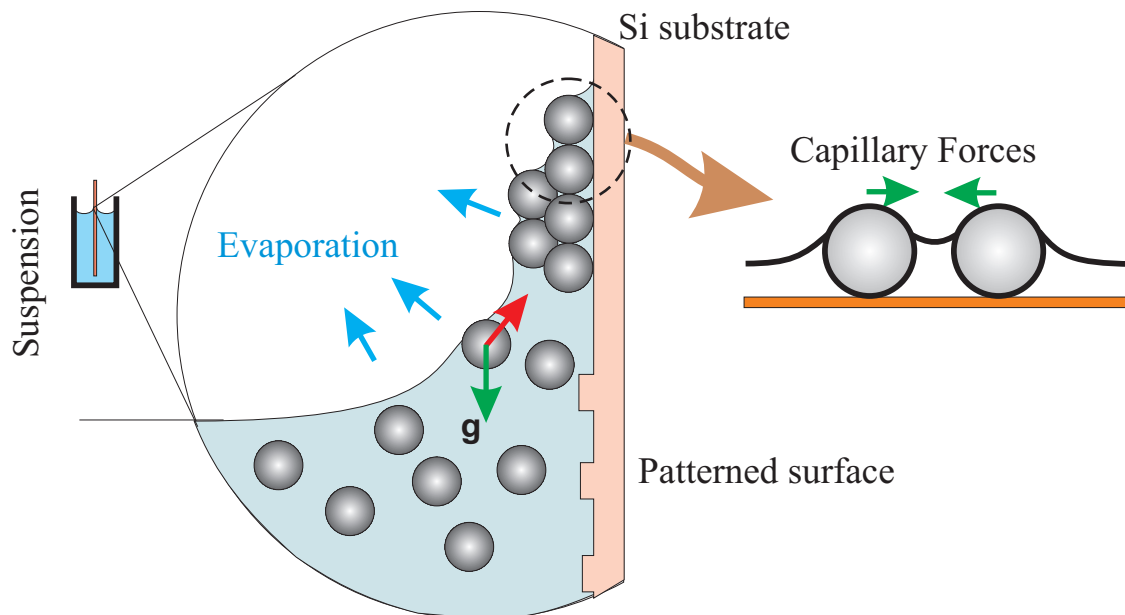
Figure 6-2 Schematic illustration of the technique of vertical controlled drying[117]: The slow evaporation of solvent at the liquid-air interface at the top of the suspension leads to a solvent and particle flux towards the curved part of the liquid-air meniscus at the substrate. Here colloidal crystallization takes place due to locally increasing particle concentration, the compressing solvent flow and the attractive capillary forces[111] induced by the meniscus during drying. The thickness of the crystal is determined by the solvent evaporation rate, the initial particle volume fraction and the wetting angle. A similar deposition process leads to the formation of ring-like deposits in coffee drops[215]. Image courtesy of Krassimir Velikov.

For vertical deposition of the larger 870 nm-diameter particles a scintillation vial was cleaned similar to the procedure described above. The experiments were carried out in an oven (Jouan) that was placed on a granite table to minimize external vibrations. Inside the oven the sample bottles were placed on a metal plate. The temperature on the metal plate was measured with a contact temperature probe (Therma-1) and was found to be $65.5 \pm 0.5°C$. The colloidal suspension was placed in the oven in a closed scintillation vial before use, together with the cleaned bottle for the deposition experiment and the silicon substrate. The suspension was then poured into the cleaned bottle and the substrate was placed into the suspension. This bottle was then placed back into the oven. A small opening was left at the door of the oven to allow ethanol vapor to escape. The evaporation rate was measured by monitoring the weight of the sample bottle and was found to be of the same order of magnitude as the sedimentation rate. Expressed as the rate at which the height of the liquid-air meniscus decreases, the evaporation rate was found to be about 0.7 µm/s. For the sedimentation rate we found 0.8 µm/s.

6.3 Results and discussion

6.3.1 Tilted-horizontal template-induced ordering

In Figure 6-3 a confocal image of the first two layers of a crystal grown on a tilted-horizontally placed polyurethane template is shown. The template consists of a pattern of cylindrical holes with the symmetry of the fcc(110)-plane. The fcc(110)-plane consists of close-packed rows of particles with the spacing between different rows being √2 times the distance within a row. For the template in Figure 6-3 these distances were 1.56 μm within the rows and 2.20 μm perpendicular to the rows. The image on the right hand side of Figure 6-3 shows an area of 100 μm by 100 μm. The focal plane cuts the crystal plane with a small angle, so that on the left hand side the bottom, templated layer is visible, while on the right hand side both first and second layer are visible. Note that only the 400 nm-diameter core of the particles is visible in fluorescence and that the shortest interparticle distance, i.e. along the rows, is only 0.16 μm larger than the sphere diameter of 1.4 μm.

The image on the left hand side of Figure 6-3 shows an enlarged view of the bottom layer, where the fcc(110)-pattern can be clearly recognized. The out-of-focus particles in the second layer are vaguely visible in between the in-focus particles. Note the presence of vacancies in the lower left corner and at the center of the enlarged image. We have not carried out a quantitative analysis of the presence of vacancies and other defects yet, but these images already illustrate the possibility to obtain such information on dried crystals using the combination of fluorescent core-shell colloids and confocal microscopy. The thickness of the dried crystal was about 8 μm, which
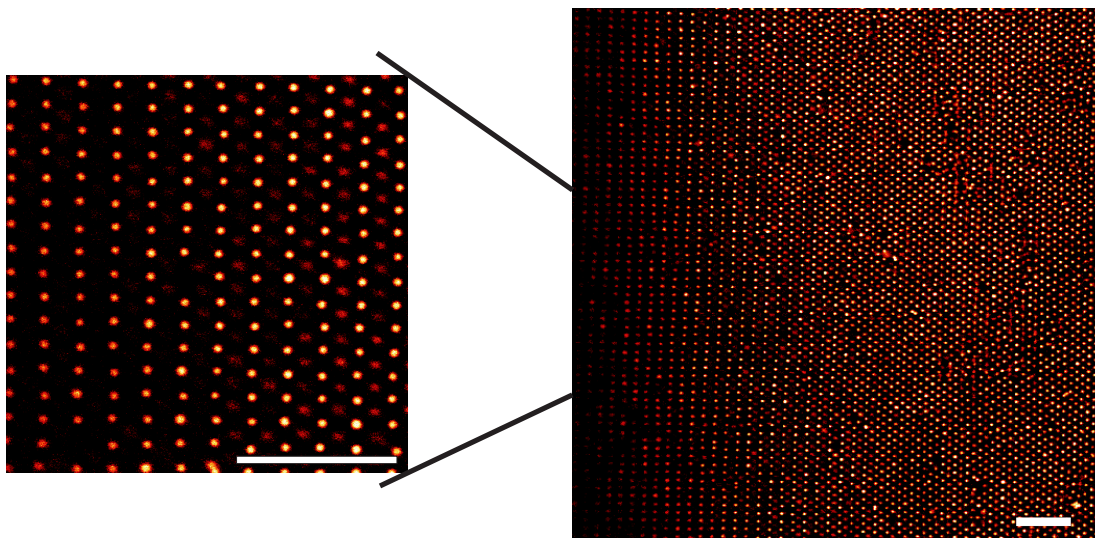
Figure 6-3 Confocal microscopy image of the first two layers of a crystal of fluorescent core-shell particles on a fcc(110)-template. In the image on the right hand side the focal plane cuts through the crystal from the first layer at the left side to the center plane in between first and second layer on the right. The image on the left side shows a detailed view of the first layer at the template. The length of the scalebars is 10 μm.

corresponds to about 11 layers. The first layers were always single-domain crystalline as in Figure 6-3. The top surface layer however always contained a considerable amount of disorder due to line and point defects.
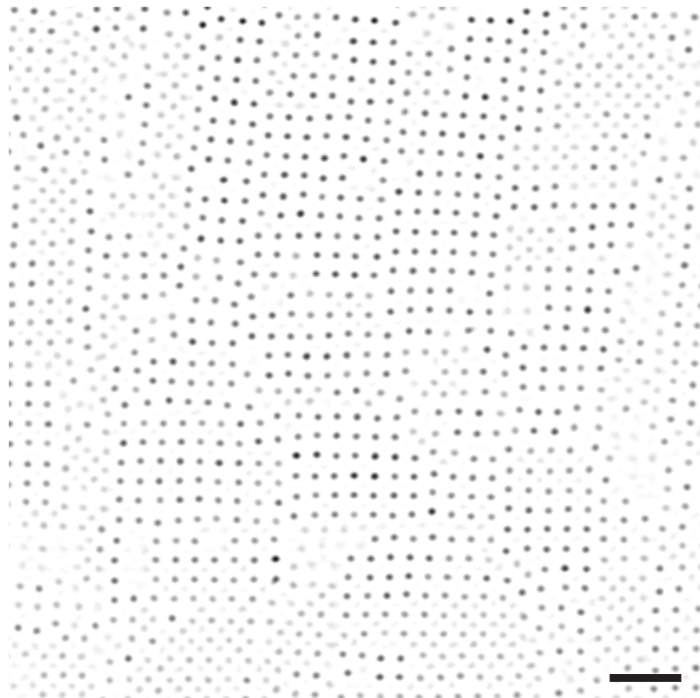
(a)

Figure 6-4 Confocal microscopy images of reconstructed fcc(100)-oriented crystal of 1.4 µm-diameter silica colloids grown on a fcc(110)-template. (a) At a template with lattice spacing of 1.10 µm, 1.56 µm. (b) At a template with lattice spacing of 1.20 µm, 1.70 µm. The length of the scalebar in both images is 5 µm.
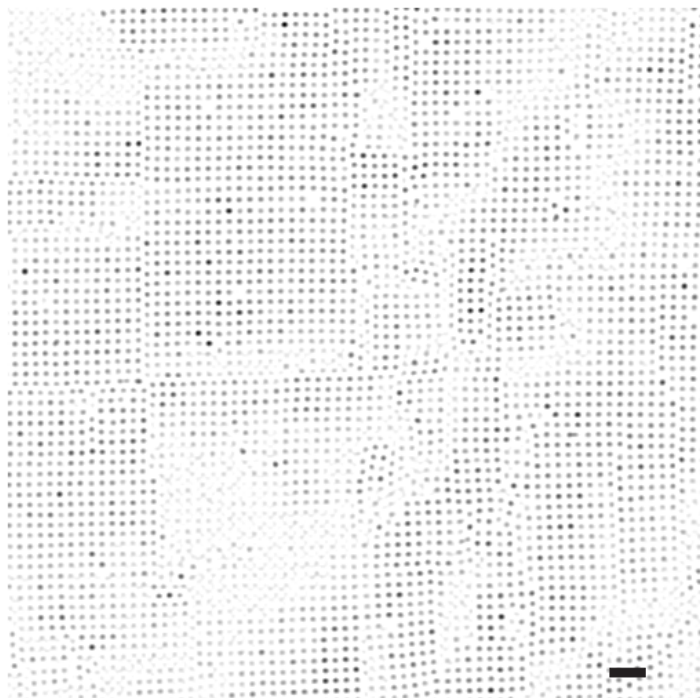
(b)
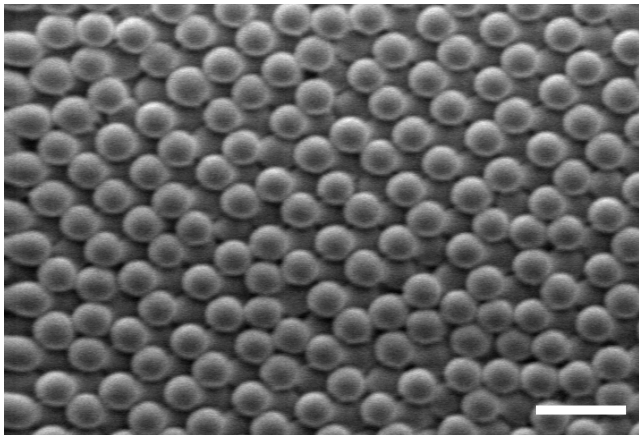
Figure 6-5 SEM image of the top layer of 870 nm-diameter colloids arranged on a poly-urethane template with an hcp(1100)-symmetry. The scalebar indicates 2 μm.

In colloidal epitaxy experiments performed in solution, a mismatch between template and crystal spacing gives rise to crystal reconstructions, stress relaxation e.g. by out-of-plane displacements, and a considerable change in crystal volume fraction[172]. In Figure 6-4, confocal images are shown of colloidal crystals formed by drying a suspension on a mismatched fcc(110)-template. The lattice distances for the (110)-template were 1.10 μm and 1.56 μm for the image in Figure 6-4a and 1.20 μm and 1.70 μm for Figure 6-4b. This results in a mismatch, expressed as the relative deviation of lattice distances with respect to the fcc(110)-crystal in Figure 6-3, of respectively -0.30 and –0.23. As can be seen in both cases the resulting fcc crystal is oriented with the square symmetric (100)-plane parallel to the (110)-template. Furthermore, in both cases the effects of template-crystal mismatch can be clearly seen.

For the larger mismatch in Figure 6-4a point defects like dislocations are visible. The regions where particles appear more vaguely correspond to regions with particles that are out-of-focus. The uniform appearance of out-of-focus particles throughout the image indicates that this is not due to a tilt of the image plane with respect to the crystal plane (like in Figure 6-3), but corresponds to out-of-plane displacements of particles and small groups of particles. In the case of the smaller mismatch in Figure 6-4b point defects other than vacancies can hardly be observed anymore and the crystal consists of coherent fcc(100)-grains that have a uniform orientation with respect to the template but are surrounded by line defects and step dislocations. Similar out-of-plane particle displacements as in Figure 6-4a are observed. These results are in agreement with the behavior of crystal structure over mismatch templates observed in experiments performed in suspension under slow sedimentation. This indicates that similar effects, like the strong variation in crystal volume fraction that was already observed for small template-crystal mismatch, can be reproduced in crystals grown by controlled drying. Furthermore, the creation of defected crystals, with known defect concentration and typical defect periodicities may again be useful in applications. The crystal structure in Figure 6-4b was found to extent for more than 80 μm above the bottom template wall, which was our maximum depth of view in the crystal.

Apart from the use of an fcc(110)-template, growth of a metastable hcp-crystal using an hcp(1100)-template (see chapter 4) was also tried. Figure 6-5 shows a SEM image of the top layer of an approximately three-layer crystal of 870 nm-particles. Although this layer contains an appreciable amount of defects and dislocations, the (zigzag) template symmetry can still be recognized. Particles in the layer below are visible in between the particles in the top layer. In
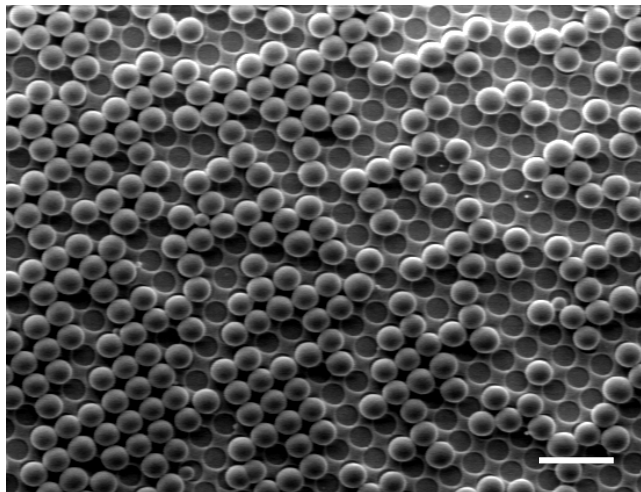
Figure 6-6 SEM image of 870 nm-diameter colloids on an all-silicon square symmetric fcc(100)-template with a pattern depth of only 100 nm. The length of the scalebar is 2 μm.

Figure 6-6 similar 870 nm-layer particles arranged on a template etched in a silicon wafer can be seen. Particles have been deposited with sub-monolayer coverage and the template is clearly visible on the uncovered areas. The template symmetry was of fcc(100)-type (square symmetry). The depth of the holes in the pattern was only 100 nm, which is already enough to localize particles during drying at the lower areas. However, the diameter of the holes in the template is comparable to the diameter of the spheres, which, at this small a pattern depth, is not sufficient to confine particles to the center position. Small displacements of particles away from the center of a template lattice point are visible in Figure 6-6.

The examples given above demonstrate the possibility to direct colloidal crystal formation in controlled drying techniques. The set-up with the tilted-horizontal sample however does not provide the optimal conditions for crystal growth by controlled drying, as was also evident from some of the results given above. Better growth conditions may be achieved by using vertical controlled drying, as is the case for plain, untemplated substrates.

6.3.2 Vertical controlled drying of 170 nm-particles on a template

Initially, experiments using vertical controlled drying were carried out using 140 nm-diameter fluorescently labeled silica spheres. However, with these particles only disordered deposits were obtained, both at the templated areas of the substrate as well as the untemplated parts of the substrate. As one of the reasons for this could be the presence of amine coupling-agent groups at the surface of the silica colloids (this can e.g. cause lowering of the surface charge resulting in particle aggregation and/or particle sticking to the surface prior to crystallization), particles were coated with a 15 nm-thick shell of plain, unlabelled silica. These particles were found to give large single-domain hexagonally stacked crystals on plain substrate using vertical controlled drying as expected. This result indicates the importance of particle stability in the controlled drying procedure.

Figure 6-7 shows a SEM image of an incomplete single-layer of these 170 nm-diameter silica colloids on a square symmetric template. This particle structure was observed for template spacings of 165 nm (shown in Figure 6-7), 170 nm, and 190 nm (±5 nm). For the image shown,
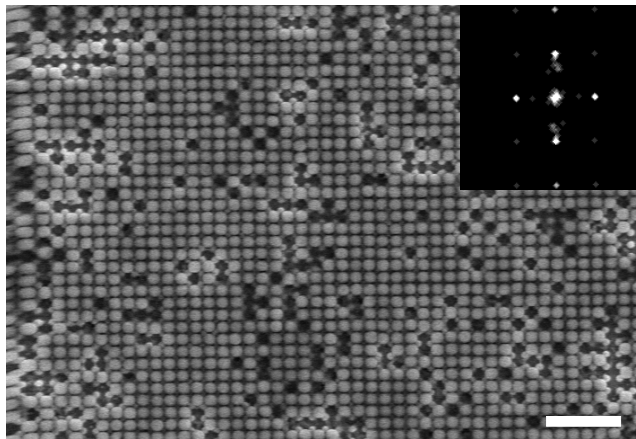
Figure 6-7 SEM image of 170 nm-diameter silica colloids arranged on a template consisting of square-symmetrically (fcc(100)) arranged pillars in silicon. The particles were deposited by vertical controlled drying. The inset shows the Fourier transform. The length of the scalebar is 1 μm.

the template consisted of regularly spaced pillars as can be seen in some of the areas without particles, for instance at the right edge below the inset. For thicker crystals, with thickness ranging from 4 to about 20 layers, we however always observed an hexagonally arranged top layer. Furthermore, crystallization other than hexagonal was never observed at a template spacing larger than 190 nm (ranging to 240 nm).

The reason for the inability to template thick 3D crystal growth is at the moment still unclear. The epitaxial patterning of a 2D layer using vertical controlled drying was previously demonstrated by Velikov et al., who examined the ordering of a sub-monolayer of smaller particles on an hexagonally arranged layer of larger particles[129]. They observed ordering of the smaller spheres in different symmetrical arrangements depending on the volume fraction of smaller spheres in suspension. For the lower volume fraction structures that they analyzed the smaller spheres order at the lowest possible sites at the midpoint between three larger spheres. In the higher volume fraction structures however, the smaller spheres did not occupy these sites, but rather ordered on the 'necks' between two touching larger spheres. At this higher particle-coverage, minimization of the surface area of the liquid-air meniscus is achieved by placing particles uniformly on otherwise metastable points instead of placing a high amount of particles at the lowest sites but thereby leaving a low amount of particles at very unfavorable positions. A similar effect may occur in the 3D crystals grown at templates. The templates, like the one shown in Figure 6-7, on which 2D ordering was observed all consist of rather sharp features, either pillar-shaped or steeply cylindrical. This provides a much different landscape than the surface of a layer of colloids. For the smaller spheres, we have so far only been able to analyze the top surface of the crystallized particles, so it has not yet been possible to analyze 3D structure in a thicker crystal. This could for instance be done for templated growth of larger spheres on which 3D confocal microscopy could be performed. Finally, the impossibility to grow a colloidal crystal epitaxially on an hexagonal surface layer of an already dried crystal of similarly sized colloids was reported by Colvin and co-workers[117]. They tried to grow thick colloidal crystals by

repeated vertical controlled drying steps with both crystals with similar as well as different thickness. In both cases they did not observe a registry between the substrate crystal and the freshly deposited crystal. In view of the results of Velikov et al., this indicates the importance of the substrate landscape with respect to the particles dimensions in determining the conditions for epitaxial crystal growth.

Another possible explanation for the impossibility to template 3D crystal growth with vertical controlled drying found so far, could be a different growth mechanism for crystals compared to drying on a tilted-horizontal substrate. For the results shown in the previous paragraph, crystallization by sedimentation can well have preceded drying of the resulting structure. In the vertical controlled drying technique the precise mechanism for crystallization is still unclear. Crystallization may occur only at the latest stage of the drying process under the influence of surface capillary forces. However, it can also well be that crystallization already occurs due to the increase in particle concentration under the liquid-air meniscus as a result of particle transport by the evaporative solvent flux. Similar to the situation for the tilted-horizontal substrates, an already formed colloidal crystal is then dried in a later stage. A main difference with the tilted-horizontal setup is however that the evaporative solvent flux generates a strong field in which particles crystallize. This force field may be predominantly oriented towards the bottom crystal plane of the already crystallized colloids instead of towards the (templated) substrate. Furthermore, in the tilted-horizontal setup, the gravitational field is directed towards the templated substrate as well, while in the vertical setup gravity acts parallel to the substrate. As in our setup, the templated areas have so far been rather small (typically 1 mm by 1 mm), crystallization always started on unpatterned substrates, so that an hexagonally stacked crystal was already formed before the template was reached. In this way the crystal may grow epitaxially on this hexagonally stacked crystal instead of on the template. We are currently carrying out experiments using larger, elongated template areas to see if there is a difference in crystal structure when the controlled drying procedure is started on a templated area of the substrate.

6.3.3 Vertical controlled drying of 870 nm-particles

In order to be able to perform vertical controlled drying with larger silica particles, experiments were carried out using silica particles with a diameter of 870 nm. Vlasov et al. have reported the vertical controlled drying of large silica particles using a well-controlled temperature gradient applied from the bottom to the top of the suspension container[91]. Similar experiments were carried out by placing the 20 ml scintillation vial in a sandbath placed in a mantle heater with varying bottom and top temperatures. These attempts were however almost always unsuccessful or with very poor success rates. Deposition of the silica particles did occur when the sample container was placed in an oven as described in the experimental section.

Figure 6-8 show a SEM image of the top layer of a crystal grown on a plain Si substrate. The crystal was deposited from a suspension with an initial volume fraction of 0.003. The Fourier
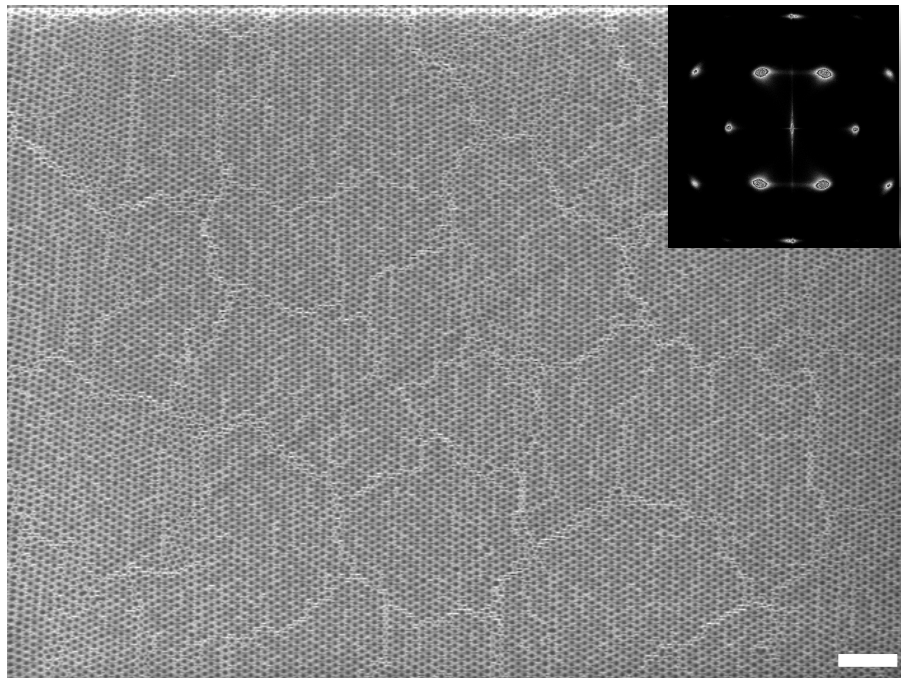
Figure 6-8 SEM image of a crystal of 870 nm-diameter particles deposited on a plain silicon substrate using vertical controlled drying. The inset shows the Fourier transform. The non-linear colortable is indicated at the right side of the inset and contains two regions of light grayscales to highlight the higher order peaks. The scalebar length is 10 μm.

transform in the inset indicates the strong hexagonal ordering. Cracks can be seen in the image, but these do not destroy long-range order. The cracks are probably caused due to shrinkage of the crystal under exposure to the electron beam. Upon further exposure or exposure at a higher electron dose of 20 kV, the cracks were not found to widen further, nor did the number of cracks increase. The lateral size of a single crystal was found to be at least 2 mm, with no orientation differences of the Fourier transform over this distance.

The position of the substrate in the scintillation vial was varied from that depicted on the right hand side of Figure 6-1 (at an angle of about 20° with the vertical direction) to almost vertical as in Figure 6-2 (angle 2° at maximum). This was not found to influence the deposition process. The crystal was always found to grow on the upper, polished side of the silicon substrate. Apart from silicon substrates, also glass substrates, cut to the same sizes as the silicon substrates were used. On the glass substrates particle deposits were always less than a monolayer. Furthermore, under conditions where growth of large crystals on the substrate took place, the inner side of the glass bottle was always covered with striped ring-like deposits, as in Figure 6-9. Each stripe consists of small crystallites with different orientation. The stripes start with a single layer deposit, quickly followed by monolayer steps. The bottom end of each stripe was found to consist of a sharp straight boundary. The bottom, rough side of the silicon substrate contained similarly striped deposits.

The initial volume fraction of colloids in the suspension was varied, but we did not notice any effect of the volume fraction on the thickness of the crystal. Rather, the thickness of the crystal
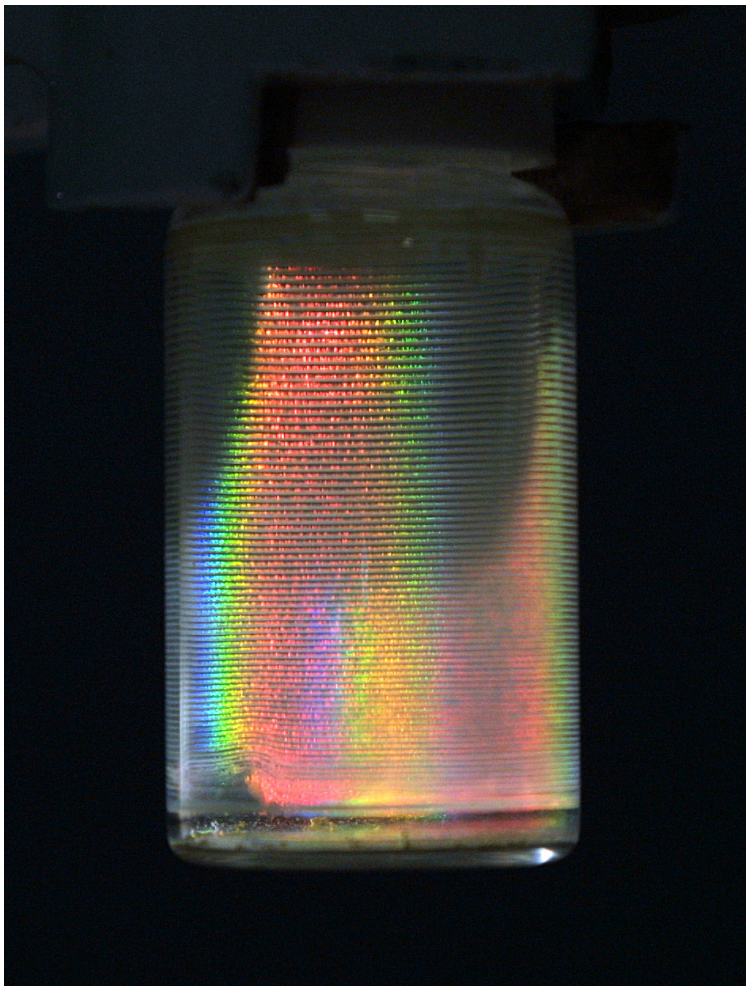
Figure 6-9 A 20 ml scintillation bottle with striped deposits of 870 nm-diameter silica colloids after vertical controlled drying from ethanol at 65.5ºC. A silicon substrate on which a large single-domain crystal was deposited had been placed in the suspension as depicted in Figure 6-1. The colors result from Bragg-reflections of the multi-domain crystallites in the striped deposits.

was found to vary between different experiments and on a single substrate monolayer steps could usually clearly be distinguished by the eye. Single-crystal deposits could easily be identified upon visual inspection due to a silverish, transparent appearance. Amorphous and multi-crystalline deposits had a white (for unlabelled silica colloids) or yellow (for FITC-labeled silica colloids) appearance. The deposition process was found to proceed best, in terms of crystal quality and lateral crystal size, with a volume fraction of 0.003.

In Figure 6-10 a SEM image is shown of 870 nm silica colloids arranged on a square symmetric template in silicon. The black arrow indicates the template edge. At the top right side the template pattern is clearly visible. The distance between the holes in the pattern is 900 nm. Particles on the plain, untemplated silicon substrate, right of the arrow, have arranged in the usual hexagonal symmetry. On the template, particle density increases in the direction of the drying front. At the low-density areas, colloids follow the template symmetry, however, as the density
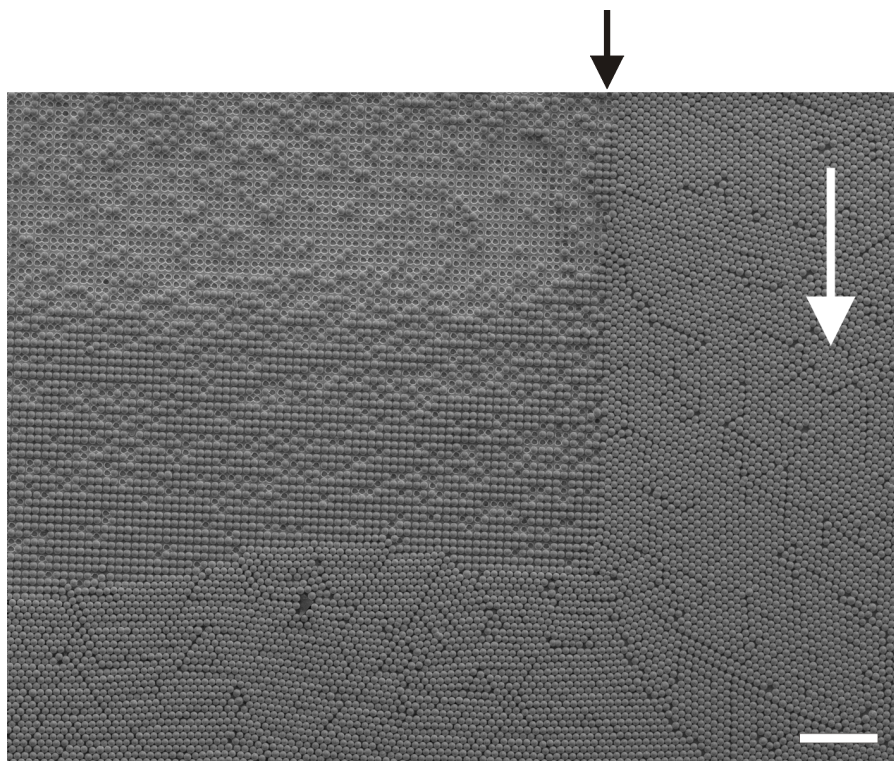
Figure 6-10 SEM image of 870 nm-diameter silica colloids arranged on a square symmetric (fcc(100)) all-silicon template after vertical controlled drying. The white arrow indicates the direction of the liquid-air interface during evaporation. The black arrow denotes the edge of the templated area. The length of the scalebar is 10 μm.

increases it can be seen that the structure changes from square symmetric to hexagonal at the point single-layer coverage would occur. This observation supports the remarks made at the end of the previous section that at higher coverage a dense single-layer arrangement is favored over a less dense arrangement. It would furthermore be interesting to see whether a decrease of the higher area at the template, e.g. making the template consist of pillars as in Figure 6-7, would result in a single-layer or possibly larger, square symmetric arrangement. Note that the orientation of the hexagonal crystal on the template is different from that of the crystal on the untemplated part and is thus influenced by the template orientation. Furthermore, the presence of the template leads to a considerable amount of defects and particles that are placed slightly lower due to the template holes.

6.4 Conclusions

In this chapter, we have presented results on the template-induced growth of colloidal crystals using controlled drying techniques. In a set-up where the substrate is placed almost horizontally, it was demonstrated that colloidal crystal growth can be directed by the use of a template. Furthermore, at templates that possess a mismatch with respect to the colloidal dimensions, a

reconstruction in surface orientation of the crystal takes place. These mismatch-templates seem to undergo similar strain relaxation phenomena, like out-of-plane displacements of particles and small particle grains, as in 'equilibrium' crystal growth in suspension.

In order to achieve more control over crystal quality and crystal thickness, the use of templates in the vertical controlled drying technique described by Jiang et al.[117] was examined. The growth of a square symmetric monolayer of 170 nm particles on a template consisting of periodically placed pillars was demonstrated. For thicker crystals, the top surface layer of the crystal however always had an hexagonal symmetry. The vertical controlled drying technique was extended to the use of silica particles with a diameter of 870 nm. Large single-crystal deposits at a silicon substrate were achieved from a suspension with a volume fraction of 0.003 at a temperature of $65.5 \pm 0.5°C$. For single-layer deposits at a square symmetric template, a transition was observed from a template-induced square symmetric arrangement of particles to an hexagonal particle arrangement with increasing particle density. A crucial parameter determining the occurrence of this transition may be the ratio between the surface area at the higher parts of the template to the lower surface area, which determines the possibility to form a stable crystalline structure at the higher parts of the template.

6.5 Acknowledgements

7

A real-space analysis of colloidal crystallization in a gravitational field at a flat bottom wall

We have studied crystallization in a system of sedimenting colloids in real-space using fluorescence confocal microscopy. During sedimentation a gradient in particle concentration develops at the bottom of the sample container. The presence of the lower boundary wall induces layering in the liquid and, upon increasing sediment thickness, crystallization occurs in these liquid layers. Crystallization in the first layer was found to proceed via a first-order transition. The formation of small crystalline nuclei in this layer, induced epitaxial crystal growth in the second layer on top of these crystallites, which resulted in both layers undergoing the phase transition simultaneously. The critical osmotic pressures for crystallization at a plain wall as well as for epitaxial crystallization on an already crystallized layer were determined. The nucleation-and-growth mechanism led to a poly-crystalline end-state. Due to this polycrystallinity we could not determine whether the crystallization process involves an intermediate 'hexatic-like' phase. Our results regarding the nature of the transition in the first two layers are in agreement with recent computer simulations[216].

7.1 Introduction

Although freezing and melting are at the basis of many everyday phenomena, the exact nature and mechanisms underlying these phase transitions are still poorly understood and subject of ongoing research. This even holds for what is arguably the simplest model system in condensed matter physics, particles interacting through a hard-sphere potential. The notion that such a system can spontaneously crystallize, driven by entropy alone[23, 24], was initially met with skepticism, but is now commonly accepted[217]. Nevertheless, the actual mechanism by which crystal nucleation in a supersaturated hard-sphere liquid proceeds has been only recently addressed as a consequence of developments in computational[217] and experimental physics[12, 159].

It took quite a number of years after the early work of Wood and Jacobson and Alder and Wainwright[23, 24], before the hard-sphere potential could be approximated in an experimental system: a dispersion of colloids. Colloids have been such an appropriate experimental realization of the hard-sphere model system for two reasons. On the one hand their interaction potential can be tuned in such a way that it spans the whole range from effective hard-sphere like, through short-range attractive, to long-range repulsive. On the other hand their length and time scales are easily accessible from an experimental point of view, e.g. using light scattering or microscopy techniques. The development of a model system of fluorescently labeled core-shell colloids[149], together with the use of three-dimensional confocal microscopy[150, 158] has led to the recent experimental realization of quantitative real-space analyses of glass-formation[11, 159, 160] and crystal nucleation[12] in hard-sphere systems.

In many natural and experimental systems, molecular crystal growth is influenced by impurities, which make it hard to observe pure homogeneous crystallization without special precautions. A lot of research has been done on crystallization at flat walls[218] both theoretically and with computer simulations as well as experimentally. The influence of a hard wall, which can be seen as the simplest external potential, on colloidal crystallization has been examined as well. In the liquid state the presence of a hard wall can already cause strong perturbations leading to layering of the colloidal liquid[103] and eventually to prefreezing or possibly even wetting[63, 64, 219, 220]. These effects can be more pronounced when the wall carries a surface pattern with similar symmetry as a crystal plane, a phenomenon called colloidal epitaxy[61, 63, 64].

In many colloidal systems, crystallization is furthermore influenced by the presence of a second force field, namely gravity. Under the influence of gravity, colloids settle towards the bottom of their container, where, at increasing density, crystallization and subsequent growth will take place. Colloidal crystals grown by sedimentation are often encountered in physical situations[1] and are routinely used in (photonic) applications[61, 88-90, 138, 193]. A thorough understanding of the mechanisms of crystallization is crucial for both our understanding of colloidal crystallization in general as well as for the further development and applicability of

colloidal crystals in applications. During sedimentation in a strong gravitational field, the formation of a layered liquid at the bottom wall will precede the formation of a crystal at the bottom of the sediment. The nature of this liquid-crystal transition with a strong one-dimensional field has so far only been addressed by Biben et al.[216]. They showed that the first two layers of the layered liquid at the bottom wall undergo a first-order phase transition with increasing gravitational strength.

The formation of a crystalline sediment is however not a priori clear. Rather, the interplay between the particle fluxes associated with both sedimentation and crystallization is crucial for determining whether a crystalline or an amorphous sediment results. Crystal growth in a sediment of particles with a small Peclet number, i.e. the ratio between the gravitational field strength and thermal energy expressed as $Pe = (\Delta\rho)gR^4/kT$ with $\Delta\rho$ the density difference between particles and solvent, g the gravitational constant, R the particles radius, k Boltzmann's constant, and T the temperature, was examined by Davis et al.[221]. Under these conditions, the gradients in the particle concentration profile are small and crystallization can be described by using local average concentrations and other thermodynamic variables. Here, the crystals grow epitaxially in a one-dimensional (1D) way. In the other extreme, at very large Peclet numbers, the Brownian motion against the field direction becomes so small that this system resembles a two-dimensional (2D) system and a monolayer of colloids can crystallize. This limit can be reached not only in a gravitational field[35], but also for instance by radiation pressure[222].

Considerable research, both theoretical as well as experimental, has been performed to elucidate the mechanisms of freezing and melting in 2D model systems. As in a 2D system true long-ranged translational order cannot exist due to a divergence in the relaxation of phonon modes, these phase transitions address the occurrence of quasi long-ranged translational order(see e.g. [40]). In the following we will simply use the term long-ranged order for 2D systems as well and assume it to be clear that in these situations we are actually dealing with quasi long-ranged order. The Kosterlitz-Thouless-Halperin-Nelson-Young (KTHNY) theory[36-39] predicts a two-stage melting process. In the KTHNY-scenario the transition from the liquid state, characterized by both short-ranged positional and short-ranged orientational order, to the solid state with long-ranged positional and orientational order proceeds via a phase with short-ranged positional order but long-ranged orientational order. This intermediate phase is called the hexatic phase. For a system of 2D hard disks the occurrence of an intermediate hexatic phase is still unclear. Its existence has been predicted theoretically[41], but computer simulations cannot rule out the possibility of a weak first-order phase transition[42]. For systems with an attractive interaction potential, computer simulations showed the occurrence of a stable hexatic phase[43], which was confirmed experimentally[223]. Furthermore, the hexatic phase has been observed in 2D colloidal systems interacting via a screened Coulomb potential[31], though the occurrence of the hexatic phase may in this case be due to the presence of short-ranged attractions[43], and in systems with dipole-dipole interactions[34, 35]. Only in a system of colloids interacting through a short-ranged repulsive potential a first-order transition directly from the liquid to the solid was observed[33]. The various order parameters that we will use to characterize the layer-wise liquid-

solid transition during particle sedimentation will incorporate those that can distinguish the presence of an intermediate hexatic phase.

Here, we present a detailed, real-space analysis of wall-induced colloidal crystallization during sedimentation of a model system of slightly charged colloidal spheres. In comparison with the work of Davis et al.[221], our system has a Peclet number that is about two orders of magnitude larger. The softness of the interactions results in a crystal volume fraction of 0.31 after complete sedimentation, compared to ~0.74 for true hard spheres. The initial stage of crystal nucleation in the sediment at the bottom wall under increasing osmotic pressure during particle sedimentation will be especially addressed. Our experimental situation resembles the already mentioned work of Biben et al.[216], who performed Monte Carlo (MC) simulations and Density Functional Theory (DFT) calculations on a system of hard spheres at a fixed density under increasing gravitational constant. We will compare our results directly to their work, by integrating the density profile in a mean-field way that is, however, only exact for small Peclet numbers[224-226]. We will address these differences and their possible consequences later in this chapter. In our system, the Peclet number is fairly high and we therefore give a description using 2D order parameters, similarly to the work of Biben et al. [216] and Heni and Löwen[63, 64]. Furthermore, crystallization will occur in liquid layers oriented perpendicular to the gravitational direction as layering of the colloidal liquid occurs before the point at which crystallization occurs[103]. These layers will order in their most densely packed structure, namely hexagonally arranged crystal layers. The fact that crystallization occurs in an already layered system raises the question whether the crystallization process in each layer can be regarded as a separate 2D process. The order parameters that will be used to probe the liquid-solid transition will enable a layer-wise (2D) analysis of the occurrence of long-ranged bond orientational and translational order, which can distinguish the presence of an intermediate hexatic phase[208].

7.2 Experimental

7.2.1 Setup and model system

Confocal microscopy was performed on a system of fluorescent silica core-shell particles to obtain three-dimensional (3D) particle coordinates[159]. The core of the particles contained the fluorescent dye rhodamine isothiocyanate (RITC) and had a radius of approximately 100 nm. These particles have been described in detail elsewhere[150]. In a continuous-feed seeded-growth synthesis as described by Giesche[154] these particles were grown to a final radius of 997 nm with a polydispersity of 3.3% as measured by Transmission Electron Microscopy. Particles were dispersed in a refractive-index matching mixture of demineralized water and glycerol (Baker, z.A grade) in a volume ratio of 1 : 7.18. The refractive index was measured on an Abbe refractometer (Jena 202853) and was found to be 1.4548 at a wavelength of $\lambda = 589$ nm at a temperature or

$T = 21°C$. Transmission spectra were taken on a Spectrophotometer (Cary 5 UV-Vis-IR) and confirmed that this solution indeed showed the highest transmission at the RITC excitation and emission wavelengths (520-580 nm) as compared to other mixtures. Apart from refractive-index matching the mixture of water and glycerol also has the advantage that due to the high viscosity (on the order of 10^2 mPa·s) the timescales for particle motion are scaled to the order of minutes, which makes a dynamical analysis of a large number of particles possible.

The bottom of the sedimentation container consisted of a 22 mm-diameter Chance no.1 coverslip, which had been immersed in chromosulfuric acid (Merck) for 20 minutes and rinsed with demineralized water and ethanol (Merck, technical grade) before coating with a layer of poly(methylmethacrylate) (PMMA) to prevent particle adhesion. PMMA (950k, 4wt% in chlorobenzene, MicroChem Corp.) was spincoated at 1000 rpm for 30 sec. and subsequently baked for 1 hour at 170°C. A bottomless flask with an internal diameter of 9.65 mm was glued to the PMMA-coated coverslip using Silicon Rubber Adhesive RTV 102 (General Electric). The sedimentation container was rinsed several times with the water/glycerol mixture before filling it with 0.86 ml of dispersion with a volume fraction of $\varphi_0 = 0.0039$.

The suspension was left to sediment mounted on a confocal microscope (Leica TCS NT-2). During sedimentation the sample was scanned regularly. The scanfield size was 100 x 100 μm, which was scanned with a resolution of 1024 x 1024 pixels. Both time-series of a 2D plane in the sample, with a time-interval between subsequent scans of 40 seconds, and stacks of 2D scans with a stepsize of 0.12 μm, were acquired.

In each 2D frame feature coordinates were retrieved using image-analysis software similar to that described in ref.[157], written in the programming language IDL[1]. For retrieving particle coordinates from the 3D stacks, feature coordinates from successive frames with 2D particle coordinates that belong to a single sphere's intensity profile were grouped in columns that extend in the direction perpendicular to the scan field. This intensity profile is the z-component of a convolution of the Point Spread Function (PSF) of our microscope with the spherical profile of the core particles. A Gaussian function was constructed of which the full-width-at-half-maximum was fixed at a value that was such that this Gaussian function mimicked the z-axis component of the convolution of the PSF with the spherical core profile. Each of the intensity-profiles in the 3D data set was then fitted to this Gaussian and the position of the maximum was taken as a particle's z-coordinate. The use of the high-viscosity water/glycerol mixture makes it possible to record the 3D intensity profiles without having to correct for intermediate particle diffusion. In the remainder of this chapter we will use a Cartesian coordinate set, with the positive z-axis parallel and opposed to the gravitational direction, so that increasing values of z correspond to increasing height in the sample. The z-direction is now along the optical axis of the confocal microscope. The error in retrieving the z-coordinates with the above-mentioned procedure is ±30 nm. The error in the lateral (xy-)coordinates is ±10 nm.

---

[1] IDL (Interactive Data Language) is a product of Research Systems Inc. and is especially suited for and widely used in the processing of array-based information

7.2.2 Sedimentation and crystallization

The process of crystallization during sedimentation is based on a complicated interplay between the time-scales associated with both processes. The time-scale for sedimentation is given by the volume-fraction dependant sedimentation velocity $U(\varphi) = U_0 \cdot K(\varphi)$, where U_0 is the sedimentation velocity at infinite dilution, $U_0 = 2/9 \cdot R^2 (\Delta\rho)g/\eta$ with R, $\Delta\rho$, and g as previously defined and η as the solvent viscosity. The factor $K(\varphi)$ denotes the reduction of sedimentation velocity at higher volume fractions and can usually be well described by $K(\varphi) = (1-\varphi)^n$ where for instance for hard-sphere $n = 6.6$[1].

In Figure 7-1 the typical form of the fluxcurve $\varphi \cdot U(\varphi)$ is given. The initial volume fraction φ_0 gives rise to a constant sedimentation flux $\varphi_0 \cdot U(\varphi_0)$. At the bottom of the container the sediment will be formed at a volume fraction denoted in Figure 7-1 with φ_s. For relatively large initial volume fractions, $\varphi_0 > \varphi_1$ with φ_1 on the order of 10^{-2}[1], the sedimentation flux of particles, $\varphi_0 \cdot U(\varphi_0)$, is larger than the maximum possible flux for a volume fraction of φ_2 and higher. When a volume fraction of φ_2 is reached during sedimentation, there will be a build-up of particles in a so-called fan. The fan constitutes a transition region where the volume fraction smoothly varies with depth from φ_2 to φ_s. With ongoing sedimentation the fan-region will expand to higher volume fractions. In this case the flux of particles into the sediment is given by the sedimentation flux at the bottom of the fan, which, in order to yield a crystalline sediment, has to be equal to or smaller than the particle flux associated with the maximum rate of crystal growth. Under these circumstances there is a maximum sphere radius, and thus a maximum Peclet number, above which crystallization in the sediment is prohibited by too high a sedimentation flux and an amorphous sediment results, as was experimentally verified by Davis and co-workers[221]. In order to be able to match the sedimentation and crystal growth fluxes, we thus have to have an initial volume fraction where the flux associated with this φ_0 is the rate-limiting step anywhere in the sample. This means that $\varphi_0 < \varphi_1$ in Figure 7-1 and thus $\varphi_0 < 0.01$. Under these circumstances $K(\varphi_0) \approx 1$ and the time-scale for sedimentation is determined by U_0.

Now, we define the time-scale associated with the flux of particles during sedimentation, t_{sed} as the average time it takes before one particle sediments through an area R^2. This time-scale depends on the initial volume fraction and is given by $t_{sed} = R/(\varphi_0 \cdot U_o) \sim \eta/(\varphi_0 (\Delta\rho)gR)$. If we now scale this t_{sed} to the typical time-scale for diffusion $t_D = R^2/D_o$, i.e. the time it takes for a particle to diffuse a distance R, where $D_0 = kT/(6\pi\eta R)$, and use the Peclet number, we find $t_{sed}/t_D = 1/(\varphi_0 \cdot Pe)$. For the system given above, with an initial volume fraction of $\varphi_0 = 0.0039$, we have $1/(\varphi_0 \cdot Pe) = 2.5 \cdot 10^3$.

7.2.3 Data analysis and order parameters

For each 3D coordinate set the linear number density, as a function of height in the sample, was calculated by integrating over the lateral (*xy-*)coordinates:
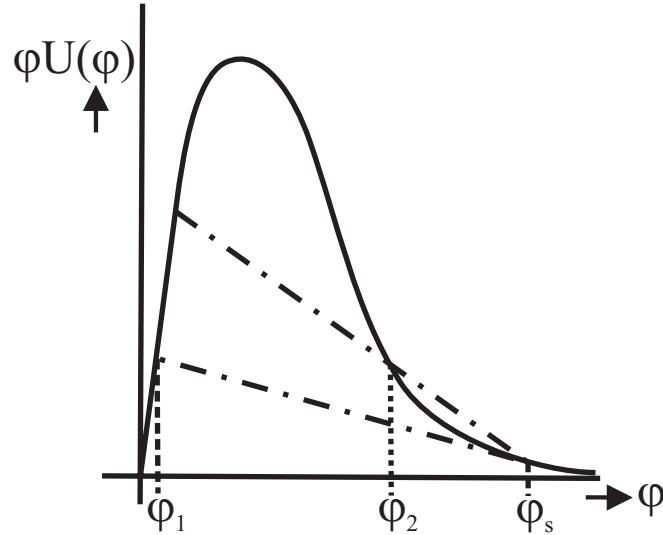
Figure 7-1 Typical form of the fluxcurve for colloidal sedimentation. φ_s denotes the volume fraction at the top of the sediment. For initial volume fractions larger than φ_1 a fan-region builds up starting from φ_2, which at continuing sedimentation expands to smaller volume fractions. For initial volume fractions smaller than φ_1, the sedimentation flux is constant throughout the sample until the top of the sediment.

$$\rho_z = \frac{\int\limits_{z-\frac{\Delta z}{2}}^{z+\frac{\Delta z}{2}} \iint \sum\limits_{i=1}^{N} \delta(x-x_i)\delta(y-y_i)\delta(z-z_i)dxdydz}{\Delta z \cdot \iint dxdy}.$$ (7.1)

Here, x_0, y_0 and z_0 denote the particle coordinates and a uniform binsize of $\Delta z = 40$ nm was chosen. The position of the first maximum in the laterally integrated density profile was taken as $z = 0$. The total number of particles in the sediment was retrieved by integrating over the z-direction. As we will see in the section containing the results, the overall volume fraction was low enough to ensure ρ_z decaying to almost zero, corresponding to the very low φ_0, so that both sediment thickness as well as the integration over z are well defined. The total number of particles in the sediment was found to increase linearly with time as would be expected. The evolution of the order parameters that we will define below will depend on the evolution of the concentration profile in the sediment. The build-up of the concentration at the bottom of the sample leads to an increased gravitational pressure on the particles in the sediment. This gravitational pressure is balanced by an osmotic pressure gradient that can be directly retrieved from the instantaneous concentration profile[224]:

$$\Pi = m_b g \int\limits_z^h \rho_z(z)dz.$$ (7.2)

The osmotic pressure at the bottom of the sample is thus directly related to the thickness of the sediment. It should be noted however that this mean-field approach is only exact for small Peclet numbers. We now express the sediment thickness in terms of an equivalent number of crystal layers by scaling the total number of particles in the sediment with the number of particles in a single crystal layer at the end of our experiment, 263 hours after homogenization of the sample:

$$
N = \frac{\iiint \sum_i \delta(x - x_i)\,\delta(y - y_i)\,\delta(z - z_i)\,dxdydz}{\left. \int_{z=-0.5}^{0.5} \iint \sum_i \delta(x - x_i)\,\delta(y - y_i)\,\delta(z - z_i)\,dxdydz \right|_{t=263\ \text{hours}}}. \tag{7.3}
$$

The number of crystal layers after 263 hours was $N = 21$. As a comparison, all data reported below fall in the time-interval from 90 to 150 hours after the start of the experiment, which gives a number of layers between 8 and 13. Expressing the sediment thickness in N has the advantage that this quantity is experimentally well defined and that it can be directly related to the (mean-field) osmotic pressure at the bottom of the sample using equations (7.1) and (7.2).

On the basis of the laterally integrated density profile we can see the onset of layering in the sample at the bottom wall. When layering occurs, particles can be assigned to belong to these 2D layers defined by the minima in ρ_z. Recently, Heni and Löwen suggested the use of these minima as a robust order parameter for layer-wise crystallization[64]. Furthermore, it was shown in the work of Biben et al., that the crystallization transition in a suspension close to a hard wall under increasing gravitational field strength, occurs through a discontinuous jump in the interlayer density to zero[216]. As this implies that the number of particles confined to this layer also increases discontinuously, this jump would imply that the crystallization transition is of first order if judged as a 2D transition.

Furthermore, for each layer both orientational and translational order can be probed. As we expect each layer to crystallize in hexagonal symmetry, the 2D local hexagonal bond orientational order parameter for each single particle in a specific layer was calculated[208]:

$$
\psi_6(r_j) = \frac{1}{N_b} \sum_k \exp\left(i6\theta(r_{jk})\right), \tag{7.4}
$$

where the summation k runs over all, in total N_b, neighboring particles of particle j and the angle θ is the angle that the bond-vector between particles j and k makes with an arbitrary fixed reference axis. In this equation as in all the following equations for layer-wise order parameters, we denote all 2D coordinates in a layer with $r = r(x,y)$. With the definition given above, $\psi_6 = 1$ for a lattice with hexagonal symmetry. The distribution of neighbors to every particle are found using a Delauney-triangulation, which is equivalent to a Voronoi polygon construction. A Voronoi polygon is defined as the area around a particle that is closer to that particle than to any other particles, thus the construction of the Voronoi polygon is similar to the Wigner-Seitz cell

used in solid-state physics. With this local order parameter, both its layer-wise average can be evaluated as well as the corresponding correlation function $g_6(r)$:

$$g_6\left(r\right) = \frac{\left\langle 2\sum_{i=1}^{N-1}\psi_6^*(\vec{r})\delta(\vec{r}-\vec{r}_i)\sum_{j=i+1}^{N}\psi_6(\vec{r}')\delta(\vec{r}'-\vec{r}_j)\right\rangle}{\left\langle 2\sum_{i=1}^{N-1}\delta(\vec{r}-\vec{r}_i)\sum_{j=i+1}^{N}\delta(\vec{r}'-\vec{r}_j)\right\rangle}. \tag{7.5}$$

The denominator in this expression is related to the translational order correlation function, or radial distribution function, defined by:

$$g(r) = \frac{1}{\rho^2}\left\langle 2\sum_{i=1}^{N-1}\delta(\vec{r}-\vec{r}_i)\sum_{j=i+1}^{N}\delta(\vec{r}'-\vec{r}_j)\right\rangle, \tag{7.6}$$

with $i \neq j$. For a 2D system the occurrence of an intermediate hexatic phase can be probed by determining the envelope function of the decay of both these correlation functions. In the liquid state both correlation functions decay to zero exponentially. For the short-ranged translational order and quasi long-ranged bond orientational order of the hexatic state the envelope function of $g_6(r)$ decays to a non-zero value with power-law dependence, while for $g(r)$ the decay is still exponentially to zero. In the crystalline end-state the decay of both functions proceed algebraically to a non-zero value[208].

Apart from these static criteria, also dynamical criteria can be used to probe a liquid-solid transition[227, 228]. Here, we will carry out a mobility analysis per layer as described by Hurley and Harrowell[229] in order to visualize kinetic heterogeneities consisting of relatively slowly diffusing, 'caged' particles on the one hand and faster diffusing particles on the other hand. Furthermore, we will evaluate the behavior of the long-time self-diffusion coefficient D_l^s:

$$D_l^s = \lim_{t\to\infty}\frac{1}{4t}\left\langle \left(r\left(t\right)-r\left(0\right)\right)^2\right\rangle, \tag{7.7}$$

which should decay towards zero upon crystallization. The behavior of the long-time self-diffusion coefficient can be used as a separate order parameters using the Löwen-Palberg-Simon criterion[227, 230]. Their criterion states that the ratio of the long-time and short-time self-diffusion coefficients reaches a uniform value of 0.1 upon crystallization. As the short-time self-diffusion coefficient can be assumed to stay constant during the phase transition, a sharp decay of D_l^s indicates a similar behavior for this order parameter.
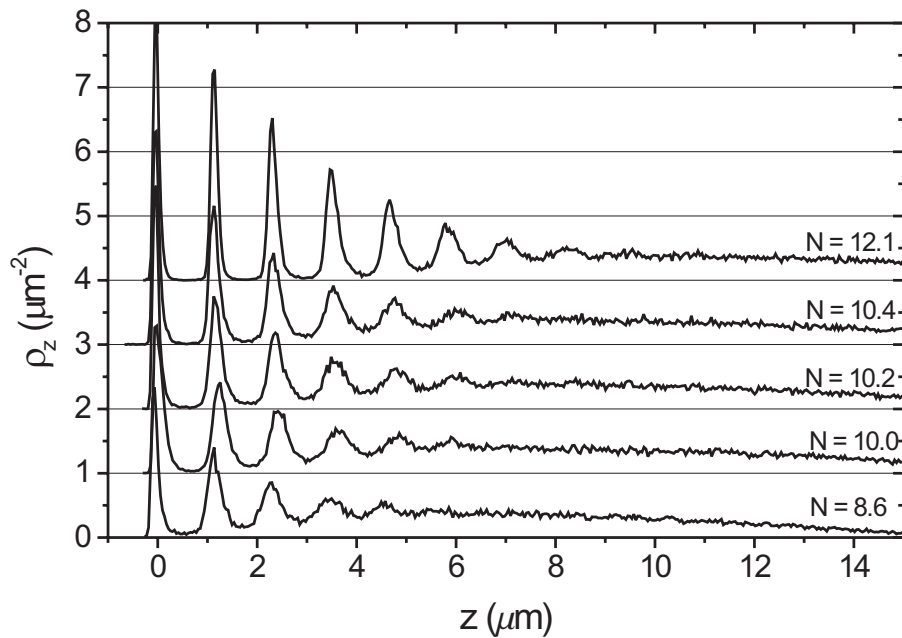
Figure 7-2 Laterally integrated density profiles as a function of sediment thickness. Profiles for different values of N have been shifted by one for clarity.

7.3 Results and discussion

7.3.1 Layering and crystallization

As a start of our analysis the laterally integrated density profile ρ_z was calculated for each of our 3D coordinate-sets. Several density profiles at different stages of the sedimentation process are shown in Figure 7-2. As can be seen, all profiles start with a sharp peak at $z = 0$ due to the presence of the bottom container wall. The exact position of the zero on the z-axis has been chosen to coincide with the position of the first maximum in the density profile, as the exact position of the wall surface was not accurately retrievable from these data sets. With increasing z the density profile goes through a minimum and shows several oscillations with decreasing peak height and increasing peak width. This shows the layering at the bottom of the suspension due to the presence of the bottom container wall[103]. The oscillations in the density profiles are followed by a smooth, almost linear decay to zero. The fact that the density profiles actually decay to essentially zero is due to the fact that a very low initial volume fraction of $\varphi_0 = 0.0039$
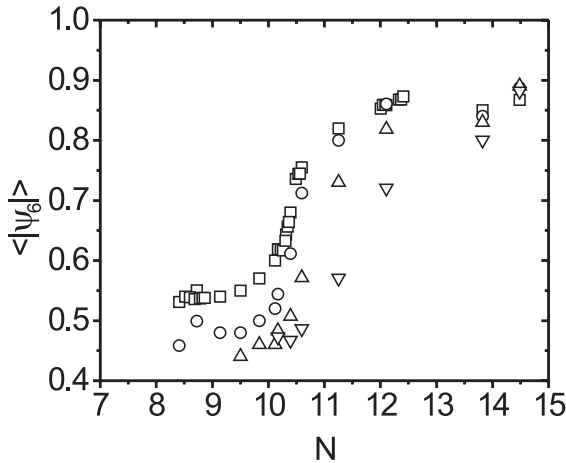
Figure 7-3 The layer-wise averaged local bond order parameter ψ_6 for the first four layers indicated with squares for layer one, circles for layer 2, up-triangles for layer 3, and down-triangles for layer 4.

was used, which makes the sediment thickness, N, well defined. This furthermore allows for a gradual increase of the osmotic pressure.

With increasing sediment thickness, the range of oscillations increases and the first peaks in the profile become sharper. The minimum in between the first two peaks falls to zero from $N = 10.2$ to $N = 10.4$ and the width of this minimum becomes broader. A similar process can be seen for the second minimum at higher N. We will analyze the relative depth of these minima as an order parameter below. Note that all peaks are asymmetric with a sharp, almost delta-peak alike rise followed by a slower decay to the minimum. This is most clearly visible for the first two peaks and becomes more pronounced for higher peaks at increasing N. For the first peak this asymmetry is due to the presence of the bottom wall, but its influence remains visible for further peaks, even when the first few layers have crystallized at $N = 12.1$. This asymmetry is solely due to the presence of the wall, as this can also be seen in simulation results where no gravitational field is present. The fact that this asymmetry is so clearly reproduced in our results shows the good statistical accuracy with which these profiles are retrieved.

In Figure 7-3 the evolution of the averaged local hexagonal bond order parameter, $<|\psi_6|>$, defined in equation (7.4), is given as a function of N, for the first four layers in the sample. For the first layer $<|\psi_6|>$ shows a sharp rise from $N = 10.2$ to $N = 10.7$, indicative of the transition to a hexagonal lattice, followed by a slower saturation towards a value of $<|\psi_6|> \sim 0.9$. For the second layer $<|\psi_6|>$ shows a similar evolution, starting however from a lower value, but showing a rise simultaneously with the first layer and catching up with the first layer in between $N = 10.4$ and 10.7. For layers three and four the transition regions are qualitatively similar, but with the transition occurring at a higher, discrete value of N. Taking halfway the rise in $<|\psi_6|>$, i.e. $<|\psi_6|> \sim 0.68$, as the location of the crystallization transition, we find this transition to occur at $N = 10.4$, 10.5, 11.0, and 11.9 for layers one to four respectively as indicated in Table 7-1. The corresponding osmotic pressures at these layers are also given in Table 7-1.

In a first-order phase transition there is a discontinuous increase in the density of the crystallizing phase. A sharp rise between the average values that can be associated with liquid and solid phases was observed for the bond orientational order parameter. We will now examine whether this phase transition is of first order. In the density profiles shown in the work of Biben

Table 7-1 Sediment thickness and osmotic pressures for the liquid-crystal transition in consecutive layers together with simulation results[216] for the transition regions for these layers. The simulation results are expressed in the parameter α that probes the strength of the gravitational field relative to kT. The corresponding osmotic pressures calculated for the experimental system based on these values are given as well.

	this research		simulation results			
layer	N	Π $(10^{-2}\,Nm^{-2})$	α_{start}	α_{end}	Π_{start} $(10^{-2}\,Nm^{-2})$	Π_{end} $(10^{-2}\,Nm^{-2})$
1	10.4	2.36	2.50	2.75	2.17	2.39
2	10.5	2.13	2.50	2.75	1.59	1.74
3	11.0	2.01	2.50	3.30	1.00	1.32
4	11.9	1.98	3.25		0.53	

et al. a clear discontinuous jump in the interlayer density to zero is observed, which occurs simultaneously with an increase in order parameter. In order to test for similar behavior of the interlayer density, the relative depth of the first two minima in the density profile was determined as was suggested by Heni and Löwen[64]. The density profile was integrated over a range of 0.12 μm around the minimum and this value was taken relative to the result of an integration from the start of the profile to the position of the second minimum. The results for the first and the second minimum are given in Figure 7-4a and 7-4b respectively. Heni and Löwen calculated a direct linear correspondence of the decrease of these minimal values with the order parameter $<|\psi_6|>$ and found the liquid-solid transition to occur when the minimal value decreased below 0.05[64]. The 0.05-criterion is indicated with the dashed line in Figure 7-4a and 7-4b. For the first minimum, the relative minimal value reaches a value of 0.05 at $N = 10.2$, while for the second minimum this occurs at about $N = 10.5$. This last position is however much harder to pinpoint as this region is not as well sampled as for the point where the first minimum traverses the criterion of Heni and Löwen. Comparing Figure 7-4a with Figure 7-4b it can be seen that in the same range around the crystallization transition, the depth of the second minimum falls down from a much higher value and more drastically than does the depth of the first minimum. Apparently, layering and crystallization in the second layer proceeds much faster over a similar increase in sediment thickness than in the first layer. The reason for this is probably the difference in crystallization on a flat surface wall compared to crystallization on an already crystallized layer. We will come back to this point later in this chapter.

Based on the criterion of Heni and Löwen for the minimal interlayer density (Figure 7-4), we found the transition in first and second layer to take place at $N = 10.2$ and $N = 10.5$ respectively. Heni and Löwen reported their criterion to coincide with an averaged value for $<|\psi_6|>$ of $<|\psi_6|> \sim 0.8$[64]. It can be seen when comparing Figure 7-4a and Figure 7-3 that in our experimental situation, the value of $N = 10.2$ found for the first layer gives $<|\psi_6|> = 0.62$. For the second layer (see Figure 7-4b and Figure 7-3) the value of $<|\psi_6|>$ at $N = 10.5$ is $<|\psi_6|> = 0.68$. Where for the first layer, this seems to correspond more to the onset of crystallization as viewed

(a)   (b)
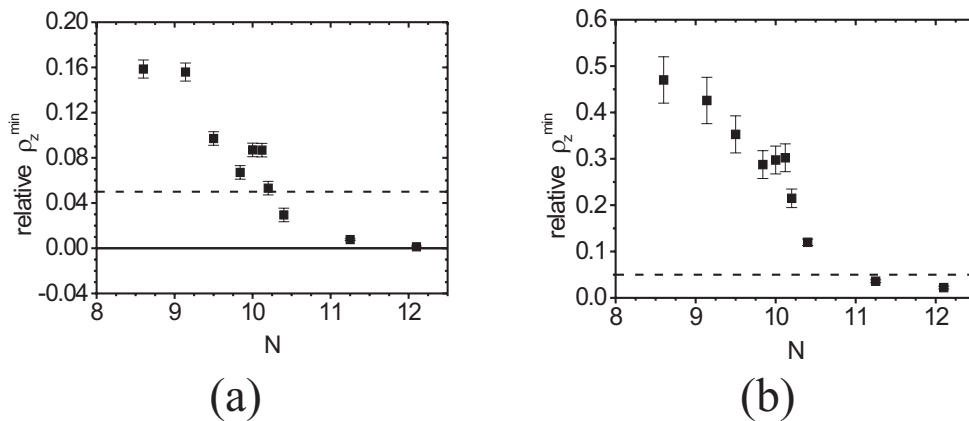
Figure 7-4 The evolution of the relative depth of the minimum in ρ_z for (a): the minimum in between the first and second layer, and (b): the minimum in between second and third layer. Noted the change in scale on the vertical axis between (a) and (b). the dashed line indicates the Heni-Löwen criterion for crystallization of 0.05.

from the development of $<|\psi_6|>$, for the second layer the 5%-criterion seems to correspond well with halfway the rise in $<|\psi_6|>$. As both the minimal density as well as the local hexagonal order parameter shows a drastic change with increasing sediment thickness these values are very sensitive to the exact location of the criterion.

In the calculation of the relative depth of the minima in ρ_z, the density in the first two layers itself is implicitly calculated. The behavior of the minima in ρ_z seems less sensitive to experimental errors than the behavior of the density itself[2], it is still instructive to take a look directly at the behavior of the density in the first two layers. This density was determined by integrating the density profile from the start of the profile and dividing this by twice the layer width. The layer width was determined as the distance between the first and the second minimum. The resulting densities are given in Figure 7-5. The regular increase of the density at the bottom of the sediment due to particle sedimentation is clearly interrupted by a sharp rise at the sediment thickness that was identified as the point where the first two layers crystallize. This clearly and directly indicates the first-order character of the phase transition. In order to probe the character of the liquid-crystal transition, we have also calculated the osmotic compressibility (Π/nkT) per layer as a function of sediment thickness The phase transition was found to occur at an osmotic compressibility which was on the order of 12. The error margins were however too large to get a discriminating critical value for the transition at a single layer.

---

[2] a discontinuous increase in the density acompagnied by a sharp decrease to zero in the interlayer density as shown by Biben et al. would show up more pronounced if the ratio of the two is considered.
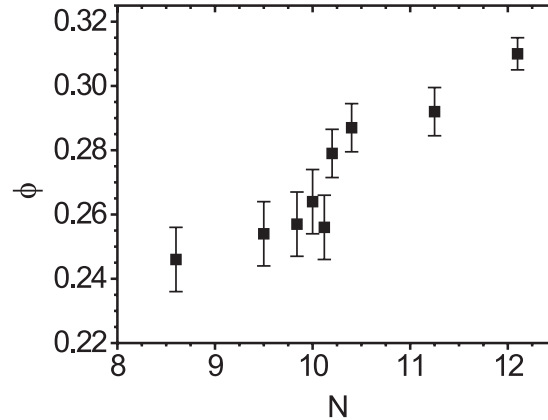
Figure 7-5 The volume fraction in the first two layers above the bottom wall as a function of sediment thickness.

7.3.2 Correlation functions of local order parameters

Above, the occurrence and nature of the phase transition were examined in terms of the density in the system and the average hexagonal symmetry of neighbors surrounding a particle. Next, correlations in particle positions and in the bond orientational order will be examined. For a liquid-solid transition both types of correlations will show a transition from short-ranged to long-ranged. The nature of this transition may indicate the presence of an intermediate hexatic phase: In an intermediate hexatic phase the envelope function of $g_6(r)$ decays algebraically to a non-zero value, while the translational correlation function $g(r)$ still decays exponentially[208]. In the liquid state the decay of both functions is exponentially, while in the solid phase the decay is algebraically for both functions. In Figure 7-6 the radial distribution function $g(r)$ (equation (7.6)) is given for various values of N. Curves for different N have been shifted by 1 for clarity. In the first curve for $N = 8.4$, we can see liquid-like behavior, with typically three or four maximums corresponding to the mean interparticle distance and integer multiples hereof, before leveling to a value of one. Starting at $N = 10.1$, it can be seen that the number of oscillations, and thus the range of correlations in particle positions, increases. The form and position of these oscillations however do not change and remain liquid-like. In between 10.2 and 10.4 a change in form of the correlations does show up: the slightly broadened second and third peak in $g(r)$ both split into two distinct maximums. The positions of these maximums correspond to hexagonal lattice distances of $D\sqrt{3}$ and $2D$, and $D\sqrt{7}$ and $3D$ for the split second and third peak respectively, where D denotes the nearest-neighbor distance in a 2D hexagonal lattice which is retrieved from the position of the first maximum in $g(r)$ at these values for N. This behavior shows the transition in the bottom-wall aligned layers from liquid-like to the order of a 2D hexagonal lattice. As was already evidenced by the rise in $\langle|\psi_6|\rangle$ the sediment consists of hexagonally stacked layers. For the curves with $N > 11.8$, where the average bond-orientational order parameter in the first layer
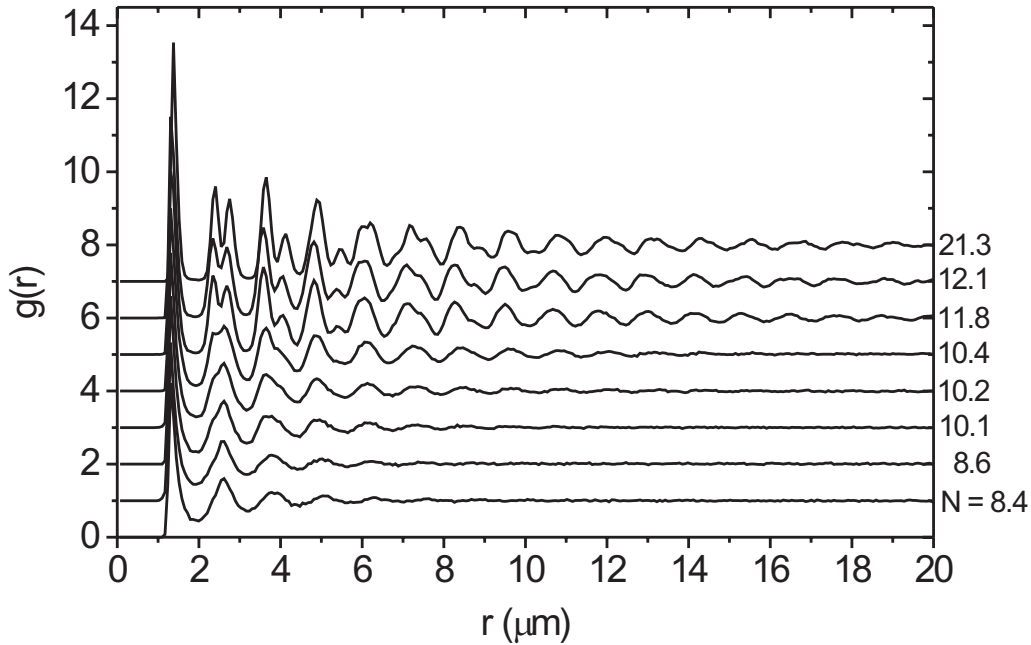
Figure 7-6 Evolution of the radial distribution function $g(r)$ for particles in the first(bottom) layer for (from bottom to top) increasing values of N. Curves for different N have been shifted by one for clarity.

had reached its saturation value (see Figure 7-3), hardly any change in the positional correlations is observed anymore.

The bond-orientational order correlation function $g_6(r)$ in the first layer is given in Figure 7-7 for various values of the sediment thickness. In the liquid phase ($N = 8.6$), $g_6(r)$ decays rapidly to zero, corresponding to the absence of long-ranged bond-order correlations in the liquid state. At the onset of crystallization (from $N = 10.1$ to $N = 10.4$), the rate of decay slows down and the range of correlations increases correspondingly. After $N = 10.4$ the number of oscillations increases only slightly more, until there is long-range bond-order correlation in the crystalline state at $N = 11.8$ (Figure 7-7b). In this stage even negative correlations at a distance of 40 to 50 μm are visible. These can be attributed to the poly-crystalline nature of the crystalline end state: as we will see in the next section, crystallization occurs through a nucleation-and-growth process, so that crystallites with different orientations will appear. Crystallites with only a small orientation difference will still have a possibility to rearrange, leaving the crystallites with a larger orientation difference (around 30º) that give rise to contributions of opposite sign in equation (7.5). The onset of sign inversion of $g_6(r)$ differs for each of these curves, because the amount of crystallites per confocal image is too low and the average crystal size too small to determine the 'true' range of ψ_6 to properly sample the average crystallite size. The poly-crystalline nature of the end state was confirmed by confocal pictures taken at the final stage of sedimentation ($N = 21.3$) as well as two months after sedimentation was completed.
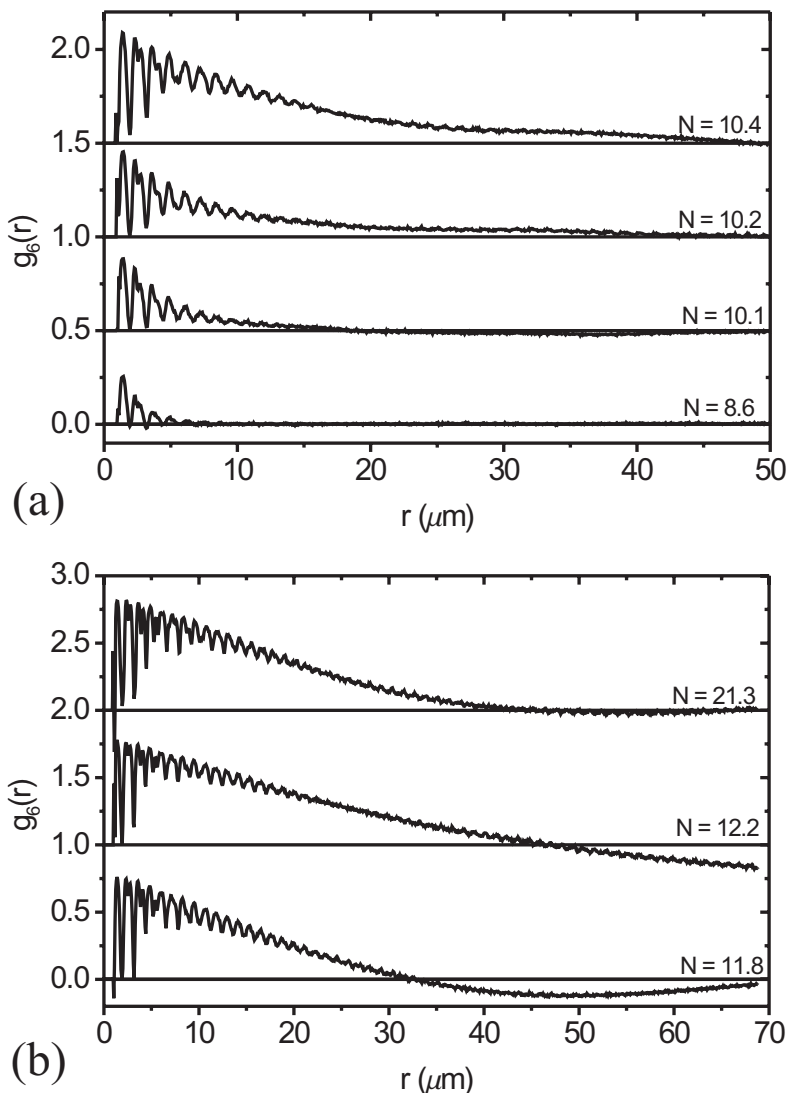
Figure 7-7 The bond order correlation function $g_6(r)$ for particles in the first (bottom) layer, for different sediment thickness in (a): the liquid phase and at the onset of crystallization, and (b): in the crystalline state. Curves in (a) have been shifted by 0.5 and curves in (b) by 1.0 for clarity. Note the different horizontal and vertical scales in (a) and (b).

As mentioned previously, we tried to fit the decay rate of the bond-order correlation function, as this might give an indication of the presence or absence of an intermediate hexatic phase. However, the decay of $g_6(r)$ was found to proceed neither exponentially nor with power-law dependence, probably because the actual behavior of the decay rate for a single crystalline domain is obscured by the finite crystallite size that causes the sign inversion mentioned before. Although this specific order parameter does not give any insight in the presence of an intermediate hexatic phase, the order parameters that were examined before indicated a single
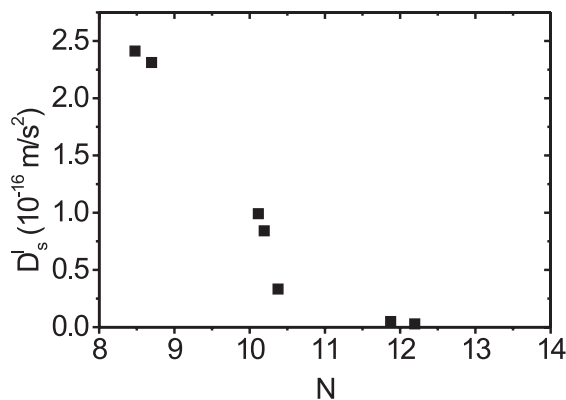
Figure 7-8 The long-time self-diffusion coefficient for particles in the bottom layer as a function of sediment thickness.

first-order transition. Furthermore, the phase transition in the first layer was found to occur at the same range of values for the sediment thickness for all order parameters, either probing orientational or translational order. Thus, based on these results we cannot rule out the occurrence of an intermediate hexatic phase, but if the liquid-crystal transition proceeds in two steps, both the liquid-to-hexatic as well as the hexatic-to-solid transition will occur very close to each other. This is however also what is expected for the occurrence of the hexatic phase in true hard-sphere systems[42]. When the occurrence of the 2D hexatic phase in crystallization during sedimentation is addressed in further experiments, it will also be interesting to examine this transition for the second and further layers in the sediment, as the occurrence of the hexatic phase is not ruled out by the presence of a patterned substrate potential[39], which in this case would be provided by the colloids in the layers below. However, with increasing height in the sediment, the crystallization behavior may become less and less 2D.

7.3.3 Structure and mobility

At several stages during sedimentation, a long time-series of confocal images of the bottom layer was taken, from which the mean-squared displacements and the long-time self-diffusion coefficient (equation (7.7)) were calculated. In Figure 7-8 D_l^s for the bottom layer is plotted as a function of sediment thickness N. As can be seen the long-time self-diffusion coefficient falls off to zero sharply for $N \rightarrow 10.4$. This is in correspondence with the increase in order parameter we saw in Figure 7-3 and the determination of the position of the liquid-solid transition for this first layer (Figure 7-3 and Figure 7-4). The decrease in D_l^s is the indication for the transition of particle motion from diffusive (with strong collective effects) to localized motions around lattice positions. In fact, as mentioned before, the behavior of the long-time self-diffusion coefficient can be used as a separate order parameter, the Löwen-Palberg-Simon-criterion[227, 230]. Their criterion states that the ratio of the long-time and short-time self-diffusion coefficients reaches a uniform value of 0.1 upon crystallization. As the short-time self-diffusion coefficient can be assumed to stay constant during the phase transition because the density differences are small, the sharp decay of D_l^s shown in Figure 7-8 indicates a similar behavior for this order parameter.

(a)
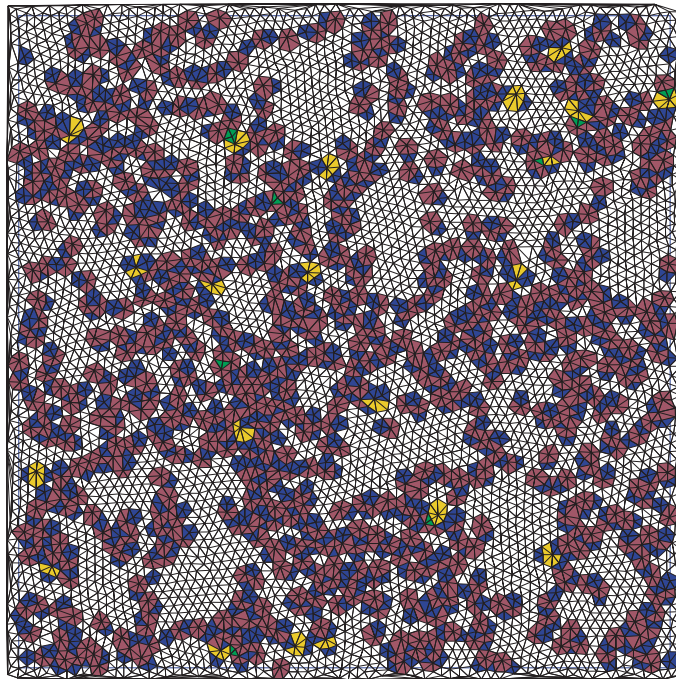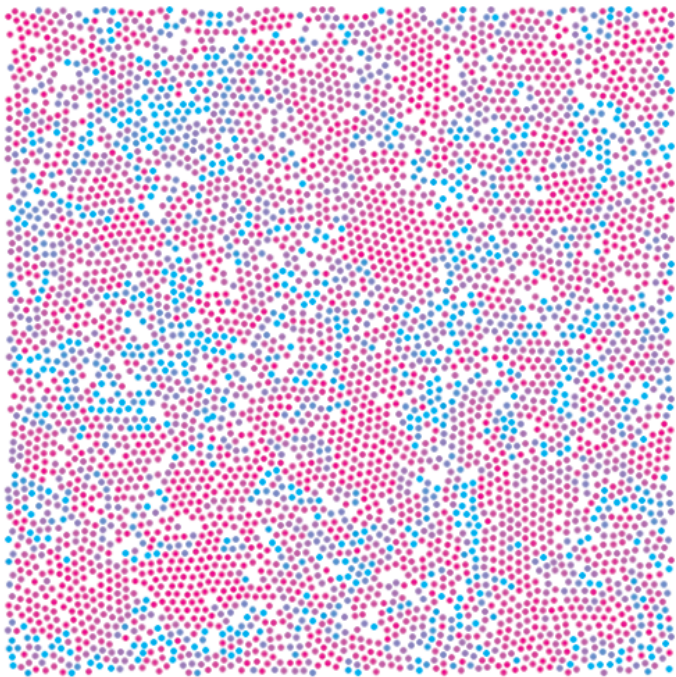
Figure 7-9 (a): Delauney triangulation for particles in the first (bottom) layer at $N = 10.2$. Triangles surrounding six-fold coordinated particles only have been left uncolored, while colored cells indicate a deviating coordination number: green for 4-fold, blue for 5-fold, brown for 7-fold, and yellow for 8-fold coordinated particles. (b): Snapshot of particle positions in the first layer at $N = 10.2$, where particles have been colored corresponding to their mean-squared displacement over a time interval larger than the typical relaxation time. The 5% of particles undergoing the smallest displacements have been colored blue and the 5% of particles with the largest displacements have been colored in red. In between the color changes gradually with a change in mobility, as indicated with the color table below the figure. The scalebar that belongs to the colortable is in $\mu m^2/h$.

(b)

In order to get more insight in the actual mechanism for crystal growth, we carried out a Delauney triangulation analysis. In Figure 7-9a a triangulation plot of the first layer at a value of $N = 10.2$ is given. Triangles have been colored based on the coordination number of the center particle, where six-fold coordinates particles have been left uncolored. Several coherent, ordered regions can clearly be distinguished, surrounded by defect-rich areas of mostly fivefold- and sevenfold-coordinated particles. For lower values of N (not shown), clusters of six-fold coordinated particles also appeared, but these were never larger than five particle diameters wide. Furthermore, a comparison of a time-sequence of triangulation plots of the same area at constant $N < 10$, showed that these regions of six-fold coordinated particles were always fluctuating in time, continuously disappearing and reappearing at other positions. This behavior is typical for a dense liquid where there is a specific correlation time that sets the time-scale in which these spatial homogeneous areas can be observed[229]. The larger regions in the triangulation plot shown in Figure 7-9a were all stationary in time and can thus be identified as small crystallites.

A similar observation can be made when examining the root-mean-squared displacements of particles. The calculated rms displacements of particles fall in a broad distribution. In Figure 7-9b particles in the same time-frame as in Figure 7-9a are shown, but with particles colored according to their averaged mean squared displacement over time. Particles undergoing relatively small displacements (the lower 5% of displacements) are shown in red, and the particles with the larger 5% of displacements in blue with the color scale gradually changing in between. A comparison of Figure 7-9b with the triangulation plot in Figure 7-9a shows that the positions of the particles with the lowest mobility strongly coincide with the larger regions of six-fold coordinated particles. Thus as might be expected, mobility decreases upon nucleation.

Figure 7-10a shows a triangulation analysis (for a different area in the sample) for $N = 10.4$. At this sediment thickness, the average local bond order parameter is now almost halfway its rise upon crystallization (see Figure 7-3). The amount of particles that are six-fold coordinated has drastically increased, resulting in a growth of the crystallites, which are now only separated by one to three particle-diameters wide defect-lines. In the ordered regions several point defects occur. The amount of dislocations in the ordered regions is however low and larger (or more) areas would have to be probed to get enough statistically accuracy to study the average number of defects in these crystallites.

In Figure 7-10b to 7-10d triangulations of the same area in the three layers above are shown. As can be seen in Figure 7-10b the second layer consists of crystallites of on average similar size on the same positions as in Figure 7-10a. This shows the second layer to crystallize epitaxially on top of the crystallites that nucleated in the bottom layer. In the third layer (Figure 7-10c) ordered regions of the same size as in Figure 7-10a can be identified. When comparing the value of $<|\psi_6|>$ for the third layer at $N = 10.4$ ($<|\psi_6|> \approx 0.5$), we see that this is still lower than the value of $<|\psi_6|>$ for the first layer at $N < 10$, where coherent ordered regions larger than five particle-diameters wide did not show up yet. However, in Figure 7-10c a few larger six-fold coordinated regions are clearly visible, which can be identified as crystal nuclei. Indeed it can be seen in Figure 7-3 that at $N = 10.4$ we are at the onset of the sharp rise in $<|\psi_6|>$ for the third layer.
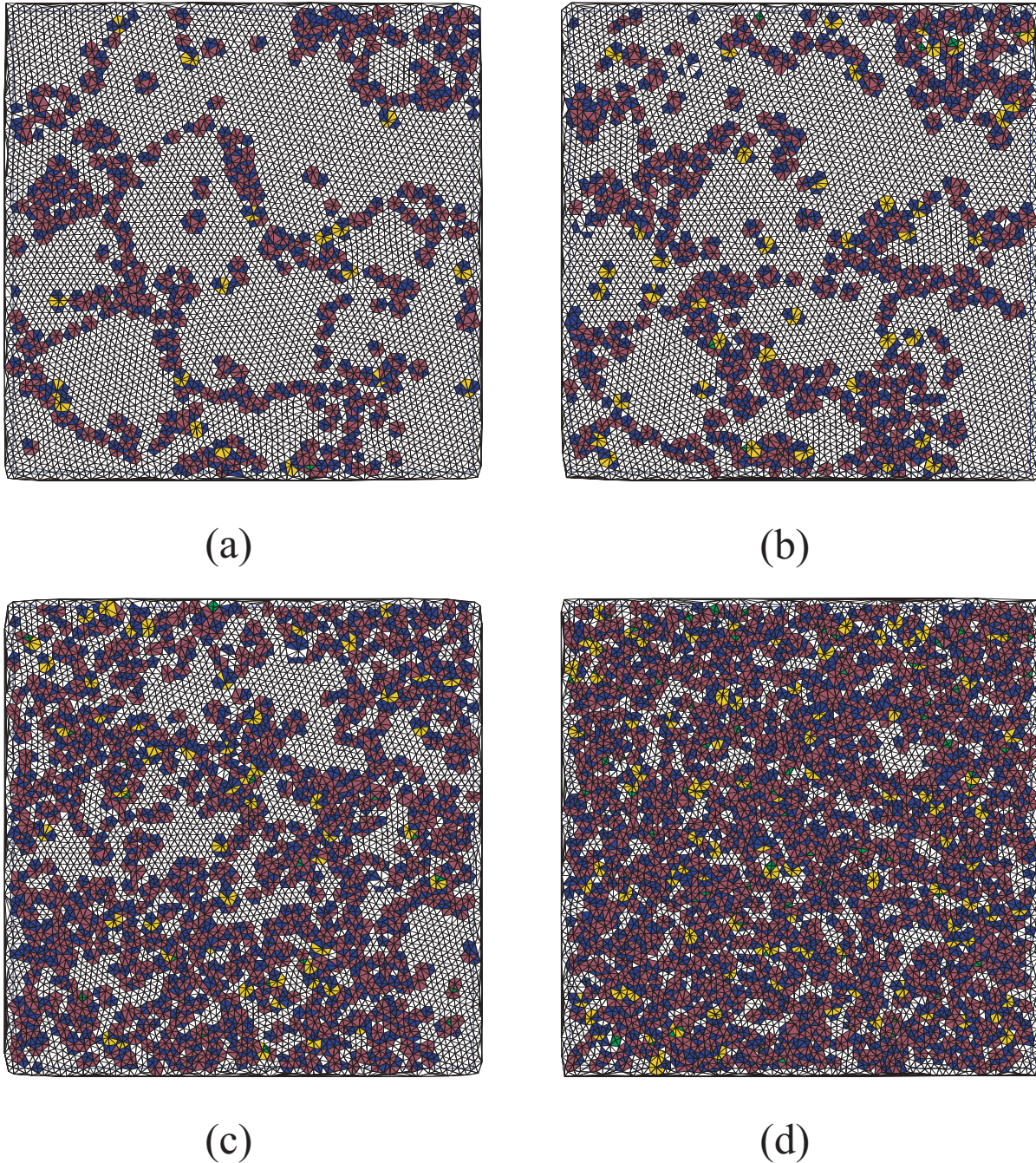
Figure 7-10 Delauney triangulations for layers (a): one, (b): two, (c): three, and (d): four at $N = 10.4$. Triangles surrounding six-fold coordinated particles only have been left uncolored, while colored cells indicate a deviating coordination number: green for 4-fold, blue for 5-fold, brown for 7-fold, and yellow for 8-fold coordinated particles.

Furthermore, it can be seen when comparing Figure 7-10b and 7-10c that the small crystal nuclei in the third layer are centered on top of the larger grains in the second layer, supporting the mechanism of epitaxial nucleation for layers two and further. Finally, for the fourth layer, typical liquid-like behavior is found, with rather few and small temporarily ordered regions.

7.3.4 Comparison to simulation results.

In the preceding paragraphs an analysis was presented on the nature of the crystallization transition in a system of sedimenting charge-stabilized colloids with relatively large Peclet numbers, i.e. for strong gravitational field strength as compared to thermal forces. At some points a brief comparison with the work of Biben et al. was already made, which we will do more extensively below. The system of Biben et al. consisted of hard-sphere particles at a flat wall at a constant areal density of 5.43 particles per squared hard-sphere diameter. These particles were subjected to an increasing gravitational field strength as expressed in the parameter $\alpha = mg\sigma/kT$, where m is the buoyant mass of the particles and σ is the hard-sphere diameter. A discontinuous jump was found to occur in both a layer-wise defined order parameter as well as the interlayer density for both the first and second layer when α was increased from 2.5 to 2.75. The order parameters for the third and fourth layer were, apart from a small jump for the third layer at $\alpha = 2.75$, found to increase continuously with α. The range of increase of their order parameter for layers one to four is summarized in Table 7-1.

One of the major differences between both systems is the use of hard-sphere particles versus the charge-stabilized silica particles used in this study. In order to quantitatively compare their results with ours, the mean-interparticle spacing in a crystalline layer was calculated both from the volume fraction after complete sedimentation ($\varphi = 0.31$, see Figure 7-5) as well as from the position of the first peak in the layer-wise $g(r)$ and this value was taken as an effective hard-sphere diameter. For a similar system consisting of the same number of sedimented hard-spheres a volume fraction at the bottom of the sediment was calculated of $\varphi_{HS} = 0.726$. With the volume fraction given above, this gives a measure of the softness of the interaction expressed as the actual particle radius over the effective hard-sphere radius of 1.33. For the hard-sphere diameter we now get $\sigma = 1.340 \, \mu m$ and equal crystal plane number densities for both studies. As the buoyant mass of the particles the actual particle buoyant mass in our experiments was taken, so that the softness of our interaction is treated by using an effective hard-sphere diameter with a lower particle density. This clearly means a great simplification of the physical situation, but it does provide us with a situation where the contribution to the osmotic pressure of a close packed layer at a certain α is similar in both studies. Thus the results for increasing α can now be mapped on our results with increasing N, by comparing the respective osmotic pressures. Note that the constant areal density of $5.43/\sigma^2$ corresponds to a sediment thickness of 4.7 close-packed layers. The values for the resulting osmotic pressures at the values of α listed in Table 7-1, are given there as well. In this study the crystallization transition in the first layer was found to occur at an osmotic pressure of $\Pi = 2.36 \cdot 10^{-2} \, N/m^2$ (see Table 7-1). This result is in remarkable good agreement with the values calculated on the basis of the results of Biben et al. Furthermore, the range in our experiment over which the bond orientational order parameter shows its rise, roughly from $N = 10.0$ to 11.2, gives an osmotic pressure difference of $\Delta\Pi = 0.30 \cdot 10^{-2} \, N/m^2$. The

difference in osmotic pressure between α_{start} and α_{end} for crystallization of the first layer in the simulations is $\Delta\Pi = 0.22 \cdot 10^{-2}$ N/m^2. Thus the steepness of the rise in order parameter is very well reproduced in our experiments as well. The nature of the phase transition reported in the work of Biben et al., namely a first-order discontinuous transition that occurs simultaneously in the first two layers, is also in correspondence with these experiment. For layers three and further Biben and co-workers observed a continuous growth of the sediment as a function of α. If we look at the values for Π at the start and end of the transition for these layers (see Table 7-1), it can be seen that these values are becoming increasingly more off with respect to our experimental values. In our experimental situation with the number of particles in the sediment increasing continuously, it can be expected that the difference in sediment thickness between the crystallization of further layers reaches a constant value of $\Delta N = 1$, corresponding to a value of the osmotic pressure that has to be reached for a liquid layer on an hexagonal substrate to crystallize. In fact, in Table 7-1 it can be seen that this situation is already almost reached at the fourth layer. Thus we get an osmotic pressure of $\Pi = 2.36 \cdot 10^{-2}$ N/m^2 at which a liquid layer of colloids crystallizes on a flat bottom wall, and a value of about $\Pi = 1.98 \cdot 10^{-2}$ N/m^2 for epitaxial crystallization on an hexagonally ordered layer of colloids.

The above values can be compared with the value for the pressure in a system of density-matched hard-spheres at liquid-solid coexistence. The reduced pressure at coexistence is $\Pi^{*} = 11.69 = \Pi \cdot \sigma^{3}/kT$. With the effective hard-sphere radius used above ($\sigma = 1.340$ μm), we get a value of $\Pi = 1.83 \cdot 10^{-2}$ N/m^2, which is in the same order of magnitude and about 20% smaller than the values reported above for a system with gravity. Furthermore, Heni and Löwen {{ref}} recently determined the pressures for prefreezing of a hard-sphere liquid at a hard wall carrying a hexagonal wall pattern. They reported a value of $\Pi^{*} = 8.53 \pm 0.12$, which gives $\Pi = 1.34(\pm 0.01) \cdot 10^{-2}$ N/m^2 for our system. This gives a reduction of ~73% compared to the bulk coexistence pressure, compared to a reduction of ~84% in our system in gravity. However, a major difference between the two results is here not only the presence of gravity and the softness of the spheres, but the character of the wall pattern (fixed spheres versus Brownian spheres) as well.

The mechanism of epitaxial crystallization for layers two and further was confirmed in the structural analysis. However, the question remains whether the epitaxial crystallization in these layers proceeds via discontinuous first-order transitions or continuously. As we have not calculated the densities in layers three and four as a function of sediment thickness (actually in order to do so the crystallization transition in these layers should be sampled more), a definite answer cannot be given. However, an indication about the nature of the transitions may be inferred from the behavior of the bond-orientational order parameter.

Above, the range of osmotic pressure over which the crystallization transition in the first layer takes place was found to be $\Delta\Pi = 0.30 \cdot 10^{-2}$ N/m^2. For layer 4 the range in sediment thickness is from $N = 11.2$ to about 12.75, which gives $\Delta\Pi = 0.39 \cdot 10^{-2}$ N/m^2. This suggests that the nature of the phase transition in $<|\psi_6|>$ does not change drastically, meaning that the growth of the sediment proceeds via layer-wise first-order transitions, however more data on the growth of the

sediment, preferentially by directly calculating the density or the relative ρ_z^{min} in the following layers, is needed. The indication mentioned above for discontinuous growth of the sediment is in contrast with the results of Biben. Furthermore, as mentioned above, there is also a discrepancy between the osmotic pressures for the crystallization of layers three and further which is remarkable in view of the good agreement of the results for the initial stage of crystallization. However, the system size in the direction perpendicular to the bottom wall is in the study of Biben et al. rather small, equivalent to only 4.7 crystal layers. Due to this fact the range of the transition region for the third and the fourth layer as expressed in $\Delta\Pi$, which as can be seen in Table 7-1 does not increase much from layer one to three, is smeared out considerably in α, as there are only few particles on top. In fact, at this point the analogy between two approaches fails: for a system like the lower layers with a sufficient amount of particles atop to well sample correlations between particles in the upper and lower parts, the increase of the osmotic pressure due to an increase in the number of particles, can be well replaced by an increase of α. However, at a low amount of particles on top, their mean-field contribution to the osmotic pressure fails to describe the physical situation with many particles higher in the sample. Here, the effect of increasing gravitational field strength cannot be mapped anymore to our experimental situation of sedimenting colloids. This is illustrated by the fact that for the top part of the sediment in the simulations of Biben, the situation at a further increase of α finally yields a 2D system. A more complete test of the effect of increasing gravitational field strength with respect to thermal motion can be achieved by performing experiments on samples with a constant number density of spheres, but with different sphere sizes. Another approach could be the use of another, more controllable, external field than gravity, e.g. radiation pressure[222].

7.3.5 Equilibration during growth and the role of softness

One of the crucial aspects of the process of crystallization during sedimentation is the interplay between the time-scales associated with both processes. Clearly, the conditions, i.e. the initial volume fraction, for sedimentation were chosen properly with respect to the nucleation kinetics, as our sediment did crystallize completely. However, this does not immediately imply that the sedimentation kinetics were sufficient for proper equilibration of the crystal structure. The crystalline end-state in each layer was polycrystalline with a typical lateral grain size of approximately 40 μm wide, which results from the nucleation and growth mechanism in each layer. Time-scales associated with the rearrangements necessary for a reduction of the polycrystallinity can be expected to be orders of magnitude larger than the timescales for nucleation and growth. In order to get some idea about the equilibration of the crystals in our sample, a structural analysis was performed and the same analysis was repeated starting from a twice lower volume fraction. For a more detailed analysis of the stacking sequence of crystals grown by colloidal sedimentation, we refer to another publication[231].

The structure of the columnar crystallites two months after starting the experiments was of fcc-type with a finite number of stacking faults of about 0.10 of the total number of layers in a crystallite. Redoing the sedimentation experiment at half the initial was found to give a reduction of the number of incorrectly stacked layers to 0.06. The polycrystallinity was not found to change observably. This indicates that the conditions that were used here were not sufficient to completely equilibrate our samples. We assume that longer equilibration will not change the character of the (first-order) phase transition as this is inherent in the nucleation- and growth-stage of the process, but a substantial increase of equilibration times, for instance by lowering the volume fraction by one or two orders of magnitude, might reduce the polycrystallinity. This will increase the range of correlations in the radial distribution function $g(r)$ and the bond-orientational order correlation function $g_6(r)$, which is necessary for determining the decay rate of these functions, and thus the occurrence of an intermediate hexatic phase. In this way for instance the occurrence of an intermediate hexatic phase can be determined which was now obscured by the finite crystallite size. To conclude, we assume that the simultaneous transition of crystallization in the first two layers is the equilibrium behavior, even although the stacking sequence is not.

A final point of discussion is the interaction potential between spheres in our system. The repulsive interaction between our spheres gives a final volume fraction of the crystalline end-state of $\varphi = 0.31$. For true hard-sphere particles this value would be 0.726 as calculated from osmotic and gravitational pressure at the bottom wall. However, the results of Biben et al. were, for as long as the mean-field approach in comparing the two systems holds, reproduced in very good agreement. Thus, despite the softness of the interactions, the nature of the phase transition and pressure at which the transition occurs are well reproduced assuming effective hard-sphere interactions. The softness can however be expected to play a large role in the kinetics of the transition. Recently, Gasser et al. reported real-space measurements probing colloidal nucleation in a system with a similar value for the crystal volume fraction[12]. The values for the nucleation rates they reported are several order of magnitude higher that the theoretically expected values[217], which gives a strong indication of the effect of the softness of the interaction on the nucleation kinetics. Thus, performing similar experiments with true hard-sphere like particles, for instance sterically stabilized colloids in apolar solvent or a system similar to ours but with salt added to screen the repulsive interaction, may require a considerably lower initial volume fraction.

7.4 Conclusions

A real-space analysis using confocal microscopy and fluorescent core-shell colloids was carried out on crystallization during particle sedimentation. Crystallization is preceded by layering of the liquid at the bottom of the sediment. Our model system consisted of 1μm-diameter, charged silica colloids, where the volume fraction in the crystal is on the order of

$\varphi = 0.31$, compared to a value of 0.726 that it would have in a hard-sphere system. The bottom-most liquid layer was found to undergo a first-order liquid-solid transition at a sediment thickness equivalent to 10.4 crystalline layers, which corresponds to an osmotic pressure of $\Pi = 2.36 \cdot 10^{-2}$ N/m^2. The phase transition in the first layer was found to give rise to an increase in the values of the order parameters for the second layer, which as a consequence crystallizes simultaneously at a local osmotic pressure of $\Pi = 2.13 \cdot 10^{-2}$ N/m^2. The simultaneous transition in the first two layers was found to be first-order, as indicated by a direct evaluation of the relative interlayer density and the overall density in these two layers. The behavior of the bond-orientational order parameter displays a similar transition for these layers as for the bottom layers, but further research is needed in order to determine whether these successive transitions in each layer are of first-order.

The crystallization process was found to proceed with the nucleation and subsequent growth of small crystallites, resulting in a polycrystalline end-state. This polycrystallinity causes a sign-inversion in the global bond-order correlation function beyond a typical crystallite size. As a consequence, the decay-rate of this correlation function could not give any insight in the possible occurrence of an intermediate hexatic phase between liquid and solid phases. However, if the hexatic phase occurs, the liquid-hexatic and hexatic-solid transitions are close.

In layers two and further the formation of small crystal nuclei was found to occur on top of already crystallized or crystallizing grains, corresponding to epitaxial crystallization. This gives rise to the lower osmotic pressure at crystallization compared to the first layer. The osmotic pressure for epitaxial nucleation could be inferred from fourth layer crystallization as $\Pi = 1.98 \cdot 10^{-2}$ N/m^2.

Our results on the nature of the phase transition in the first two layers of the sediment are in good agreement with computer simulations that examined the phase transition in a hard-sphere system under increasing gravitational field strength. For the subsequent growth of the sediment, the results contradict the simulations, probably because of a different number of layers in the simulations as compared to our experiment.

7.5 Acknowledgements

8

Stacking faults in colloidal crystals grown by sedimentation

A real-space study is presented on the occurrence of stacking faults in crystals of silica colloids with diameters of about 1 μm and 1.4 μm formed through sedimentation. The softness of the interaction potential is varied from slightly repulsive to hard-sphere like, both intrinsically by variation of the diameter, as well as through the addition of salt, which screens the surface charges. Our results indicate that the equilibrium crystal structure for these colloids is an fcc-crystal, with the number of stacking faults determined by the interplay between sedimentation and crystallization kinetics, irrespective of the softness of the interaction potential. For spheres with a certain diameter the number of stacking faults decreases with decreasing initial volume fractions. These results provide a way to grow fcc-crystals of hard-sphere particles by slow sedimentation. The relative number of stacking faults in the first few layers above the bottom wall can be as much as a factor of 10 higher than deeper into the crystal. This effect is due to the crystallization kinetics on a plain wall in a gravitational field. A patterned bottom wall that favors a specific hexagonal orientation was found to drastically reduce the number of stacking faults in the crystal.

8.1 Introduction

The ability of colloidal particles to self-assemble into a variety of crystalline phases lies at the heart of many materials-science studies, especially in the fields of photonics[70, 84, 88-91], catalysis[73], sensors[70] and lithography[74-76]. In these applications the colloids can either serve directly as the functional building block[70, 74-76, 84] or they form a template for making so-called inverse-opal structures[72, 73, 88-91]. For most applications, especially in the field of photonic materials, knowledge of and control over the formation of defects is crucial. Firstly, the uncontrolled formation of defects destroys most optical characteristics, for instance by broadening and doubling of Bragg peaks[205, 206]. Secondly, the controlled incorporation of defects may again be useful for instance by creating specific, localized defects modes. Considerable research has been devoted to the creation of such materials, but much less work focuses on the occurrence of defects. Recently, several papers discussed the influence of stacking faults, the most common type of defect in hard-sphere like colloidal crystals, on the photonic properties of colloidal inverse-opal materials[205, 206]. However, a detailed knowledge of the parameters that influence the formation of defects like stacking faults in colloidal materials is however still lacking.

More research has been devoted to the occurrence of stacking faults in the hard-sphere model system from a theoretical point of view. This is mostly due to the almost degenerate nature of different close-packed hard-sphere stacking sequences and the related question as to what is the stable crystal structure. The free energy differences between face-centered cubic (fcc), hexagonal close packed (hcp), and crystals exhibiting an arbitrary number of randomly distributed stacking faults, solely arise from entropic interactions. These free-energy differences have only recently been calculated using computational methods and are only on the order of 10^{-4} k_BT per sphere at the melting volume fraction, where k_B is Boltzmann's constant[194-199]. The fcc crystal is the most stable structure, but these differences are so small that stacking faults can easily occur. Furthermore, Pronk and Frenkel showed that when a finite crystallite size is taken into account a completely randomly stacked sequence (denoted as random hexagonal close packed (rhcp)) is found to be more stable for crystallites containing less than about 30000 particles[199]. This is an important consideration for experimental situations where often a polycrystalline state results or where the start of crystallization is examined. The subsequent relaxation from rhcp to fcc is estimated to be slow, on a time-scale of months to years for 200 nm-diameter particles, and is furthermore predicted to be dependent on the grain-size[199]. In recent computer simulations, the crystal nuclei in a supersaturated liquid were found to be of rhcp type[217].

Several experimental papers confirm this scenario. Zhu and co-workers found in space, thus without the influence of gravity, a pure rhcp stacking[200]. Most papers dealing with crystal nucleated on earth under conditions of bulk crystallization also report a strong tendency towards a random stacking[189, 201, 202, 204], however the actual number of stacking faults as

compared to the fcc structure can differ considerably upon method of preparation and the relaxation time after crystal nucleation[204].

Research on the structure of colloidal crystals has mostly been performed using light scattering[189, 204, 232] or other diffraction methods[233, 234]. With these techniques a well-averaged structure factor is obtained from which for instance the stacking sequence can only be obtained by performing an *overall* fitting procedure, despite the fact that the occurrence of faults may vary throughout the crystal[199, 205]. The recent rise of quantitative 3D microscopy methods in colloid science[6-8] has also led to papers in which the stacking sequence was probed directly in real-space[12, 201, 202]. Furthermore, Gu and co-workers used confocal microscopy to illustrate the quality of their dried crystals, but they did not present an analysis of defects or stacking faults in their crystals[118]. Clearly, the question of getting reasonable statistical accuracy in a real-space analysis is of importance compared to diffraction methods – see e.g. the large error margins reported in ref.[201] –, but it has the big advantage of determining the stacking sequence *in situ*. Furthermore, by making clever use of the information provided by specific crystal orientations, stacking-fault counting can be simplified considerably[202]. Complementary to the previously mentioned papers, we will in this chapter show the usefulness of real-space measurements by also probing the *location* of stacking faults. This will be done for a system of silica colloids that crystallized during sedimentation. Colloidal crystallization by sedimentation is one of the most commonly used techniques for making colloidal crystals for applications[72, 73, 88-91]. As such, the results presented here will be a first step towards a better understanding of and control over defect formation in photonic crystals. Moreover, several papers have claimed proofs for fcc crystallization of sedimented, charge-stabilized silica colloids and related these observations to hard-sphere behavior[235, 236]. Here, we will also address the role of the 'softness' of the interactions between the particles on the stacking sequence of colloidal crystals.

Crystallization during sedimentation is a situation much different from the zero-gravity or nearly zero-gravity systems mentioned previously. In fact, many of the 'deviations' reported in those papers –i.e. the occurrence of a higher stacking sequence than pure rhcp- have been ascribed to the presence of a gravitational field, e.g. through gravity-induced shear or hydrodynamic interactions during settling, be it that its magnitude was low[200, 204]. The magnitude of the gravitational field is usually described by the Peclet number, $Pe = \Delta \rho g R^4 (kT)^{-1}$, which expresses the gravitational energy relative to the thermal energy. For small Peclet numbers, typically $Pe = O(10^{-4})$ corresponding to colloids with a radius of about 100 nm, the variation of volume fraction in the region above the sediment, which is called the 'fan', is rather smooth. In this case, the growth of the sediment can be well described by conventional hard-sphere crystal growth from the supersaturated solution just above the sediment[221]. For larger spheres, for instance with a radius of about 500 nm, the Peclet number is two orders of magnitude higher. Thus, the one-dimensional (1D) gravitational force field has a much larger influence on crystallization. The influence of a strong 1D force field on crystallization has been only recently addressed[216, 237].

Apart from the presence and influence of gravity on the crystallization of sedimenting colloids, the presence of a substrate wall on which crystallization occurs also influences the behavior of the colloidal suspension prior to and during crystallization[63, 64, 103, 219, 237]. For crystallization at a patterned wall, the occurrence of the best quality crystal with respect to the amount of defects, is, due to the presence of gravity, determined by the prefreezing and/or wetting behavior of the liquid[172].

The conditions for obtaining a crystalline sediment for colloids at high Peclet-numbers are not immediately straightforward. At initial volume fractions commonly used for sedimentation experiments, $\varphi_0 \sim 10^{-1}$, of smaller, low Peclet-number particles, typically on the order of 10^{-1}, spheres with a radius higher than about 400 nm do not form a crystalline sediment anymore[221]. Though this gave rise to some remarks that it would not be possible to crystallize colloids in this size-range by sedimentation[193], but clearly this should be a matter of the balance between the particle flux due to sedimentation and the maximum growth velocity of the crystal. This balance can be tuned by slowing down sedimentation with an electric field like the authors of ref[193] did, but can also be tuned by adjusting the intrinsic parameters of the sedimentation process, like the initial volume fraction. There are indications from electron microscopy data that the amount of fcc stacking in crystals of sedimenting colloids can be rather high[235, 236]. It remains however unclear whether this is due to a softer interaction potential compared to hard-spheres due to repulsive interactions between surface charges that are not completely screened the presence of surface charges, or whether it is due to the crystal growth kinetics or to the presence of the gravitational force-field directed towards the hard bottom wall.

In this chapter we will investigate the occurrence of stacking faults in colloidal silica crystals grown under sedimentation. We will show that there is a finite number of stacking faults, but that the overall stacking parameter has a large tendency towards fcc. Furthermore, for a given particle size and interaction potential, the number of stacking faults decreases with decreasing initial volume fraction. This study is carried out using real-space measurements that allow for a direct determination of stacking faults, as well as their location. In the first few layers of the crystal over the bottom wall, we find an increased probability for stacking faults to occur, which also decreases on further reduction of the initial volume fraction. In addition to recent results showing the possibility to epitaxially grow any desired stacking sequence by using a template that directly dictates the stacking sequence, the occurrence of stacking faults is also shown to be influenced by a wall pattern that favors a specific hexagonal orientation of crystal planes.

8.2 Experimental details

Silica colloids that contained a fluorescently labeled core and a non-fluorescent shell were prepared using methods reported in the literature[149, 154]. Particles with an outer radius of 499 nm as measured by Transmission Electron Microscopy (TEM) contained a 50 nm-radius core that was labeled with rhodamine isothiocyanate (RITC)[150]. The polydispersity, defined as the

relative width of the size distribution, of these particles was 0.033. Particles with an outer radius of 692 nm, measured with TEM, contained a 96 nm-radius core labeled with fluorescein isothiocyanate (FITC). The polydispersity of these particles was 0.015.

For both batches, the particles were dispersed in a refractive-index matching mixture of demineralized water and glycerol (Baker, z.A grade) in a volume ratio of 1 : 7.18. In some of the experiments with the 692 nm-radius particles, N,N-dimethylformamide (DMF, Merck) and a refractive index matching mixture of 3:7 (volume ratio) DMF and dimethylsulfoxide (DMSO, Merck) were used. In order to screen interactions lithiumchloride (Merck) salt was added. Below we will explicitly mention which results have been retrieved with DMF, DMF-DMSO, and mixtures with salt added. For all other experiments, the water-glycerol mixture without added salt was used.

For the 499 nm-radius colloids, the bottom of the sedimentation container consisted of a 22 mm-diameter Chance no.1 coverslip, which had been immersed in chromosulfuric acid (Merck) for 20 minutes and rinsed with demineralized water and ethanol (Merck, absolute grade) before being coated with a layer of poly(methylmethacrylate) (PMMA) to prevent particle adhesion. PMMA (950k, 4wt% in chlorobenzene, MicroChem Corp.) was spin-coated at 1000 rpm for 30 seconds and subsequently baked for 1 hour at 170°C. This results in a layer thickness of approximately 450 nm. A bottomless flask with an internal diameter of 9.65 mm was glued to the PMMA-coated coverslip using Silicon Rubber Adhesive RTV 102 (General Electric). The sedimentation container was rinsed several times with the water/glycerol mixture before filling it with a low-volume fraction suspension of colloids. For the 692 nm-radius spheres the sedimentation container was similar, except that parts of the PMMA bottom wall had been patterned with an hcp(1100)-template using electron-beam lithography[172].

The 499 nm-radius particles were dispersed at two different volume fractions, $\varphi_0 = 0.004$ and $\varphi_0 = 0.002$. The 692 nm-radius particles were sedimented from a $\varphi_0 = 0.005$ suspension (see Table 8-1). The Peclet-numbers, $Pe = \Delta\rho g R^4 (kT)^{-1}$, for these two sizes are respectively 0.13 for the 499 nm-radius colloids and 0.5 for the 692 nm-radius colloids. Note that the water-glycerol mixture that was used has a rather high viscosity ($\sim 10^2$ mPa·s, so the time-scale of settling is scaled up considerably, but this does not affect the interplay between crystallization and sedimentation as both the settling speed as well as Brownian diffusion, and thus the rate of crystallization, are inversely proportional to the viscosity.

In order to quantify the softness of the interaction potential, the effective hard-sphere diameter, d_{HS}, in the bottom part of the sediment was determined. This value was determined from the interparticle spacing as calculated from confocal microscopy data (see below), which was then multiplied by the volume fraction, relative to 0.74, that a hard-sphere system with the same initial volume fraction, Peclet number, and overall sample volume would have, using the fact that the osmotic pressure at the bottom of the sample balances the gravitational pressure. This value for d_{HS} was compared to the diameter, d, of the particles. The ratio d_{HS}/d for each of our samples is also indicated in Table 8-1. The dependence of hard-sphere volume fraction on the distance from the bottom wall was determined as well, as described in [207]. At the maximum
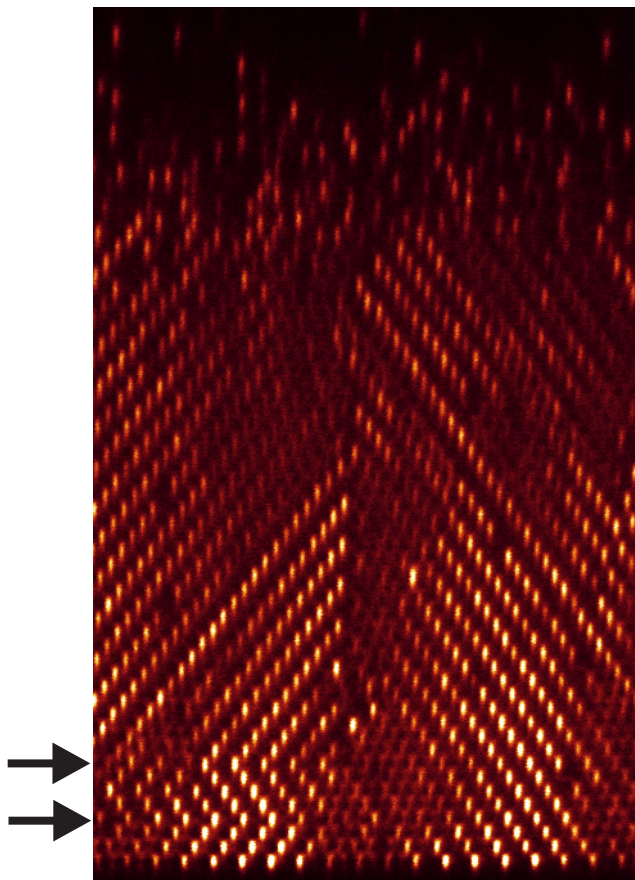
Figure 8-1 Confocal image of a (110)-plane in two adjacent grains in a sedimented crystal. The optical axis of the microscope runs in the vertical direction. The elongated shape of particle images results from the different form of the points spread function parallel and perpendicular to the optical axis. The arrows indicate two stacking faults in the left grain. At the top of the image the fluid like tail of the colloidal sediment profile is visible. The change in focus for different particles results from a small tilt of the sample with respect to the optical axis.

depth in the crystal that was used to determine the stacking sequence, the volume fraction was always almost similar to the volume fraction at the bottom, i.e. higher than 0.70.

Samples were analyzed using fluorescence confocal microscopy (Leica TCS SP2) two months after homogenization of the dispersion. The samples were scanned in *xy*- and *xz*-mode, i.e. parallel and perpendicular to the bottom wall of the container respectively (the *z*-direction is along the optical axis, while the *x*-and *y*-directions are the lateral coordinates parallel to the bottom wall). Crystallization of hard-sphere like colloids at a wall yields crystals that are oriented with their densest plane, an hexagonally packed layer, parallel to the wall. The stacking sequence of close-packed layers on top of each other can be easily probed by evaluation of particles positions in the (1100)-plane[8, 202], perpendicular to the bottom wall. In fact, by using a template for crystal growth that carries a pattern of holes with similar symmetry as the (1100)-positions in crystal with a specific stacking sequence, a crystal with this hard-sphere stacking sequence can be grown[172]. In the Leica TCS SP2-system the scan field can be rotated. In this

way the *xz*-scan can be chosen to coincide with the (1100)-plane (see Figure 8-1), which allows for an easy and fast way to probe crystal stacking. The elongated appearance of particles in Figure 8-1 results from the decreased resolution along the optical axis of the microscope. The use of core-shell particles makes it however possible to clearly distinguish separate particles. Note that the fact that two adjacent crystal grains are displaying their (1100)-plane in the same projection is purely coincidental.

The stacking sequence of hexagonal layers is usually denoted with the letters *A*, *B*, and *C*. If the positions in a specific layer are denoted by *B* then there are two sets of possible positions for both the layer above and the layer below, which are the *A*- and *C*-positions. Given the positions of the layer below as *A*, the layer atop can either have the same lateral coordinates, resulting in an *ABA*- or hexagonal close packed (hcp)-type stacking, or it can occupy the third set of coordinates *C*, which results in an *ABC*- or face centered cubic (fcc)-stacking. To each layer *i* in the crystal a value $\sigma_i = \{0,1\}$ can now be assigned depending on its environment. If the stacking is fcc-type $\sigma_i = 1$ and if it is hcp-type $\sigma_i = 0$. For a crystal consisting of *N* layers, this results in *N*-2 different σ_i (for the bottom and top layer σ_i is not defined), and the overall stacking parameter α of the crystal can be calculated by averaging σ_i. In the (1100)-plane an ABA-stacking is visible as a kink (indicated by the arrows in Figure 8-1), so that determination of the stacking sequence comes down to counting the number of layers in the crystal as well as the number of kinks, κ. The stacking parameter α of a crystal grain is thus given by[202]:

$$\alpha = \frac{1}{N-2}\sum_{i=2}^{N-1}\sigma_i = 1 - \frac{\kappa}{N-2} \qquad (8.1)$$

For the two crystal grains displayed in Figure 8-1, this gives $\alpha = 1$ and $\alpha = 0.95$ for the right and left crystal respectively. The overall stacking parameter of a sample is calculated as the total average $<\alpha>$ over the (1100)-images taken of one sample. This averaging was performed with the value of α for each stack calculated over the same number of layers, $N = 22$.

8.3 Sedimentation and crystallization

A description of a sedimentation process usually divides the liquid with sedimenting colloids into four regimes: a clear liquid on top, a part where colloids are freely settling at the initial volume fraction φ_0, the so-called 'fan' in which there is a gradient in particle concentration from the initial volume fraction to the volume fraction at which particles accumulate at the bottom, the sediment[1] (see also Figure 7-1 and section 7.2.2). The sedimentation velocity in the free settling regime is given by $U(\varphi_0) = U_0 \cdot K(\varphi_0)$, where U_0 is the sedimentation velocity at infinite dilution and $K(\varphi)$ is a volume-fraction dependent correction factor that takes into account the hindered motion at higher volume fractions. A good approximation of $K(\varphi)$ for hard-spheres is given by $K(\varphi) = (1-\varphi)^{6.6}$.

In the sediment the volume fraction is about 0.60 or higher (either in a compressed crystalline sediment or in an glassy sediment) and its structure can, depending on the kinetics of sedimentation versus crystallization, be crystalline or amorphous. In the fan above the sediment, the sedimentation velocity is dependent on the local volume fraction φ as given by $K(\varphi)$. The volume fraction at the bottom of the fan is equal to or higher than the melting volume fraction. The flux of particles into the sediment is independent of the initial volume fraction and is just given by the melting volume fraction times the corresponding sedimentation velocity. The sediment will crystallize as long as this flux equals the flux of particles into the crystal. The criterion for obtaining a crystallized sediment is that the sedimentation velocity at the bottom of the fan should be smaller than the maximum crystal growth velocity. As under similar conditions the sedimentation velocity is proportional to R^2, while the crystal growth velocity goes as R^{-2}, there is a maximum sphere radius above which the sediment does not crystallize anymore. This scenario was confirmed by Davis and co-workers who found that for initial volume fractions on the order of 10^{-1}, colloids with a radius of 0.430 μm formed an amorphous sediment[221].

This scenario holds as long as the particle flux from the free settling regime into the fan is higher than the maximum possible flux $\varphi \cdot U(\varphi)$ for some value of φ between φ_0 and the volume fraction of the sediment. In other words, when on the flux-curve ($\varphi \cdot U(\varphi)$ vs. φ) the line connecting the starting point on the flux-curve (i.e. corresponding to the initial volume fraction) and the volume fraction of the sediment crosses the flux-curve. For hard-spheres this holds for initial volume fractions larger than about 0.02[1]. For smaller initial volume fractions the process is limited by the particle flux at the initial volume fraction. As the volume fraction at which the colloids crystallize is constant, the process can be described by the maximum rate of crystallization ($\sim kT/R^2$), the initial rate of sedimentation ($\sim \Delta\rho gR^2$) and the initial volume fraction φ_0. A proper parameter for characterizing the system is then $kT/(\varphi_0\Delta\rho gR^4) = 1/(\varphi_0 \cdot Pe)$, assuming $K(\varphi_0) \approx 1$. This value is given in Table 8-1 for the different systems we have investigated.

8.4 Results and discussion

8.4.1 Overall stacking parameters

In Table 8-1 values for the overall stacking parameter, $<\alpha>$, for the three systems with different $(\varphi_0 Pe)^{-1}$ are given. As can be seen the values of $<\alpha>$ are rather high, > 0.80 for all three samples, indicating a strong preference for an fcc stacking. These high stacking parameters are in strong contrast with results for hard-spheres in zero-gravity or under conditions of effective micro-gravity, where an almost pure rhcp-stacking ($<\alpha> \rightarrow 0.5$) is found. Furthermore it can be seen that the amount of stacking faults decreases with increasing $(\varphi_0 Pe)^{-1}$, from about 0.20 at $(\varphi_0 Pe)^{-1} = 400$ to 0.06 at $(\varphi_0 Pe)^{-1} = 5000$. This indicates that the presence of stacking faults is to a

Table 8-1 Stacking parameters for the four different systems investigated in this study[*]

R (nm)	d_{HS}/d	φ_0	Pe	$(\varphi_0 Pe)^{-1}$	$<\alpha>$	$<\alpha>_{L>4}$
499	1.322	0.004	0.13	$2.5 \cdot 10^3$	0.90 ± 0.13	0.95 ± 0.05
499	1.322	0.002	0.13	$5.0 \cdot 10^3$	0.94 ± 0.07	0.97 ± 0.02
692	1.027	0.005	0.50	$0.4 \cdot 10^3$	0.78 ± 0.11	0.81 ± 0.08
692[†]	1.027	0.005	0.50	$0.4 \cdot 10^3$	0.91 ± 0.07	0.91 ± 0.06

[*]R is the sphere radius, d_{HS}/d is a measure for the softness of the interaction potential and gives the effective hard-sphere diameter over particle diameter, φ_0 the initial volume fraction, Pe stands for the Peclet number, and $<\alpha>$ and $<\alpha>_{L>4}$ are the overall stacking parameter and the stacking parameter averaged over layers five and higher (counted from the bottom wall) respectively.

[†]Particles sedimented on a patterned wall that favors a specific hexagonal orientation.

large amount influenced by the kinetics of the sedimentation process and that by further decreasing of the initial volume fraction, thus increasing the equilibration time for the growing crystal, the resulting structure will be fcc.

The reason for the high amount of fcc-stacking maybe three-fold: Firstly, the presence of surface charges might give deviations from hard-sphere behavior. Secondly, the growth mechanism or the kinetics of the growth process might lead to a preference for fcc stacking. Thirdly, the presence of a one-dimensional force field, i.e. gravity, possibly in combination with the presence of the bottom wall could favor the fcc stacking. These three possibilities will be discussed one by one.

I. Repulsive versus hard-sphere interactions
Our silica particles are charge-stabilized with a steep, but not ideal hard-sphere, repulsion. This may change the behavior from that of hard-spheres and might give a tendency towards fcc, as fcc has been found to be the stable structure for colloids with long-ranged repulsive interactions at high volume fractions[54, 210]. The softness of the interaction could explain the lower value of $<\alpha>$ for the 692 nm-radius particles, as for these larger particles the range of repulsion as expressed in d_{HS}/d (see Table 8-1), is shorter. For a system with a softness of interactions in between our values, Gasser and et al. reported rhcp crystallization in a nearly density-matched system[12]. In their work, they examined the structure of nucleating crystals, which will clearly be in the size range for which Pronk and Frenkel predicted rhcp to be the stable structure[199]. However, also measurements performed by Verhaegh et al. indicate an appreciable amount of stacking faults, higher than the values reported here, for a system of charged colloids[201]. Furthermore, the differences in the distribution of neighboring particles between fcc and hcp are very small and occur only at interparticle distances larger than $3.27 \cdot R_{eff}$. Thus short-ranged and smoothly varying potentials may be expected to give only a minor energy difference between the two structures. In fact, recent free-energy calculations indicate that the free-energy differences between hcp and fcc remain almost constant when increasing the softness of the interparticle potential[238]. This would mean that the origin of fcc-crystallization of long-

ranged repulsive particles would be due to another reason than the contribution to the free-energy of a soft potential. In order to take a closer look at the effects of charge on the crystallization of sedimented silica colloids, some additional measurements with the 692 nm-radius particles were carried out. These results will be presented below, where we will come back to this point.

II. Growth mechanism and growth kinetics.

A second reason for the high amount of fcc stacking in our crystals compared to hard-spheres in micro-gravity may be the growth mechanism of the crystal nuclei. For the Lennard-Jones system, where differences between hcp and fcc are also negligibly small[239] but an fcc crystal structure is usually observed in simulations, growth mechanisms were suggested to explain fcc crystallization, for instance through an initial crossed stacking-fault that uniquely promotes fcc-growth[240]. As mentioned previously, at the Peclet-numbers examined in this research, the growth mechanism of crystals may be different from bulk crystallization. However, crystallization under sedimentation for similar silica colloids was recently shown to proceed via the growth of hexagonally stacked layers, with crystallization in a new layer starting with the formation of nuclei on top of already crystallized (111)-grains[237]. As an fcc-promoting growth mechanism would have to occur through either a non-degenerate crystal plane, or via self-repeating defects or surface steps, the growth mechanism can well be ruled out as the reason for the preference for fcc-stacking observed here. In fact, the growth mechanism in our system, which proceeds through stacking of (111)-planes, would seem the perfect growth mechanism for generating a heavily faulted crystal structure.

For this growth mechanism, the kinetics of growth however still play an important role, as was shown in the results given above. In bulk homogeneous crystallization the crystal growth rate is determined by the supersaturation. In fact, Pusey et al. already noted that the stacking parameter increased at lower supersaturation and thus lower rates of crystal growth[189]. In our system, the rate of crystal growth is uniquely determined by the initial volume fraction before sedimentation. By slowing down the sedimentation flux, each crystal layer has more time to equilibrate, thus reducing the amount of crystal layers that get trapped in a metastable state, i.e. a stacking-fault.

III. The gravitational field and the bottom wall.

A third reason could be the influence of the one-dimensional asymmetry in the system, in the presence of the gravitational force field and the bottom wall, on the equilibrium crystal structure. As the particles used in this study have Peclet-numbers that are considerably larger than in previous studies, this could explain the increased tendency towards fcc. The influence of a one-dimensional force field on the equilibrium structure of hard-spheres has not yet been investigated. Mau and Huse recently determined the strength of the entropic interactions between next-nearest close packed planes and further and found these differences to be very small[198]. This situation could however be different in the presence of a force field directed perpendicular to these close packed planes. Similarly, the surface free energy between a hard-sphere crystal and a hard wall was recently calculated[108], but the influence of a hard wall on the structure of a hard-sphere crystal has, to our knowledge, also not been addressed yet.

8.4.2 A closer look at surface charge screening

For the 692 nm-radius particles, additional measurements were carried out using both DMF and a refractive-index matching mixture of DMF and DMSO as a solvent, at high initial volume fractions of $\varphi_0 = 0.052$ and $\varphi_0 = 0.026$. To both these solvents, small amounts of salt were added (order 1mM), which changes the amount of screening of particle surface charges and thus changes the interaction towards more hard-sphere like. From these additional experiments three important observations were made:

1. At a volume fraction of $\varphi_0 = 0.052$, only the sample without any salt added crystallized. In a sample with 2 mM of salt added, after sedimentation only small crystallites appeared on the bottom, which extended only a few layers in the sample. The rest of the sample had a glass-like, disordered appearance. At a volume fraction of $\varphi_0 = 0.026$ ($1/(\varphi_0 \cdot Pe) \approx 80$, so one order of magnitude lower than in table 1) all samples, with added salt concentrations ranging from 1 mM to 30 mM showed crystallization. From the interparticle distance at the bottom of the sediment after complete sedimentation, we found values for d_{HS}/d of $d_{HS}/d = 1.029$ in the samples with salt, compared to $d_{HS}/d = 1.140$ for the sample without salt.

2. We did not find any changes in the stacking parameter outside the error margins for all of these samples. The overall stacking parameter was $\langle\alpha\rangle = 0.67\pm0.10$. Note that this is again substantially lower than the value of 0.78 in Table 8-1 for an order of magnitude higher value of $1/(\varphi_0 \cdot Pe)$.

3. The samples with salt added were all polycrystalline with a typical grain size of about 40 µm wide (similar to the water/glycerol-dispersed samples in Table 8-1). The samples without any salt added on the other hand showed crystallites with lateral sizes up to 500 µm.

The lower stacking parameter in all of these samples confirms the trend in Table 8-1. The result for $\varphi_0 = 0.052$ shows that there is indeed an upper limit to the volume fraction needed to yield crystallization in the sediment at all. The increase in the range of the repulsion of the sample without salt lowers the sedimentation speed and affects the growth rate through the diffusion coefficient, which is enough to shift this limiting φ_0 above $\varphi_0 = 0.052$. However, the influence on the kinetics of the process is not enough to increase the stacking parameter, at least not within the error margins. It does however influence the average domain size, which increases by an order of magnitude. Further research is needed, both theoretically as well as experimentally to study the effects of the softness of the interaction potential by slowly changing the interaction potential from hard-sphere like to short-ranged and finally long-ranged repulsive. This should be performed first without the presence of gravity, but as mentioned before, the additional influence of the gravitational field and the presence of a hard bottom wall need to be investigated as well. Experimentally this could be done for small spheres at density matching or at low Peclet number

during sedimentation like in the work of Davis, Russel and Glantschnig[221], in a set-up where it is possible to work with an ion-exchanged sample with the possibility to carefully control the amount of deionization[241]. The influence of the gravitational field can then be tested by comparing results on high Peclet-number samples.

8.4.3 Location of stacking faults

For the samples given in Table 8-1 a layer-wise averaging of α was carried out in order to probe a possible change in the number of stacking faults as a function of height in the sample. In Figure 8-2 $<\alpha>_L$ is shown for the two samples with 499 nm-radius particles for the first 22 layers in the crystal. Note that the data starts at layer 2, as the stacking parameter is not defined for the first layer in the sample. As can be seen $<\alpha>_L$ is for both samples remarkably lower in the second and third layer compared to higher in the sample. For layers four and higher the layer-wise averaged stacking parameter is constant within the error-margins.

The origin of the higher probability for the occurrence of stacking faults in the first three layers of a sedimented crystal may be kinetic. Previously, it became already evident that the kinetics of the sedimentation process influences the number of stacking faults in the crystals. Recently, we carried out a detailed analysis of the crystallization process at the wall during sedimentation, where it was found that the net osmotic pressure at which the first layer above the bottom wall crystallizes is higher than that for successive layers[237]. This effect leads to a decreased equilibration time for the first few layers in the sediment compared to layers higher in the sample. The relaxation time for each layer finally becomes a constant, fixed by the initial volume fraction and the sedimentation speed, and equal to the amount of time needed to add a number of particles to the sediment equal to the number of particles in one layer. The layer at which this happens is dependant on the difference in osmotic pressure at which the first and next layers crystallize. Our results indicated that this steady state was almost reached at crystallization of the fourth layer[237], in correspondence with the results in Figure 8-2. Furthermore, the fact that the number of stacking faults in layer two and three decreases when the initial volume fraction decreases, supports the notion that the effect has a kinetic origin and again stresses the importance of equilibration for the final crystal structure.

This effect is of importance for the use of sedimented colloidal crystals for photonic applications. For instance, thin crystals are sufficient to have a large bandgap[242], but if conditions for colloidal crystal growth are then chosen such that there is an increased probability for stacking faults in the first few layers, this will have a strong effect on the photonic band structure. After the first four layers, the value for $<\alpha>_L$ seems to converge to a constant value for both two samples. The 'converging' value of the stacking parameter for the bulk of the crystal was calculated by averaging over layers five and higher. These results are given in the last column of Table 8-1. It should be noted that in view of the error margins on both values for $<\alpha>_{L>4}$, we can not exclude the possibility that the difference in stacking parameter for both
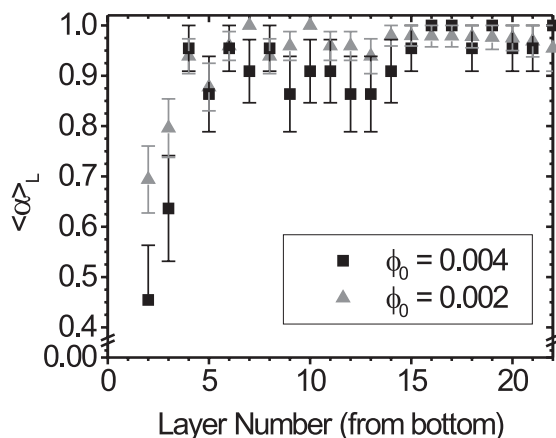
Figure 8-2 Layer-averaged stacking parameter as a function of layer number from the bottom plane of the sample for a system of 1-μm diameter silica colloids sedimented from volume fractions of 0.004 and 0.002.

volume fractions could be solely due to this bottom-layers effect. The difference between these samples and the 692 nm-radius samples would then be due to the difference in 'hardness' of the interaction potential. However, the additional measurements for the 692 nm-radius particles also show an increase in stacking parameter upon decreasing initial volume fraction, while the bottom-layers effect can be expected to be smaller at these higher Peclet-numbers (also compare Figure 8-2 and Figure 8-3).

8.4.4 Influence of a bottom wall pattern

Finally, we want to illustrate how the interaction between the bottom wall and the crystallizing colloids influences the crystallization process and thus the stacking sequence as well. To this end, the stacking parameter was determined for the system of 692 nm-radius particles over a plain wall as well as over an hcp(1100)-patterned wall that was stretched in one direction. This pattern serves as a template for crystallization, lowering in the ideal case the surface free energy for a specific crystal orientation that then nucleates. At this specific template crystallization occurs in hexagonally stacked layers oriented parallel to the bottom wall, just like on the unpatterned wall. However, the orientation of the crystal over the template was found to be uniform for larger crystallites (lateral sizes > 150 μm) and only smaller crystallites (lateral sizes < 150 μm) had a different orientation. At the plain wall crystallites had a typical lateral size of ~ 40 μm, without any apparent (i.e. by visual inspection) correlations in orientation. The measurements at the plain (untemplated) wall and the templated wall were performed in the same sample cell, so all further conditions are exactly similar.

In Table 8-1 the stacking parameter for the templated crystal is indicated as well. Furthermore, in Figure 8-3 the layer-wise averaged stacking parameters are given for both templated and untemplated bottom wall. As can be seen, the overall stacking parameter on the templated wall is increased considerably with almost 20%. Furthermore, the increased probability for stacking faults to occur in the first few layers is also reduced with respect to the untemplated crystal. As there was such a clear distinction between smaller and larger crystallites, the stacking parameter over the templated wall was also analyzed as a function of grain-size. No stacking-faults were observed in the larger, template-oriented crystals, which were 6 crystallites out of a total of 67.
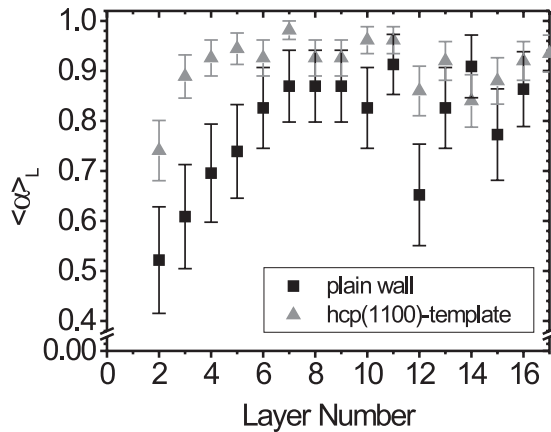
Figure 8-3 (a) Layer-averaged stacking parameter for a system of 1.4-μm diameter silica colloids sedimented at a plain wall (black squares) and at a mismatch hcp(1100)-template, that gives rise to a fcc(111)-surface alignment. (b) Stacking parameter as a function of grain-size for defect grains inside the otherwise monocrystalline fcc(111)-crystal at the mismatch template.

For the smaller grains no correlation between crystallite size and the number of stacking faults was observed. More statistics is however needed to analyze the dependence of the stacking parameter on the crystal size, which is interesting in view of the stability of the rhcp structure for small crystals shown by Pronk and Frenkel[199].

The comparison between crystals that crystallized at a plain wall and those that crystallized at a templated wall indicates that the interaction between the wall and the crystallizing suspension is of importance to the crystal quality as well. The effect of the bottom wall on the crystal structure plays a role through the surface free energy, so a change of $<\alpha>$ higher up in the crystal is not expected. In that respect the values for $<\alpha>_{L>4}$ in the last column of Table 8-1 can also be expected to be the 'true' representation of the bulk stacking sequence. It would however still be interesting to test whether the favorable interaction of a template might be able to direct crystallization close to the wall to stacking-fault free fcc with the hexagonal fcc(111)-plane aligned parallel to the surface. This template might even be a simple hexagonal patterned template as used by Heni and Löwen[63] in a recent simulation study of wetting and prefreezing in a hard-sphere system.

8.5 Conclusions

A real-space analysis was performed on the crystal structure of sedimented silica colloids with Peclet-numbers on the order of 10^{-1}. The softness of the interaction potential was furthermore varied from ratios between interparticle spacing and hard-sphere diameter of $d_{HS}/d = 1.027$ to $d_{HS}/d = 1.322$. These crystals showed a remarkably high amount of fcc stacking compared to bulk crystallization of hard-sphere particles. The tendency towards fcc may have two origins. It can be caused by the reduced crystal growth velocities compared to bulk homogeneous crystallization, which gives the growing crystal more time for equilibration, or it can be caused by the presence of the gravitational force field and the bottom wall of the sedimentation container, which may favor fcc crystal structure. The amount of stacking faults is being reduced by changing the kinetics of sedimentation and crystallization through the initial volume fraction. The softness of

the interactions is reflected in larger crystalline domain sizes, but does not seem to influence the stacking parameter. Furthermore, the range of the interaction influences the kinetics of sedimentation and crystallization, which is reflected in the possibility to crystallize particles from a higher initial volume fraction than for more hard-sphere like particles. Our results indicate that by slow sedimentation it is possible to grow fcc crystals of hard-sphere particles.

It was also shown that even under conditions where the stacking parameter towards the bulk of the crystal approaches values as high as 0.97, there is a remarkably higher probability for stacking faults to occur in the first four layers on top of the bottom wall. This decreased stacking parameter in the first few layers is also, at least partly, of kinetic origin and results from the different mechanism of crystallization, i.e. on a plain wall for the first layer and on top of an hexagonally packed lattice for layers two and further.

The importance of the free energy of the crystal layers at the bottom wall surface was shown by comparing the stacking sequence of silica particles sedimented on a plain wall with that on a template that favors a specific hexagonal orientation as reflected in larger domain sizes of oriented crystallites. Under similar conditions the overall stacking parameter is improved considerably towards fcc, from 0.78 ± 0.11 to 0.91 ± 0.07. There are indications that, at this template, the smaller crystallites (with lateral size < 150 μm) have a lower stacking parameter, but more statistics is needed to further investigate the size-dependence of the stacking sequence of colloidal crystals.

These results are important for people using sedimentation as a means to grow colloidal crystals for applications like photonic materials, as control over and decreasing of the amount of stacking faults is crucial for these applications. Our results also indicate the need for more extensive investigations, both theoretically as well as experimentally on heterogeneous crystal growth, both in the presence of gravity as well as without the gravitational field. This knowledge is needed in order to understand and predict the phase behavior of colloids, but is furthermore crucial for the application and engineering of colloidal materials.

8.6 Acknowledgements

9

Summary

In this chapter an overview of the work described in the previous chapters will be given. **Chapter 1** gives a general introduction to the subject of this thesis: the real-space analysis of colloidal epitaxy. Colloidal particles are macroscopic particles with a size ranging from several nanometers to a few micrometers, that, due to their Brownian motion, can explore phase space in thermodynamic equivalence with atoms and molecules. This, together with the fact that colloidal systems are easily accessible from an experimental point of view, e.g. by light microscopy, makes colloids an important model system for the study of phenomena like crystallization. The technique of confocal microscopy together with the use of a model system that consists of fluorescently labeled colloids with a core-shell morphology, allows for a three-dimensional (3D) analysis of particles in a suspension.

Apart from the theoretical interest in the colloidal model system, colloids are also an important building block for applications in many diverse areas of research. For most of these applications either the functionality of the application or its production process relies on the ability of colloids to self-assembly. In colloidal epitaxy a patterned substrate surface, or template, is used to direct colloidal self-assembly. This technique can on the other hand also serve as a model system for studying the influence of boundaries and substrate potentials on (epitaxial) crystal growth. In this research we have explored the technique of colloidal epitaxy, both concerning its use as a model system in the study of epitaxial crystallization, as well as its use in manipulating colloidal crystallization.

The lithographic techniques that we have used for patterning substrates for colloidal epitaxy are described in **Chapter 2**. With electron-beam lithography templates can be created by direct writing of a pattern in a poly(methylmethacrylate) (PMMA) layer. In Chapter 2 examples are shown of templates consisting of regular arrays of holes in the PMMA-layer, with lattice distances varying from about 100 nm to a few micrometer. The subsequent transfer of these patterns to solid substrates like glass, quartz or silicon using wet etching or plasma etching is demonstrated as well. These solid substrates can, among other things, be used as a master for soft-lithography. In soft-lithography an elastomeric mold is created with which the original pattern can be easily and in a comparably cheap way replicated. The use of soft-lithography in making polyurethane relief structures is demonstrated in Chapter 2. Furthermore, we show the chemical patterning of glass substrates using an elastomeric mold and a sol-gel mixture that contains a silane-coupling agent.

Apart from lithographic techniques, a method was devised for positioning colloidal particles on surfaces in any designed pattern. This method is described in **Chapter 3**. These colloid-patterned substrates can be used in various applications, but can also serve as a template in colloidal epitaxy, complementary to the lithographically made templates that were described in Chapter 2. In this technique optical tweezers are used to bring particles from a reservoir to the substrate where opposite surface charges immobilize particles on the surface. Both chemical surface modification and polyelectrolyte coating of either substrate or colloids make the method generally applicable. We demonstrate that using this technique large, two-dimensional patterns can be created that can be dried without distortions by critical point drying. As an example we

demonstrate the positioning of particles with a diameter ranging from 80 nm to 700 nm. The application of these 2D patterns in 3D epitaxial crystal growth is demonstrated as well.

In **Chapter 4** epitaxial growth of colloids that interact via a hard-sphere like potential is described. We have found that it is possible to grow metastable hard-sphere hcp and 'double hcp' (dhcp) crystals by using a surface pattern that directly dictates the stacking sequence. A detailed 3D analysis based on real-space measurements was performed on crystal structure as a function of template-crystal mismatch. Perfect template-induced hcp-crystal growth was found to occur at an isotropically deformed template, which is a strong indication for prefreezing at the template. At stretched and compressed lattices we observed growth of a non-close-packed superstructure and of a perfectly layered and (100)-aligned fcc crystal. Small mismatches led to increased out-of-plane displacements followed by a structural breakup in 'crystal' grains where particle positions in successive layers are strictly periodic and 'defect' grains where these positions are displaced with respect to each other. At an anisotropically stretched surface pattern, increasing the hexagonal c/a-ratio, these displacements as well as the mutual orientation of these grains were directed perpendicular to the stretched direction.

Apart from the study of colloidal epitaxy in a system with hard-sphere like interaction, the use of colloidal epitaxy in a model system with long-ranged repulsive interaction was examined as well. In this system the role of gravity was eliminated from the epitaxial growth process by density matching colloids and solvent and using a set-up in which the resulting small gravitational field is directed away from the template.

In **Chapter 5** we describe how a simple 1D pattern of repulsive, charged lines was found to direct 3D crystallization in this system. At volume fractions where the bulk phase behavior led to bcc crystallization, the 1D template was found to induce formation of a metastable fcc crystal. At lower volume fractions and different line spacing, bcc crystals were oriented with the (100)- or the (110)-plane, with two-fold twinning, parallel to the template. The template further induced prefreezing of the (100)-plane. At a large mismatch between template and interparticle spacing, 1D strings formed in the surface layer of a 3D crystal.

The research described in Chapters 4 and 5 mostly focused on the study of colloidal epitaxy under equilibrium conditions, which is important for a fundamental understanding of (colloidal) crystallization and for the use of colloidal epitaxy as a model system for molecular epitaxy. The ability to create crystal structures that are metastable in bulk crystallization is however also a promising development for the use of colloidal crystals in applications. Many techniques to make (functional) colloidal assemblies rely on particle ordering directly during the evaporation of the solvent liquid, so called controlled drying techniques.

In **Chapter 6** the use of templates in directing colloidal crystallization in controlled drying techniques is examined. Template-induced colloidal crystallization is demonstrated in a tilted-horizontal setup of the templated substrate for crystals that are both a few layers as well as more than 100 layers thick. Furthermore, at templates that possessed a mismatch with respect to the colloidal dimensions, a reconstruction in surface orientation of the crystal took place. The strain relaxation phenomena observed on these mismatched templates are similar to those observed in

epitaxial crystal growth in suspension during slow sedimentation. For vertical controlled drying, where in general there is more control over crystal thickness and uniformity, template-induced growth was examined for silica colloids ranging in diameter from about 100 nm to over 1 μm. Our results indicate that the ability to form a templated crystal is crucially dependant on the surface topography of the template. For a square symmetric fcc(100)-template, 2D crystal growth was only observed on a pillar-shaped template.

In the last two chapters in this thesis, crystallization of colloids that are subjected to a relatively large gravitational field (i.e. large Peclet numbers) on a flat bottom wall is investigated. Where crystallization of colloids without gravity or in a weak gravitational field has often been examined, the role of the gravitational field has so far hardly been addressed. Apart from this fundamental interest, the study of colloidal crystallization in such a system at a flat wall also provides a first step towards an understanding of crystallization at a patterned wall, like for instance for the system studied in Chapter 4.

In **Chapter 7** a real-space study on the crystallization process in a system of sedimenting colloids is presented. During sedimentation a gradient in particle concentration develops at the bottom of the sample container. The presence of the lower boundary wall induces layering in the liquid and, upon increasing sediment thickness, crystallization occurs in these liquid layers. Crystallization in the first layer was found to proceed via a first-order transition. The formation of small crystalline nuclei in this layer, induced epitaxial crystal growth in the second layer on top of these crystallites, which resulted in both layers undergoing the phase transition simultaneously. The critical osmotic pressure for crystallization at a plain wall, as well as for epitaxial crystallization on an already crystallized layer, was determined. The nucleation-and-growth mechanism leads to a poly-crystalline end-state. Due to this polycrystallinity we could not determine whether the crystallization process involved an intermediate 'hexatic-like' phase. Our results regarding the nature of the transition in the first two layers are in agreement with recent computer simulations.

Finally, the structure of colloidal crystals formed by sedimentation was examined, focusing especially on the occurrence of stacking faults. The results that are presented in **Chapter 8**, indicate that the equilibrium crystal structure for these colloids is an fcc-crystal, with the number of stacking faults determined by the interplay between sedimentation and crystallization kinetics, irrespective of the softness of the interaction potential. The number of stacking faults was found to decrease with decreasing initial volume fraction. These results thus provide a way to grow fcc-crystals of hard-sphere particles by slow sedimentation. There is an increased probability for stacking faults to occur in the first few layers above the bottom wall, which is due to the crystallization kinetics on a plain wall in a gravitational field. A patterned bottom wall that favored a specific hexagonal orientation was found to drastically reduce the number of stacking faults in the crystal.

Samenvatting

Deze samenvatting is een Nederlandstalige bewerking van de samenvatting in hoofdstuk 9 en bevat een overzicht van het werk beschreven in hoofdstuk 1 tot en met 8.

Hoofdstuk 1 geeft een algemene introductie op het onderwerp van dit proefschrift: de analyse van colloïdale epitaxie in de reële ruimte (i.e. door middel van microscopie). Colloïdale deeltjes zijn macroscopische deeltjes met een grootte variërend van enkele nanometers (één-miljoenste millimeter) tot een paar micrometer (één-duizendste millimeter). De belangrijkste eigenschap van colloïden is hun zogenaamde Brownse beweging. Door deze Brownse beweging kan een colloïdaal systeem in principe alle microtoestanden in de fase-ruimte doorlopen, thermodynamisch gezien op identieke wijze als atomen en moleculen. Dit, samen met het feit dat colloïdale systemen makkelijk toegankelijk zijn vanuit een experimenteel gezichtspunt, bijvoorbeeld met behulp van licht microscopie, maakt dat colloïden een belangrijk model systeem zijn voor het bestuderen van verschijnselen als kristallisatie. De techniek van de confocale microscopie, samen met het gebruik van een modelsysteem van fluorescent gemerkte colloïden met een kern-schil morfologie, maakt het mogelijk om de drie-dimensionale (3D) coördinaten van de deeltjes in een oplossing te bepalen.

Naast het theoretische belang van colloïdale modelsystemen, vormen colloïden ook belangrijke bouwstenen voor toepassingen in verscheidene takken van de wetenschap. Voor de meeste van deze toepassingen is het feit dat colloïden geordende structuren kunnen vormen van wezenlijk belang voor hetzij de functionaliteit van de toepassing dan wel voor het productieproces. In de afgelopen jaren is dan ook een aanzienlijke hoeveelheid onderzoek gedaan naar mogelijkheden om het ordeningsgedrag van colloïden te controleren of zelfs te beïnvloeden. In de techniek van colloïdale epitaxie wordt een substraat met daarop een regelmatige patroon, een template, gebruikt om colloïdale kristallisatie te beïnvloeden. Zoals beschreven in dit proefschrift geeft ons dit niet alleen een manier om colloïdale kristallisatie te manipuleren, maar vormt colloïdale epitaxie ook een modelsysteem voor de studie naar de invloed van grensvlakken en oppervlakte-potentialen op (epitaxiale) kristalgroei.

Allereerst zijn in **Hoofdstuk 2** de lithografische methoden beschreven die we gebruikt hebben om oppervlaktes van een regelmatig patroon te voorzien zodat deze gebruikt kunnen worden in colloïdale epitaxie. Met elektronenbundel-lithografie kunnen templates worden gemaakt die bestaan uit een regelmatige structuur van cilindervormige gaten in een laag van poly(methylmethacrylaat) (PMMA). De roosterafstanden van de structuren kunnen we variëren van zo'n honderd nanometer tot een paar micrometer. Zulke PMMA-structuren zijn gebruikt in de experimenten beschreven in de Hoofdstukken 4 en 5. In Hoofdstuk 2 wordt eveneens getoond hoe deze patronen vervolgens kunnen worden overgebracht in 'vaste' substraten als glas, kwarts of silicium. Dit gebeurt door het PMMA patroon als masker te gebruiken bij een of meer volgende etsstappen, bijvoorbeeld met een zuur of met een reactief plasma. Deze 'vaste' substraten kunnen worden gebruikt in experimenten waarbij de colloïdale oplossing gecontroleerd gedroogd wordt, zoals beschreven in Hoofdstuk 6. Ze kunnen echter ook gebruikt

worden als origineel in zogenaamde zachte lithografie. Hierin wordt een rubberachtig negatief gemaakt waarmee het originele patroon simpel en relatief goedkoop kan worden vermenigvuldigd. In Hoofdstuk 2 wordt getoond hoe met behulp van zachte lithografie replica structuren in polyurethaan kunnen worden gemaakt. Daarnaast laten wij zien hoe zo'n rubberachtig negatief samen met een reactiemengsel dat een koppelingsproduct voor glas bevat, kan worden gebruikt om een chemische oppervlakte structuur, dus zonder reliëf, te maken.

Naast deze lithografische technieken hebben wij ook een methode ontwikkeld waarmee het mogelijk is om colloïden rechtstreeks op een oppervlak te positioneren. Deze methode wordt beschreven in **Hoofdstuk 3**. De op deze manier van een structuur van colloïden voorziene substraten kunnen worden gebruikt voor verscheidene toepassingen. Daarnaast kunnen ze echter ook worden gebruikt als een template voor colloïdale epitaxie, in aanvulling op de templates gemaakt met lithografische methoden die beschreven zijn in Hoofdstuk 2. In deze techniek wordt een optisch pincet gebruikt om deeltjes vanuit een reservoir naar een oppervlak te brengen. Op dit oppervlak worden de deeltjes vast gezet door tegengestelde oppervlakteladingen van deeltjes en substraat. Deze tegengestelde ladingen kunnen worden verkregen door een chemische behandeling van het oppervlak van de deeltjes dan wel van het substraat, maar ook door één van beide oppervlakken te coaten met een polyelectroliet. Deze beide coating procedures maken dat deze methode voor een grote verscheidenheid aan deeltjes en substraten te gebruiken is. In Hoofdstuk 3 wordt getoond hoe met deze methode grote 2D patronen van colloïden kunnen worden gemaakt. Deze patronen kunnen worden gedroogd door gebruik te maken van kritisch-punt drogen. In kritisch-punt drogen wordt het oplosmiddel eerst boven het kritisch punt gebracht, waar er geen onderscheid en dus ook geen grensvlak meer is tussen vloeistof en gas. De verstoringen van het patroon die op zouden treden ten gevolge van de oppervlaktespanning van het vloeistof-gas grensvlak, kunnen op deze manier vermeden worden. Als voorbeeld wordt het positioneren van deeltjes met een straal variërend van 80 tot 700 nanometer getoond. Ook de toepassing van deze 2D patronen als template in 3D epitaxiale groei wordt getoond.

In **Hoofdstuk 4** wordt de epitaxiale groei onderzocht van colloïden met een onderlinge wisselwerking zoals die tussen harde bollen. In dit hoofdstuk laten wij zien hoe met colloïdale epitaxie hcp en 'dubbel'-hcp (dhcp) kristalstructuren kunnen worden gegroeid. Deze kristallen zijn voor harde bollen zonder oppervlaktepatroon metastabiel. Het gebruikte template legt rechtstreeks de stapelingsvolgorde van de dichtstgepakte lagen in een harde-bollen kristal op. Een gedetailleerde 3D analyse is uitgevoerd gebaseerd op metingen met een confocale microscoop. Hierbij is de kristal structuur geëvalueerd als functie van de mismatch tussen het template en het kristal. Deze analyse laat duidelijk zien welke de mogelijkheden zijn van colloïdale epitaxie als modelsysteem voor de studie van de effecten van een wandpatroon op de structuur van het nabijgelegen kristal. De beste kristalkwaliteit van het hcp kristal werd aangetroffen bij een ten opzichte van het kristal dat groeit op een vlakke wand isotroop uitgerekt template. Dit is een sterke indicatie dat de colloïdale oplossing in ons systeem aan het wandpatroon bevriest bij een lagere druk dan dat het zou doen in de bulk van een oplossing. Verder werd ontdekt dat bepaalde uitgerekte en ingekrompen template roosters aanleiding geven tot de groei van een niet-dichtst

gepakt 'superkristal' en van een perfect gelaagd fcc kristal met het (100)-vlak uitgelijnd langs het template. Een kleine mismatch tussen template en kristal afmetingen leidde tot verplaatsingen van deeltjes uit hun kristalvlak, gevolgd door een scheiding in de structuur in 'kristal'-gebieden en 'defect'-gebieden. In de 'kristal'-gebieden zijn de posities van deeltjes in opeenvolgende lagen periodiek, terwijl deze posities in de 'defect'-gebieden verplaatst zijn ten opzichte van elkaar. Op een anisotroop uitgerekt template waren deze verplaatsingen, net als de onderlinge oriëntatie van deze gebieden, uitgelijnd in de richting loodrecht op de richting van uitrekken.

Naast de studie van colloïdale epitaxie in een systeem met een harde-bollen wisselwerking, werd ook het gebruik van colloïdale epitaxie onderzocht in systemen met interacties die over lange afstand repulsief zijn. In deze systemen werd de invloed van de zwaartekracht geminimaliseerd door de dichtheid van het oplosmiddel nagenoeg gelijk te maken aan die van de colloïden en vervolgens een opstelling te gebruiken waarin het resulterende kleine zwaartekrachtsveld van het template af werd gericht.

In **Hoofdstuk 5** is beschreven hoe een simpel 1D patroon van repulsieve, geladen lijnen de 3D kristalgroei in dit systeem beïnvloedt. Bij dichtheden waar in de bulk van de oplossing kristallen met een bcc symmetrie groeien, leidde het 1D template tot de groei van kristallen met een metastabiele fcc structuur. Bij lagere dichtheden en andere afstanden tussen de lijnen van het template werden bcc kristallen georiënteerd met hun (100)-vlak of, met tweevoudige twinning, hun (110)-vlak parallel aan het template. Verder werd ontdekt dat het template leidde tot de vorming van enkele kristallagen aan de wand als de colloïden in bulk van de oplossing nog in de vloeistoffase zijn. Bij een relatief grote mismatch van template en interdeeltjes afstanden, vormden zich 1D lijnen van deeltjes in de oppervlaktelaag van een 3D kristal.

Het onderzoek dat beschreven is in de Hoofdstukken 4 en 5 concentreerde zich grotendeels op de studie van colloïdale epitaxie onder condities van evenwicht. Naast het fundamentele belang van deze resultaten voor het begrijpen van colloïdal kristallisatie en de invloed van grensvlakken en randvoorwaarden daarop, is de daar beschreven mogelijkheid om kristalstructuren te maken die metastabiel zijn in kristallisatie in de bulk van een oplossing een veelbelovende ontwikkeling voor het gebruik van colloïdale kristallen in toepassingen. De kristalstructuren zoals die beschreven in Hoofdstuk 4 en 5 zouden bijvoorbeeld na polymerisatie uit de oplossing gehaald kunnen worden. Veel technieken om (functionele) colloïdale structuren te maken, gebruiken echter de ordening van deeltjes tijdens de verdamping van het oplosmiddel. Deze technieken worden aangeduid als 'gecontroleerd drogen'.

In **Hoofdstuk 6** wordt het gebruik van templates voor het manipuleren van colloïdale kristallisatie tijdens gecontroleerd drogen onderzocht. In een opstelling waar het template licht gekanteld is ten opzichte van een horizontale positie, was het mogelijk om kristalgroei te beïnvloeden. De dikte van deze kristallen varieerde van ongeveer vijf lagen tot meer dan honderd lagen. In kristallen gedroogd op templates met een mismatch ten opzichte van de afmetingen van het kristal kwamen dezelfde reconstructie- en relaxatie mechanismen voor als bij epitaxiale kristalgroei in een oplossing na langzame sedimentatie. Voor gecontroleerd drogen met een verticale opstelling van het substraat, waarbij er in het algemeen meer controle is over dikte en

uniformiteit van het kristal, is template-geïnduceerde kristalgroei onderzocht voor colloïden met een diameter van ongeveer 100 nm tot meer dan 1 μm. Onze resulaten laten zien dat de mogelijkheid om de kristalstructuur in deze methode met templates te beïnvloeden, afhangt van de oppervlakte topografie van het template. Voor een vierkant-symmetrisch fcc(100)-template vormde zich alleen op een template dat bestond uit pilaren in plaats van gaten, een vierkant-symmetrische colloïdale monolaag.

In de laatste twee hoofdstukken van dit proefschrift, wordt kristallisatie op een vlakke wand beschreven. Zoals ook het geval was bij de experimenten beschreven in Hoofdstuk 4, heeft in dit geval de zwaartekracht een relatief (ten opzichte van de thermische of Brownse krachten) grote invloed op de colloïden. Naast het fundamentele belang van het onderzoek naar de invloed van de zwaartekracht op colloïdale kristallisatie, vormt dit onderzoek ook een eerste stap naar het begrijpen van kristallisatie op een gestructureerde wand onder condities zoals in Hoofdstuk 4.

De resultaten van de studie naar de kristallisatie van sedimenterende colloïden worden beschreven in **Hoofdstuk 7**. Tijdens sedimentatie ontwikkelt zich een gradient in deeltjesconcentratie op de bodem van het systeem. Hier vormen zich lagen in de vloeistof parallel aan de wand. Bij toenemende dikte van het sediment, vindt kristallisatie in deze lagen plaats. Kristallisatie in de eerste laag ging gepaard met een sprong in de dichtheid onder in het systeem. Dit duidt op een eerste-orde fase-overgang. Dit resultaat is in overeenstemming met onlangs gepresenteerde computersimulaties en theoretische berekeningen. De vorming van kleine kristallijne nucleï in de onderste laag, leidde tot epitaxiale kristalgroei in de tweede laag bovenop deze nucleï. Als gevolg hiervan doorliepen beide lagen de fase-overgang simultaan. De kritische osmotische druk die benodigd is voor kristallisatie op een vlakke wand en die voor kristallisatie op een reeds gekristalliseerde laag werden bepaald. Het nucleatie- en groei-mechanisme waarmee het sediment kristalliseerde leidde tot een poly-kristallijne eindtoestand. Door deze polykristallijniteit kon er niet bepaald worden of de vloeistof-vast overgang verloopt via een tussenliggende hexatische fase.

Tenslotte is de structuur van de door sedimentatie gevormde kristallen bepaald. De resultaten hiervan worden gepresenteerd in **Hoofdstuk 8**. Deze laten zien dat de evenwichtsstructuur van aldus gegroeide kristallen een fcc kristal is. Het aantal foutief gestapelde lagen werd bepaald door de verhouding van sedimentatie en kristallisatie kinetiek, ongeacht de zachtheid van de colloïdale wisselwerking. Voor deeltjes van één bepaalde straal daalde het aantal foutief gestapelde lagen met afnemende initiële volume fractie. Op deze manier kan er dus een puur fcc kristal gegroeid worden door langzame sedimentatie. Verder was er een verhoogde kans op stapelingsfouten in de eerste vier lagen boven de bodem: Bij vaste initiële volume fractie was het aantal maal dat de tweede laag foutief gestapeld was tien keer hoger dan voor lagen dieper in het kristal. Dit effect is toe te schrijven aan de kinetiek van kristallisatie op een vlakke wand beschreven in Hoofdstuk 7. Een wand die een template bevatte, waarbij het template één bepaalde hexagonale oriëntatie van de lagen induceerde, bleek het aantal stapelingsfouten te verkleinen.

Dankwoord

Een groot aantal mensen heeft in meer of mindere mate een bijdrage geleverd aan de totstandkoming van dit proefschrift. In de eerste plaats is dat, uiteraard, mijn promotor geweest. Alfons, ik wil jou bij deze hartelijk danken voor het feit dat je mij als eerste oio in je 'groep' hebt aangenomen. In de afgelopen jaren heb ik met erg veel plezier gewerkt aan dit onderzoek. Het noemen van veel geboden vrijheid in het doen van onderzoek mag dan vaak een eufemisme voor weinig leiding en bemoeienis zijn, bij jou is dat zeker niet het geval geweest. Zelden heb ik iemand meegemaakt die zo snel zo veel informatie kan opnemen en kan overzien, maar waar dat zou kunnen leiden tot een eenzijdige invulling van het onderzoek, heb jij altijd veel mogelijkheden tot eigen invulling en planning gegeven. Ook toen de resultaten op zich lieten wachten, is er, naar mijn idee, altijd veel vertrouwen in de goede afloop geweest. Dat heb ik zeer gewaardeerd. Daarnaast wil ik je niet in de laatste plaats bedanken voor je rol als (illegale) woningverhuurder en het, gelukkig mislukte, 'samenwonen' met Yvonne (jaja, daar kunnen we wel even grappen over blijven maken!). En zo gaan we naadloos van de een op de ander over.

Maar al te vaak komt vriend of vriendin in een dankwoord als laatste aan bod, hoe onterecht zou dat in dit geval zijn! Yvonne, jouw input in de totstandkoming van dit boekje is vele malen groter dan je zelf waarschijnlijk denkt. Ik mag hopen dat er nog veel van zulke goede (maar wellicht iets rustiger) jaren zullen volgen.

Tijdens mijn periode als oio heb ik mogen zien hoe onze 'groep' steeds verder uitgroeide tot een echte GROEP. Henk Lekkerkerker wil ik bedanken voor het feit dat hij mijn promotor heeft willen zijn voordat Alfons zelf hoogleraar werd. Dat jij, ondanks je erg drukke werkzaamheden nog tijd vond voor en altijd interesse toonde in mijn onderzoek waardeer ik zeer. Met de mensen die in de eerste jaren de groep zijn komen versterken heb ik lange tijd erg plezierig samengewerkt. Hen wil ik dan ook met name bedanken. Krassimir, ik zou kunnen zeggen 'for joining the team' en misschien zegt dat ook wel genoeg. Dirk, als 'ons' hoofdstuk 3 een aantal pagina's had naar ratio van het plezier waarmee ik er aan gewerkt heb, dan had ik de drukkosten van dit boekje waarschijnlijk niet meer op kunnen brengen. En dan hebben we het nog niet eens over de vele discussies en gesprekken daaromheen. Anand, waarschijnlijk de wetenschapper met de grootste dosis nieuwsgierigheid en geduld, om jaloers op te worden! Carlos, de ongekroonde koning van de colloid-synthese, die de tijd nam om al mijn basis-vragen over de chemie te beantwoorden, wat uiteindelijk leidde tot de synthese van de pot van 400.000.000 (inmiddels de pot van 181.512.910, maar dat bekt toch een stuk minder). Tenslotte Astrid, tja, die laser onder de tafel was misschien niet echt praktisch, maar het gepuzzel om met een spiegel de levensduur af te lezen had toch ook zijn charme. Bedankt!

Daarnaast hebben de studenten die ik heb mogen begeleiden bij stage- of afstudeeronderzoek, een wezenlijke bijdrage tot enkele hoofdstukken in dit boekje geleverd. Als eerste Didi, die tegen een aantal experimentele tegenslagen opliep, maar ondertussen monter en (vooral) vrolijk door bleef werken, wat resulteerde in een aantal metingen beschreven in hoofdstuk 8. Daarna Peter, die het voorbereidende werk van Didi voor hoofdstuk 7 gestaag heeft uitgebouwd en daarna met

163

veel ijver en intellect in korte tijd heel veel vruchten heeft weten te plukken. Karin, nog zo'n studente die met ontzettende vrolijkheid haar werk aanpakte. Het zijn hier maar een paar regeltjes in hoofdstuk 3 geworden, maar de uitbouw daarvoor komt ongetwijfeld in Dirks proefschrift verder aan bod. Tenslotte Erik, die de moeilijke taak had te werken voor iemand die op een gegeven moment vol aan het proefschrift schrijven ging. Desondanks is het gelukt met minutieus werk de verwacht lage succesfactor van de controlled drying opstelling behoorlijk omhoog te krijgen, zodat het schrijven van hoofdstuk 6 bijna een never-ending story leek. Alle vier van harte bedankt!

In mijn eerste jaar als oio heb ik vier dagen in de week op het Van 't Hoff lab gewerkt. Het Van't Hoff lab was een erg prettige werkomgeving, waarvoor ik iedereen die daar in die tijd werkte en met name Gerard, Felix, Els, Gerrit, Karen, Gijsje, Willem, Tjerk, Carel en Bonny, wil bedanken. Daarnaast wil ik Jan Dhont en Gert-Jan Vroege nog apart noemen omdat ik veel heb geleerd van het onderwijs dat ik met hen mocht geven (hoewel dat bij dat eerste University-College jaar niet van het niveau van de studenten kwam.....). Tot slot wil ik Diana Maas bedanken voor het met Carlos samen geduldig bijspijkeren van mijn chemische vaardigheden.

Dit onderzoek zou niet mogelijk zijn geweest zonder het lithographie werk dat met Anja van Langen-Suurling en Hans Romijn op DIMES is verricht. Anja, bedankt voor het vele werk, de geduldige uitleg en de lunchgesprekken. Hans, bedankt voor de uitleg, de c-programmaatjes, en de nieuwe ideeën om templates te maken. Verder wil ik Arnold van Run bedanken voor de assistentie tijdens Anja's zwangerschapsverlof. Het laatste jaar is het lithographie-werk met name verricht door Maurice van den Boer en Chris Rétif, die ik daarvoor ook van harte wil bedanken.

Na de Van 't Hoff periode kwam ik eindelijk wat meer tijd doorbrengen op mijn feitelijke werkplek, AMOLF. Een stimulerender werkomgeving is nauwelijks denkbaar (zeker niet met de Overloop). In ons cluster is dat met name de verdienste van Daan Frenkel, Bela Mulder en Marileen Dogterom. Iedereen in hun groepen wil ik dan ook bedanken voor de fijne werksfeer. Een aantal mensen wil ik met name noemen. Marcel Janson voor de vele gesprekken over onderzoek, alles daaromheen en voor het delen van de eerste-oio-ervaring. Stefan Auer voor de vele discussies en de prettige en nuttige samenwerking tussen 'experimentator' en 'simulator'. Hetzelfde geldt voor Sander Pronk. Een belangrijk deel van het succes van AMOLF rust op het ondersteunend personeel. Zonder de rest van de organisatie tekort te doen, wil ik Wim Barsingerhorn (voor de glasbewerkingen), Iliya Cerjak (de eindeloze reeks posters), Hans Zeijlemaker (AFM-metingen) bedanken. Ook iedereen uit de groep van Albert Polman wil ik, hoewel mijn project niet direct binnen die samenwerking viel, danken voor de vele discussies en samenwerking, met name Christof, Teun en Michiel.

En aan het eind was er dan de 'van Blaaderen-groep' op het Ornsteinlab. Naast al eerde genoemde mensen hebben ook Christina-Tina, Christina-Chrissy, Alan, Job, Arnout, Alexander, Paddy, Patrick, Antti-Pekka, en Marjolein middels discussies en gesprekken hun bijdrage tot dit werk geleverd. Marjolein wil ik nog extra bedanken voor de buitengewoon grondige wijze waarop zij de eerste versie van dit proefschrift doorgelezen heeft.

Veel werkplekken zijn aan bod gekomen, alle kamergenoten wil ik nog extra bedanken voor de zeer verschillende, maar altijd plezierige atmosfeer: (in order of appearance) Alfons, Marileen, Hans, Marcel, Martin, Steven, Felix, Krassi, Dirk, Jacob (jaja, daar kunnen we wel even grappen over blijven maken!), Chinmay, Wen-Bing, Nicolas, Antti-Pekka, Chrissy.

Twee pagina's wetenschappelijke dank. Misschien is dat nog iets dat ik op Alfons' conto moet schrijven: het zien van mogelijkheden tot en inspireren van samenwerking. Ondertussen zou je bijna gaan denken dat er geen leven naast de wetenschap is geweest. Dat is gelukkig geenszins het geval geweest en een aantal personen wil ik hier niet onvernoemd laten. Allereerst Astrid, nogmaals bedankt voor het tijdelijk in huis nemen van een dakloze promovendus. Dat ik ook nog lopend naar mijn werk kon was een prettige bijkomstigheid, die dode muis was wat minder. Mike en Nynke wil bedanken voor de bijzonder hechte vriendschap die we ondertussen hebben opgebouwd en waarvan ik hoop dat die nog lang stand houdt. Van mijn overige vrienden wil ook Bart en Martien nog noemen, van wie beide ik vind dat ze een bewonderingswaardig doorzettingsvermogen hebben.

Veel plezier en ontspanning heb ik beleefd aan unihockey. Iedereen die sinds de oprichting mee is komen spelen in Utrecht wil ik dan ook bedanken voor de geboden spelvreugde. Dank gaat ook uit naar mijn mede-NeFUB-bestuursleden van het eerste uur, van wie ik met name Hans apart wil noemen voor zijn inzet en de vele gesprekken over unihockey, en Rudi, wiens drive je alleen kunt begrijpen als je hem espresso uit koffiemokken ziet drinken. Erik wil ik danken voor het overnemen van de voorzittershamer. Met veel plezier heb ik ook getraind met de selectie voor Finland, een bijzondere ervaring om zo'n spirit mee te maken. Erg veel heb ik geleerd van Mats en Marius, zowel bij de trainingen als in het spel, als bij het altijd gezellige naborrelen na training (overigens zal zelden iemand zo verbaasd zijn geweest over het bestaan van het fenomeen naborrelen en het zich vervolgens zo eigen hebben gemaakt als laatstgenoemde).

Tot slot wil ik mijn familie, als ook mijn (als Martien het zou zeggen) 'pseudo-schoon'familie bedanken voor hun continue ondersteuning. Voor mijn peettante hoop ik van harte dat dit boekje wat goed kan maken van het tekort aan bezoeken en brieven van het afgelopen jaar.

Tot slot nog een:

Ondanks-woord

Dit proefschrift is tot stand gekomen, ondanks:
- Dr. Watson (wat een compleet nutteloze vent).
- 'Wat is het toch een gore boel op de badkamer', 'Het is hier zo ontzettend smerig', 'Als volgende week mijn moeder komt......' (en dat voor iemand die op een campusflat heeft gewoond!)
- Boxman (ja Mike, reuze bedankt! Level 15 heeft niet alleen mijn productiviteit tijdelijk verlaagd maar ook die van een substantieel deel van de amolf-bevolking...)
- Clausthal 1998 (had alles in zich om een buitengewoon geslaagd toernooi te worden....)

Over de auteur

Ten tijde van het hier beschreven onderzoek was Jacob Hoogenboom (Nijmegen, 01-12-1972) als promovendus (onderzoeker in opleiding) verbonden aan het Instituut voor Atoom- en Molecuulfysica van de Stichting Fundamenteel Onderzoek der Materie (FOM) te Amsterdam en aan de vakgroep Zacht Gecondenseerde Materie van de Universiteit Utrecht. Daarnaast werden in het kader van dit onderzoek werkzaamheden verricht op het Van't Hoff Laboratorium (vakgroep Fysische en Colloid Chemie) van de Universiteit Utrecht en bij het Delft Instituut voor Micro-electronica en Submicron Technologie (DIMES) van de Technische Universiteit Delft. Resultaten uit dit onderzoek werden door de schrijver gepresenteerd op de volgende conferenties:

- 10th IACIS Conference on Colloid and Interface Science, Bristol (2000)
- FOM bijeenkomst Gecondenseerde Materie, Veldhoven (2000)
- FOM bijeenkomst Statistische Fysica, Lunteren (2001)
- International Conference on Crystal Growth (ICCG) 13, Kyoto (Japan) (2001)
- CW bijeenkomst Vloeistoffen en Grensvlakken, Lunteren (2002)

en tijdens postersessies op diverse andere gelegenheden. Een lijst met publicaties is te vinden op de volgende pagina.

Zijn natuurkundige opleiding genoot Jacob aan de Universiteit Twente. De studie Technische Natuurkunde werd afgerond met een stage-onderzoek aan de Università degli Studi di Pavía (Italië) en met een specialisatiejaar in de Chemische Fysica. Hiervoor volgde hij een gymnasium-β opleiding aan het R.K. Lyceum Dominicus College te Nijmegen.

List of Publications

Publications related to the work described in this thesis:

- J. P. Hoogenboom, D. L. J. Vossen, C. Faivre-Moskalenko, M. Dogterom, and A. van Blaaderen, *Patterning surfaces with colloidal particles using optical tweezers*, Applied Physics Letters **80**, 4828 (2002)   (Chapter 3)
- D. L. J. Vossen, J. P. Hoogenboom, K. Overgaag, and A. van Blaaderen, *Building two- and three-dimensional structures of colloidal particles on surfaces using optical tweezers and critical point drying*, Materials Research Society Symposium Proceedings **705**, Y 6.8.1 (2002)   (Chapter 3)
- J. P. Hoogenboom, A. K. van Langen-Suurling, J. Romijn, and A. van Blaaderen, *Growth of hard-sphere hcp crystal and non-close packed crystals by colloidal epitaxy*, submitted to Physical Review Letters   (Chapter 4)
- J. P. Hoogenboom, A. K. van Langen-Suurling, J. Romijn, and A. van Blaaderen, *Epitaxial growth of a hard-sphere hcp crystal and the effects of template-crystal (mis)match*, in preparation.   (Chapter 4)
- J. P. Hoogenboom, A. Yethiraj, A. K. van Langen-Suurling, J. Romijn, and A. van Blaaderen, *Epitaxial crystal growth of charged colloids*, submitted to Physical Review Letters.   (Chapter 5)
- J. P. Hoogenboom, E. de Bres, C. Rétif, M. van den Boer, A. K. van Langen-Suurling, J. Romijn, and A. van Blaaderen, *Template-induced colloidal crystallization during controlled drying*, in preparation.   (Chapter 6)
- J. P. Hoogenboom, P. Vergeer, and A. van Blaaderen, *A real-space analysis of colloidal crystallization in a gravitational field at a flat bottom wall*, in preparation.   (Chapter 7)
- J. P. Hoogenboom, P. Vergeer, D. Derks, and A. van Blaaderen, *Stacking faults in sedimented colloidal crystals*, submitted to Journal of Chemical Physics.   (Chapter 8)
- A. van Blaaderen, K. P. Velikov, J. P. Hoogenboom, D. L. J. Vossen, A. Yethiraj, R. P. A. Dullens, T. van Dillen, and A. Polman, *Manipulating colloidal crystallization for photonic applications: from self-organization to do-it-yourself organization*, in: *Photonic crystals and light localization in the 21st century*, edited by C. M. Soukoulis (Kluwer, 2001), p. 239.
- A. van Blaaderen, J. P. Hoogenboom, D. L. J. Vossen, A. Yethiraj, A. van der Horst, K. Visscher, M. Dogterom, *Colloidal Epitaxy: playing with the boundary conditions of colloidal crystallization*, Faraday Discussions **123**/19 (2002), to be published.

Other publications:

- C. Strohhöfer, J. P. Hoogenboom, and A. Polman, *Diffration grating formation in ion-exchanged glass by ion-irradiation through a mask of colloidal particles*, submitted.
- J. P. Hoogenboom, H. L. Tepper, N. F. A. van der Vegt, and W. J. Briels, *Transport diffusion of argon in AlPO4-5 from equilibrium molecular dynamics simulations*, Journal of Chemical Physics **113**, 6875 (2000).
- H. L. Tepper, J. P. Hoogenboom, N. F. A. van der Vegt, and W. J. Briels, *Unidirectional diffusion of methane in AlPO4-5*, Journal of Chemical Physics **110**, 11511 (1999)

Bibliography

[1]   W. B. Russel, D. A. Saville, and W. R. Schowalter, *Colloidal dispersions* (Cambridge University Press, Cambridge, 1989).

[2]   D. Fennel Evans and H. Wennerström, *The colloidal domain: where physics, chemistry, biology, and technology meet* (VCH Publishers, New York, 1994).

[3]   G. Bosma, C. Pathmamanoharan, E. H. A. de Hoog, W. K. Kegel, A. van Blaaderen, and H. N. W. Lekkerkerker, *Preparation of monodisperse, fluorescent PMMA-Latex colloids by dispersion polymerization*, Journal of Colloid and Interface Science **245**, 292-300 (2002).

[4]   A. Vrij, E. A. Nieuwenhuis, H. M. Fijnaut, and W. G. M. Agterof, Faraday Discussions of the Chemical Society **65**, 101-113 (1978), and references cited

[5]   P. N. Pusey, in: *Liquids, freezing, and the glass transition (Les Houches Session LI, 1989)*, edited by D. Levesque, J. P. Hansen and J. Zinn-Justin (Elsevier, Amsterdam, 1990).

[6]   A. van Blaaderen, *Quantitative real-space analysis of colloidal structures and dynamics with confocal scanning light microscopy*, Progress in Colloid and Polymer Science **104**, 59-65 (1997).

[7]   A. D. Dinsmore, E. R. Weeks, V. Prasad, A. C. Levitt, and D. A. Weitz, *Three-dimensional confocal microscopy of colloids*, Applied Optics **40**, 4152-4159 (2001).

[8]   M. S. Elliot and W. C. K. Poon, *Conventional optical microscopy of colloidal suspensions*, Advances in Colloid and Interface Science **92**, 133-194 (2001).

[9]   E. J. W. Verweij and J. Th. G. Overbeek, *Theory on the stability of lyophobic colloids* (Elsevier, New York, 1948).

[10]   J. Israelachvili, *Intermolecular and surface forces* (Academic Press, San Diego, 1991).

[11]   W. K. Kegel and A. van Blaaderen, *Direct observation of dynamical heterogeneities in colloidal hard-sphere suspensions*, Science **287**, 290-293 (2000).

[12]   U. Gasser, E. R. Weeks, A. Schofield, P. N. Pusey, and D. A. Weitz, *Real-space imaging of nucleation and growth in colloidal crystallization*, Science **292**, 258-262 (2001).

[13]   A. K. Van Helden, J. W. Jansen, and A. Vrij, *Preparation and characterization of spherical monodisperse silica dispersions in nonaqueous solvents*, Journal of Colloid and Interface Science **81**, 354-368 (1981).

[14]   A. Vrij, J. W. Jansen, J. K. G. Dhont, C. Pathmamanoharan, M. M. Kops-Werkhoven, and H. M. Fijnaut, *Light scattering of colloidal dispersions in non-polar solvents at finite concentrations. Silica spheres as model particles for hard-sphere interactions*, Faraday Discussions **76**, 19-36 (1983).

[15]   S. Asakura and F. Oosawa, *On interaction between two bodies immersed in a solution of macromolecules*, Journal of Chemical Physics **22**, 1255-1256 (1954).

[16]   V. J. Anderson and H. N. W. Lekkerkerker, *Insights into phase transition kinetics from colloid science*, Nature **416**, 811-815 (2002).

[17]   U. Dassanayake, S. Fraden, and A. van Blaaderen, *Structure of electrorheological fluids*, Journal of Chemical Physics **112**, 3851-3858 (2000).

[18]   K. Zahn and G. Maret, *Two-dimensional colloidal structures responsive to external fields*, Current Opinion in Colloid & Interface Science **4**, 60-65 (1999).

[19]   E. M. Furst and A. P. Gast, *Micromechanics of dipolar chains using optical tweezers*, Physical Review Letters **82**, 4130-4133 (1999).

[20]   A. Yethiraj and A. van Blaaderen, in preparation.

170

[21]   J. G. Kirkwood, Journal of Chemical Physics **7**, 911 (1939).

[22]   D. Frenkel, *De tweede jeugd van entropie*, Radar **1**, 145-162 (1995).

[23]   W. W. Wood and J. D. Jacobson, *Preliminary results from a recalculation of the Monte Carlo equation of state of hard spheres*, Journal of Chemical Physics **27**, 1207-1208 (1957).

[24]   B. J. Alder and T. E. Wainwright, *Phase transition for a hard sphere system*, Journal of Chemical Physics **27**, 1208-1209 (1957).

[25]   W. Luck, M. Klier, and H. Wesslau, *Kristallisation uebermolekularer Bausteine*, Die Naturwissenschaften **14**, 485-494 (1963).

[26]   J. B. Jones, J. V. Sanders, and E. R. Segnit, *Structure of opal*, Nature **204**, 990-991 (1964).

[27]   S. Hachisu, Y. Kobayashi, and A. Kose, *Phase separation in monodisperse latices*, Journal of Colloid and Interface Science **42**, 342-348 (1973).

[28]   S. Hachisu and Y. Kobayashi, *Kirkwood-Alder transition in monodisperse latexes. II. Aqueous latexes at high electrolyte concentration*, Journal of Colloid and Interface Science **46**, 470-476 (1974).

[29]   P. N. Pusey and W. van Megen, Nature **320**, 340- (1986).

[30]   P. N. Pusey and W. Van Megen, *Observation of a glass transition in suspensions of spherical colloidal particles*, Physical Review Letters **59**, 2083-2086 (1987).

[31]   C. A. Murray and D. H. Van Winkle, *Experimental observation of two-stage melting in a classical two-dimensional screened coulomb system*, Physical Review Letters **58**, 1200-1203 (1987).

[32]   A. H. Marcus and S. A. Rice, *Phase transitions in a confined quasi-two-dimensional colloid suspension*, Physical Review E **55**, 637-656 (1997).

[33]   P. Karnchanaphanurach, B. H. Lin, and S. A. Rice, *Melting transition in a quasi-two-dimensional colloid suspension: Influence of the colloid-colloid interaction*, Physical Review E **61**, 4036-4044 (2000).

[34]   R. E. Kusner, J. A. Mann, J. Kerins, and A. J. Dahm, *2-Stage melting of a 2-dimensional colloidal lattice with dipole interactions*, Physical Review Letters **73**, 3113-3116 (1994).

[35]   K. Zahn, R. Lenke, and G. Maret, *Two-stage melting of paramagnetic colloidal crystals in two dimensions*, Physical Review Letters **82**, 2721-2724 (1999).

[36]   J. M. Kosterlitz and D. J. Thouless, Journal of Physical Chemistry **6**, 1181 (1973).

[37]   J. M. Kosterlitz and D. J. Thouless, Journal of Physical Chemistry **7**, 1046 (1974).

[38]   A. P. Young, *Melting and the vector Coulomb gas in two dimensions*, Physical Review B **19**, 1855-1866 (1979).

[39]   B. I. Halperin and D. R. Nelson, *Theory of two-dimensional melting*, Physical Review Letters **41**, 121-124 (1978).

[40]   K. J. Strandburg, *Bond-orientational order in condensed matter systems* (Springer-Verlag, New York, 1992).

[41]   A. Jaster, *Computer simulations of the two-dimensional melting transition using hard disks*, Physical Review E **59**, 2594-2602 (1999).

[42]   M. A. Bates and D. Frenkel, *Influence of vacancies on the melting transition of hard disks in two dimensions*, Physical Review E **61**, 5223-5227 (2000).

[43]   P. Bladon and D. Frenkel, *Dislocation unbinding in dense 2-dimensional crystals*, Physical Review Letters **74**, 2519-2522 (1995).

[44] A. Pertsinidis and X. S. Ling, *Diffusion of point defects in two-dimensional colloidal crystals*, Nature **413**, 147-150 (2001).

[45] A. Pertsinidis and X. S. Ling, *Equilibrium configurations and energetics of point defects in two-dimensional colloidal crystals*, Physical Review Letters **87** (9), art. no.-098303 (2001).

[46] B. Pansu, Pi. Pieranski, and Pa. Pieranski, *Structures of thin layers of hard spheres: high pressure limit*, Journal de Physique **45**, 331-339 (1984).

[47] M. Schmidt and H. Löwen, *Freezing between two and three dimensions*, Physical Review Letters **76**, 4552-4555 (1996).

[48] M. Schmidt and H. Löwen, *Phase diagram of hard spheres confined between two parallel plates*, Physical Review E **55**, 7228-7241 (1997).

[49] R. Zangi and S. A. Rice, *Phase transitions in a quasi-two-dimensional system*, Physical Review E **58**, 7529-7544 (1998).

[50] R. Zangi and S. A. Rice, *Nature of the transition from two- to three-dimensional ordering in a confined colloidal suspension*, Physical Review E **61**, 660-670 (2000).

[51] R. Zangi and S. A. Rice, *Hexagonal to square lattice conversion in bilayer systems*, Physical Review E **61**, 671-681 (2000).

[52] B. Pansu, P. Pieranski, and L. Strzelecki, Journal de Physique **44**, 531+ (1983).

[53] S. Neser, C. Bechinger, P. Leiderer, and T. Palberg, *Finite-size effects on the closest packing of hard spheres*, Physical Review Letters **79**, 2348-2351 (1997).

[54] E. B. Sirota, H. D. Ou-Yang, S. K. Sinha, P. M. Chaikin, J. D. Axe, and Y. Fujii, *Complete phase diagram of a charged colloidal system: A synchrotron X-ray scattering study*, Physical Review Letters **62**, 1524-1527 (1989).

[55] J. A. Weiss, D. W. Oxtoby, D. G. Grier, and C. A. Murray, *Martensitic Transition in a Confined Colloidal Suspension*, Journal of Chemical Physics **103**, 1180-1190 (1995).

[56] H. J. Schöpe, *Physikalische Eigenschaften kolloidaler Festkörper* (thesis), Fachbereich Physik, Johannes Gutenberg Universität, Mainz (2000).

[57] E. H. A. de Hoog, W. K. Kegel, A. van Blaaderen, and H. N. W. Lekkerkerker, *Direct observation of crystallization and aggregation in a phase-separating colloid-polymer suspension*, Physical Review E **6402**, 1407+, art. no. 021407 (2001).

[58] R. Tuinier and H. N. W. Lekkerkerker, *Polymer density around a sphere*, Macromolecules **35**, 3312-3313 (2002).

[59] P. G. Bolhuis and A. A. Louis, *How to derive and parameterize effective potentials in colloid- polymer mixtures*, Macromolecules **35**, 1860-1869 (2002).

[60] E. M. Furst and A. P. Gast, *Micromechanics of magnetorheological suspensions*, Physical Review E **61**, 6732-6739 (2000).

[61] A. van Blaaderen, R. Ruel, and P. Wiltzius, *Template-directed colloidal crystallization*, Nature **385**, 321-324 (1997).

[62] A. van Blaaderen and P. Wiltzius, *Growing large, well-oriented colloidal crystals*, Advanced Materials **9**, 833 (1997).

172

[63] M. Heni and H. Löwen, *Surface freezing on patterned substrates*, Physical Review Letters **85**, 3668-3671 (2000).

[64] M. Heni and H. Löwen, *Precrystallization of fluids induced by patterned substrates*, Journal of Physics-Condensed Matter **13**, 4675-4696 (2001).

[65] R. P. Feynman, *There's plenty of room at the bottom. An inivitation to enter a new field of physics*, presented at American Physical Society annual meeting, Pasadena, California (1959), *Engineering and Science (issue Feb. 1960)*, California Institute of Technology

[66] A. van Blaaderen, *Harde bollen, zachte materie, slimme materialen.* Inaugural lecture presented at: Universiteit Utrecht, to be published (2002).

[67] F. Caruso, R. A. Caruso, and H. Mohwald, *Nanoengineering of inorganic and hybrid hollow spheres by colloidal templating*, Science **282**, 1111-1114 (1998).

[68] G. Ibarz, L. Dahne, E. Donath, and H. Mohwald, *Smart micro- and nanocontainers for storage, transport, and release*, Advanced Materials **13**, 1324-1327 (2001).

[69] J. H. Holtz and S. A. Asher, *Polymerized colloidal crystal hydrogel films as intelligent chemical sensing materials*, Nature **389**, 829-832 (1997).

[70] S. A. Asher, J. Holtz, J. Weissman, and G. S. Pan, *Mesoscopically periodic photonic-crystal materials for linear and nonlinear optics and chemical sensing*, MRS Bulletin **23**, 44-50 (1998).

[71] L. Grondahl, B. J. Battersby, D. Bryant, and M. Trau, *Encoding combinatorial libraries: A novel application of fluorescent silica colloids*, Langmuir **16**, 9709-9715 (2000).

[72] A. Imhof and D. J. Pine, *Ordered macroporous materials by emulsion templating*, Nature **389**, 948-951 (1997).

[73] B. T. Holland, C. F. Blanford, and A. Stein, *Synthesis of macroporous minerals with highly ordered three-dimensional arrays of spheroidal voids*, Science **281**, 538-540 (1998).

[74] H. W. Deckman and J. H. Dunsmuir, *Natural lithography*, Applied Physics Letters **41**, 377-379 (1982).

[75] F. Burmeister, W. Badowsky, T. Braun, S. Wieprich, J. Boneberg, and P. Leiderer, *Colloid monolayer lithography-A flexible approach for nanostructuring of surfaces*, Applied Surface Science **145**, 461-466 (1999).

[76] C. L. Haynes and R. P. Van Duyne, *Nanosphere lithography: A versatile nanofabrication tool for studies of size-dependent nanoparticle optics*, Journal of Physical Chemistry B **105**, 5599-5611 (2001).

[77] Y. Lu, Y. D. Yin, and Y. N. Xia, *A self-assembly approach to the fabrication of patterned, two- dimensional arrays of microlenses of organic polymers*, Advanced Materials **13**, 34-37 (2001).

[78] M. H. Wu and G. M. Whitesides, *Fabrication of arrays of two-dimensional micropatterns using microspheres as lenses for projection photolithography*, Applied Physics Letters **78**, 2273-2275 (2001).

[79] R. Rosensweig, *Ferrohydrodynamics* (Cambridge University Press, Cambridge, 1985).

[80] M. J. Hostetler and R. W. Murray, *Colloids and self-assembled monolayers*, Current Opinion in Colloid & Interface Science **2**, 42-50 (1997).

[81] K. Visscher and S. M. Block, *Versatile optical traps with feedback control*, in: *Methods in Enzymology*, edited by R. B. Vallee (Academic Press, San Diego, 1997), Vol. 298, p. 460-489, and references cited.

[82] K. A. Ramirez-Aguilar and K. L. Rowlen, *Tip characterization from AFM images of nanometric spherical particles*, Langmuir **14**, 2562-2566 (1998).

[83] P. Mulvaney and M. Giersig, *Imaging nanosized gold colloids by atomic force microscopy: A direct comparison with transmission electron microscopy*, Journal of the Chemical Society-Faraday Transactions **92**, 3137-3143 (1996).

[84] A. van Blaaderen, K. P. Velikov, J. P. Hoogenboom, D. L. J. Vossen, A. Yethiraj, R. P. A. Dullens, T. van Dillen, and A. Polman, *Manipulating colloidal crystallization for photonic applications: from self-organization to do-it-yourself organization*,in *Photonic crystals and light localization in the 21st century*, edited by C. M. Soukoulis (Kluwer, 2001), p. 239-251.

[85] T. F. Krauss and R. M. De la Rue, *Photonic crystals in the optical regime - past, present and future*, Progress in Quantum Electronics **23**, 51-96 (1999).

[86] J. D. Joannopoulos, P. R. Villeneuve, and S. H. Fan, *Photonic crystals: Putting a new twist on light*, Nature **386**, 143-149 (1997).

[87] G. S. Pan, R. Kesavamoorthy, and S. A. Asher, *Optically nonlinear Bragg diffracting nanosecond optical switches*, Physical Review Letters **78**, 3860-3863 (1997).

[88] J. E. G. J. Wijnhoven and W. L. Vos, *Preparation of photonic crystals made of air spheres in titania*, Science **281**, 802-804 (1998).

[89] A. A. Zakhidov, R. H. Baughman, Z. Iqbal, C. X. Cui, I. Khayrullin, S. O. Dantas, I. Marti, and V. G. Ralchenko, *Carbon structures with three-dimensional periodicity at optical wavelengths*, Science **282**, 897-901 (1998).

[90] A. Blanco, E. Chomski, S. Grabtchak, M. Ibisate, S. John, S. W. Leonard, C. Lopez, F. Meseguer, H. Miguez, J. P. Mondia, G. A. Ozin, O. Toader, and H. M. van Driel, *Large-scale synthesis of a silicon photonic crystal with a complete three-dimensional bandgap near 1.5 micrometres*, Nature **405**, 437-440 (2000).

[91] Y. A. Vlasov, X. Z. Bo, J. C. Sturm, and D. J. Norris, *On-chip natural assembly of silicon photonic bandgap crystals*, Nature **414**, 289-293 (2001).

[92] A. Moroz, *Three-dimensional complete photonic-band-gap structures in the visible*, Physical Review Letters **83**, 5274-5277 (1999).

[93] K. P. Velikov, A. Moroz, and A. van Blaaderen, *Photonic crystals of core-shell colloidal particles*, Applied Physics Letters **80**, 49-51 (2002).

[94] C. Graf and A. van Blaaderen, *Metallodielectric colloidal core-shell particles for photonic applications*, Langmuir **18**, 524-534 (2002).

[95] I. V. Markov, *Crystal growth for beginners. Fundamentals of nucleation, crystal growth and epitaxy* (World Scientific Publishing, Singapore, 1995).

[96] H. L. Skriver, *Crystal structure from one-electron theory*, Physical Review B **31**, 1909-1923 (1985).

[97] A. T. Paxton, M. Methfessel, and H. M. Polatoglou, *Structural energy-volume relations in 1st-row transition-metals*, Physical Review B **41**, 8127-8138 (1990).

[98] W. Donner, N. Metoki, A. Abromeit, and H. Zabel, *Molecular-Beam-Epitaxy growth and structural characterization of high-quality single-crystal Co/Cr(001) superlattices*, Physical Review B **48**, 14745-14748 (1993).

[99] N. Metoki, W. Donner, and H. Zabel, *Grazing-Incidence X-Ray-scattering study of (001)-oriented high-quality epitaxial Co/Cr superlattices*, Physical Review B **49**, 17351-17359 (1994).

[100] Z. Q. Wang, S. H. Lu, Y. S. Li, F. Jona, and P. M. Marcus, *Epitaxial growth of a metastable modification of copper with body-centered-cubic structure*, Physical Review B **35**, 9322-9325 (1987).

[101] H. Wormeester, E. Huger, and E. Bauer, H*cp and bcc Cu and Pd films*, Physical Review Letters **77**, 1540-1543 (1996).

[102] H. Wormeester, E. Huger, and E. Bauer, *Au on W(001): Change in structure and orientation*, Physical Review B **57**, 10120-10131 (1998).

[103] D. H. Van Winkle and C. A. Murray, *Layering in colloidal fluids near a smooth repulsive wall*, Journal of Chemical Physics **89**, 3885-3891 (1988).

[104] J. P. Hoogenboom, D. L. J. Vossen, C. Faivre-Moskalenko, M. Dogterom, and A. van Blaaderen, *Patterning surfaces with colloidal particles using optical tweezers*, Applied Physics Letters **80**, 4828-4830 (2002), Chapter 3 of this thesis.

[105] S. Ito, H. Yoshikawa, and H. Masuhara, *Optical patterning and photochemical fixation of polymer nanoparticles on glass substrates*, Applied Physics Letters **78**, 2566-2568 (2001).

[106] J. Won, T. Inaba, H. Masuhara, H. Fujiwara, K. Sasaki, S. Miyawaki, and S. Sato, *Photothermal fixation of laser-trapped polymer microparticles on polymer substrates*, Applied Physics Letters **75**, 1506-1508 (1999).

[107] C. Mio and D. W. M. Marr, *Tailored surfaces using optically manipulated colloidal particles*, Langmuir **15**, 8565-8568 (1999).

[108] M. Heni and H. Löwen, *Interfacial free energy of hard-sphere fluids and solids near a hard wall*, Physical Review E **60**, 7057-7065 (1999).

[109] K.-H. Lin, J. C. Crocker, V. Prasad, A. Schofield, D. A. Weitz, T. C. Lubensky, and A. G. Yodh, *Entropically driven colloidal crystallization on patterned surfaces*, Physical Review Letters **85**, 1770-1773 (2000).

[110] O. Pouliquen, M. Nicolas, and P. D. Weidman, *Crystallization of non-Brownian spheres under horizontal shaking*, Physical Review Letters **79**, 3640-3643 (1997).

[111] P. A. Kralchevsky and N. D. Denkov, *Capillary forces and structuring in layers of colloid particles*, Current Opinion in Colloid & Interface Science **6**, 383-401 (2001).

[112] Y. N. Xia, D. Qin, and Y. D. Yin, *Surface patterning and its application in wetting/dewetting studies*, Current Opinion in Colloid & Interface Science **6**, 54-64 (2001).

[113] N. D. Denkov, O. D. Velev, P. A. Kralchevsky, I. B. Ivanov, H. Yoshimura, and K. Nagayama, *Mechanism of formation of 2-dimensional crystals from latex-particles on substrates*, Langmuir **8**, 3183-3190 (1992).

[114] N. D. Denkov, O. D. Velev, P. A. Kralchevsky, I. B. Ivanov, H. Yoshimura, and K. Nagayama, *2-Dimensional crystallization*, Nature **361**, 26-26 (1993).

[115] P. A. Kralchevsky, N. D. Denkov, V. N. Paunov, O. D. Velev, I. B. Ivanov, H. Yoshimura, and K. Nagayama, *Formation of 2-dimensional colloid crystals in liquid-films under the action of capillary forces*, Journal of Physics-Condensed Matter **6**, A395-A402 (1994).

[116] H. W. Deckman, J. H. Dunsmuir, S. Garoff, J. A. McHenry, and D. G. Peiffer, *Macromolecular self-organized assemblies*, Journal of Vacuum Science and Technology B **6**, 333-336 (1988).

[117] P. Jiang, J. F. Bertone, K. S. Hwang, and V. L. Colvin, *Single-crystal colloidal multilayers of controlled thickness*, Chemistry of Materials **11**, 2132-2140 (1999).

[118] Z. Z. Gu, A. Fujishima, and O. Sato, *Fabrication of high-quality opal films with controllable thickness*, Chemistry of Materials **14**, 760-765 (2002).

[119] Z.-Z. Gu, Q.-B. Meng, S. Hayami, A. Fujishima, and O. Sato, *Self-assembly of submicron particles between electrodes*, Journal of Applied Physics **90**, 2042-2044 (2001).

[120] L. M. Goldenberg, J. Wagner, J. Stumpe, B. R. Paulke, and E. Gornitz, *Ordered arrays of large latex particles organized by vertical deposition*, Langmuir **18**, 3319-3323 (2002).

[121] Y. H. Ye, F. LeBlanc, A. Hache, and V. V. Truong, *Self-assembling three-dimensional colloidal photonic crystal structure with high crystalline quality*, Applied Physics Letters **78**, 52-54 (2001).

[122] E. Kim, Y. N. Xia, and G. M. Whitesides, *Two- and three-dimensional crystallization of polymeric microspheres by micromolding in capillaries*, Advanced Materials **8**, 245-& (1996).

[123] S. M. Yang and G. A. Ozin, *Opal chips: vectorial growth of colloidal crystal patterns inside silicon wafers*, Chemical Communications, 2507-2508 (2000).

[124] Y. D. Yin, Y. Lu, B. Gates, and Y. N. Xia, *Template-assisted self-assembly: A practical route to complex aggregates of monodispersed colloids with well-defined sizes, shapes, and structures*, Journal of the American Chemical Society **123**, 8718-8729 (2001).

[125] W. K. Kegel, H. Reiss, and H. N. W. Lekkerkerker, *Freezing transition in very small systems of hard spheres*, Physical Review Letters **83**, 5298-5301 (1999).

[126] Y. H. Ye, S. Badilescu, V. V. Truong, P. Rochon, and A. Natansohn, *Self-assembly of colloidal spheres on patterned substrates*, Applied Physics Letters **79**, 872-874 (2001).

[127] D. K. Yi, M. J. Kim, and D. Y. Kim, *Surface relief grating induced colloidal crystal structures*, Langmuir **18**, 2019-2023 (2002).

[128] S. H. Park, D. Qin, and Y. Xia, *Crystallization of mesoscale particles over large areas*, Advanced Materials **10**, 1028-+ (1998).

[129] K. P. Velikov, C. G. Christova, R. P. A. Dullens, and A. van Blaaderen, *Layer-by-layer growth of binary colloidal crystals*, Science **296**, 106-109 (2002).

[130] K. M. Chen, X. Jiang, L. C. Kimerling, and P. T. Hammond, *Selective self-organization of colloids on patterned polyelectrolyte templates*, Langmuir **16**, 7825-7834 (2000).

[131] H. P. Zheng, I. Lee, M. F. Rubner, and P. T. Hammond, *Two component particle arrays on patterned polyelectrolyte multilayer templates*, Advanced Materials **14**, 569-572 (2002).

[132] I. Lee, H. P. Zheng, M. F. Rubner, and P. T. Hammond, *Controlled cluster size in patterned particle arrays via directed adsorption on confined surfaces*, Advanced Materials **14**, 572-577 (2002).

[133] J. Aizenberg, P. V. Braun, and P. Wiltzius, *Patterned colloidal deposition controlled by electrostatic and capillary forces*, Physical Review Letters **84**, 2997-3000 (2000).

[134] Q. Guo, C. Arnoux, and R. E. Palmer, *Guided assembly of colloidal particles on patterned substrates*, Langmuir **17**, 7150-7155 (2001).

[135] S. Friebel, J. Aizenberg, S. Abad, and P. Wiltzius, *Ultraviolet lithography of self-assembled monolayers for submicron patterned deposition*, Applied Physics Letters **77**, 2406-2408 (2000).

[136] P. Mesquida and A. Stemmer, *Attaching silica nanoparticles from suspension onto surface charge patterns generated by a conductive atomic force microscope tip*, Advanced Materials **13**, 1395-1398 (2001).

[137] L. M. Demers and C. A. Mirkin, *Combinatorial templates generated by dip-pen nanolithography for the formation of two-dimensional particle arrays*, Angewandte Chemie-International Edition **40**, 3069-3071 (2001).

[138] P. V. Braun, R. W. Zehner, C. A. White, M. K. Weldon, C. Kloc, S. S. Patel, and P. Wiltzius, *Epitaxial growth of high dielectric contrast three-dimensional photonic crystals*, Advanced Materials **13**, 721-724 (2001).

[139] Y. D. Yin and Y. N. Xia, *Growth of large colloidal crystals with their (100) planes oriented parallel to the surfaces of supporting substrates*, Advanced Materials **14**, 605-608 (2002).

[140] T. Wilson, *Confocal microscopy* (Academic Press, London, 1990).

[141] M. Minsky, Microscopy apparatus, U.S. patent 301467 (1961).

[142] M. Minsky, *Memoir on inventing the Confocal Scanning Microscope*, Scanning **10**, 128-138 (1988).

[143] J. K. Stevens, L. R. Mills, and J. E. Trogadis, *Three-dimensional confocal microscopy: Volume investigation of biological systems* (Academic Press, San Diego, 1994).

[144] M. H. Chestnut, *Confocal microscopy of colloids*, Current Opinion in Colloid & Interface Science **2**, 158-161 (1997).

[145] M. Gu, *Principles of three-dimensional imaging in confocal microscopes* (World Scientific, Singapore, 1996).

[146] M. Born and E. Wolf, *Principles of optics* (Cambridge University Press, Cambridge (UK), 1999).

[147] D. R. Sandison, D. W. Piston, and W. W. Webb, *Background rejection and optimization of signal to noise in confocal microscopy*, in: *Three-dimensional confocal microscopy: Volume investigation of biological systems*, edited by J. K. Stevens, L. R. Mills and J. E. Trogadis (Academic Press, San Diego, 1994).

[148] K. Ito, H. Yoshida, and N. Ise, *Void structure in colloidal dispersions*, Science **263**, 66-68 (1994).

[149] A. van Blaaderen and A. Vrij, *Synthesis and characterization of colloidal dispersions of fluorescent, monodisperse silica spheres*, Langmuir **8**, 2921-2931 (1992).

[150] N. A. M. Verhaegh and A. van Blaaderen, *Dispersions of rhodamine-labeled silica spheres - Synthesis, characterization, and fluorescence Confocal Scanning Laser Microscopy*, Langmuir **10**, 1427-1438 (1994).

[151] M. P. Lettinga, M. van Zandvoort, C. M. van Kats, and A. P. Philipse, *Phosphorescent colloidal silica spheres as tracers for rotational diffusion studies*, Langmuir **16**, 6156-6165 (2000).

[152] M. J. A. de Dood, B. Berkhout, C. M. van Kats, A. Polman, and A. van Blaaderen, *Acid-based synthesis of monodisperse rare-earth-doped colloidal SiO_2 spheres*, Chemistry of Materials, accepted for publication, (2002).

[153] W. Stöber, A. Fink, and E. J. Bohn, *Controlled growth of monodisperse silica spheres in the micron size range*, Journal of Colloid and Interface Science **26**, 62-69 (1968).

[154] H. Giesche, *Synthesis of monodispersed silica powders II. Controlled growth reaction and continuous production process*, Journal of the European Ceramic Society **14**, 205-214 (1994).

[155] A. van Blaaderen, J. van Geest, and A. Vrij, *Monodisperse colloidal silica spheres from tetraalkoxysilanes - Particle formation and growth-mechanism*, Journal of Colloid and Interface Science **154**, 481-501 (1992).

[156] A. van Blaaderen et al., in preparation.

[157] J. C. Crocker and D. G. Grier, *Methods of digital video microscopy for colloidal studies*, Journal of Colloid Interface Science **179**, 298 (1996).

[158] A. van Blaaderen, A. Imhof, W. Hage, and A. Vrij, *3-Dimensional imaging of submicrometer colloidal particles in concentrated suspensions using confocal scanning laser microscopy*, Langmuir **8**, 1514-1517 (1992).

[159] A. van Blaaderen and P. Wiltzius, *Real-Space Structure of Colloidal Hard-Sphere Glasses*, Science **270**, 1177-1179 (1995).

[160] E. R. Weeks, J. C. Crocker, A. C. Levitt, A. Schofield, and D. A. Weitz, *Three-dimensional direct imaging of structural relaxation near the colloidal glass transition*, Science **287**, 627-631 (2000).

[161] C. Graf, *Farbstoffmarkierte Polyorganosiloxan-μ-gele als neuartige Sondensysteme* (thesis), Fachbereich Chemie und Pharmazie, Johannes Gutenberg Universität, Mainz (1999).

[162] A. van Blaaderen, *From the de-Broglie to visible wavelengths - Manipulating electrons and photons with colloids*, MRS Bulletin **23**, 39-43 (1998).

[163] B. Michel, A. Bernard, A. Bietsch, E. Delamarche, M. Geissler, D. Juncker, H. Kind, J. P. Renault, H. Rothuizen, H. Schmid, P. Schmidt-Winkel, R. Stutz, and H. Wolf, *Printing meets lithography: Soft approaches to high-resolution printing*, IBM Journal of Research and Development **45**, 697-719 (2001).

[164] Y. N. Xia and G. M. Whitesides, *Soft lithography*, Angewandte Chemie-International Edition **37**, 551-575 (1998).

[165] S. Yasin, D. G. Hasko, and H. Ahmed, *Fabrication of < 5 nm width lines in poly(methylmethacrylate) resist using a water : isopropyl alcohol developer and ultrasonically-assisted development*, Applied Physics Letters **78**, 2760-2762 (2001).

[166] A. Golzhauser, W. Eck, W. Geyer, V. Stadler, T. Weimann, P. Hinze, and M. Grunze, *Chemical nanolithography with electron beams*, Advanced Materials **13**, 806-+ (2001).

[167] X. M. Lin, R. Parthasarathy, and H. M. Jaeger, *Direct patterning of self-assembled monolayers by electron beams*, Applied Physics Letters **78**, 1915-1917 (2001).

[168] A. Bernard, J. P. Renault, B. Michel, H. R. Bosshard, and E. Delamarche, *Microcontact printing of proteins*, Advanced Materials **12**, 1067-1070 (2000).

[169] P. Ghosh and R. M. Crooks, *Covalent grafting of a patterned, hyperbranched polymer onto a plastic substrate using microcontact printing*, Journal of the American Chemical Society **121**, 8395-8396 (1999).

[170] W. M. Lackowski, P. Ghosh, and R. M. Crooks, *Micron-scale patterning of hyperbranched polymer films by micro-contact printing*, Journal of the American Chemical Society **121**, 1419-1420 (1999).

[171] P. Ghosh, M. L. Amirpour, W. M. Lackowski, M. V. Pishko, and R. M. Crooks, *A simple lithographic approach for preparing patterned, micron- scale corrals for controlling cell growth*, Angewandte Chemie-International Edition **38**, 1592-1595 (1999).

[172] J. P. Hoogenboom, A. K. van Langen-Suurling, J. Romijn, and A. van Blaaderen, *Hard-sphere crystals with hcp and non-close packed structure grown by colloidal epitaxy*, Submitted (2002), Chapter 4 of this thesis

[173] J. P. Hoogenboom, A. Yethiraj, A. K. van Langen, J. Romijn, and A. van Blaaderen, *Epitaxial crystal growth of charged colloids*, Submitted (2002), Chapter 5 of this thesis

[174] A. Bietsch and B. Michel, *Conformal contact and pattern stability of stamps used for soft lithography*, Journal of Applied Physics **88**, 4310-4318 (2000).

[175] H. Schmid and B. Michel, *Siloxane polymers for high-resolution, high-accuracy soft lithography*, Macromolecules **33**, 3042-3049 (2000).

[176] G. S. Ferguson, M. Chaudhury, G. B. Sigal, and G. M. Whitesides, *Contact adhesion of thin gold films on elastomeric supports: cold welding under ambient conditions*, Science **253**, 776-777 (1991).

[177] S. A. Maier, M. L. Brongersma, P. G. Kik, S. Meltzer, A. A. G. Requicha, and H. A. Atwater, *Plasmonics - A route to nanoscale optical devices*, Advanced Materials **13**, 1501-1505 (2001).

[178] A. N. Shipway, E. Katz, and I. Willner, *Nanoparticle arrays on surfaces for electronic, optical, and sensor applications*, Chemphyschem **1**, 18-52 (2000).

[179] O. D. Velev and E. W. Kaler, *In situ assembly of colloidal particles into miniaturized biosensors*, Langmuir **15**, 3693-3698 (1999).

[180] S. I. Bozhevolnyi, J. Erland, K. Leosson, P. M. W. Skovgaard, and J. M. Hvam, *Waveguiding in surface plasmon polariton band gap structures*, Physical Review Letters **86**, 3008-3011 (2001).

[181] H. T. Miyazaki, H. Miyazaki, K. Ohtaka, and T. Sato, *Photonic band in two-dimensional lattices of micrometer-sized spheres mechanically arranged under a scanning electron microscope*, Journal of Applied Physics **87**, 7152-7158 (2000).

[182] A. Ashkin, J. M. Dziedic, J. E. Bjorkholm, and S. Chu, *Observation of a single-beam gradient force optical trap for dielectric particles*, Optics Letters **11**, 288-290 (1986).

[183] T. N. Buican, M. J. Smyth, H. A. Crissman, G. C. Salzman, C. C. Stewart, and J. C. Martin, *Automated single-cell manipulation and sorting by light trapping*, Applied Optics **26**, 5311-5316 (1987).

[184] L. M. Liz-Marzan, M. Giersig, and P. Mulvaney, Langmuir **12**, 4329 (1996).

[185] D. L. J. Vossen, M. J. A. de Dood, T. van Dillen, T. Zijlstra, E. van der Drift, A. Polman, and A. van Blaaderen, *Novel method for solution growth of thin silica films from tetraethoxysilane*, Advanced Materials **12**, 1434-1437 (2000).

[186] G. Decher, J. D. Hong, and J. Schmitt, *Buildup of ultrathin multilayer films by a self-assembly process .3. Consecutively alternating adsorption of anionic and cationic polyelectrolytes on charged surfaces*, Thin Solid Films **210**, 831-835 (1992).

[187] F. Caruso, *Nanoengineering of particle surfaces*, Advanced Materials **13**, 11-22 (2001).

[188] D. L. J. Vossen, J. P. Hoogenboom, K. Overgaag, and A. van Blaaderen, *Building two- and three-dimensional structures of colloidal particles on surfaces using optical tweezers and critical point drying*, Materials Research Society Symposium Proceedings **705**, Y 6.8.1 (2002)

[189] P. N. Pusey, W. van Megen, P. Bartlett, B. J. Ackerson, J. G. Rarity, and S. M. Underwood, *Structure of crystals of hard colloidal spheres*, Physical Review Letters **63**, 2753-2756 (1989).

[190] T. Palberg, *Colloidal crystallization dynamics*, Current Opinion in Colloid & Interface Science **2**, 607-614 (1997).

[191] D. G. Grier and C. A. Murray, *The microscopic dynamics of freezing in supercooled colloidal fluids*, Journal of Chemical Physics **100**, 9088-9095 (1994).

[192] S. H. Park and Y. N. Xia, *Assembly of mesoscale particles over large areas and its application in fabricating tunable optical filters*, Langmuir **15**, 266-273 (1999).

[193] M. Holgado, F. Garcia-Santamaria, A. Blanco, M. Ibisate, A. Cintas, H. Miguez, C. J. Serna, C. Molpeceres, J. Requena, A. Mifsud, F. Meseguer, and C. Lopez, *Electrophoretic deposition to control artificial opal growth*, Langmuir **15**, 4701-4704 (1999).

[194] L. V. Woodcock, *Entropy difference between the face-centred cubic and hexagonal close-packed crystal structures*, Nature **385**, 141-143 (1997).

[195] P. G. Bolhuis, D. Frenkel, S. C. Mau, and D. A. Huse, *Entropy difference between crystal phases*, Nature **388**, 235-236 (1997).

[196] L. V. Woodcock, *Entropy difference between crystal phases - Reply*, Nature **388**, 236-237 (1997).

[197] A. D. Bruce, N. B. Wilding, and G. J. Ackland, *Free energy of crystalline solids: A lattice-switch Monte Carlo method*, Physical Review Letters **79**, 3002-3005 (1997).

[198] S. C. Mau and D. A. Huse, *Stacking entropy of hard-sphere crystals*, Physical Review E **59**, 4396-4401 (1999).

[199] S. Pronk and D. Frenkel, *Can stacking faults in hard-sphere crystals anneal out spontaneously?*, Journal of Chemical Physics **110**, 4589-4592 (1999).

[200] J. X. Zhu, M. Li, R. Rogers, W. Meyer, R. H. Ottewill, W. B. Russell, and P. M. Chaikin, *Crystallization of hard-sphere colloids in microgravity*, Nature **387**, 883-885 (1997).

[201] N. A. M. Verhaegh, J. S. van Duijneveldt, A. van Blaaderen, and H. N. W. Lekkerkerker, *Direct observation of stacking disorder in a colloidal crystal*, Journal of Chemical Physics **102**, 1416-1421 (1995).

[202] M. S. Elliot, B. T. F. Bristol, and W. C. K. Poon, *Direct measurement of stacking disorder in hard-sphere colloidal crystals*, Physica A **235**, 216-223 (1997).

[203] Z. D. Cheng, W. B. Russell, and P. M. Chaikin, *Controlled growth of hard-sphere colloidal crystals*, Nature **401**, 893-895 (1999).

[204] W. K. Kegel and J. K. G. Dhont, *"Aging" of the structure of crystals of hard colloidal spheres*, Journal of Chemical Physics **112**, 3431-3436 (2000).

[205] Y. A. Vlasov, V. N. Astratov, A. V. Baryshev, A. A. Kaplyanskii, O. Z. Karimov, and M. F. Limonov, *Manifestation of intrinsic defects in optical properties of self-organized opal photonic crystals*, Physical Review E **61**, 5784-5793 (2000).

[206] V. Yannopapas, N. Stefanou, and A. Modinos, *Effect of stacking faults on the optical properties of inverted opals*, Physical Review Letters **86**, 4811-4814 (2001).

[207] J. S. van Duijneveldt, J. K. G. Dhont, and H. N. W. Lekkerkerker, *Expansion and crystallization of a sediment of charged colloidal spheres*, Journal of Chemical Physics **99**, 6941-6949 (1993).

[208] C. A. Murray, *Experimental studies of melting and hexatic order in two-dimensional colloidal suspensions*, in *Bond-orientational order in condensed matter systems*, edited by K. J. Strandburg (Springer-Verlag, New York, 1992), p. 137-215.

[209] F. A. Lindemann, Physikalisches Zeitschrift **11**, 609 (1910).

[210] F. El Azhar, M. Baus, J. P. Ryckaert, and E. J. Meijer, *Line of triple points for the hard-core Yukawa model: A computer simulation study*, Journal of Chemical Physics **112**, 5121-5126 (2000).

[211] S. Alexander and J. P. McTague, *Should all crystals be bcc? Landau theory of solidification and crystal nucleation*, Physical Review Letters **41**, 702-705 (1978).

[212] P. R. ten Wolde, M. J. Ruiz-Montero, and D. Frenkel, *Numerical evidence for bcc ordering at the surface of a critical fcc nucleus*, Physical Review Letters **75**, 2714-2717 (1995).

[213] L. Antl, J. W. Goodwin, R. D. Hill, R. H. Ottewill, S. M. Owens, S. Papworth, and J. A. Waters, Colloid and Surfaces **17**, 67 (1986).

[214] M. Yamaki, J. Higo, and K. Nagayama, *Size-dependent separation of colloidal particles in 2-dimensional convective self-assembly*, Langmuir **11**, 2975-2978 (1995).

[215] R. D. Deegan, O. Bakajin, T. F. Dupont, G. Huber, S. R. Nagel, and T. A. Witten, *Capillary flow as the cause of ring stains from dried liquid drops*, Nature **389**, 827-829 (1997).

[216] T. Biben, R. Ohnesorge, and H. Löwen, *Crystallization in sedimentation profiles of hard-spheres*, Europhysics Letters **28**, 665-670 (1994).

[217] S. Auer and D. Frenkel, *Prediction of absolute crystal-nucleation rate in hard-sphere colloids*, Nature **409**, 1020-1023 (2001).

[218] S. Dittrich, *Phase transitions and critical phenomena* (Academic Press, London, 1988).

[219] D. J. Courtemanche and F. van Swol, *Wetting state of a crystal-fluid system of hard-spheres*, Physical Review Letters **69**, 2078-2081 (1992).

[220] D. J. Courtemanche, T. A. Pasmore, and F. van Swol, *A Molecular-Dynamics study of prefreezing hard-spheres at a smooth hard-wall*, Molecular Physics **80**, 861-875 (1993).

[221] K. E. Davis, W. B. Russel, and W. J. Glantschnig, *Disorder-to-order transition in settling suspensions of colloidal silica - X-Ray measurements*, Science **245**, 507-510 (1989).

[222] M. Brunner, C. Bechinger, W. Strepp, V. Lobaskin, and H. H. van Grünberg, *Density-dependant pair-interactions in 2D colloidal suspensions*, Europhysics Letters (to be published).

[223] A. H. Marcus and S. A. Rice, *Observations of first-order liquid-to-hexatic and hexatic-to- solid phase transitions in a confined colloid suspension*, Physical Review Letters **77**, 2577-2580 (1996).

[224] J. L. Barrat, T. Biben, and J. P. Hansen, *Barometric equilibrium as a probe of the equation of state of colloidal suspensions*, Journal of Physics-Condensed Matter **4**, L11-L14 (1992).

[225] R. Piazza, T. Bellini, and V. Degiorgio, *Equilibrium sedimentation profiles of screened charged colloids - a test of the hard-sphere equation of state*, Physical Review Letters **71**, 4267-4270 (1993).

[226] M. A. Rutgers, J. H. Dunsmuir, J. Z. Xue, W. B. Russel, and P. M. Chaikin, *Measurement of the hard-sphere equation of state using screened charged polystyrene colloids*, Physical Review B **53**, 5043-5046 (1996).

[227] H. Löwen, *Dynamical criterion for two-dimensional freezing*, Physical Review E **53**, R29-R32 (1996).

[228] K. Zahn and G. Maret, *Dynamic criteria for melting in two dimensions*, Physical Review Letters **85**, 3656-3659 (2000).

[229] M. M. Hurley and P. Harrowell, *Kinetic structure of a 2-dimensional liquid*, Physical Review E **52**, 1694-1698 (1995).

[230] H. Löwen, T. Palberg, and R. Simon, *Dynamic criterion for freezing of colloidal liquids*, Physical Review Letters **70**, 1557-1560 (1993).

[231] J. P. Hoogenboom, D. Derks, P. Vergeer, and A. van Blaaderen, *Stacking faults in colloidal crystals grown by sedimentation*, Submitted (2002), Chapter 8 of this thesis.

[232] C. Dux and H. Versmold, *Light diffraction from shear ordered colloidal dispersions*, Physical Review Letters **78**, 1811-1814 (1997).

[233] H. Versmold, *Neutron-diffraction from shear ordered colloidal dispersions*, Physical Review Letters **75**, 763-766 (1995).

[234] W. L. Vos, M. Megens, C. M. van Kats, and P. Bosecke, *X-ray diffraction of photonic colloidal single crystals*, Langmuir **13**, 6004-6008 (1997).

[235] H. Miguez, F. Meseguer, C. Lopez, A. Mifsud, J. S. Moya, and L. Vazquez, *Evidence of fcc crystallization of SiO_2 nanospheres*, Langmuir **13**, 6009-6011 (1997).

[236] B. Y. Cheng, P. G. Ni, C. J. Jin, Z. L. Li, D. Z. Zhang, P. Dong, and X. C. Guo, *More direct evidence of the fcc arrangement for artificial opal*, Optics Communications **170**, 41-46 (1999).

[237] J. P. Hoogenboom, P. Vergeer, and A. van Blaaderen, *A real-space analysis of colloidal crystallization in a gravitational field at a flat bottom wall*, Submitted (2002), Chapter 7 of this thesis.

[238] S. Auer and D. Frenkel, *Crystallization of weakly charged colloidal spheres: A numerical study*, Journal of Physics-Condensed Matter **14**, 1-14 (2002).

[239] A. N. Jackson, A. D. Bruce, and G. J. Ackland, *Lattice-switch Monte Carlo method: Application to soft potentials*, Physical Review E **65**, art. no.-036710 (2002).

[240] B. W. Van de Waal, *Can the Lennard-Jones solid be expected to be fcc?*, Physical Review Letters **67**, 3263-3266 (1991).

[241] T. Palberg, W. Hartl, U. Wittig, H. Versmold, M. Wurth, and E. Simnacher, *Continuous deionization of latex suspensions*, Journal of Physical Chemistry **96**, 8180-8183 (1992).

[242] K. Ohtaka and Y. Tanabe, *Photonic bands using vector spherical waves .2. Reflectivity, coherence and local field*, Journal of the Physical Society of Japan **65**, 2276-2284 (1996).

'And when you have wrought and laboured
Till the gift is all complete
You may humbly lay your offerings
At the Lady's feet.

Should her mood perchance be gracious –
With disdainful smiling pride,
She will place it with her trinkets
Glittering at her side'

(Adelaide Procter)